The Formation Mechanisms of Classical Emission Line Stars

Dissertation
zur
Erlangung des Doktorgrades (Dr. rer. nat.)
der
Mathematisch-Naturwissenschaftlichen Fakultät
der
Rheinischen Friedrich-Wilhelms-Universität Bonn

von
Ben James Hastings
aus
Chester, United Kingdom

Bonn, 2023

Abstract

Classical emission line stars are known fast rotators hosting a decretion disc in which emission lines are formed. Since their discovery in 1866, the formation mechanism of this class of stars has proved difficult to identify. A robust understanding of how emission line stars ultimately came to be would constrain both the stars' previous and future evolution. Classical emission line stars make up a significant proportion of massive stars, with recent observations showing that around one third of massive stars display emission lines, thus knowledge of these stars is important for the study of massive stars in general.

To explain the rapid rotation, two formation channels exist; single and binary star evolution respectively. The single star formation channel is whereby a star with a given amount of seed angular momentum undergoes structural changes during its evolution that cause the centrifugal force at the equator to approach the gravitational force, causing the star to effectively spin up. A fast rotating star is formed through binary evolution via mass-transfer, whereby an accreting star gains angular momentum as well as mass, and thus can attain large rotational velocities.

This thesis investigates the contributions of both the single and binary star evolution channels to the observed population of emission line stars. Numerical models of single rotating stars were used to predict the rotational velocities of a stellar population. The failure of the models to explain the large number of emission line stars found in open clusters suggests that binary evolution to be the dominant formation mechanism.

As the outcome of binary star evolution is sensitive to uncertain physics, a simple and flexible analytic model of binary evolution was developed. Comparison of the model with an observed population found a good match between the two, but only when the model contains certain specific assumptions, which may or may not be realised in nature, such as very inefficient mass-transfer.

Both formation mechanisms suffer from distinct uncertainties. For the single star channel, stellar winds, which govern rotational evolution, are affected by rapid rotation in ways which are often ignored. A self-consistent description of the wind of a fast rotator revealed however the effects to be minimal and the spin evolution was not expected to differ significantly from previous models. In the binary channel, mass-transfer efficiency was constrained using stripped-star binaries. It was found that around half of the mass removed from the donor star is accreted by its companion, challenging the validity of the assumptions required for the binary channel to dominate.

Based on the theoretical arguments set out in each of the four chapters, this thesis cannot fully endorse one formation channel over the other, with the most probable situation being that both channels co-exist to produce emission line stars.

Contents

5   Constraints on mass-transfer from Be + stripped star binaries   89

6   Summary and Outlook   103

Bibliography   107

A   Appendix to Chapter 2   127

B   Appendix to Chapter 3   143

C   Appendix to Chapter 4   157

List of Figures   171

List of Tables   175

Introduction

If there is one common experience that binds all cultures, then surely it is to gaze upon the stars, to see them twinkle and dance. Even the modern city dweller, despite their protestations, can taste this joy. The night sky has served as inspiration for countless endeavours, from visual arts to music to the focus of this work: science. For centuries the positions and brightness of the stars have been measured with remarkable ingenuity and dedication. Ancient astronomers, most notably the Greeks, are credited with the observation that the "wandering stars" (planētēs in ancient Greek) trace a curious pattern with their motion across the night sky, as shown in Fig. 1.1. Mars for example moves from west to east most of the time, but for 72 out of every 780 days, Mars moves in the opposite direction across the sky. This is known as retrograde motion. Every planet exhibits such behaviour, which can be explained by placing the Earth and other planets on orbits around the Sun. When the Earth on its orbit moves past another planet, the motion of the planet appears to change direction on the sky. It was thus deduced by the ancient Greeks that the Earth and all other planets orbit around the Sun. Hence through this simple, yet powerful observation we can determine the structure of our local environment.

Instead of focusing on the apparent positions of stars, we may study how bright they are. For this one must have a keen eye, as ancient Arab astronomers did to notice the regular periodic flickering of a certain "daemon star". Every 2.9 days the second brightest star in the constellation Perseus dims suddenly and dramatically, after which it quickly recovers to its original brightness, as shown in Fig. 1.2. Against a company of seemingly immovable and dependably steady stars, this behaviour did not sit well with those who witnessed it. The three thousand year old Cairo Calendar predicts whether a day should be lucky or unlucky, with the unlucky periods matching seamlessly to the times of minimum brightness of the star (Jetsu et al., 2013). With period just less than 3 days, the unlucky days are depressingly common. It was named the daemon's head, or ra's al-ghūl in Arabic (interestingly this is where the English word ghoul comes from). The star's modern name, Algol is taken from this Arabic name and is the eponym for a class of stars which show similar variations. Although Algol's brightness varies by a factor of three, it is a testament to the skill of ancient astronomers that the next variable star to be discovered was not until 1596 [1]. Algol kept its secrets until the 1880s, when the fundamental nature of the star's variability was determined (the impatient may skip to Section 1.6.1).

These two examples highlight how astronomy was practised from the beginnings of civilisation until the middle of the 19th century: by studying the movements of objects upon the sky or charting

---

[1] Some evidence suggests unconvincingly that Mira was known to Chinese and Korean astronomers. However the first proven discovery was that by Fabricius in 1596 (Hoffleit, 1997)
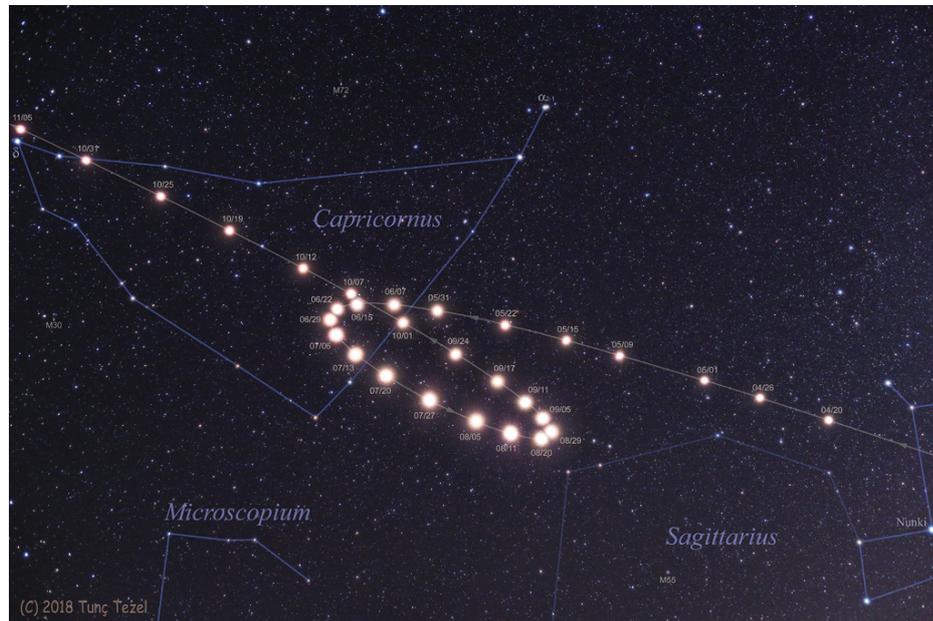
Figure 1.1: The motion of Mars across the sky from late April to November 2018 with the retrograde loop visible. Separate images were taken on the dates indicated (note American date format) and stacked. Constellations are marked. **Image credit:** Tunç Tezel
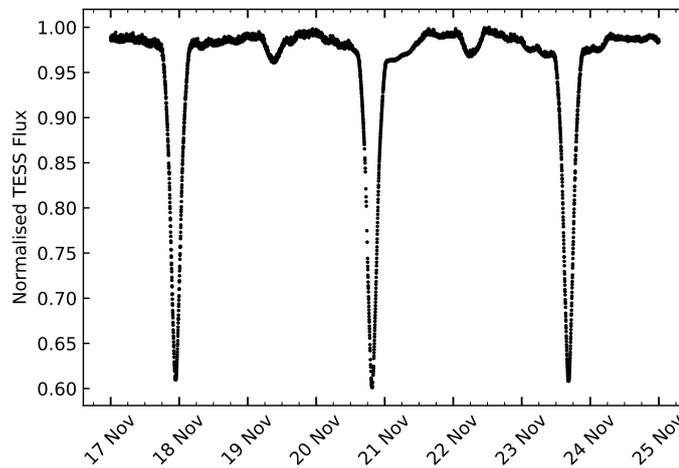
Figure 1.2: The lightcurve of Algol as observed by the Transiting Exoplanet Survey Satellite (TESS) in November 2019, showing 3 minima. The y-axis shows the flux normalised to the maximum over the displayed period of time. Plotted with publicly available data from the TESS archive.

Figure 1.3: The solar spectrum with Fraunhofer lines as drawn by Joseph von Fraunhofer. Image credit: Deutsches Museum, Archiv, BN 43952

their brightness. Sometimes, in the case of comets for example, both can be done simultaneously. Indeed from only these two simple measurements, we have learnt about novae and supernovae, the laws of gravity, discovered planets and comets and have come to firmly understand our Solar System.

In the mid 1800s, scientists had discovered a new and powerful way to analyse starlight that would shape the future of astronomy and revolutionise our understanding of the stars. This method is spectroscopy and its development shall be charted in the next section.

1.1 Stellar spectroscopy

Around two centuries ago astronomers gained a new and exceedingly powerful tool to explore the sky with; the spectroscope. Even more importantly, they also understood how to interpret the device's measurements in order to gain new insights into the motions, properties and even chemical make-up of the stars. Spectroscopy hailed the modern era of astrophysics. Ultimately a spectroscope allows us to measure the colours of an object in an incredibly fine and quantitative way. Take for example a rosy red apple and the red breast of a robin. Both are of course red, but how red? Is one more red than the other? Is red the only colour that one sees? To the human eye, these questions are almost impossible to answer, or even for two people to agree upon the same answer. However if we could split up the light from each object into its principal components, we would be able to analyse the colour in great detail. This is what spectroscopy is. Light from a source is split using either a prism or diffraction grating such that intensity can be mapped according to the light's wavelength.

Initial understanding of the components of light came from Isaac Newton, who realised that white light is in fact a combination of a multitude of colours. As technology improved, scientists were able to study light in greater detail. In 1802 William Hyde Wollaston was the first to notice that when sunlight is split up, several dark gaps can be observed in the spectrum. That is to say that sunlight is missing several very specific colours. These gaps appear as lines when the spectrum is projected onto a screen and as such they are known as Fraunhofer lines after glass-maker Joseph von Fraunhofer who observed and studied them in great detail from 1814. Fraunhofer painstakingly charted over 500 lines in the solar spectrum (see Fig. 1.3) and also worked on starlight from other stars.

Secchi class	Description	Example stars
I	White and blue stars with only a few broad lines	Vega, Altair
II	Yellow stars with several metallic lines	Sun, Capella
III	Orange-red stars with very complex spectra	Betelgeuse, Antares

Table 1.1: The original three spectral classes proposed by Angelo Secchi in the mid 1860s.

By the 1820s, after significant progress had been made on improving the instruments, the fainter light of stars aside from the sun could be studied spectroscopically. It was noted that not all stars display the same lines. This lead Fraunhofer to conclude that the lines are not produced by the Earth's atmosphere but are, at least in part, an inherent property of the starlight itself. Sadly Fraunhofer would never find out what caused these dark lines, as he died in 1826 aged 39 from tuberculosis.

Gradually, a frustration grew within the astronomical community, as without knowing the physical origin of spectral lines, their existence remains a mere novelty. Fraunhofer himself hinted at broad classifications based on a star's colour. White stars (e.g. Vega, Sirius) seem to show very few spectral features, whereas red stars (e.g. Betelgeuse) possess a dense forest of lines. However enthusiasm for collecting and comparing spectra seems to have been lacking until as late as the 1860s.

This changed dramatically when physicists Robert Bunsen and Gustav Kirchhoff were able to determine what produces the Fraunhofer lines. Utilising the now commonplace Bunsen-burner, they established a link between a chemical element and the spectrum emitted when that element is burnt. They concluded that each element has a unique fingerprint that is apparent in the light it gives off when burnt (Kirchhoff and Bunsen, 1860). This meant that by comparing spectra from the stars to the results of burning elements in a laboratory, the chemical compositions of the stars could be determined. Armed with this crucial knowledge, the race was now on to discover what the stars are made of.

One of the pioneers of early stellar spectroscopy was Father Angelo Secchi, a catholic priest working in the observatory of the Roman College. He was the first to formally declare a classification scheme of stars based upon their spectra. Initially he proposed three distinct classes, tabulated in Table 1.1, according to the spectral morphology. Secchi's scheme shows us how different spectra can be from one another, ranging from being almost featureless to containing dense patches of lines. It was also noticed that the star's colour seemed to be directly related to the spectrum, with red stars displaying the most complex spectra and blue-white stars the simplest.

The spectral classification system that modern astronomers use is descended not from Secchi's classes but from the Draper system. The Draper Catalogue of stellar spectra (Pickering, 1890) was an ambitious project to photograph and classify the spectra of over 10,000 stars from Harvard, USA. A new classification system was devised based upon the strength of hydrogen lines in the spectra, running alphabetically from A to M. Those stars with the most apparent hydrogen lines were designated "A", and those with no hydrogen lines at all were "M". The Secchi class I corresponds to Draper classes A-D, class II is equivalent to Draper classes E-L and Secchi class III is Draper class M. The Draper Catalogue is the fruit of the enormous efforts made mostly by Williamina Fleming, Annie Jump Cannon and a group of women known as the Harvard computers who quantitatively assessed many thousands of spectra to assign classifications.

The modern classification scheme is known as the Harvard system and retains only the classes O,B,A,F,G,K,M. After the development of quantum and statistical mechanics that gave scientists an understanding of the basic physical processes in atoms and ions that produce spectral lines, the
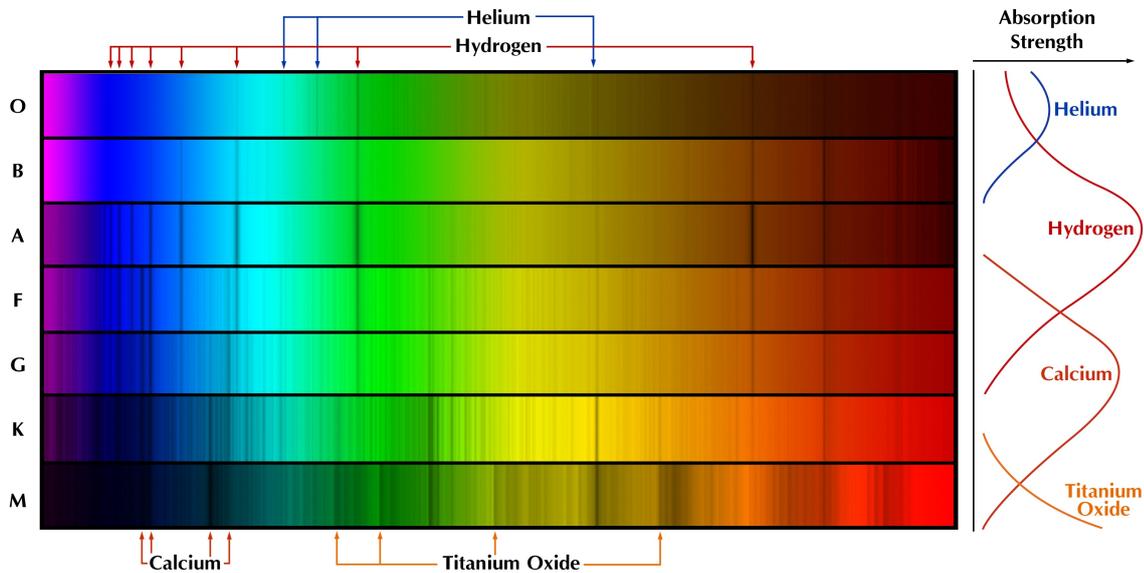
Figure 1.4: The optical spectra of stars in classes of the Harvard stellar classification system. Features arising from various species are marked. The right axis shows the dominating species which forms each spectrum's lines. Image credit: National Optical Astronomy Observatory

ordering of the classes was changed to O,B,A,F,G,K,M. Thus the need to reclassify of tens of thousands of stars was avoided. In her visionary doctoral thesis, Cecilia Payne showed that the classes can be arranged into a temperature sequence where O class stars are the hottest and M the coolest.

The spectral lines are the result of electronic transitions between energy levels in ions or atoms. In the very hottest stars, the O stars, all species except helium are fully ionised, thus it is only helium that can offer any strong spectral features. Going to cooler stars, neutral hydrogen can form in the atmosphere in substantial quantities, so that it can be recognized in a spectrum - these are the A class stars, with the strongest hydrogen features as can be seen in the third spectrum from the top of Fig. 1.4. In even cooler stars, the temperatures are not sufficient enough to facilitate electronic transitions in hydrogen atoms, however photons in the stellar atmospheres can excite metals such as calcium and titanium oxide. Thus in the K and M stars, hydrogen lines are not seen but the spectrum does contain many features resulting from metals. Fig. 1.4 shows stellar spectra arranged from top to bottom in order of decreasing temperature, where one can see first the prevalence of helium lines in the hottest stars, then hydrogen lines dominating and lastly a forest of metal lines in the coolest stars.

The fundamental parameter that determines a star's surface temperature is the star's mass. More massive stars must battle with a larger gravitational force trying to compress the star. This results in a higher central temperature, increasing thermonuclear reaction rates which in turn increases the star's luminosity and thus produces a higher surface temperature. Hence the spectral sequence can also be interpreted as an approximate sequence of mass. This thesis focuses on B-type stars, which have masses of between 2 and 16 $M_\odot$ and effective temperatures in the range 10,000 - 30,000K (the Sun for comparison has an effective temperature of around 5000K).

Schreiben des Herrn Prof. *Secchi*, Dir. der Sternwarte des Collegio Romano, an den Herausgeber.

Dans ma dernière je vous annonçais la grande facilité d'observer les spectres stellaires avec la nouvelle construction de spectroscope que j'ai réussi à combiner. Bientôt j'espère de pouvoir vous envoyer une liste des objets examinés, mais pour le moment je ne pourrais différer davantage à vous signaler une particularité curieuse de l'étoile γ Cassiopée, unique jusqu'à présent. Celle-ci est que pendant que la grande majorité des étoiles blanches montre la raie *f* très-nette et large, et comme αLyre, Sirius etc., γ Cassiopée a à sa place une ligne lumineuse très-belle et bien plus brillante que tout le reste du spectre. La place de cette raie est, autant que j'en ai pu prendre des mesures, exactement coïncidente avec celle de *f*, et on peut très-bien en faire la comparaison avec l'étoile voisine β Cassiopée. La mesure je l'ai prise en plaçant une pointe de repère dans le chercheur et couvrant la raie dans la grande lunette avec la pointe micrométrique du spectroscope: si les deux lunettes sont portées de l'étoile γ à l'étoile β et placées de la même manière sur l'une et sur l'autre on

trouve que la position de la raie luisante de la première correspond à la raie obscure de la seconde. J'espère pouvoir faire ces mesures d'une manière plus exacte encore. En comparant ainsi l'étoile β Pégase on trouve que la *f* tombe sur une région noire des bandes que cette étoile présente. Du reste la bande luisante que montre γ Cassiopée, n'est pas unique, il y en a plusieurs autres, mais assez plus petites, et je ne les ai pas mesurées. Cette étoile présente donc un spectre inverse de celui du type ordinaire des étoiles blanches.

Pour vous donner une idée pratique de l'effet de cette bande je vous dirai que cette ligne brille sur le reste du spectre comme le groupe du magnésium brille sur le fond lumineux du spectre lorsqu'on brûle ce métal.

Dans une autre lettre les détails des autres étoiles. — M. *Respighi* a vérifié ces résultats et a même vu avec sa lunette de 5 pouces seulement plusieurs beaux spectres avec l'usage de ma combinaison.

Ro me, 1866 Août 23.   *A. Secchi.*

Figure 1.5: The publication announcing the discovery of the first Be star from Secchi (1866)

1.2 A historical introduction to classical emission line stars

It must be noted that there are several classes of stars which exhibit emission lines (Wolf-Rayet stars, interacting binaries such as β Lyrae and Herbig Ae stars). Classical emission line stars are formally classified as main-sequence stars displaying emission (i.e. bright) features in the spectra. These features are most often observed in hydrogen lines. Classical emission line stars are set apart from other types of stars with emission lines by the facts that they are hydrogen-burning and host a decretion disc that is maintained at least partly by rapid rotation.

The emission line phenomenon is concentrated mostly on stars of spectral class B, and hence emission line stars are also known as Be stars. In this section, an overview is given of the two most significant findings related to Be stars: their discovery and the inference of the decretion disc.

1.2.1 Discovery

In 1866 Angelo Secchi pointed his new high quality spectroscope at the star γ Cassiopeiae and noticed that, in the opposite fashion to every other star previously observed, γ Cassiopeiae displayed bright lines instead of dark ones. Secchi immediately understood the gravity of his observation and wrote to the German journal Astronomische Nachrichten (Astronomical News), albeit in French. This publication is given in its entirety in Fig. 1.5. A complete translation reads:

In my last correspondence I told you how easy it is to observe stellar spectra with the new spectroscope that I have managed to construct. Soon I hope to be able to send you a list of the objects examined, but for the moment I could not delay any longer in pointing out to you a curious peculiarity of the star γ Cassiopeiae, which remains unique. This is that while the vast majority of the white stars show the very clear and broad f-line, such

as α Lyrae, Sirius etc., γ Cassiopeiae has in its place a very beautiful bright line much brighter than the rest of the spectrum. This line is, as far as I have been able to measure, exactly coincident with that of f, and one can very well make the comparison with the neighbouring star β Cassiopeiae. I took the measurement by placing a point of reference in the finder and covering the line in the large telescope with the micrometer point of the spectroscope: if the telescope is moved from the star γ to the star β, the position of the bright line of the first corresponds to the dark line of the second. I hope to be able to repeat these measurements in a more exact manner. By comparing with β Pegasi, the f line is found to fall on a dark region of the bands which this star presents. Of the rest, the bright band that Cassiopeiae displays is not unique, there are several others, but quite smaller, and I have not overlooked them. This star therefore presents an inverse spectrum to that of the ordinary type of white stars. To give you a practical idea of the effect of this line I will tell you that this line shines on the rest of the spectrum as the magnesium line shines when this metal is burned. In another letter I will expand on the details of other stars. - Mr. Respighi verified these results and saw the same with his 5-inch telescope several beautiful spectra with the use of my spectrograph.

Rome, 1866 August 23. A Secchi

But why do "normal" stars display only dark spectral lines? Dark spectral lines, known as absorption lines result from the fact that the outer atmospheres of stars are fairly transparent to radiation. Photons of all wavelengths radiate from the stellar interior outwards, passing through the atmosphere. Atomic species (atoms, ions and molecules) have distinctly defined electronic transitions. Electrons can be moved between energy levels by either absorbing or emitting a photon of equal energy to the transition energy. In the stellar atmosphere, species are absorbing photons of a specific wavelength in order to enter an excited state. The excited species is unstable and so decays back to the ground state and in the process emitting a photon. This photon is emitted in a random direction in space, meaning that it almost never makes it along the line of sight of the observer, instead it is scattered away. Photons whose energy does not correspond to an electronic transition are able to pass freely through the stellar atmosphere. Thus the stellar spectrum exhibits a lack of photons corresponding to a given transition energy, which produces an absorption line.

The opposite to an absorption line is an emission line. Secchi later found more stars with emission lines and added a fourth class to his stellar classification scheme for them. Today we denote the presence of emission lines with the letter "e" in the spectral class. Thus Be stars are simply stars of spectral class B with emission features. However Secchi did not understand the fundamental physical origins of the bright lines - this would be known to science 70 years after his discovery.

1.2.2 Decretion disc model

Throughout the late 19th and early 20th centuries an astonishing amount of progress had been made in science and technology. Astronomy was no exception with scientists like, among others, Arthur Eddington and Edwin Hubble enlightening our understanding of what makes the stars shine and revealing the nature of our Universe as a whole. Stellar spectroscopy underwent several advancements in both the instrumental and scientific sides. Improvements in photography and optics allowed for more detailed spectra to be recorded with less difficulty. Spectra were also being analysed in fine

detail. Spectra yielded information about star's detailed chemical composition, their temperatures, their surface gravities and crucially for the study of Be stars, their rotation.

Doppler shift is a phenomenon by which the wavelength of light can be elongated if the emitting body is travelling away from the observer. Conversely, when the body moves towards the observer, wavelength decreases. This effect leaves an imprint on the spectral lines of rotating stars, because when we observe a rotating star, one edge constantly turns away from us and the other towards us. This leads to a spectral line becoming broadened, as light emitted from one side of the star is blueshifted while that from the other is redshifted. The width of the spectral line then represents the rotation velocity of the star, with fast rotators having very broad spectral features.

Otto Struve noticed in 1931 that the spectral lines of Be stars are indeed often "extremely flat and broad", suggesting "rapid axial rotation". He proposed that Be stars rotate so rapidly that they become "lens-shaped bodies which eject matter at the equator, thus forming a nebulous ring which revolves around the star and gives rise to emission lines" (Struve, 1931). At the equator of a rotating star, there is a balance of forces - gravity pulls material towards the centre, whereas the centrifugal force attempts to lift material off of the star. There exists a certain rotation velocity, known as the critical rotation velocity, at which the gravitational and centrifugal forces are equal, meaning that nothing is holding matter onto the star. When a star rotates at the critical velocity therefore, gas is free to leave the star and form a decretion disc.

Struve's idea was that a decretion disc is responsible for the emission features. The central B star emits a large number of ionising photons (photons energetic enough to strip a hydrogen atom of its electron). When a decretion disc is present, these high energy photons interact with atoms in the disc, ionising them. Within the disc, electrons and ions are reuniting with the electron cascading through the various energy levels and in the process emitting photons of very distinct wavelengths. As these photons do not posses enough energy to ionise the gas, they are able to escape the disc and are apparent in a bright spectral line.

Struve cited the varying morphology of emission lines in Be stars as evidence for the disc scenario. He argued that because the disc itself also spins around the star, when an observer views a star-disc system edge-on, Doppler shift will cause a splitting of the emission line, as shown in sketch C of Fig. 1.6. When the system is observed instead pole-on, there is no rotational motion along the line of sight, hence a single-peaked emission line results like in sketch A of Fig. 1.6. Fig. 1.7 shows the variation of emission line shapes in the spectacular Pleiades star cluster where four of the seven brightest stars display emission features.

1.3 Properties of Be stars

Since the ideas of Struve, many scientists have worked on understanding Be stars, enhancing greatly our knowledge of the phenomenon. Here several basic properties of Be stars are discussed. For a more detailed review see Porter and Rivinius (2003) and Rivinius, Carciofi and Martayan (2013).

Rotation The most obvious property of the Be stars is that they rotate, on average, faster than normal B stars. This fast rotation has several effects which are detailed in Sec. 1.5.3. Fast rotating stars are expected to have an oblate shape and spatially variable surface properties (such as surface brightness) as shown in the interferometric image of the Be star Achernar in Fig. 1.8.

Transient nature For at least some stars, the presence of emission lines is only temporary. Examples
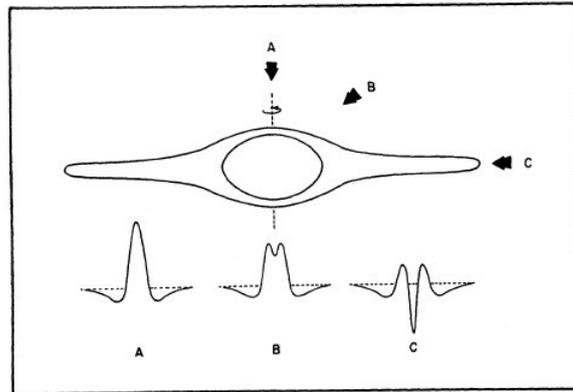
Figure 1.6: The variation of emission line morphology in a Be star according to viewing angle. The star with decretion disc produces line profiles labelled A,B and C when viewed by an observer from directions A,B and C respectively. Figure taken from Slettebak (1979)
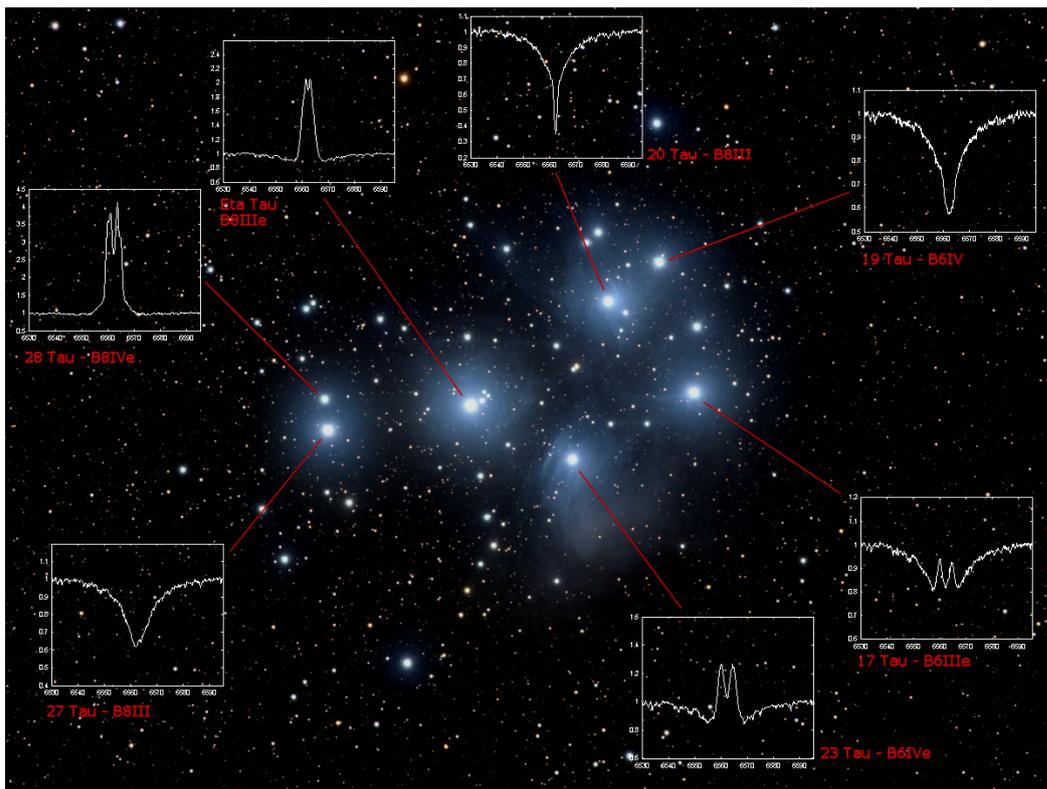
Figure 1.7: The Pleiades star cluster with Hα line profiles the seven brightest stars. Names and spectral types are given beside spectra. Image credit: Christian Buil, astrosurf.com
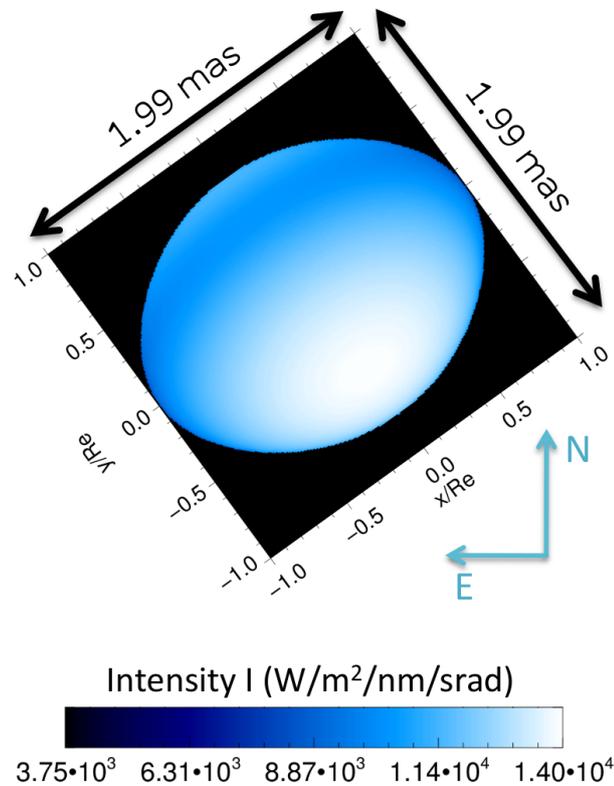
Figure 1.8: Reconstructed interferometric image of the fast spinning star Achernar showing the star's oblateness and varying surface intensity. Figure taken from Domiciano de Souza et al. (2014)

of stars whose Be status flickers are χ Persei (Telting et al., 1998), ω Canis Majoris (Ghoreyshi et al., 2018), EM Cephus (Kjurkchieva et al., 2016), Achernar (Kervella et al., 2022) and 66 Ophiuchi (Marr et al., 2021). Fig. 1.9 shows the Hα line profiles of Achernar at times 15 months apart. During this inteval the star transitioned from showing a deep and broad absorption line to a strong double peaked emission line. Disc build-up and decay events occur on timescales ranging from a few years to 20 years, so characterising this behaviour demands patience and dedication. It is important to note that in this domain, every kind of behaviour is observed from regular transitions between disc and discless states (ω Canis Majoris) to the sudden appearance followed by decay of a disc never to return again (μ Centaurus (Rivinius, Baade, Stefl, Stahl et al., 1998)). Many Be stars however do not show a transient behaviour, serving to further complicate efforts to determine the cause of the transience, which remains unknown.

Disc Being the source of the observed emission, the disc has been widely studied. Interferometric observations have confirmed that circumstellar material around Be stars is indeed disc-like (Quirrenbach, Buscher et al., 1994; Porter and Rivinius, 2003). Further efforts using polarimetry (a spherically asymmetric distribution of gas, such as a disc, will scatter light along a preferred direction, introducing a polarimetric signal) have demonstrated that the disc is thin (Quirrenbach, K. S. Bjorkman et al., 1997). The disc has a sizeable extent, with diameters of infrared emitting regions measuring some
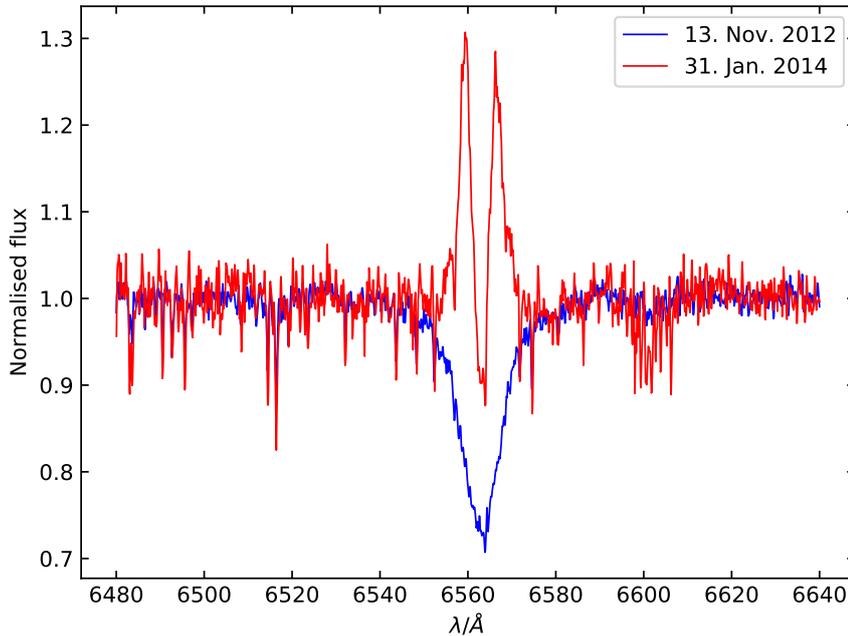
Figure 1.9: Spectra of the Be star Achernar, centred on the Hα line at two different epochs, 13th November 2012 (blue line) and 31st Januray 2014 (red line). Plotted with data from the BeSOS catalogue (Arcos et al., 2018)

10-15 stellar radii (Rivinius, Carciofi and Martayan, 2013). Material in this thin disc is believed to rotate in a Keplerian manner (Meilland, Stee et al., 2007; Meilland, Millour et al., 2012; Wheelwright, J. E. Bjorkman et al., 2012), meaning that everywhere in the disc the force of gravity from the central star balances with the centrifugal force. The analysis of absorption lines formed within the disc suggests that there are no significant radial outflows occurring (Hanuschik, 2000). In order for a Keplerian disc to form, angular momentum must be transported from the inner to the outer disc. The most popular model for this process is known as the viscous decretion disc model (Lee, Osaki and Saio, 1991), where viscous stresses transport angular momentum.

Binarity Given that the majority of massive stars are believed to reside in binaries (Sana, de Mink et al., 2012), it is reasonable to assume that many Be stars should too. Indeed Be stars are observed with a variety of companions. This is important because the nature of the companion can help to determine the system's previous evolution, assess whether a given star was significantly effected by binary interaction and pinpoint the likely formation mechanism of the Be star.

The most observed companion is a neutron star, seen in Be-Xray binaries. The neutron star, after being subject to a birth kick orbits the Be star in an eccentric orbit. During part of the orbit the neutron star passes through the Be disc, emitting Xrays in the process. There are more than 100 known Be-Xray binaries (Raguzova and Popov, 2005). Also seen are subdwarf, or stripped star, companions, which are direct result of a star having lost its envelope through binary interactions. Such companions are difficult to detect because they have low masses compared to the Be star and are dim at visible wavelengths (owing to their hot temperatures), however dedicated searches are being carried out (e.g. L. Wang, Gies, Peters et al. 2021) and more of these systems are revealing themselves.

White dwarves - the end stage in the life of a low mass ($< 8M_\odot$) star are also found to orbit Be stars. Although detection represents a significant challenge, a handful of Be-white dwarf systems have been found (K. L. Li et al., 2012; Coe et al., 2020). A single Be-black hole binary has been detected in the Milkyway: MCW 656 (Casares et al., 2014). However recently several candidate Be-black hole systems were found to contain in fact no black hole due to the inherent difficulties in interpreting spectra from binary stars (Shenar et al., 2020; Bodensteiner, Shenar, Mahy et al., 2020; El-Badry and Quataert, 2020; El-Badry and Burdge, 2022) The only type of companion that Be stars do not apparently have is main-sequence stars (Bodensteiner, Shenar and Sana, 2020). This view is being challenged by claims of several Be stars hosting main-sequence companions. These are Achernar (Kervella et al., 2022), ν Geminorum (Klement, Hadrava et al., 2021) and β Cephei (Wheelwright, Oudmaijer and Schnerr, 2009). To confirm their nature, they require further study but could well be a new class of Be binary stars.

1.4 Open questions relating to Be stars

The simple picture of a Be star presented by Struve is not a perfect description of the phenomenon and there are still many unanswered questions relating to Be stars which shall be briefly discussed here.

How fast do Be stars rotate? The rotation of Be stars can be characterised using the concept of critical rotation. The critical rotation rate is that at which the centrifugal force and that of gravity balance at the equator which reads

$$v_{\text{crit}} = \sqrt{\frac{GM}{R_e}}, \tag{1.1}$$

where M is the stellar mass an R_e the equatorial radius. Formally, one only expects material to become unbound from the equator and to form a disc when the critical velocity is exceeded. Many studies have found that Be stars are typically rotating at 70% of the critical velocity (Porter, 1996; Rivinius, Stefl and Baade, 2006; McSwain, Huang et al., 2008; Meilland, Millour et al., 2012; Rivinius, Carciofi and Martayan, 2013; Zorec, Frémat, Domiciano de Souza et al., 2016; Dufton, Lennon et al., 2022), albeit with a broad range of rotation rates stretching from 40% to 100% of critical. Several authors have however refuted these measurements (Collins and Truax, 1995; Townsend, Owocki and Howarth, 2004). Rotation rates are typically determined by measuring the broadening of spectral lines (see Sec. 1.2.2).

When rotation is fast, deformation occurs which can alter the flux profile of the stellar surface according to the von Zeipel theorem (von Zeipel, 1924), dimming the equatorial regions of the stellar photosphere which exhibit the largest Doppler shifts. It has thus been argued that the relationship between line-width and rotation is a complex affair, with rotation velocities of Be stars having been underestimated (Townsend, Owocki and Howarth, 2004). On the other hand, the most recent works do take these effects into account (Zorec, Frémat, Domiciano de Souza et al., 2016; Dufton, Lennon et al., 2022) and still find that Be stars rotate sub-critically. Care must also be taken to avoid contamination of the starlight with light originating form the disc, known as the veiling effect (Ballereau, Chauville and Zorec, 1995; Zorec, Cidale et al., 2009).

Cranmer (2005) report the average rotation rate of Be stars to be a strong function of spectral type,

with the earliest (hottest, most massive) types rotating at 40% of critical, and the latest (cooler, less massive) types at 60-80%. A similar trend is found by Huang, Gies and McSwain (2010). This may point either to measurement or interpretation errors or to different physics driving the Be phenomenon in different spectral types.

Is rotation the only prerequisite? If Be stars rotate at around 70% of the critical velocity, material is expected to be firmly bound to the equator and no opportunity for a disc to form will arise. There are several very fast rotating stars which do not show emission lines (Huang, Gies and McSwain, 2010) - a well known example is Regulus (Cotton et al., 2017). It would thus follow that some further property is required to drive the Be phenomenon.

Pulsation, where material is shaken off of the stellar surface (Cranmer, 2009), is a popular candidate. Pulsational outbursts have been linked in several stars to the appearance of emission features (Rivinius, Baade, Stefl, Stahl et al., 1998; Stefl, Baade et al., 2003) however there is no clear link between pulsation and the Be phenomenon in general. Be stars exhibit a zoo of different pulsation modes and frequencies (Rivinius, Carciofi and Martayan, 2013; Labadie-Bartz, Carciofi et al., 2022) which suggests that pulsation may not be the necessary agent. Normal B stars are also given to pulsate and a comparison of the general pulsational properties of B and Be stars has not yet been made. The most promising avenue to determine the role of pulsation in the Be phenomenon would be to compare pulsations of the fast rotating B stars to the Be stars. The study of pulsations is complicated by fast rotation which can mimic pulsational signals (Porter and Rivinius, 2003) and drive and interact with pulsational instabilities.

The δ Scorpii system is a very eccentric binary (e=0.94) with a 10 year period (Meilland, Delaa et al., 2011). The curiosity of this system lies in that during the periastron of the year 2000, the Be phenomenon was awoken in the primary star (Miroshnichenko et al., 2001). Also, during the previous periastron, in 1990, emission lines were also present in the spectrum (Cote and van Kerkwijk, 1993). Although only a single object, δ Scorpii provides evidence that in some Be stars, the presence of a close binary companion might have a causal role in producing emission lines.

Several mechanisms based upon magnetism have been proposed, although they have found neither widespread support nor confirmation, a fact perhaps owing to the complexity and our lack of understanding of stellar magnetic fields. One of which is the magnetically confined wind model, whereby stellar winds are funnelled into an equatorial disc by magnetic fields (Cassinelli et al., 2002). An appropriate magnetic field has been observed in the Be star β Cephei (Donati et al., 2001). Balona and Ozuyar (2020) have suggested that Be discs are fed by outbursts driven by small-scale magnetic fields. Similar to coronal mass ejections in the Sun, small magnetically active regions on the stellar photosphere can occasionally produce outbursts, ejecting mass from the star and building a disc. One advantage of magnetic models is that in general, they predict an unstable decretion disc, and hence explain why the emission feature is often transient.

What causes the duty cycle? The emission feature is not permanent - there are many examples of Be stars whose emission turns off and on, typically on a timescale of years to decades. However, not all Be stars display this behaviour. The basic physical principle driving the duty cycle remains unknown.

Why is the phenomenon restricted to B stars? Oe and Ae stars do exist, although they are extremely rare. It may be that very massive stars are not able to host a decretion disc because they

have strong stellar winds and emit large amounts of radiation which simply blows any disc away. Furthermore, strong stellar winds may cause an aggressive spin down due to angular momentum loss, making O stars unlikely to host decretion discs. Lower mass stars may not radiate enough ionising photons to cause any existing disc to produce emission lines, which might explain the lack of Ae stars. Alternatively, the emission phenomenon may be restricted to B stars owing to the underlying formation mechanism preferring stars in this mass range.

Do the star and disc interact? It may be imagined that a circumstellar disc has some impact upon its host. This may be in the form of contributing to the star's angular momentum budget by draining angular momentum from the central star via viscous coupling (Krtička, Owocki and Meynet, 2011). Furthermore, magnetic processes are predicted to operate inside the disc (Krtička, Kurfürst and Krtičková, 2015), hence magnetic interactions between the star and disc could take place, possibly affecting the star's spin. Lastly, the disc's presence may effect the star's basic surface properties, such as mass density and temperature. This may impact the radiative acceleration at the surface, which could provide an important contribution in launching a disc. The stellar wind may also thus be affected.

What is the origin of the Be stars? The question is the focus of this thesis. In fundamental terms, it is not well understood what causes any given star to display the emission line phenomenon. Rotation may or may not underpin the building up of a disc. How emission line stars came to rotate faster than average is unknown, although several mechanisms have been proposed (see Section 1.7).

1.5 Single star evolution

1.5.1 Stellar models

Currently almost all [2] of the information that we have about any given star comes from electromagnetic radiation, otherwise known as starlight. As starlight is emitted from near to the stellar surface, stars reveal the secrets of their inner structures very unwillingly. The main tool that we have for understanding the structure and evolution of stars is theoretical modelling. This involves formulating and solving equations to describe the behaviour and structure of stars, always under simplifying assumptions.

One of the first quantitative stellar models is the polytropic model, where the pressure and mass-density throughout the star follow a specific assumed relation. With this relation and Newton's law of gravity enforcing hydrostatic equilibrium, the density and pressure structure throughout the star can be found. This model was independently proposed by Lane (1870) and Emden (1907), after whom the Lane-Emden equation is named. However to describe a star in more detail, one needs more than just gravity and an equation of state.

Modern stellar evolution models cover five concepts:

- hydrostatic equilibrium

- mass conservation

---

[2] Some stars such as the Sun and Supernova 1986A (Hirata et al., 1987) have been observed in neutrinos. In the future, gravitational wave observations can also be expected to provide insights.

- energy generation

- energy transport

- chemical structure

Hydrostatic equilibrium demands that (on short timescales at least) a star is neither collapsing or expanding - it is stable. This is enforced by demanding that the force of gravity is counteracted by an opposing force originating from a pressure gradient. The pressure source may be ideal gas pressure, radiation pressure, electron degeneracy pressure or a mixture of all three.

That matter can never be created or destroyed in encapsulated in mass conservation. Certain sinks or sources of mass however are possible, for example massive stars lose significant amounts of mass to stellar winds or stars in binary systems may accrete material from a companion (see Sec. 1.6). These variations need to be properly accounted for.

Deep in the central regions of a star, temperatures become hot enough for certain nuclear reactions to occur. As the products of such reactions are less massive than the sum of their constituent parts, energy is released in the form of photons. The most important of these reactions is known as hydrogen burning - that is where four hydrogen nuclei are combined to produce one helium nucleus (the exact mechanics of the reaction vary according to the conditions in the star, but the net result is always the same). A detailed stellar model must predict the energy generated by these reactions.

Furthermore once energy is produced by a nuclear reaction, that energy may be transported throughout the star. In stars there are two main mechanisms by which this can occur: radiation and convection. Radiative energy transport is where electromagnetic radiation is the carrier of energy. In contrast to our everyday perception of radiation (or light) which freely streams across large distances, a stellar interior is very opaque, meaning that radiation does not pass easily through the material. Instead, matter and radiation interact, bouncing off of each other like snooker balls. In fact these interactions are so common that a photon typically travels 1cm before being scattered by another particle, meaning that on average it takes ten thousand years for a photon produced in the centre of the Sun to reach the photosphere [3].

In some cases, radiative energy transport cannot transport enough energy to maintain thermal equilibrium, here convection takes over the strain. Convection is a cyclic macroscopic motion of material which can transport energy very efficiently. The conditions under which convection occur where first outlined quantitatively by Karl Schwarzschild in the early 20th century. Convection occurs in regions with either large opacity or high luminosity. This can be understood intuitively as high opacity blocks the flow of radiation and regions with high luminosities demand efficient energy transport. The Schwarzschild criterion predicts therefore that convection occurs in the centre of massive stars (more massive than $2\,M_\odot$) where the luminosity is large, and in the envelopes of low mass stars, where the opacity is high. Lastly conduction may also occur in stars composed of degenerate material, such as white-dwarves.

In a given region of a star various processes may cause a change in the chemical composition. Examples of these processes are nuclear reactions, convection and rotational mixing. These changes in chemical composition must be followed throughout the interior of the star as they affect the subsequent

---

[3] The mean free path of a photon, l, is given by $l = 1/\kappa\rho$, where κ and ρ are the opacity and mass density. Taking the average density of the sun and assuming electron scattering opacity gives $l \approx 1$cm. The problem can then be thought of as a random walk with step size 1cm. Approximately, one can expect a photon to "walk" from the centre to the photosphere of the Sun in around 10^4 years.

evolution. A pertinent example of this is when the central hydrogen burning regions have exhausted their supply of hydrogen - the stellar structure must react to this.

The five listed concepts are described mathematically by time-independent differential equations which are solved by a computer to predict the structure of a star. Once a solution is found at a particular time, the clock is run forward by one "timestep" and a new solution is calculated using the updated equations at the new time.

Stellar evolution models are precisely that: they are simplifications of the real world. Just as a dolls' house is a model of a real house that captures the features required for a child's play, a stellar evolution model attempts to encompass all of the processes relevant to the life of a star. A stellar model is only as good as what is put in to it and the input physics is never comprehensive or complete, so naturally all models suffer shortcomings. There are several processes that occur in massive stars that are generally not included in stellar models, either due to lack of physical understanding (e.g. turbulence) or the belief that the processes have a small effect (e.g. magnetic fields). Furthermore, what is included is almost always dealt with as a stand alone process. For example, in a real massive star, the central convective zone interacts with the zone where rotation drives circulation currents, however in a model, these two processes are considered separately and are completely blind to each other.

Perhaps the largest simplification made in modelling efforts is the one-dimensional approximation. Stellar models assume spherical symmetry, meaning that the structure equations only need to be solved in one dimension thus reducing the computational requirements for such models. Three-dimensional models of non-rotating stars show however that this approximation can easily break down due to turbulence (Jiang et al., 2015). More over, a rotating star is a two-dimensional object, so any attempt to describe it in one dimension must result in a loss of accuracy. In one-dimensional models of rotating stars, the structure is typically computed by performing an average over the two-dimensional structure. This method works well when the resulting average does not deviate much from the actual structure. However when rotation is fast, the stellar structure can vary significantly from pole to equator, for example due to the onset on convection at the equator only, or a strong variation in local opacity from the recombination of a certain species. This means that the computed and actual structures of a rotating star could differ significantly. The difficulties in stellar modelling are well summarised by the following line from Heger, Langer and Woosley (2000):

> The instabilities discussed in the previous section are not a complete list of all rotationally induced instabilities for massive stellar evolution. However, they appear to be the most relevant ones, or at least the best understood.

1.5.2 The life of a star

Before a star can shine, it must form from its parent molecular cloud. Star formation is a topic in itself which presents many problems and challenges to the curious scientist and it is unfortunate that the intricacies must be ignored here. Let us follow the trials and tribulations of a star that has formed from a collapsing molecular cloud.

Initially a cloud consisting mostly of molecular hydrogen cools and collapses. This process continues until a central object is formed in which temperatures are hot enough for nuclear reactions to produce helium nuclei from hydrogen. This phase is known as the main-sequence or the hydrogen burning phase and the moment at which hydrogen is "ignited" in the core of a young star marks the very beginning of the star's life (this point in time is named the zero-age main-sequence).

The main-sequence is the longest lived period of a star's life during which the central supply of hydrogen is steadily converted into helium. The exact mechanism by which this occurs depends on the central temperature, which is ultimately determined by the star's mass. For stars less massive than around $2\,M_\odot$, burning is achieved by the proton-proton chain reactions which combines protons (i.e. hydrogen nuclei) together in a stepwise fashion until a helium nucleus is formed. The three steps are

$$^1_1H + {}^1_1H \longrightarrow {}^2_1D + e^+ + \nu_e$$

$$^2_1D + {}^1_1H \longrightarrow {}^3_2He + \gamma$$

$$^3_2He + {}^3_2He \longrightarrow {}^4_2He + 2\,{}^1_1H + \gamma$$
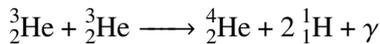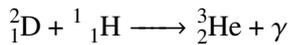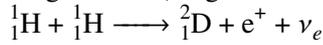
To create one helium nucleus, the first and second reactions are needed twice. The net result is that four hydrogen nuclei react to give one helium nucleus, two electron neutrinos and 26.7Mev [4] released as photons. As the proton-proton chain combines nuclei with low charge numbers, the electrostatic repulsion (or Coulomb barrier) between the particles is not so strong, so the reactions can occur at the relatively low temperatures found in lower mass stars.

Stars more massive than $2\,M_\odot$ in contrast have higher central temperatures, meaning that protons have faster kinetic velocities, which enables them to more easily overcome the large Coulomb barrier necessary to react with heavier nuclei. In such stars, hydrogen burning proceeds via the CNO cycle, whereby seed nuclei act as catalysts either absorbing a proton or decaying to produce the next nucleus in the cycle. The CNO cycle produces a larger energy output than the proton-proton chain at temperatures found in stars more massive than $2\,M_\odot$, and hence dominates in these stars. The dominant cycle is

1. $^{12}_6C + {}^1_1H \longrightarrow {}^{13}_7N + \gamma$

2. $^{13}_7N \longrightarrow {}^{13}_6C + e^+ + \nu_e$

3. $^{13}_6C + {}^1_1H \longrightarrow {}^{14}_7N + \gamma$

4. $^{14}_7N + {}^1_1H \longrightarrow {}^{15}_8O + \gamma$

5. $^{15}_8O \longrightarrow {}^{15}_7N + e^+ + \nu_e$

6. $^{15}_7N + {}^1_1H \longrightarrow {}^{12}_6C + {}^4_2He.$
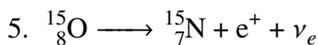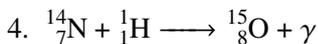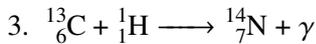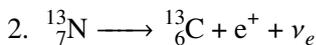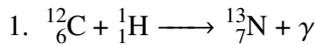
In common with the proton-proton chain, the CNO cycle also has the net result of fusing four hydrogen nuclei into one helium nucleus. During the cycle, the seed nuclei build up their mass and proton numbers by absorbing a proton until an unstable nucleus results. This unstable nucleus then undergoes β^+ decay, where a proton decays into a neutron, a position and an electron neutrino. The pattern of absorption and decay continues until the final reaction produces a helium nucleus and $^{12}_6C$ nucleus to end the cycle. The seed carbon nucleus is regenerated in the last reaction. Although during one cycle, CNO nuclei are neither created or destroyed, the fact that the different reactions occur at differing rates means that there are bottlenecks in the cycle. For example reactions 2 and 5 typically occur on a timescale of minutes, whereas reaction 4 typically needs several hundred thousand years to complete as $^{14}_7N$ is a very stable nucleus. This results in $^{14}_7N$ becoming the most abundant CNO species in regions where the CNO cycle occurs.

As this thesis is focused on massive stars, we shall now consider the structure and evolution of stars burning hydrogen via the CNO cycle. These stars consist of a central convective core surrounded by a

---

[4] this includes the annihilation of the two positrons produced by the first reaction

radiative envelope. Convection occurs in the centre because the CNO cycle is extremely sensitive to temperature, meaning that energy is generated in only a small part of the core where temperatures are highest. This gives rise to a large luminosity to mass ratio in the centre and so convection occurs. Convection mixes material throughout the core, serving to feed the central burning region.

The subsequent evolution of the star is driven by hydrogen burning, which causes the mean molecular weight of particles in the core to increase. To illustrate this compare a fluid of pure ionised hydrogen with that of pure ionised helium. Ionised hydrogen is an equal mixture of protons (weighing one atomic mass unit) and electrons (with negligible mass) and so has a mean molecular weight of 0.5 atomic mass units (a.m.u). While ionised helium has a mean molecular weight of $\frac{4}{3}$ a.m.u because a helium nucleus has a mass of 4 a.m.u and for every helium nucleus there are two electrons, so there are 3 particles to count in total.

The star itself reacts to this change of mean molecular weight in several ways. Firstly, the fraction of the star occupied by the convective core shrinks. This is because deep inside a star, where all species are fully ionised, the major source of opacity is from photons colliding with electrons (known as Thomson scattering). As hydrogen is burnt, the number density of nuclei in the core decreases, resulting in fewer charged particles to scatter photons. In this way, the central opacity drops, meaning that the convective core retreats, because the occurrence of convection is sensitive to opacity, as outlined previously.

The CNO cycle has a thermostatic action, owing to the extreme sensitivity of the energy generation rate on temperature - the energy generation rate is proportional to temperature raised to the 18th power. This means that the central temperature and density do not vary much for most of hydrogen burning. However, because the mean molecular weight increases, ideal gas physics demands that the central pressure must decrease. This can only be achieved if the density of the material enveloping the core decreases. The envelope must expand to reduce pressure on the core, so the star's overall radius swells slightly during hydrogen burning. This effect is gentle with the radius typically doubling over the main-sequence lifetime.

Once the supply of hydrogen in the core becomes scarce, the central temperature must increase to maintain both the nuclear reaction rate and thermal equilibrium. To do this, the core becomes denser. This behaviour continues until all of the hydrogen in the stellar core is converted into helium. This point marks the end of the main-sequence.

The star now finds itself unable to maintain thermal equilibrium as it loses more energy from its surface than is generated in its core. A very brief period of core contraction follows until the central temperatures are high enough to ignite helium burning. Similarly, but more pronounced, to the radius expansion during hydrogen burning, the star's radius swells by a factor of several hundred times, with the star becoming a red giant.

Once the star has settled onto the red-giant branch, it burns helium into carbon via the triple alpha process, until the supply of heliumruns out. If the star is massive enough (i.e. initial mass greater than around $8\,\mathrm{M_\odot}$) to attain high enough core temperatures, then evolution continues through the advanced burning stages; carbon burning; neon burning; oxygen burning; silicon burning. Once silicon burning is complete, the star's core consists mostly of iron, from which no more energy can be extracted through nuclear processes - iron is the most energetically stable nucleus so adding any more nucleons only costs energy. Therefore the star is finally unable to fight against gravitational contraction and explodes as a core-collapse supernova. After the supernova, either a black-hole or neutron star is formed. The final product of the evolution of a massive star varies depending on the physical structure of the star.

Stars less massive than around $8\,M_\odot$ do not suffer the same violent end. Instead, as their core temperatures are not hot enough to ignite carbon burning, their chemical evolution is arrested when the core is composed of carbon and oxygen. The star then sheds its outer layers to reveal a carbon-oxygen white dwarf, which shines like a hot coal in space. Stars of spectral type B have initial masses between 2 and $16\,M_\odot$ and hence members of the Be class are expected to form both white dwarves and neutron stars.

1.5.3 Rotation in stars

All stars rotate, and Be stars rotate significantly faster than stars that do not exbihit emission lines (Struve, 1931), so it is important to give a brief account of the effects of rotation. For stars which spin slowly, rotation does not play a large role in the structure or evolution. However, moderately or fast rotating stars, rotation affects both the surface and internal structure.

Rotation manifests itself in the form of the centrifugal force, which is directly opposed to the gravitational force at the equator. The centrifugal force is responsible for altering several surface properties of a rotating star. Firstly, the surface gravity becomes weakened at the equator, but remains unchanged at the poles. This causes the star to become oblate, as the centrifugal force "pulls" the equator into a bulge. Fig. 1.8 shows the lens shape which arises.

Furthermore, the surface of a rotating star is affected by gravity darkening, with polar regions appearing hotter and brighter than equatorial regions (von Zeipel, 1924), as showin in Fig. 1.8. Gravity darkening can be understood intuitively by considering that where the effective gravity is weaker, the mass-density in the envelope is reduced. This means that a lower temperature is required to maintain hydrostatic equilibrium. It then follows that these cooler regions are dimmer because of blackbody physics. Gravity darkening causes the effective temperature and luminosity of a rotating star to depend on how the star is oriented in space relative to an observer - the same star viewed pole-on will not be identical to that viewed equator-on.

Another consequence of rotation is that the stellar wind may be impacted. Stellar winds remove not only mass but also angular momentum from a star, so can play an important role in a star's spin evolution. Massive stars host radiatively-driven winds, where particles are ejected from the stellar atmosphere after exchanging momentum with photons streaming out of the stellar core. As rotation affects the physical conditions from where the wind is launched, and so one expects a spatially anisotropic wind because the stellar surface is non-uniform.

The internal structure of a star is also influenced by rotation. One might reasonably expect that when a gaseous object rotates, several mixing processes will occur. These instabilities serve to transport both particles and angular momentum throughout the star. One of the strongest rotational mixing processes is called Eddington-Sweet circulation. Here rotation drives large-scale currents inside the stellar atmosphere that transport particles between the stellar core and surface (Sweet, 1950). Another prominent example is shear mixing, which occurs when neighbouring fluid layers rotate with different angular velocities, causing those layers to mix together (Maeder, 1997). These mixing processes serve to mix fresh fuel into the central burning regions and to transport burning products to the surface. When mixing is effective, the star may burn its entire supply of hydrogen, unlike in the non-rotating case when only the central portion of the star undergoes nuclear burning. Under the influence of rotational mixing, a star becomes hotter and more luminous that its non-rotating counterpart due to the mixing of fresh fuel into the central burning region. Many fast rotating stars display surface enrichments of nuclear burning products like nitrogen and helium (Heger, Langer and Woosley, 2000;

Brott, C. J. Evans et al., 2011) as mixing also brings material from the core to the surface.

Rotational instabilities transport not only chemicals but also angular momentum. A particle on the surface of a star will have a larger angular momentum than an equivalent particle with the same angular velocity near the centre. Therefore when the surface particle is mixed into the central region, the conservation of angular momentum demands that the central region must adjust its spin accordingly. In this way, rotational mixing the angular velocity profile of a star. There are however processes that transport angular momentum without transporting chemicals. These are generally magnetic in nature such as the Tayler-Spruit dynamo (Spruit, 2002), which transports angular momentum very efficiently so as to enforce near-solid-body rotation. The dynamo's basic mechanism is that in a star with large differential rotation, magnetic field lines would become twisted around one another. To prevent this unstable configuration, angular momentum is transported via magnetic interactions so as to smooth out large angular velocity gradients. The Tayler-Spruit dynamo has been invoked to explain the slow spins of young pulsars (Heger, Woosley and Spruit, 2005) and white-dwarves (Suijs et al., 2008).

1.6 Binary star evolution

A single star by definition lives an isolated and lonely life. Astronomers have long suspected that not all stars are doomed to such a tedious fate. Since the invention of the telescope in the early 1600s, several stars were noticed to lie close to one another. It is difficult to determine whether these so-called double stars just appear to be close through alignment along our line of sight, or whether they truly share a common space. Michell (1767) argued that there are simply too many double stars and clusters of stars for them to be chance alignments, instead they must "in confluence of some general law (such perhaps as gravity) are collected together in great numbers". This was confirmed by the illustrious astronomer Sir William Herschel after 25 years of measuring the positions of stars in doubles. He found that such stars do indeed appear to revolve around each other (Herschel, 1803) and the study of binary stars was born.

A binary star consists of two stars orbiting a common centre of mass. The time that each star takes to do one revolution around its partner is called the orbital period. The orbit may be either circular or eccentric, however in this work only circular orbits are considered. The components orbit each other in Keplerian motion, meaning that the required centripetal force is provided by gravity. Accordingly, the distance between the two stars (often termed the binary separation) can be related to the stellar masses and the orbital period through Kepler's third law.

1.6.1 Observations of binary stars

The study of binary stars is largely focused on observing two properties; eclipses and radial velocity variations. Using these methods, we can deduce that a given pin-prick of light on the sky is in fact a binary star and deduce its properties.

When two stars move around each other, at certain times, one star may be obscured by the other. This situation is known as an eclipse. If an eclipsing binary star is observed for long enough, with the brightness measured, a pattern will eventually emerge. At certain intervals, one star will pass in front of the other, and when this happens, light from the eclipsed star will be blocked by its companion. Accordingly the binary star will temporarily become dimmer as not as much light makes its way to the observer. As the stars continue on their orbit, the eclipse will end and the binary will recover its full

brightness. Thus an eclipsing binary will dim and brighten at a regular periodic interval. Note that whether a binary star shows eclipses depends of the geometry of the system and its orientation with respect to the observer. For example if the observer is looking perpendicular to the orbital plane, the stars will just encircle one another, without ever occulting each other. Measurements of the eclipses can provide the relative luminosities and sizes of stars in the system, as well as the orbital period.

Radial velocity measurements take advantage of the fact that when looking along the orbital plane of a binary, one star is moving away from the observer and the other towards. As each star continues around its orbit, it alternates between moving towards and away from the observer. A wave-emitting body (in this case the wave is electromagnetic radiation) undergoes the Doppler effect, whereby the wavelength of the waves is altered depending on the relative movements of the emitter and observer. When the emitter is moving towards the observer, the wavelength becomes shorter; this is known as blueshift. Redshift is the opposite, when the emitter and observer are moving away from each other. Therefore the binary orbit produces periodic Doppler shifts, with the light being blueshifted and redshifted alternately as each star moves on its orbit. This Doppler shift manifests itself as the changing positions of features in the spectrum. When wavelength at which absorption lines are seen is tracked over a binary's orbital period, information about the binary such as the speeds of the stars' movement and the mass-ratio of the binary can be determined. Similarly to eclipsing binaries, not every binary displays Doppler shift, and again the reason is due to the observer-binary orientation. Those systems that do exhibit periodic Doppler shifts are called spectroscopic binaries.

The star Algol, mentioned in Section 1, is indeed a binary. In the 1880s, the ancient problem of what makes Algol wink was solved - Algol is an eclipsing binary, as first suggested by Pickering (1881). Shortly afterwards, study of the spectral lines of the system by Hermann Carl Vogel in 1889 revealed it to also be a spectroscopic binary (Batten, 1989), solidly confirming Algol's status as a binary star.

1.6.2 Mass transfer and its effects

A test particle sitting on the surface of one star in a binary feels several forces;

- gravity from the star

- gravity from the other star in the binary

- a centrifugal force from the binary orbit.

- a centrifugal force from the star's rotation

As long as the test particle remains close to the star, the dominating force will be gravitational attraction from that star. However, if the particle strays far enough away, it can be transferred to the other star or even be ejected from the system. The Roche lobe is the bounding surface within which a test particle remains bound to one star. An example of the Roche lobe seen in the orbital plane is given in Fig. 1.10, showing that it is teardrop shaped with the star in the centre.

During its natural evolution, a star's radius increases (see Sec. 1.5.2) meaning that it can overflow its Roche lobe. When this happens, a mass transfer episode is initiated, with material passing through the first Lagrange point (L1) before entering the Roche lobe of the companion star and being accreted onto the companion's surface. The component losing mass is termed the donor and is usually the
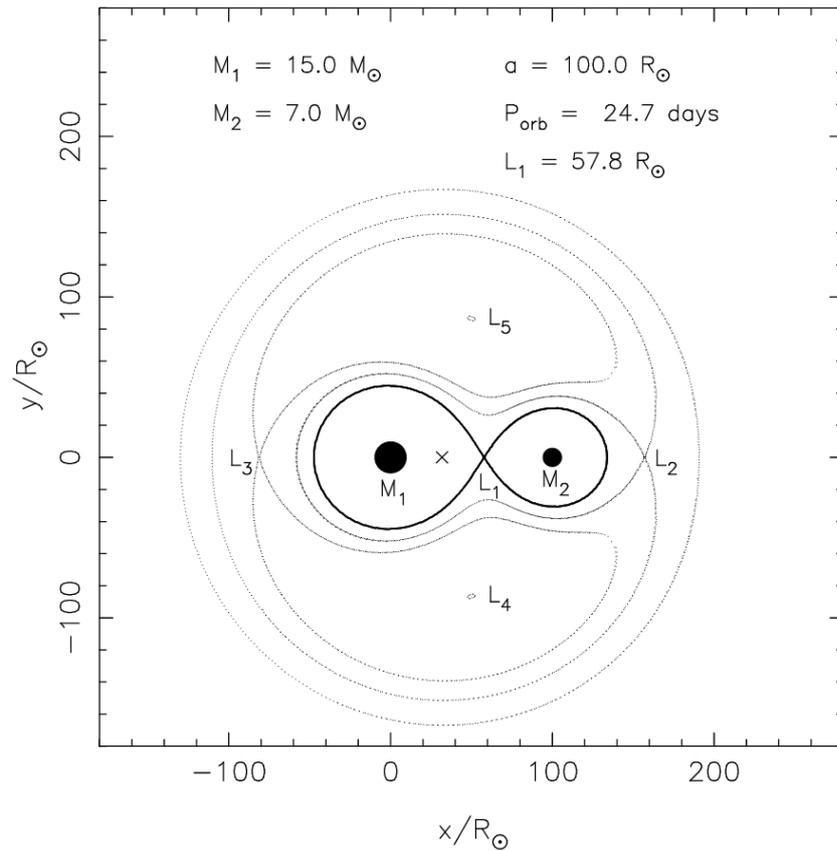
Figure 1.10: The equipotential lines of the Roche potential for a binary consisting of stars with masses 15 and $7\,M_\odot$ and binary separation $100R_\odot$. Considered are the forces of gravity from each star, the centrifugal force due to the binary orbit and the centrifugal force due to the spin of each star, assuming the orbital and spin periods are equal. The perspective is that of the orbital plane, such that the stars move on their orbits in the plane of the figure. The equipotential lines passing through Lagrangian points L_1, L_2, and L_3 are shown. The centre of mass is marked by a cross. The thick curve crossing through L_1 is the Roche-lobe. Figure taken from Tauris and van den Heuvel (2006)

initially more massive star in the system owing to the fact that more massive stars evolve on shorter timescales. The component gaining mass is named the accretor.

Mass transfer brings about multiple changes to both the orbit of the binary and the evolution of the stars themselves. The orbital separation changes due to the the changing ratio of the component masses, a quantity defined as the mass ratio, often denoted q. Here we will define the mass radio as the accretor mass divided by the donor mass, $q = M_{acc}/M_{donor}$, although it is often defined the other way around - there is no convention. For systems with mass ratios less than unity, the orbital separation generally [5] decreases. While for systems with a less massive donor ($q > 1$), the orbital separation usually increases. This means that typically the binary orbit shrinks during the first stages of mass transfer, then when the mass ratio inverts, the orbit begins to widen.

The most obvious effect of mass-transfer is that it changes the masses of both stars in the binary. When the donor star has a radiative envelope, this can be stripped away from the star, leaving essentially the convective core known as a stripped star. If mass transfer is halted prematurely or the accretor starts to fill its own Roche lobe, then the stripping will be incomplete.

For the accretor, the incoming material can have several effects. Firstly, because the mass of the star increases, the central temperature will increase accordingly and thus the luminosity will also increase. The increased luminosity will in turn reduce the expected lifetime of the star, following the lifetime-luminosity relation. The increase in mass will cause the convective core to grow, as the star emulates a more massive star. The advancing core will envelop material that has not been previously subjected to nuclear burning. This virgin material, which contains fresh fuel for hydrogen burning, will quickly become mixed with the core by convection. In this way the star accesses a new supply of hydrogen which rejuvenates the star. A rejuvenated star is hotter and more luminous than a normal star, hence they occupy the blue straggler region of the Hertzsprung-Russell diagram.

The accreted material might have a different chemical composition to that of the accretor's surface. As the donor star becomes stripped, the transferred material originates from deeper inside the donor and as such may be contaminated with the products of nuclear burning. In this way stars which have accreted a lot of material through binary interaction are expected to have enriched nitrogen and helium abundances. Furthermore, if accreted material has a higher mean molecular weight than that of the accretor's surface, then the accreted material will "sink" through the atmosphere of the accretor star. This process is known as thermohyaline mixing and can serve to mix fresh fuel into the burning regions of a star, thus further rejuvenating an accreting star.

An accreting star does not only gain mass but also angular momentum. The accretion of angular momentum may cause the accretor star to spin up, and perhaps attain critical velocity. When mass is accreted through a Keplerian accretion disc, angular momentum accretion is very efficient, with a star needing to gain only a few percent of its initial mass to rotate critically (Packet, 1981). Numerical simulations of binary stars predict that critically rotating accretors are a common result of binary interaction (Langer et al., 2020). However the process of angular momentum accretion is not without its uncertainties.

1.6.3 Mass transfer efficiency

Mass that leaves the donor star might not necessarily end up becoming a part of the accretor star. This concept is known as mass transfer efficiency. The mass transfer efficiency is defined as the fraction

---

[5] the specifics of mass transfer efficiency and angular momentum loss can change this, as discussed further on.

of mass gained by the accretor to the mass lost by the donor. Efficient mass transfer (also known as conservative mass transfer) is where all the accretor accretes all material that is stripped from the donor, thus preserving the total mass of the binary. In inefficient mass transfer (also known as non-conservative), the accretor only receives a certain amount of the material leaving the donor, with the rest being ejected from the binary. For totally inefficient mass transfer, the mass of the accretor is unaffected by mass transfer.

Material that is ejected from the binary takes with it a certain amount of orbital angular momentum. This loss of orbital angular momentum effects the orbital separation, which in turn may effect the mass transfer rate or initiate Roche lobe overflow of the accretor. There are many distinct ways that material can leave the binary, with each removing a differing amount of specific angular momentum. For example, material may be ejected as a fast wind from either star in the binary. Another possibility is that material leaves the system through the second Lagrangian (L2) point. The loss of angular momentum is a significant uncertainty in binary evolution. A popular prescription is the isotropic re-emission model, where material is ejected from the surface of the accretor or donor as a fast wind. However, simple considerations of the energy required to drive this fast wind cast doubt on the realism of this model.

Mass transfer efficiency is poorly constrained, with many numerical binary star models treating the mass transfer efficiency as a free parameter. Comparisons between models and observations of double-lined eclipsing binaries give evidence that "there is no single value of mass transfer efficiency for which we can fit all systems" (de Mink, Pols and Hilditch, 2007) and show a wide range of best fitting mass transfer efficiency values, spanning conservative to near fully non-conservative. A study of Algol binaries by Sen et al. (2022) "implies rather conservative mass transfer in some systems, while a very inefficient one in others".

Recent binary evolution models (Langer et al., 2020) operate using the rotation limited principle, whereby accretion is efficient until the mass-gainer attains critical rotation, after which accretion proceeds fully non-conservatively. As accreted material typically carries a large specific angular momentum, this scheme generally produces very low mass-transfer efficiencies. The exception is for close systems in which tidal forces inhibit the spin of of the accretor, thus allowing more mass to be accreted. Therefore in this scheme, a range of mass-transfer efficiencies is expected, with wide binaries evolving non-conservatively and close binaries more conservatively. However there remain uncertainties related to the action of tides, with suggestions that there is variation in the behaviour of tidal interactions (Justesen and Albrecht, 2021).

1.6.4 Mergers

In certain cases mass transfer can proceed unstably, resulting in a coalescence of the two stars in the binary to produce a single merger star. There are several criteria that predict whether or not a merger will occur in any binary system. Whether a given binary system will merge or not is one of the largest uncertainties in binary evolution. The response of the donor to mass loss is a long standing probe of mass transfer stability. If the donor's size during mass transfer increases at a greater rate than its Roche lobe, this suggests that mass transfer will be unstable, as the donor's Roche lobe overflow will not be able to be stemmed (Hurley, Tout and Pols, 2002).

Alternatively, one may consider the rates at which the donor and accretor typically undergo mass adjustments. The donor typically loses mass on its own thermal timescale, while the accretor can only accept material at a rate given by its own thermal timescale (Hurley, Tout and Pols, 2002). If there is a

big discrepancy between the thermal timescales of accretor and donor, the accretor will not be able to bring the newly accreted material into thermal equilibrium with itself. In this situation, material will not be able to be accreted and will form a tenuous cloud around the binary. This situation is known as common envelope evolution. The two stars experience a drag force as they orbit through the common envelope, ultimately sapping orbital energy until the stars merge (Iben and Livio, 1993).

Lastly, for binary evolution models that evolve non-conservatively, one may place constraints depending on the mass ejected from the system. To eject material from a binary, work must be done to overcome the gravitational attraction from both stars. Thus inefficient mass transfer must have a source of energy to be viable. The most obvious sources of energy are the stellar luminosities and the orbital energy. If this energy does not suffice to eject material during mass transfer, then that material will again form a common envelope and result in a merger. This merger criteria is applied in the binary evolution models of Langer et al. (2020).

A merger star is predicted to undergo rejuvenation. The mixing of hydrogen into the core during the merger process adds fresh fuel to the fire, causing the star to become hotter and more luminous. As merger stars are predicted to be bluer and brighter than stars that did not merge, they may explain the population of such observed stars, known as blue stragglers in the Herzsprung-Russell diagram (Mateo et al., 1990). Modern magneto-hydrodynamical models predict that merger stars have strong magnetic fields (Schneider, Ohlmann et al., 2019). These same models predict that although merger stars are initially formed as rapid rotators (due to agglomeration of orbital angular momentum into rotational angular momentum), they spin down quickly due to internal structural changes. This suggests that mergers are unlikely to produce rapid rotators, and hence merging is not a viable channel for the formation of emission line stars.

The merging process is believed to result in a luminous red nova, although this is not certain (Pastorello et al., 2019). A handful of such novae have been observed within the last 20 years and are typified by a very red colour, and a slow fading (lasting several months) from maximum brightness accompanied by a resurgence in the infrared. The first confirmed luminous red nova was observed in the galaxy Messier 85 (Kulkarni et al., 2007). The study of luminous red novae is young and and suffers from the lack of observed events and doubts about whether they are produced by merging stars.

1.7 Formation channels of classical emission line stars

Classical emission line stars are a distinct class that are fairly easily identifiable from the body of the massive star population. It follows that some process has made them different to those stars that neither rotate rapidly nor host a decretion disc. A star's previous evolution offers very strong constraints on its future evolution, and so emission line stars offer a promising window into the lives of massive stars. Many emission line stars are expected to explode as supernovae, showering their local environments with heavy elements and contributing to the chemical evolution of the Universe, which can be better understood when their early history is well constrained. Looking further ahead, emission line stars may be progenitors of gravitational wave merger events, given that several emission line stars are observed with binary companions, one of which is a black hole (Casares et al., 2014). Therefore emission line stars offer valuable insights into graviational wave astronomy.

To describe the population of classical emission line stars that we see in the sky, there are two competing formation channels, each with distinct characteristics and properties that shall be briefly explained here. It is assumed that emission line stars are rapidly rotating hydrogen-burning stars. The

formation channels focus on explaining the stars' rapid rotation.

1.7.1 Single star formation channel

The rotation velocity at which the force of gravity is matched by the centrifugal force at the equator is known as the Keplerian critical velocity and is inversely proportional to the square root of the radius (see Eq. 1.1). During main-sequence evolution, the stellar radius increases, which naturally leads to a decrease in the critical velocity.

At the same time, local conservation of angular momentum demands that if the star's outer layers are expanding, then the surface rotational velocity must decelerate. However, there are internal mechanisms within the star that transport angular momentum towards the surface, thus maintaining a fast rotational velocity at the surface. Internal angular momentum transport is believed to be achieved principally by magnetic interactions (Spruit, 2002) or rotationally driven circulation currents (Aerts, Mathis and T. M. Rogers, 2019).

The two effects of a decreasing critical velocity and steady surface rotational velocity mean that a star evolves towards its critical velocity, effectively spinning up. Given rapid enough initial rotation, critical velocity may be reached during the main-sequence. In this way a single star born with moderately fast rotation may evolve to become near critically rotating, and thus form a decretion disc and exhibit the emission line phenomenon.

As the star must have a seed birth angular momentum, emission line stars formed through this channel are expected to show the effects of rotational mixing; namely surface nitrogen enrichment (Maeder and Meynet, 2001; Heger and Langer, 2000).

A tell-tale sign that an emission line star was formed through the single star channel would be if that star was in a binary with a main-sequence companion. A binary consisting of two main-sequence stars is in the pre-interaction phase, meaning that both stars are essentially single, i.e. no mass transfer could have occurred. Therefore the emission line star in such a binary must have been formed through the single star channel. It has been claimed that there are no such emission line + main-sequence binaries (Bodensteiner, Shenar and Sana, 2020). However concerted efforts have revealed several promising candidates such as ν Gem. (Klement, Hadrava et al., 2021), Achernar (Kervella et al., 2022) and β Ceph. (Wheelwright, Oudmaijer and Schnerr, 2009). Future results in this area are eagerly anticipated.

1.7.2 Binary star formation channel

Critically rotating stars can form via mass transfer in binary systems, as outlined in Section 1.6.2. The accretion of mass must be accompanied by the accretion of angular momentum, thus spinning up the mass gaining star in the binary. This is depicted schematically in Fig. 1.11.

We have direct evidence of this scenario through observations of emission line stars with stripped star companions (L. Wang, Gies, Peters et al., 2021), which are the mass donors just after mass transfer has stopped. Also observed are emission line star binaries with white dwarves (K. L. Li et al., 2012; Coe et al., 2020), black holes (Casares et al., 2014) and neutron stars (Raguzova and Popov, 2005). The latter objects are a class known as Be-Xray binaries. Here the neutron star is sent on an eccentric orbit after receiving a birth kick. When the neutron star passes close to or through its companion's decretion disc, Xrays are emitted. This situation is shown in the rightmost sketch of Fig. 1.11.

| MS + MS | Mass & ang. mom. transfer | Be + stripped star | Be-Xray binary |
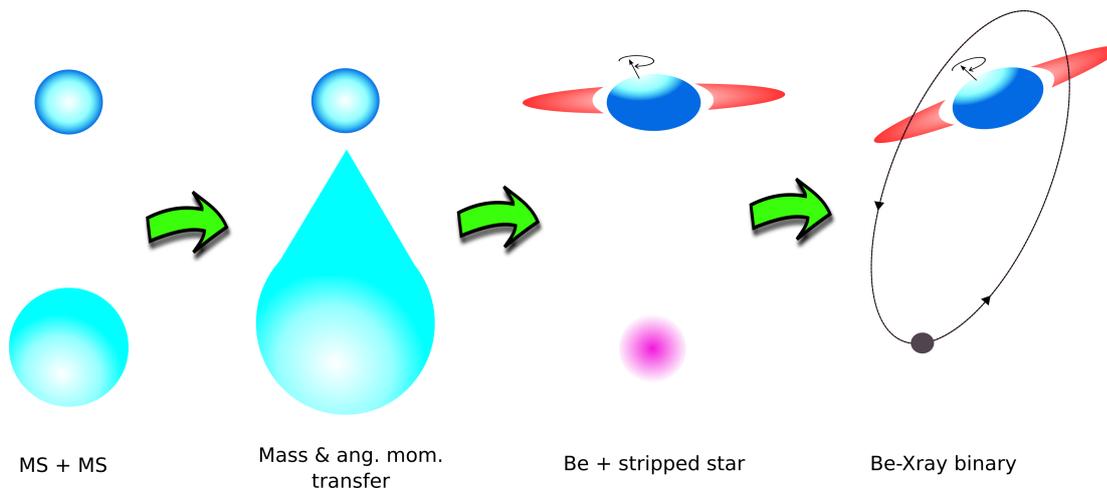
Figure 1.11: Schematic of binary evolution channel leading to the formation of an emission line star. Shown are the states of pre-interaction, mass transfer, Be + stripped star binary and Be-Xray binary.

It is believed that in most systems, the neutron's stars birth kick will break the binary system apart (N. Brandt and Podsiadlowski, 1995), resulting in an emission line star travelling through space with a fast velocity. Such stars are known as runaways, or walkaways if they are not moving so quickly. The star ζ Oph. is an example of such a runaway emission line star for which the corresponding neutron star has been found (Hoogerwerf, de Bruijne and de Zeeuw, 2001).

During the mass transfer, there is no known process that would cause the accretor star to be only partially spun up, that is not to reach critical velocity. It is thus assumed that binary interaction produces emission line stars that are rotating at the critical velocity. This is in contrast to the single star channel, for which various mechanisms operate to limit the evolution towards the critical velocity. Although emission line stars formed through the binary channel may quickly spin down, a diagnostic to distinguish the formation channel could be the rotation rate of the emission line stars, with those produced from binary interaction expected to be spinning critically.

Depending on the mass transfer efficiency, the surface nitrogen abundance of mass accretors may be enriched. If mass transfer is inefficient, the accretor would have accreted little material, and its surface chemical composition is not expected to be dramatically altered. However, if mass transfer is efficient, then the accretor will accrete material that lay deep inside the donor. This material will be contaminated with the products of nuclear reactions, and hence will be nitrogen rich. Therefore conservative binary evolution predicts the accretors to have surface nitrogen enrichment, while for non-conservative mass-transfer one does not expect significant nitrogen enrichment.

1.8 Context of this thesis

This thesis investigates the formation channels of classical emission line stars from a theoretical perspective to determine the contributions of each channel to the observed populations. The previous evolution of a star offers strong constraints on its future evolution and so studying the formation channels of classical emission line stars enables us to enrich our understanding of several distinct areas of astrophysics, especially as emission line stars represent a large proportion of massive stars (Milone,

Marino et al., 2018; Bodensteiner, Sana et al., 2020; Schootemeijer, Lennon et al., 2022). Diverse phenomena such as supernovae, gravitational wave events, star-disc interactions, stellar winds and galactic chemical evolution to name but a few can be illuminated by the study of classical emission line stars.

The defining feature of an emission line star is assumed to be its fast rotation and the origin of this fast rotation shall be studied. Theoretical predictions of emission line star populations resulting from both the single and binary formation channels shall be confronted with observations. Furthermore, the distinct uncertainties plaguing each formation channel shall be explored; namely stellar winds for the single star channel and mass transfer efficiency for the binary channel.

1.8.1 The single star path to Be stars

Chapter 2 explores the single star Be production channel. The evolutionary models of rotating single stars from Brott, de Mink et al. (2011) are used to investigate the factors affecting the evolution of a single star's rotation. The strength of stellar winds and the size of the convective core are found to be the key factors governing spin evolution. Trends in initial mass and metallicity are explored.

Using a distribution of observed rotation velocities from the Small Magellanic Cloud, the spin evolution is followed for members of a synthetic population. The synthetic population is coeval and hence represents a young open star cluster. By assuming different minimum fractions of critical velocity for the emission line phenomenon, emission line stars within the synthetic population are highlighted and their positions in the colour-magnitude diagram are predicted.

The synthetic population is compared with observations of the young open cluster NGC 330, in which emission line stars are seen as Hα emitters. It is found that the models can only explain the observed number of emission line stars located near the cluster main-sequence turn-off if the criteria to show emission features is relaxed to 70% of the critical velocity. The models are not able to explain the significant presence of Hα emitters up to two magnitudes below the turn-off. This failure leads to the conclusion that the single star channel cannot be the sole formation mechanism of emission line stars.

1.8.2 A Stringent upper limit on Be star fractions produced by binary interaction

Motivated by the findings of Chapter 2, focus is turned to investigating whether the binary evolution channel alone can explain the population of emission line stars in NGC 330. Several distinct uncertainties such as mass transfer efficiency and the occurrence of mergers make the predictions from detailed evolutionary binary models unreliable.

Chapter 3 details a simple analytic toy model of binary evolution in which every binary system is assumed to form a Be star. The model deliberately produces the largest possible numbers of Be stars. Using such extreme assumptions is helpful as it provides an upper limit that can gauge the binary Be star production channel with nature.

The number of Be stars at the main-sequence turn-off of the open cluster NGC 330 is described well by the upper limit. Below the turn off however, the toy model over-predicts the numbers of Be stars. The model is corrected to match the Be star population along the main-sequence by assuming that certain binary systems merge and hence do not produce Be stars. Chapter 3 concludes that binary evolution can in principle accurately mirror the Be star populations in nature, although extreme assumptions are required which might not be realistic.

1.8.3 A model of anisotropic winds from rotating stars for evolutionary calculations

A significant uncertainty in a single star's ability to evolve towards the critical velocity is stellar winds. Stellar winds drain angular momentum and hence effect a star's spin evolution. Chapter 4 investigates the relationship between rotation and mass and angular momentum loss through stellar winds.

Rotation introduces a centrifugal force whose strength varies over the stellar surface. This results in rapidly rotating stars becoming oblate and having spatially variable surface properties. Stellar winds depend on the surface properties, hence it follows that the winds of rotating and non-rotating stars are not identical. Evolutionary models, such as those used in Chapter 2, make simple assumptions about the mass-loss rates of fast spinning stars, ignoring the two dimensional geometry of a rotating star. Hence the spin evolution predicted by such models is uncertain.

This uncertainty is alleviated by the work contained in Chapter 4. A prescription for calculating the mass and angular momentum loss rates of a distorted star is developed. The prescription is designed to be easy to implement in one-dimensional stellar evolution codes and exploits theoretical mass-loss recipes for non-rotating stars. The mass-loss recipe is applied locally to every point on the stellar surface to calculate a surface mass flux which is then integrated to give global mass and angular momentum loss rates.

It is predicted that mass-loss rates are largely insensitive to rotation. The new prescription suggests that angular momentum loss rates have thus previously been slightly overestimated in evolutionary models such as those of Brott, de Mink et al. (2011). This may imply that the single star Be production channel is more viable than previously thought, however adopting the improved prescription does not greatly alter the spin evolution of the models presented. This gives confidence in the conclusions of Chapter 2

1.8.4 Constraints on mass transfer physics from Be + stripped star binaries

Binary star evolution also suffers from distinct uncertainties. Chapter 5 attempts to constrain some of these uncertainties through a comparison of binary evolution calculations to observations of Be + stripped star systems.

During mass-transfer, the path that material takes once it has left the donor is not well known. It may either be efficiently accreted onto the accretor star, or be ejected entirely from the system. Previous studies have argued that both cases are realised in nature (de Mink, Pols and Hilditch, 2007). The efficiency of mass-transfer can severely alter the evolutionary pathway of the accreting star, as well as the orbital properties of the binary, making mass-transfer efficiency one of the largest uncertainties in binary evolution. Furthermore, when mass-transfer is inefficient, it is not clear how much angular momentum leaves the binary. Angular momentum loss affects the orbital evolution of the system, and high angular momentum loss can lead to the coalescence of the two stars.

Be + stripped star systems are in the stage just after mass-transfer has terminated and before the stripped star either explodes as a supernova or forms a white dwarf. This short lived state offers the clearest window onto the mass-transfer process because the system has not yet been affected by a supernova kick or the formation of a planetary nebula.

"Extremely rapid" binary evolution calculations are performed, whereby only the mass and orbital period of the system is followed during mass-transfer, over a large parameter space. The calculation results are compared with observations of three Be + stripped star systems to determine the most likely parameters governing mass-transfer.

Mass-transfer efficiencies are found to be in the range 30-50% and angular momentum loss is found to be weaker than the commonly adopted isotropic re-emission scenario. These results can guide further study and influence the design of the next generation of detailed binary evolution models.

The single star path to Be stars

Ben Hastings[1], Chen Wang[1], Norbert Langer[1]

[1] Argelander-Institut für Astronomie, Universität Bonn, Auf dem Hügel 71, 53121 Bonn, Germany

SUMMARY

Be stars, also known as classical emission line stars, are a class of rapidly rotating B main sequence stars, which show line emission due to an out-flowing disc. Despite these stars making up an appreciable fraction of the massive star population, the origin of their rapid rotation is not well understood. One possibility is that Be stars are single stars which were born with sufficient angular momentum to allow for fast rotation during their evolution. The study of rotating single star models allows us to assess the contribution of single stars to the observed Be star populations, as well as study the factors governing a single star's spin evolution.

We analysed a dense grid of stellar models with initial masses ranging from 3 to 30 solar masses and initial equatorial velocities spanning 0 to 600 km/s at three chemical compositions representing the Milky Way, Large and Small Magellanic Clouds. The models include efficient core-envelope coupling mediated by internal magnetic fields. This has the effect of ensuring near solid-body rotation and results in larger rotational velocities over the stellar lifetime than models without such coupling.

Internal structural changes during hydrogen burning cause a rotating stellar model to evolve towards the critical velocity, at which gravity balances the centrifugal force at the equator. The factors governing this evolution were found to be stellar wind mass-loss and the size of the convective core. Stellar winds remove both mass and angular momentum, so it is clear that strong winds will cause a rotating star to spin down due to the loss of angular momentum. A large convective core enables a star to maintain its surface rotation. As a star evolves, the surface expands, while contrastingly, the convective core contracts. Local conservation of angular momentum demands the core spins up and the surface spins down. However, under solid-body rotation, angular momentum must be transferred from the core to the surface. This transfer allows the surface to maintain a high rotation rate. Increasing initial stellar mass brings about a larger convective core, but more

massive stars also host stronger winds. Lower mass stars have weak winds, but very small convective cores. In between these two regimes exists a "Goldilocks zone" where the approach to the critical velocity is most effective. It was found that this occurs for stars with an initial mass of approximately 17 solar masses.

An empirical distribution of initial rotational velocities was used to produce a synthetic population that was designed to represent young open clusters. Positions of fast rotators were predicted in the colour-magnitude diagram. Assuming different threshold rotation rates to define a Be star, the Be star fraction in various regions along the main-sequence was determined.

The single star models can reproduce the trends observed in Be star fractions with metallicity and cluster age. Higher atmospheric opacities brought about by an increased proportion of metals allow for effective momentum exchange between radiation and gas. Thus metal rich stars suffer from strong winds and spin down quickly. Older clusters contain less massive stars, with smaller convective cores and hence are not able to effectively maintain rapid rotation throughout their evolution.

The colour-magnitude diagram of the Small Magellanic Cloud cluster NGC 330 was directly compared to the synthetic population. It was found that the high numbers of Be stars at the main-sequence turn-off can only be explained if the threshold rotation rate for the emission line phenomenon is relaxed to 70% of critical rotation. The high incidence of Be stars up to two magnitudes below the turn-off cannot be explained by the synthetic population, irrespective of the chosen threshold rotation rate. Although many of the more evolved Be stars may originate from single star evolution, none of the significant population of unevolved Be stars can be explained by single rotating stellar models.

It is thus concluded that the single star channel does not act alone in the production of Be stars and that the binary channel must play role, especially for the relatively unevolved stars away from the main-sequence turn-off.

2.1 Introduction

Ever since their discovery over 150 years ago (Secchi, 1866), Be stars have offered a promising, although misted window into massive star evolution and structure. It was proposed by Struve (1931) that Be stars are fast rotators, whose emission lines originate from a circumstellar decretion disc, a picture which is maintained until today (Rivinius, Carciofi and Martayan, 2013). Yet, it is still not clear how fast a B-type star must rotate in order to become a Be star.

For a decretion disc to form, the equatorial rotation velocity v_{rot} is expected to be a significant fraction of the critical rotation velocity, v_{crit}, defined as the rotation velocity at which material at the equator becomes unbound from the star. Observational evidence suggests that the threshold rotation rate for the Be phenomenon is mass dependant, and could be as low as $v_{rot}/v_{crit} = 0.6$ for stars more massive than 8.6 $M_\odot$ and as high as $v_{rot}/v_{crit} = 0.96$ for stars with $M < 4$ $M_\odot$ (Huang, Gies and McSwain, 2010). Similarly Zorec, Frémat, Domiciano de Souza et al. (2016) find that the Be phenomenon is characterized by a wide range of true velocity ratios ($0.3 < v_{rot}/v_{crit} < 0.95$) and that the probability that Be stars are critical rotators is small. In this case one must look for an additional mechanism to feed the Be disc. Pulsations seem promising as they can serve to kick matter from the surface of a star, however it is found that not all Be stars pulsate (Baade et al., 2002) and that among those that do there is a wide range of pulsation frequencies and types (Rivinius, Carciofi and Martayan, 2013). Another possibility is that the disc is fed through outbursts of magnetically active starspots, similar to coronal mass ejections as seen in the Sun, as suggested by Balona and Ozuyar (2019) based on recent TESS results.

On the other hand, Townsend, Owocki and Howarth (2004) have argued that all Be stars in fact rotate very close ($v_{rot}/v_{crit} > 0.95$) to the critical velocity, with those which have low measured rotation rates being strongly affected by gravity darkening. Following the Von Zeipel law (von Zeipel, 1924), gravity darkening in a fast rotating star makes the stellar pole, which has a low rotational velocity, more luminous than the equator which has a high rotational velocity, resulting in the star appearing as though it is rotating slower than in reality.

A further question surrounding Be stars is why the phenomenon seems to be restricted mostly to B-type stars and why Be stars are more common in certain spectral classes than others. Observations in the Milky Way show that the fraction of Be stars in a certain spectral class varies across spectral type with the most Be-stars found at B1-B2 classification, where the Be fraction is 34% while in comparison the Be fraction for B9 stars is 8% and the total fraction of Be stars to B stars was measured to be 17% (Zorec and Briot, 1997). Furthermore, Oe stars seem to be rather rare, with less than 20 having been detected in the Milky Way (G.-W. Li et al., 2018). It is not clear whether this is caused by processes within O stars themselves, the mechanisms responsible for forming a disc around a fast rotating star, or the conditions under which very massive stars form.

The existence of around 150 (Raguzova and Popov, 2005) detected binary systems consisting of a Be star and a compact object (so called Be/X-ray binaries) demonstrates that binary interactions can spin up a star significantly (Kriz and Harmanec, 1975; Pols et al., 1991a; Liu, van Paradijs and van den Heuvel, 2006; Langer, 2012). In order to build a full model of the Be phenomenon, binary evolution must be as well understood as the channels for forming single Be stars.

van Bever and Vanbeveren (1997) used binary star evolution calculations to predict that at most 20% of the Be star population results from binary interactions. Despite this, observations of surface nitrogen abundances in Magellanic Cloud Be stars are in disagreement with fast rotating single star models (Dunstall et al., 2011). Thus questions such as, which is the dominant Be star formation channel and what are the differences between the single and binary Be population remain open.

Considerable efforts have been made to predict the relative fractions of Be stars through single star modelling, most notably by Ekström et al. (2008). These models include coupling between core and envelope by hydrodynamic viscosities through the shear instability. However, a stronger coupling may be produced by internal magnetic fields known as the Tayler-Spruit dynamo (Spruit, 2002) which produces very efficient angular momentum transport throughout the star so that near solid-body rotation occurs. The models analysed here include such effects, and therefore employ the maximum efficiency of spinning up the surface layers due to the core contraction during hydrogen burning, which is a key factor to produce single Be stars. At present the Tayler-Spruit dynamo is used to explain relatively slow rotation rates in white dwarfs (Suijs et al., 2008) and young pulsars (Heger, Woosley and Spruit, 2005).

In Section 5.3 the models are introduced and our approaches are outlined. In Section 5.4, models from the grid are analysed under conditions of fast and slow rotation for MW and SMC metallicities, the factors governing the approach to the critical velocity are investigated and the expected surface nitrogen abundances of Be stars is investigated. In Section 2.4, population synthesis is performed to calculate the expected fractions of single Be stars in clusters of differing ages and metallicities and predict the positions of fast rotating stars in the colour-magnitude diagram.

2.2 Method

2.2.1 Stellar models

We analyse the single star evolutionary models of Brott, de Mink et al. (2011) to predict the properties of rotating single stars throughout their main-sequence evolution. We consider masses from $3\,M_\odot$ to $30\,M_\odot$ at various initial rotation velocities ranging from zero to approximately $600\,\mathrm{km\,s^{-1}}$. Because the model grid is spaced in initial rotational velocities, but the initial critical rotation velocity increases with mass, our grid does not contain models with initial values of $v_{\mathrm{rot}}/v_{\mathrm{crit}}$ greater than around 0.7 for initial masses greater than $25\,M_\odot$.

Three initial chemical compositions represent metallicities of the Milky Way (MW), Large Magellanic Could (LMC) and Small Magellanic Cloud (SMC). The models include internal transport of angular momentum via the Taylor-Spruit dynamo (Spruit, 2002) which has the effect of enforcing near solid-body rotation throughout most of the main-sequence evolution. The adopted mass-loss scheme is given by Vink, de Koter and Lamers (2000). An enhancement of the mass loss due to rotation is used as outlined in Yoon and Langer (2005), whereby the mass loss rates are increased by a factor depending on the ratio of the rotation velocity to the critical velocity like

$$\dot{M}(\Omega) = \dot{M}(0)\left(\frac{1}{1 - \frac{v_{\mathrm{rot}}}{v_{\mathrm{crit}}}}\right)^{0.43} \tag{2.1}$$

where

$$v_{\mathrm{crit}} = \sqrt{\frac{GM}{R}(1-\Gamma)}\;;\;\Gamma = \frac{\kappa L}{4\pi c G M}. \tag{2.2}$$

For a detailed description of the models see Brott, de Mink et al. (2011).

2.2.2 Population synthesis

To predict properties of populations of rotating stars we use population synthesis to model open star clusters (i.e. collections of coeval stars without any continuous star formation) at various ages. For a cluster age t, we select pairs of random values from a Salpeter initial mass distribution (with exponent 2.35) and a distribution of initial critical velocity fraction, M_i and $v_{\mathrm{rot}}/v_{\mathrm{crit}\,i}$. Then we find the masses, M_1, M_2 on the model grid that are straddling the chosen mass value, such that $M_1 < M_i < M_2$. For M_1 and M_2 we interpolate the hydrogen burning lifetimes, t_{MS} as a function of initial critical velocity fraction to obtain the hydrogen burning lifetimes at the chosen value, $v_{\mathrm{rot}}/v_{\mathrm{crit}\,i}$. Next the hydrogen burning lifetime, $t_{MS,i}$, of a model with mass M_i and initial rotation $v_{\mathrm{rot}}/v_{\mathrm{crit}\,i}$ is found by interpolating between the hydrogen burning lifetimes of M_1 and M_2. The fractional lifetime is then given by $t/t_{MS,i}$. If the fractional lifetime is greater than 1, the star will not be hydrogen burning anymore so the process is abandoned and new samples are drawn. We then select models with masses M_1 and M_2 at fractional hydrogen burning times $t/t_{MS,i}$. An interpolation of the quantity of interest, Q across initial critical velocity fraction gives the values of Q for masses M_1, M_2 with initial rotation $v_{\mathrm{rot}}/v_{\mathrm{crit}\,i}$ and fractional hydrogen burning time $t/t_{MS,i}$. One final interpolation between M_1 and M_2 gives the predicted quantity of the selected mass M_i at the given cluster age. The quantities of interest are luminosity, critical velocity fraction at the current time and effective temperature.

The initial rotational velocity distribution used was taken from VLT-FLAMES observations of early B stars in the 30 Doradus region of the LMC (Dufton, Langer et al., 2013) and is shown in Fig. 2.1. The deconvolved distribution of equatorial rotational velocities was converted to a distribution in critical velocity fraction by applying a mapping between the two as determined from the $15\,M_\odot$ LMC models at ZAMS and then normalizing such that the integral over the whole probability density function equals unity. It is noted that for the heaviest masses on the grid, the distribution extends beyond its limits. When such a massive, very fast rotating star is chosen from the distributions, instead the fastest rotator in the grid is used. Observations in 30 Doradus show that no O stars are observed to rotate with deconvolved equatorial velocities much greater than $500\,\mathrm{km\,s^{-1}}$ (Ramirez-Agudelo, Simón-Diaz et al., 2013; Dufton, Dunstall et al., 2011). For a $25\,M_\odot$ star to rotate at a critical velocity fraction of 0.7, it would require an equatorial rotation velocity of the order $700\,\mathrm{kms^{-1}}$. It is thus safe to assume that O stars do not enter the ZAMS with initial critical velocity fractions much greater than 0.65, or that if they do, they spin down very quickly.

We note that adopting the observed distribution of rotational velocities of Dufton, Langer et al. (2013) as the initial velocity distribution for stars in our synthetic populations may introduce an inconsistency, since the the sample of Dufton, Langer et al. (2013) consists of field stars of all ages. However, as discussed in Dufton, Langer et al. (2013) (see also Sect. 3.1
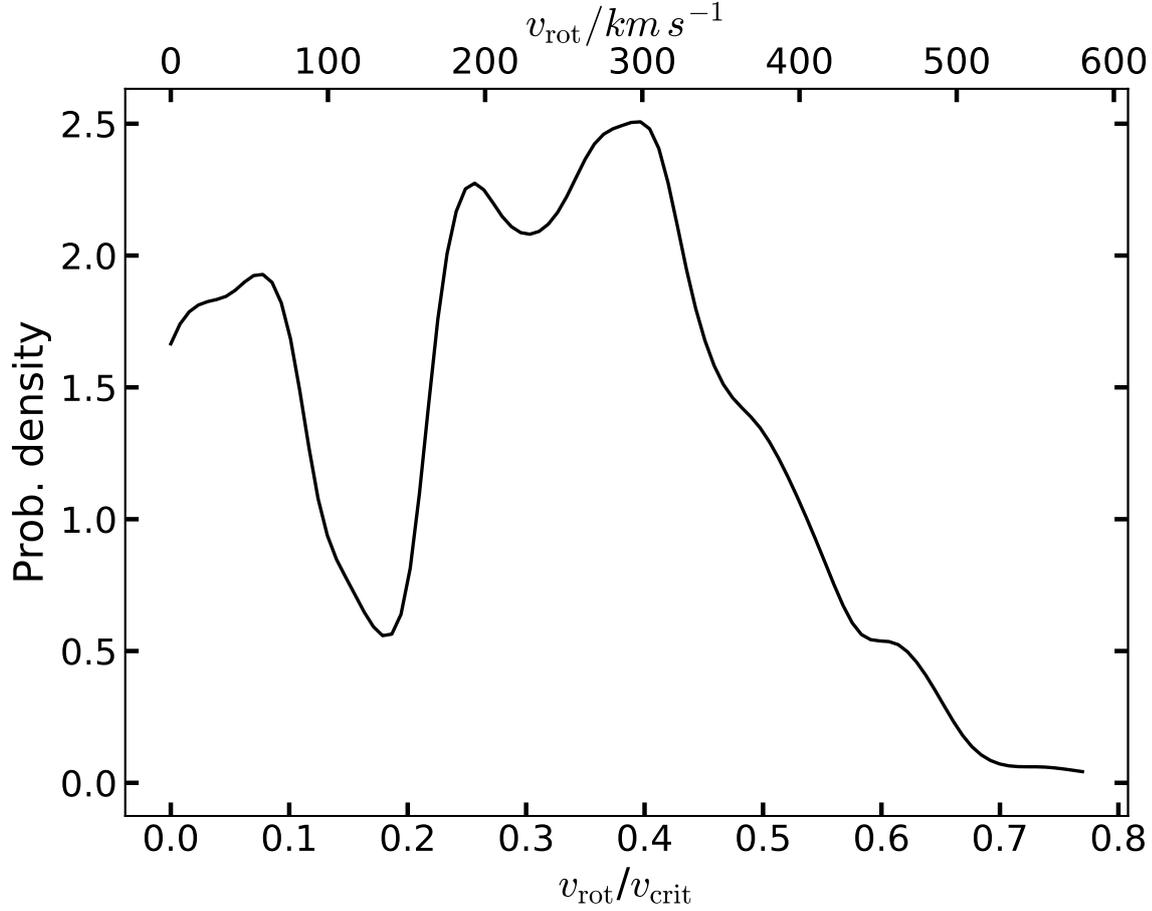
Figure 2.1: Deconvolved rotation distribution of early B stars as observed by VLT-FLAMES Survey (Dufton et al., 2013). The distribution was converted to $v_{\mathrm{rot}}/v_{\mathrm{crit}}$ using $15\,\mathrm{M}_\odot$ LMC models at ZAMS. The upper scale shows how the critical velocity fraction values, $v_{\mathrm{rot}}/v_{\mathrm{crit}}$ match to the equatorial velocities, v_{rot}.

below), the rotational velocities of the considered single stars are expected to change very little during their main sequence evolution. If binary evolution affects this distribution de Mink, Langer, Izzard et al., 2013, then we would overestimate the number of stars which are born rotating very rapidly. In this case, the predicted number of Be stars from our models may be considered as upper limits.

To compare the models with observations of the SMC open cluster NCG 330 (Milone, Marino et al., 2018) in the colour-magnitude diagram, the bolometric luminosities and effective temperature are converted to absolute magnitudes in the Hubble Space Telescope Wide-Field Camera 3 filters F814W and F336W by interpolating tables based on synthetic stellar spectra (Girardi et al., 2002). The values of distance modulus and reddening adopted are $(m - M) = 18.92$ and $E(B - V) = 0.06$ respectively. The absorption coefficients used are $A_{F814W} = 2.04E(B - V)$ and $A_{F336W} = 5.16E(B - V)$ (Milone, Bedin et al., 2009). The effects of gravity darkening are included as described by Espinosa Lara and Rieutord (2011), whereby the effective temperature and luminosity of a star are multiplied by parameters that depend on the inclination angle and fraction of angular critical velocity. Then using these corrected effective temperature and luminosity values, we calculate the absolute magnitudes as described above. The inclination angles, i, in our synthetic population are chosen such that $\cos(i)$ is uniformly distributed between 0 and 1, meaning that it is more likely to observe any given star equator-on than pole-on. Such a distribution describes a random orientation of the rotation axis.
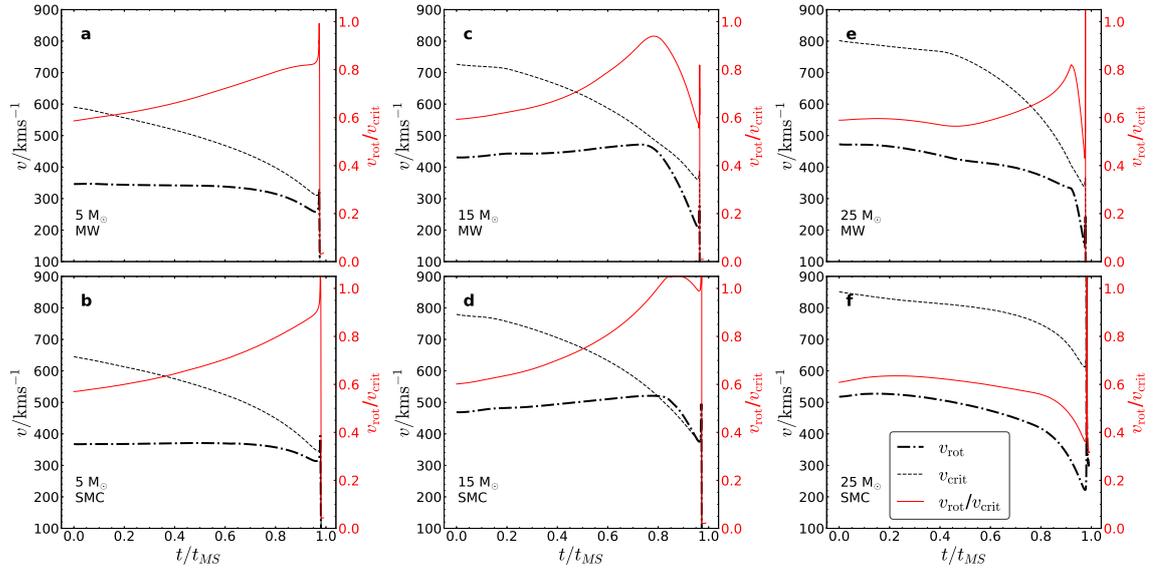
Figure 2.2: Evolution of equatorial rotational velocity v_{rot} (thick dot-dashed), critical velocity v_{crit} (dashed) and the critical velocity fraction v_{rot}/v_{crit} (solid red) for $5\,M_\odot$ (panels a, b), $15\,M_\odot$ (panels c, d) and $25\,M_\odot$ (panels e, f) models at MW metallicity (panels a, c, e) and SMC metallicity (panels b, d, f). The initial critical velocity fraction values are all approximately 0.6. The X-axis indicates the fractional main sequence lifetime, t/t_{MS}.

2.3 Results

2.3.1 Spin evolution

During the evolution of a slowly rotating star during core hydrogen burning, a strong chemical gradient develops between the convective core and the radiative envelope. The core density increases, and as a reaction the envelope must expand in order to maintain hydrostatic and thermal equilibrium. Eq. 2.2 shows that as the stellar radius increases, the critical velocity decreases, thus during main-sequence evolution, the critical velocity will fall.

In the absence of internal angular momentum transport, as core density increases, the local conservation of angular momentum will demand that the angular velocity of the core increases. Likewise as the envelope expands, the angular velocity of the envelope will decrease. This results in an angular velocity gradient developing between the convective core and radiative envelope. However when the core and envelope are coupled via angular momentum transport, angular momentum is transported from the core to the envelope, decreasing the angular velocity gradient throughout the star. The physical processes responsible for the angular momentum transport in the models studied here are magnetic torques arising from the Tayler-Spruit dynamo (Spruit, 2002), which leads to near solid body rotation. While the envelope is expanding and the star is rotating as a solid body, the critical rotation velocity will decrease while the equatorial rotation velocity drops only slowly or even increases (see Section 2.3.3).

Fig. 2.2 gives examples of the evolution of critical velocity, equatorial velocity and fraction of critical velocity during main-sequence evolution for MW and SMC models of initial masses 5, 15 and $25\,M_\odot$. All models in the plot have an initial critical velocity fraction of approximately 0.6. Although the less massive models have slower equatorial velocities, they also have lower critical velocities (because of a relatively weak dependance on radius with mass), making the critical velocity fraction nearly the same for all models in the plot. It is seen that for the $5\,M_\odot$ models the equatorial rotation velocity remains nearly constant, while the critical velocity decreases. For the $15\,M_\odot$ models, the equatorial rotation velocity increases due to the effects of angular momentum transport. As a result, the critical velocity fraction is generally increasing during hydrogen burning such that the stars are evolving closer to critical rotation, unless angular momentum is drained at a high rate due to mass loss (see Section 2.3.2).

2.3.2 The effect of mass loss

The dominating effect of mass loss through stellar winds is to remove angular momentum, not mass. This is so because even in the absence of magnetic fields, the rate of angular momentum loss relative to the total angular momentum is about 10 times larger than the rate of mass loss relative to the stellar mass (Langer, 1998). Thus a star's mass-loss may strongly affect the spin evolution.

Panels a, c, e of Fig. 2.2 show that models at MW metallicity experience a turn-over in the evolution of their critical velocity fraction. This is because in the late stages of hydrogen burning, the star's mass-loss rate increases significantly which has the effect of removing angular momentum from the surface at a rate which cannot be compensated by internal angular momentum transport mechanisms, meaning that solid body rotation is no longer a good approximation and the equatorial velocity decreases. This period of strong mass-loss is caused by the iron opacity bistability in which partial recombination of Fe ions at effective temperatures of around 22kK causes a sharp increase in opacity and hence mass-loss (Lamers, Snow and Lindholm, 1995). This behaviour is strongly dependant on metallicity and so weaker in the SMC or LMC models. Comparing Panels c and d of Fig. 2.2, it can be seen that despite both MW and SMC models starting with approximately equal critical velocity fractions, the SMC model achieves a much larger critical velocity fraction at the end of the main-sequence. This comparison between MW and SMC models illustrates the effect of mass-loss on the approach to the critical velocity.

Fig. 2.3 shows the ratio of angular momentum at the end of hydrogen burning to the initial angular momentum for models of varying mass and initial critical velocity fraction for MW and SMC models. It is clear that almost every SMC model loses much less angular momentum than the corresponding model at MW metallicity. The exceptions are fast rotating massive SMC models which undergo quasi-chemically homogeneous evolution, and during so become very luminous which leads to increased mass loss rates. For SMC models one may judge that mass-loss becomes irrelevant to the angular-momentum budget below masses of around $10 \, M_\odot$, where most models (except very fast initial rotators, say with $v_{\mathrm{rot}}/v_{\mathrm{crit}} > 0.7$) retain more than 90% of their angular momentum. For MW models we see that only slowly rotating models less massive than $5 \, M_\odot$ retain more than 90% of their angular momentum. As expected, the effect of mass-loss is strongly metallicity dependant. It is also seen that below $15 \ldots 20 \, M_\odot$, angular momentum loss becoming less dependant on mass.

Fig. 2.3 shows that for any given mass the fraction of angular momentum lost is a strong function of the initial rotation. For example a $5 \, M_\odot$ model at MW metallicity can lose between 2 and 30 % of its initial angular momentum. One contributing factor is the lifetime effect, whereby under the effects of rotation, rotational mixing causes hydrogen to be mixed into the centre of the star and so hydrogen burning can continue for a longer time. For all of our models, the hydrogen burning lifetime enhancement between the non-rotating model and that with an initial rotation velocity of $600 \ \mathrm{km \, s^{-1}}$ never exceeds a factor of 1.5. Thus for models losing only small fractions of their total angular momentum as slow rotators (such as low mass MW metallicity models and all SMC metallicity models), the lifetime effect cannot explain wholly the increase in angular momentum loss.

Another effect is rotationally enhanced mass loss. As a star approaches the critical rotation velocity, material at the equator becomes less tightly bound due to the centrifugal force, thus one would expect angular momentum lost through winds to increase with rotation velocity. In the models this is governed by Eq. 2.1. With $v_{\mathrm{rot}}/v_{\mathrm{crit}} = 0.8$, the mass loss rates are doubled, so rotationally enhanced mass loss plays only a large role when very high critical rotation fractions are achieved. As an example the $5 \, M_\odot$ models at MW metallicity in Fig. 2.3 show that in the range of initial $v_{\mathrm{rot}}/v_{\mathrm{crit}}$ from 0 to 0.4, the total angular momentum lost is almost the same. However when approaching critical rotation, the enhancement factor becomes divergent, so models rotating near the critical velocity experience tremendous mass loss.

A further effect of rotationally induced mixing is to increase the overall mean molecular weight, μ in the star, compared to models with no rotationally induced mixing. Homologous models suggest a strong dependance on luminosity with mean molecular weight such that $L \propto \mu^4$ (Kippenhahn and Weigert, 1990). In turn, mass-loss rates are dependant on the luminosity, for the wind prescription used in the models the dependance is approximately $\dot{M} \propto L^2$ (Vink, de Koter and Lamers, 2000). Thus rotationally induced mixing leads to higher mass loss and angular momentum loss. For models which experience quasi-chemical homogeneous evolution, where the star can become a helium star, this effect becomes very apparent. Models which undergo quasi-chemical homogeneous evolution for the duration of hydrogen burning (defined by a monotonically increasing surface helium mass fraction) are marked with black circles in Fig. 2.3. Similarly models which undergo a phase of quasi-chemical homogeneous evolution (defined by having a slowly increasing difference between surface and central helium mass fraction for longer than one third of the hydrogen burning lifetime) are marked by a red circle. Although these models do not have high initial critical rotation fractions, they still lose large fractions of their angular momentum. Quasi-homogeneous evolution occurs more readily in the lower metallicity models because mass loss being a strong function of metallicity, so the MW metallicity models slow down relatively quickly, rotational mixing becomes less effective and the homogeneous evolution stops (Yoon, Langer and Norman, 2006).
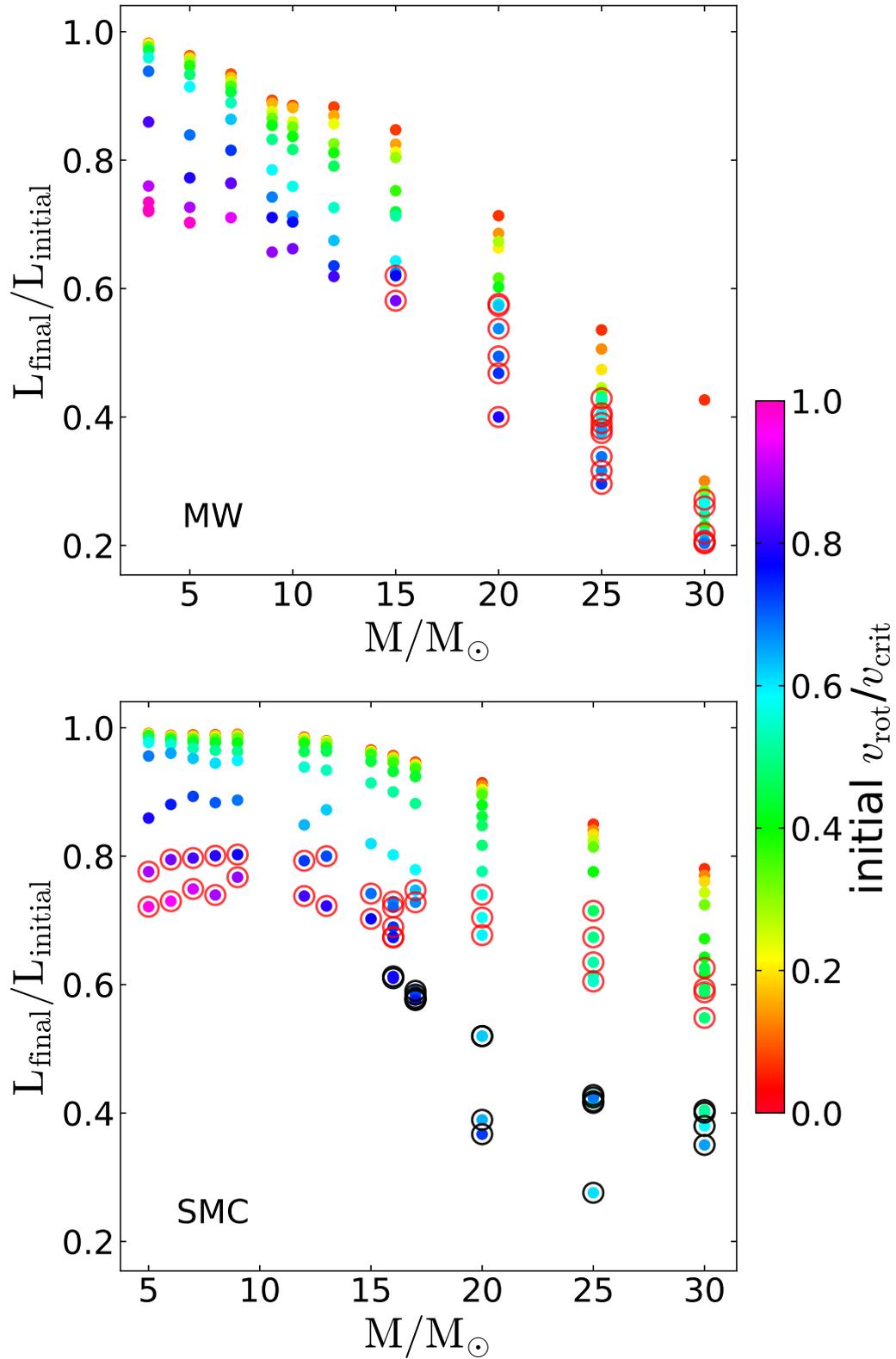
Figure 2.3: Fraction of angular momentum at the end of hydrogen burning L_{final}, to angular momentum at the start of hydrogen burning $L_{initial}$, as a function of mass for MW (top) and SMC (bottom) metallicities. The colour of the points represents the initial critical velocity fraction v_{rot}/v_{crit}. Models with a growing helium surface abundance throughout the duration of their evolution are marked by a black circle. Models with a growing helium surface abundance for part of their evolution are marked by a red circle.
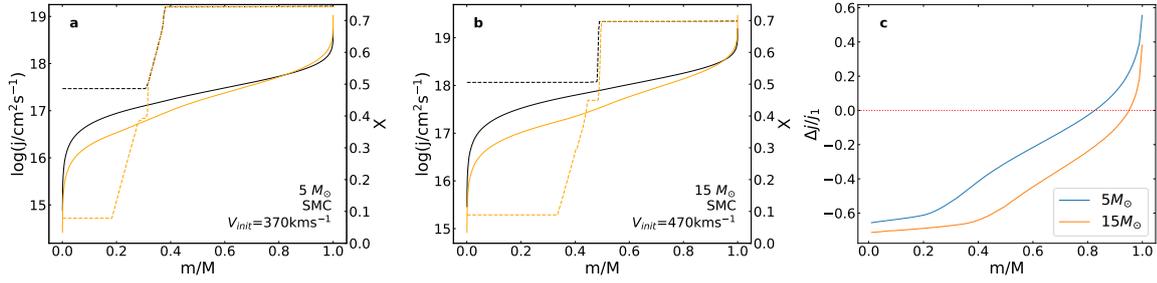
Figure 2.4: **a-b:** Specific angular momentum (solid lines) and hydrogen mass fraction (dotted lines) profiles for two SMC models of masses 5 and $15\,M_\odot$ and initial equatorial velocities of 370 and 470 kms^{-1} respectively. These are the same models plotted in panels b & d of Fig. 2.2 and both models have initial critical velocity fractions of around 0.6. Profiles are plotted for models where central helium mass fraction is 0.45 (black) , and 0.91 (orange). **c:** For each model in panel a & b the fractional difference in specific angular momentum is plotted between the two times. The blue line represents the $5\,M_\odot$ model,the orange the $15\,M_\odot$ model. The dotted red line gives a reference for no angular momentum transport. The X-axis in all plots indicates the fractional mass co-ordinate.

2.3.3 The effect of convective core mass

During the main-sequence evolution of a massive star, the convective core contracts while the radiative envelope expands. The conservation of angular momentum will therefore demand that in the absence of any internal angular momentum transport, the convective core and radiative envelope increases and decreases respectively their overall angular velocity (i.e. the core "spins up" while the envelope "spins down"). This tells us that to enforce solid body rotation during core contraction and envelope expansion, angular momentum must be transported from the core to the envelope. This is achieved by magnetic interactions which transport angular momentum along the angular velocity gradient within the star.

Let us now consider two extreme examples. In a rotating star with a negligible envelope mass, the core will dominate the angular momentum budget. Thus to maintain a constant rotational velocity during envelope expansion, a relatively low angular momentum transport rate is required. On the other hand, for an envelope dominated star to rotate at a constant velocity while the envelope is expanding, the angular momentum transport rate from core to envelope must be high. It is then likely that internal angular momentum transport mechanisms are unable to meet this demand, and as a result the rotational velocity of the stellar surface will decrease due to the effect of local angular momentum conservation.

In our models, there is an inner region of the star from which angular momentum is being transported and there is an outer region which the angular momentum is being transported to. Inbetween these regions there must be a point which neither gains nor loses any specific angular momentum. The location of this angular momentum "valve" will give an indication as to the strength of the core mass effect as discussed above. Figs. 2.4. a, b show the specific angular momentum profiles of a 5 and $15\,M_\odot$ model at one time early in their evolution and one time near the end of hydrogen burning. Hydrogen mass fraction profiles are plotted to show how advanced the evolution is. The models shown are the same as in Figs. 2.2b,d and have equal initial critical velocity fractions of 0.6. It can be seen that there is a point for each mass at which the specific angular momentum does not change.

Figure 2.4.c shows this more clearly, where the difference in angular momentum at both times, divided by the angular momentum at the earlier time, $\Delta j / j_1$, is plotted. Here, regions where angular momentum is gained have a positive value, whereas regions were angular momentum is lost have a negative value. For the more massive model, the point with a constant specific angular momentum is closer to the star's edge than for the less massive model. For the $15\,M_\odot$ model, approximately 90% of the total mass is acting as a donor of angular momentum, while for the $5\,M_\odot$ mode the figure is 80%. Using the arguments above, therefore the $15\,M_\odot$ model will approach the critical rotation velocity more easily. Furthermore by inspecting the area under the curves, in the region where $\Delta j / j_1$ is positive in Fig. 2.4.c one can determine how much relative angular momentum is gained. For example, if a region from $\frac{m}{M} = m_i$ to $\frac{m}{M} = 1$ had doubled its total angular momentum, the integral $\int_{m_i}^{1} \Delta j / j_1 d(\frac{m}{M})$ would be equal to $(2 - 1)(1 - m_i)$. Fig. 2.4.c shows that the relative angular momentum gain of the matter in the envelope of the $5\,M_\odot$ model is greater than that of the $15\,M_\odot$ model. This tells us that to maintain near solid body rotation, a relatively smaller amount of angular momentum must be transported in the more massive model.

2.3.4 The effect of efficient rotational mixing

When a star rotates initially at high velocities, quasi-chemically homogeneous evolution can occur. During such evolution, rotational mixing is so efficient that any chemical gradient between core and envelope cannot develop, meaning that the radiative envelope does not expand and the star's radius remains roughly constant (Maeder, 1987; Yoon, Langer and Norman, 2006). However because the luminosity of a quasi-chemically homogeneously evolving star approaches the Eddington limit, the critical velocity of such a star does decrease (through Eq. 2.2). Furthermore the increased luminosity causes a strong increase in the mass-loss rate, meaning that the equatorial velocities of stars undergoing quasi-chemically homogeneous evolution are likely to decrease with time. Thus such stars will evolve with a decreasing critical velocity fraction while quasi-chemically homogeneous evolution occurs.

This behaviour is shown for $25\,M_\odot$ models in Figs. 2.2 e,f. It can be seen that the highest critical velocity fractions occur during the early part of the stars' lifetimes because the critical velocities (dashed lines) decrease relatively slowly while the equatorial velocities (dot-dashed lines) fall due to angular momentum loss. In the MW model, quasi-chemically homogeneous evolution is shutdown when the star reaches an age of around 80% of the hydrogen burning lifetime and from this point on the star evolves normally and advances towards the critical velocity. The phase of quasi-chemically homogeneous evolution ends because as the rotational velocity decreases, rotational mixing processes become less efficient and a chemical gradient eventually develops in the star which provides a barrier to mixing through buoyancy forces (Heger, Langer and Woosley, 2000) and effectively "turns off" quasi-chemically homogeneous evolution.

For a star to evolve to a high critical velocity fraction, it must have a significant initial rotation velocity but also be rotating slowly enough to avoid quasi-chemically homogeneous evolution. As the minimum rotation rate required for quasi-chemically homogeneous evolution decreases with increasing mass (Yoon, Langer and Norman, 2006), very massive stars rotate at high critical velocity fractions for only very short fractions of their lifetimes, thus explaining the rarity of Oe stars.

2.3.5 Nitrogen enrichment

Here we address the question of whether or not Be stars formed through a single star evolving towards the critical velocity are expected to show significant surface nitrogen enrichment, where nitrogen is the product of hydrogen burning and is brought to the stellar surface through rotationally induced mixing. Fig. 2.5 shows the evolution of both surface nitrogen abundance and critical velocity fraction as a function of the fractional hydrogen-burning lifetime. Displayed are models with initial masses 5, 15 and $25\,M_\odot$ with SMC, LMC and MW metallicities. As discussed by Brott, de Mink et al. (2011) the relative increase of the nitrogen abundance goes down with increasing metallicity, therefore we see weaker nitrogen enrichment in the MW models than the LMC or SMC models. It is also clear that rotationally induced mixing is more efficient in more massive stars, owing to the effects of increased radiation pressure in more massive stars (Maeder, 1987; Yoon, Langer and Norman, 2006).

From the bottom panels of Fig. 2.5, we expect that in the Milky-way, nitrogen is never enhanced by much more than a factor of 10 for models that rotate near the critical velocity. On the other hand, the LMC and SMC models that attain near critical rotation velocities show surface nitrogen enhancements of at least a factor 10 and up to approximately a factor 30.

We therefore judge that single Be stars in the LMC should have surface nitrogen abundances $\epsilon = 12 + \log(N/H)$ no smaller than around 7.7, and in the SMC no smaller than around 7.4. In the Milky-way, we no not expect the single Be stars to have outstanding nitrogen surface abundances.

2.4 Population synthesis results

2.4.1 Predicted fractions of Be stars

In this section, we discuss synthetic populations of coeval rotating single stars as described in Sec. 2.2.2. These results can then be compared to the number of Be stars observed in young star clusters of various ages. From our models, we derive the fraction of Be stars within one bolometric magnitude (assumed to be equal to one visual magnitude) of the turn-off. We consider a stellar model to correspond to a Be star when its rotational velocity exceeds a predefined fraction of critical rotation. Figure 2.6 shows the result as a function of age for various threshold critical velocity fractions and metallicities.

A striking feature of this plot is the maximum in Be fraction for all metallicities near 10 Myr. At $t = 0$ there are no Be stars because, as discussed earlier, the initial rotation distribution prevents O stars entering the ZAMS with v_{rot}/v_{crit} fractions greater than around 0.7. The $30\,M_\odot$ models take approximately 5 Myr to evolve towards critical rotation, shortly after which point they leave the main-sequence. From 5 to 10 Myr the Be fraction grows sharply as angular momentum loss from
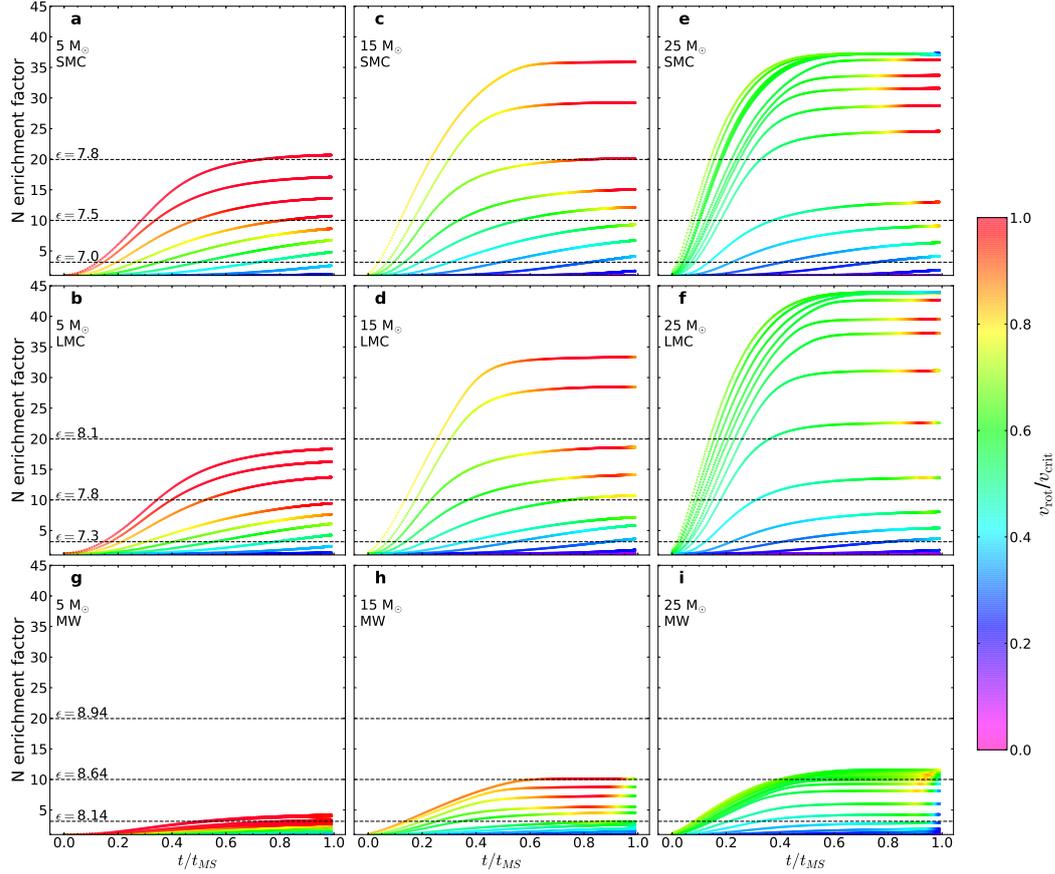
Figure 2.5: Surface nitrogen enrichment factor, computed as the nitrogen mass fraction divided by the initial nitrogen mass fraction as a function of the fractional hydrogen-burning lifetime, t/t_{MS} for models with initial rotational velocities between 0 and $600\,\mathrm{km\,s^{-1}}$ and initial masses 5, 15, 25$\,\mathrm{M_\odot}$ as marked in the plot. SMC, LMC and MW compositions are shown in the top, middle and bottom panels respectively. The colour scale corresponds to the critical rotation fraction, $v_{\mathrm{rot}}/v_{\mathrm{crit}}$. For each metallicity, various nitrogen abundances, $\epsilon = 12 + \log(N/H)$ are displayed as dotted black lines with the value given in the left column plots.
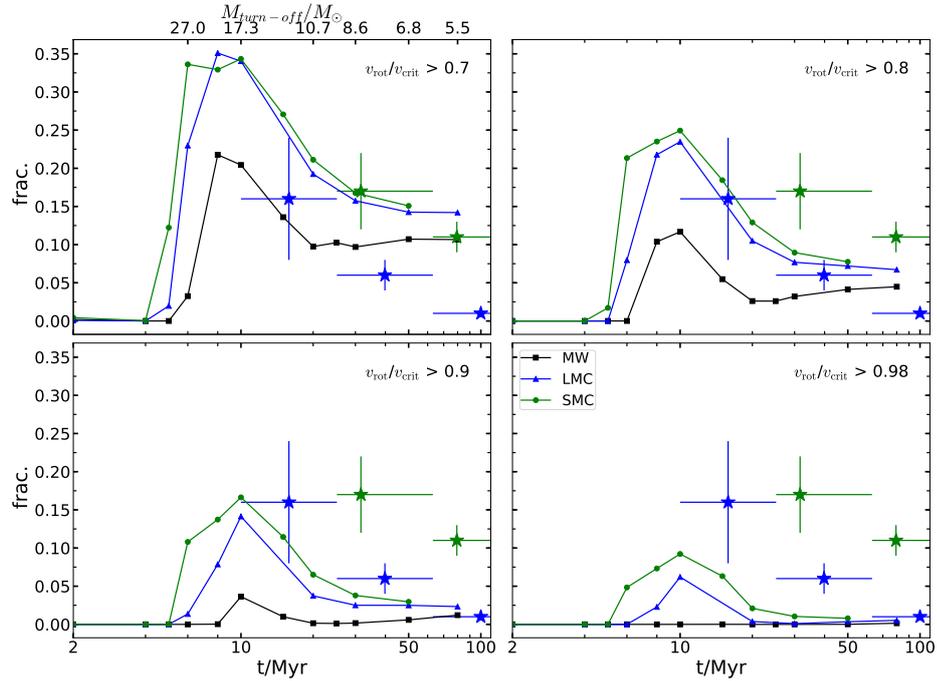
Figure 2.6: Fractions of stars rotating faster than various values of the critical rotation fraction, $v_{\rm rot}/v_{\rm crit}$, as given in the top left corner of each plot, in our synthetic coeval single star populations as function of their age. Considered only are stars brighter than one bolometric magnitude below the main-sequence turn-off. Metallicities are displayed as MW (black), LMC (blue) and SMC (green). For the top left panel the top scale gives the main-sequence turn off mass for non-rotating MW models. Observations with error bars from Iqbal and Keller (2013) are shown as green and blue stars for SMC and LMC observations respectively.

winds diminishes. From 10 to 20 Myr the Be fraction falls because the of the core-mass effect as discussed in Section 2.3.3. Comparing the hydrogen burning lifetimes of non-rotating MW models, it is found that populations with ages from 10 to 20 Myr have a main sequence turn off mass of around $17\,{\rm M}_\odot$. These models are in a "Goldilocks" situation where they are massive enough to have an appreciable convective core but not so massive to lose large amounts of angular momentum.

Furthermore we see that the Be fraction increases at earlier times for the lower metallicity models and that there is a clear trend in metallicity which shows that single Be stars become more common with decreasing metallicity. Both of these features are a result of the fact that the strength of angular momentum loss is metallicity dependant as discussed in Section 2.3.2.

It is also found that the Be fraction is strongly dependant on the chosen Be criterion. When critical velocity fraction, $v_{\rm rot}/v_{\rm crit}$ of 0.7 is chosen as the Be criterion, we predict Be fractions in the Magellanic Clouds in the range 15 to 35%. Where as when we restrict Be stars to being nearly critical rotators ($v_{\rm rot}/v_{\rm crit} > 0.98$), the Magellanic Cloud Be fraction lies in the range 0 to 10% and is almost 0 for population ages greater than 50 Myr.

2.4.2 Fast rotators in the colour-magnitude diagram

Using the procedure outlined in Section 2.2.2 we build synthetic colour-magnitude diagrams to indicate the expected positions of fast rotators. Fig. 2.7 shows the colour-magnitude diagram positions and critical velocity fractions of our SMC models with a coeval age of 35 Myr. Over plotted on our theoretical predictions are Hubble Space Telescope observations of the SMC cluster NGC 330 (Milone, Bedin et al., 2009), We see that the nearly critically rotating stars are located very close to the turn-off, as can be expected by the fact that our models only achieve high fractions of critical rotation near core hydrogen exhaustion (see Figs. 2.2,2.1). Fig. 2.7 also shows the effects of gravity darkening, with the slowly rotating models almost confined to a single isochrone while the fast rotators suffer strong gravity darkening and display a wider range of

colours, due to a relatively large spread in effective temperatures. Appendix B shows the same colour-magnitude diagram but ignoring the effects of gravity darkening for comparison.

In the following analysis we shall assume that the Hα emitters in NGC 330 are Be stars. The observations in Fig. 2.7 show that most of the observed Hα emitters are redder than the ordinary main sequence stars. This segregation is not a unique feature to NGC 330, with many LMC and SMC clusters exhibiting the same trait (Milone, Marino et al., 2018). Telting et al. (1998) have suggested through observations of Be stars whose spectra show rapid switching between containing emission lines and not, that the decretion disc can contribute up to 40% of a Be star's flux. Because our models do not include the contribution of a Be star's decretion disc to the observed fluxes, it is not meaningful to compare the colours of our fast rotating models with those of observed Be stars. However, assuming that the error on the magnitudes of our synthetic Be stars is at most 0.35 mag, we may consider the relationship between the relative number of Be stars and apparent magnitude.

Fig. 2.8 shows the Be fraction of our model predictions in F814W apparent magnitude bins for various threshold rotation rates for stellar models to be considered a Be star. We see that our model Be stars are strongly biased to being located near the main-sequence turn off, around $m_{F814W} = 15.4$ mag, where depending on how fast we require a Be star to rotate, the Be fraction is between 30 and 90%. Fig. 2.8 compares our model predictions to Be star counts in NGC 330 (Milone, Marino et al., 2018). The observations show that in NGC 330 the Be fraction is approximately 0.6, and it remains rather constant within a wide magnitude range of 17.0 to 15.6 mag. This result is quantitatively confirmed by a recent study of Bodensteiner, Sana et al. (2019), who used MUSE spectroscopy to identify Be stars in the core of NGC 330.

Comparing our models with the observations, Fig. 2.8 reveals that when assuming that Be stars are required to rotate only at 70% or more of the critical rotation velocity, our single star models agree with the observed Be star count in NGC 330 at the turn off region. However, they strikingly fail in two respects. Firstly, even adopting the least stringent threshold value for Be stars, our models fail to produce the large number of observed Be stars. Secondly, our models can not reproduce the fact that the Be star fraction in NGC 330 is constant over a range of 1.5 magnitudes.

Here, the second failure seems the worst. The total number of Be star can in principle be boosted by lowering the rotation threshold for considering the models a Be star, or by adopting larger initial rotation velocities. However, it is an intrinsic feature of the rotating single star models to increase the ratio of rotation to critical rotation velocity with time (Fig. 5; see als Ekström et al. 2008) . Thus, it appears quite unlikely that single star evolution that the observed distribution of Be stars in NGC 330 can be explained solely by single star evolution.

2.5 Discussion

2.5.1 Uncertainties

It is important to keep in mind that models are simply that and at some point they must fail to reflect the behaviour of real stars. Martins and Palacios (2013) have found that the hydrogen burning lifetimes given by models studied here differ to those of MESA models by approximately 15%. As this is merely a discrepancy in the clock, but not in the physical behaviour of the models (Marchant, 2017a), this is concerning, but should not change the main results presented here.

Another issue is the treatment of mass-loss, which is a strong factor in determining a model's evolution towards the critical velocity. The mass-loss prescription used (Vink, de Koter and Lamers, 2000) was calibrated for models in the range 15-20 $M_{\odot}$, so it may be questionable whether this scheme is accurate for models outside this range. Furthermore the correct treatment of a star rotating close to the critical velocity is complex. Near the critical velocity, two distinct winds are expected to form, a cold equatorial wind (which carries away angular momentum) and a warm polar wind (which carries away less angular momentum). It is not apparent which wind has the dominating effect, although the winds of models presented here always carry away angular momentum. Eq. 2.1 demands that as a star approaches the critical rotation velocity, the mass loss rate becomes infinite. It can also be questioned whether this is a correct treatment of the mass loss of a critically rotating star.

In the SMC, Rimulo et al. (2018) matched light-curve models to observations of 54 Be stars and determined that the typical mass-loss rate of a Be star in the mass range 10 to 20 $M_{\odot}$ is of the order 10^{-10} $M_{\odot}$ yr^{-1}. Our models predict that only stars with initial masses less than around 10 $M_{\odot}$ have such mass-loss rates on the main-sequence. This discrepancy highlights the fact that the models studied here are 1-dimensional and hence may struggle to represent accurately the mass-loss of a rotating star (which is a 2-dimensional problem).

Our definition of a Be star is one that is rotating close to the critical velocity. However it would appear that nature has a slightly different definition, with pulsations perhaps playing a role (Rivinius, Baade, Stefl, Townsend et al., 2001; Neiner and Mathis, 2014). Pulsations could serve to kick matter off of the stellar surface and aid the formation of a circumstellar disc. Observations with the CoRoT space telescope show that Be stars display pulsations that can transport angular momentum through the star (Huat et al., 2009), thus affecting the evolution of rotation velocities. The interaction of rotation and
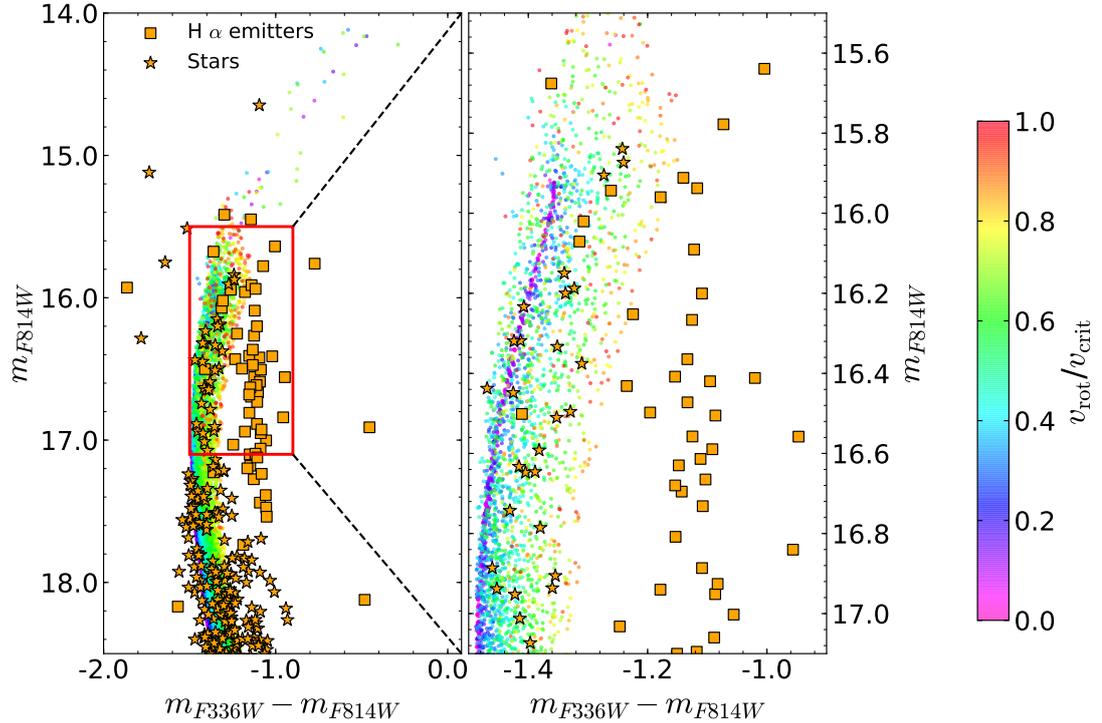
Figure 2.7: Synthetic colour-magnitude diagram of a 35Myr star cluster at SMC metallicity, where each dot represents one single star and the colour gives the critical velocity fraction, v_{rot}/v_{crit} as indicated by the colour bar. Gravity darkening is included assuming a random orientation of the rotation axis. Over plotted are observations of SMC cluster NGC 330 (Milone, Marino et al., 2018), with H α emitters marked by orange squares and normal stars as orange star symbols. The right panel shows the region indicated by the red box in the left panel. To convert the models to apparent magnitudes a distance modulus of 18.92 mag and a reddening of 0.06 mag were used.

pulsations is out of the scope of this work and the results of such endeavours are eagerly awaited. Furthermore recent observations with the TESS space telescope imply that the Be star disc could be fed by mass ejections from starspots (Balona and Ozuyar, 2019). Be stars are complex objects, with rotation being a key ingredient of the Be phenomenon, but perhaps not the only one.

Our population synthesis results are dependant on the initial rotation distribution that is assumed. Whereas Dufton, Langer et al. (2013) used high quality data, a large and unbiased sample of star, and corrected for effects as macro turbulence, other rotational velocity distributions are available (Martayan, Frémat et al., 2006; Hunter et al., 2008; Huang, Gies and McSwain, 2010)While our quantitative results might change using one of them, we do not expect a change in the qualitative behaviour of our results, which appears to be determined by the evolutionary factors discussed in Sect. 5.4

2.5.2 Comparison with previous models

The frequencies of single Be stars have been predicted from models by Ekström et al. (2008), Granada, Ekström et al. (2013) and Granada, Georgy et al. (2016). A major difference between these sets of models and the models studied here is the inclusion of the effects of an internal magnetic field which strongly couples the core and envelope, which may increase the predicted numbers of critically rotating stars.

Ekström et al. (2008) predict at solar metallicity and an age of 25 Myr the fraction of stars with a brightness of up to two magnitudes below the turn-off and rotating at the critical velocity is 5%, compared to 0% found here. However when one looks at the fraction of stars rotating faster than v_{rot}/v_{crit} =0.7 at 20 Myr, Ekström et al. (2008) finds a Be fraction of around
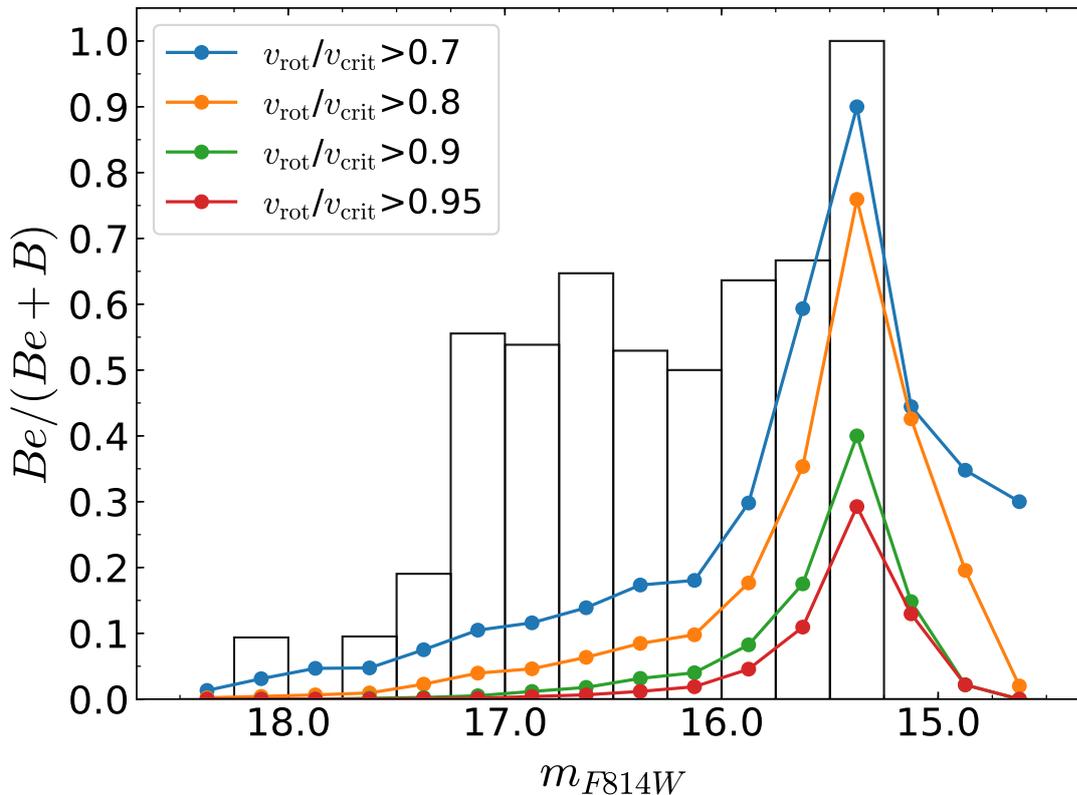
Figure 2.8: Histogram of the Be fraction of stars in SMC cluster NGC 330 (Milone, Marino et al., 2018) as a function of apparent magnitude in the Hubble Space Telescope Wide-field Camera 3 filter F814W, m_{F814W} plotted as white columns. It is assumed that H α emitters are Be stars. Over plotted as coloured lines are our model predictions in the same magnitude bins for various minimum rotation rates to be counted as a Be star, as given in the legend.

15%, compared to 8% found here. Both sets of models agree that at ages greater than around 40 Myr, almost no stars rotate at the critical velocity. Ekström et al. (2008) used a Gaussian-like initial rotation distribution with a peak at $\Omega/\Omega_{crit} = 0.6$, which in the Roche model corresponds to $v_{rot}/v_{crit} \approx 0.4$, and therefore is judged to be a similar initial rotation distribution to the one used in this work. As demonstrated by Ekström et al. (2008) mass loss rates play a crucial role in the evolution of the surface rotation. In our models above $10\,M_\odot$, a turn over in v_{rot}/v_{crit} is caused by strong mass-loss at late times (see Figure 2.2). When using the R.-P. Kudritzki and Puls (2000) mass-loss scheme, Ekström et al. (2008) found this turn over not to occur, and so those models spend more time at high v_{rot}/v_{crit} values and so Be stars become more common. It is therefore concluded that mass-loss is just as important as angular momentum transport in producing stars which rotate close to the critical velocity at galactic metallicity. At $Z = 0.002$ (a metallicity similar to our SMC models) Ekström et al. (2008) calculate a maximum in Be fraction at an age of 10Myr of around 10%, in good agreement with the results presented here.

Both Ekström et al. (2008) and Granada, Ekström et al. (2013) find that Be stars should become rarer at lower metallicities, which is in contradiction to the results presented here and the general trend seen by observers (Iqbal and Keller, 2013; Maeder, Grebel and Mermilliod, 1999; Martayan, Baade and Fabregat, 2010).

2.5.3 Comparison with further observations

Iqbal and Keller (2013) observed Be star fractions within 1 visual magnitude of the turn-off in LMC and SMC clusters. Such observations are directly comparable with Fig. 2.6, with the data over-plotted on our predictions. In clusters of ages from 7 to 8 Myr the Be fraction decreases from 15 % to 0 %. When defining the Be criterion to be 0.9 v_{rot}/v_{crit}, a similar behaviour

is found albeit at later ages. Iqbal and Keller (2013) also find that Be fractions increase with decreasing metallicity, in agreement with our models.

Both Maeder, Grebel and Mermilliod (1999) and Martayan, Baade and Fabregat (2010) found that Be stars are three to five times more frequent in the SMC than the galaxy, again in fairly good agreement with the model predictions. Martayan, Baade and Fabregat (2010) reported that the distribution of Be star frequency across spectral types does not depend on metallicity. As Fig. 2.6 shows similar trends for all metallicities, this behaviour is confirmed by the models.

Observations from Tarasov (2017) show that Be stars become most common in clusters with ages of 12-20Myr, in relatively good agreement to the model predictions.

Golden-Marx et al. (2016) found that in the SMC the frequency of Oe stars is strongly peaked around spectral types O9. Furthermore the Oe to O star fraction was measured as 0.26, compared to 0.03 for the MW. This measurement supports our result that very few stars with high critical velocity fractions and ages less than 10Myr should be found in the MW, but are found at lower metallicities (see lower Panels of Fig. 2.6).

Owing to the fact that the results of our population synthesis rely strongly on the adopted initial rotation distribution, one may question whether it is appropriate to assume that stars in the MW and Magellanic Clouds have equivalent initial critical rotation fractions. Whether the observed trends in Be fraction with metallicity are due to stellar evolution or a metallicity dependant rotation distribution is not clear. If lower metallicity stars were to rotate significantly faster, rotationally enhanced mass-loss would hinder the formation of Be stars at lower metallicities, therefore there is a limit to how much faster stars at lower metallicities can rotate. Even though Penny et al. (2004) found no significant difference between rotational velocities of O-type stars in the galaxy and Magellanic Clouds, Keller (2004) concludes that LMC stars are more rapidly rotating than galactic stars. It is curious to consider that even if LMC stars have faster equatorial velocities, due to their compactness they have larger critical velocities, and hence perhaps the same initial $v_{\rm rot}/v_{\rm crit}$ as galactic stars.

2.5.4 Comparing the single and binary star formation channels of Be stars.

Whereas in this work we focus on the single star formation channel for Be stars, it is evident that Be stars can also be formed through close binary evolution. The main mechanism is spin-up by accretion, which is expected to occur as a consequence of mass transfer (Langer 2012). The class of Be/X-ray binaries (Reig, 2011) provides strong support for this picture. Pols et al. (1991a) showed through detailed models that Be stars may be produced by mass accretion from a companion star in the course of close binary evolution. Using simplified binary evolution calculations, Shao and X.-D. Li (2014) demonstrated that potentially a large enough number of them could emerge from binary evolution to explain the currently observed Be star populations. In the following, we discuss several basic differences which can be expected between Be stars formed through binary interaction compared to those formed through the single star channel.

As we have seen above, when using the rotational velocity distribution of Dufton, Langer et al. (2013), it is difficult for single star models to achieve very close to critical rotation (lower right panel of Fig. 2.6). To remedy this would require that a significant fraction of stars is already born with near critical rotation. For low enough mass or metallicity, this group of stars would the remain rapidly rotating throughout their main sequence life. Such a picture appears not to be supported by observations (McSwain and Gies, 2005). Accordingly, single star evolution appears to be able to explain significant Be star populations only if decretion discs could form also in stars rotating significantly below critical.

In mass transferring binary evolution models, this is different. The angular-momentum of the mass-gainer increases quickly, such that critical rotation can be achieved after a relative mass increase of the mass gainer of 10% or less (Packet, 1981). During mass-transfer there is no fine-tuning mechanism that switches off accretion when a given rotation rate is reached, instead the only limit is critical rotation. Therefore, all mass transferring binaries where tides do not limit the spin-up of the mass gainer — which is the vast majority — are expected to produce a critically rotating main sequence star (Langer, 2012). After the accretion phase, the two mechanisms which affect the single stars, i.e., spin-down by mass loss and spin-up due to core contraction, will also work in the spun-up mass gainer. Whereas the wind induced drain of angular momentum may spin down some of the most massive mass gainers, the core contraction accompanying central hydrogen burning ensures that most of them remain at critical rotation for the rest of their main sequence evolution.

Consequently, whereas single star evolution leads to an increase of the rotation velocity compared to its critical value in many cases, the binary channel can produce a much larger number of stars living at critical rotation for a long time, compared to the single star channel. Furthermore, Chen et al. (2020) find that the initial mass ratio limit for stable mass transfer leads naturally to a restriction of binary-produced Be stars to within about two magnitudes of the cluster turn-off, which compares well with observations when interpreting the Hα emitting stars in NGC 330 as Be stars (Milone, Marino et al., 2018).

A further important difference between the Be stars produced via single and binary evolution concerns their expected surface abundances. As discussed above, the mass-gainer of a binary system may only accrete a small amount of mass to spin up. In this case, only material from the outer envelope of the donor star is incorporated into the mass gainer. As this

material is generally not enriched in hydrogen burning products, one would expect that Be stars formed through the binary channel are not significantly polluted by accretion. Detailed binary evolution models with LMC metallicity (Langer et al., 2020) suggest that the surface nitrogen mass fraction of spun-up mass gainers is at most tripled compared to the baseline nitrogen abundance. Additionally, the spun-up mass gainers had ordinary rotation rates before the mass transfer episode. As such, they established a strong mean molecular weight barrier between core and envelope, which prevents any significant rotationally induced mixing after their spin-up.

In Sec. 2.3.5 we argue that single Be stars ought to have much larger surface nitrogen enhancements (by as much as a factor 30; cf., Fig. 2.5). A diagnostic to discriminate single and binary Be stars would then be their surface nitrogen abundances. Dunstall et al. (2011) find that in the LMC cluster NGC 2004, only two Be stars from a sample of 11 were measured to have a nitrogen abundance $\epsilon = 12 + \log(N/H)$ greater than 7.8, while the other 9 Be stars had ϵ less than 7.4. This observed bimodal distribution supports the idea of the binary and single Be star formation channels producing populations with different nitrogen enrichments, and would suggest that in NGC 2004 the binary formation channel dominates. Also Dunstall et al. (2011) found that the nitrogen abundances of the majority of the LMC Be stars observed in the VLT-FLAMES Survey of Massive Stars are not consistent with single star evolution. Also, the Be star NGC 330-B 12 was found to be almost devoid of nitrogen lines and possessing a spectrum inconsistent with single star evolution models (Lennon et al., 2005), giving further evidence that Be stars can be formed by binary interactions.

Finally we note that a key difference between Be stars produced by the two channels concerns their potential binary companions. Since the initial rotational velocity distribution for single stars and stars in binaries appears to be similar (Ramirez-Agudelo, Sana et al., 2015), we would expect a significant fraction of Be stars formed through the single star channel (i.e., without accretion-induced spin-up) to have unevolved main sequence companions. However, essentially no such stars are known. Vice versa, whereas massive binary-produced Be stars may be single since they lost their companion when it produced a supernova explosion, the lower mass binary-produced Be stars should all have evolved companions: subdwarfs or white dwarfs. While those are very hard to detect (Schootemeijer, Götberg et al., 2018), recent studies of disc truncation of apparently single Be stars suggest that indeed unseen companions are present in the majority of cases (Klement, Carciofi, Rivinius, Ignace et al., 2019b).

2.6 Conclusions

We have identified and discussed three factors which affect a star's evolution towards the critical velocity throughout main-sequence evolution. Mass-loss through stellar winds has the effect of removing angular momentum from a star, and so hinders the approach to the critical velocity. The fraction of convective core mass to the total stellar mass strongly affects the internal angular momentum transport, which is crucial for an expanding envelope to maintain a fast rotational velocity. Lastly the occurrence of quasi-chemically homogeneous evolution prevents the stellar envelope from expanding and thus critical velocity decreasing, and also increases the angular momentum lost through stellar winds.

When using an observed distribution of B star rotational velocities for constructing synthetic stellar populations, we find that our single star models predict few stars rotating at near critical velocities, although we do predict as much as 35% of OB stars to rotate with more than 70% of their critical velocity. We therefore conclude that if Be stars are near-critical rotators, then single star models cannot explain the observed numbers of Be stars. In this case, most Be stars must be the product of mass-transfer in binary systems.

If Be stars instead only rotate at say 70-80% of their critical velocity, then the observed Be star fractions can be reasonably described by single star evolution (see Fig 2.6). However, in the ~40 Myr old SMC cluster NGC 330, Be stars are observed in significant numbers down to almost two magnitudes below the main-sequence turn-off. Independent of the rotation threshold for the Be phenomenon, our single star models predict that Be stars should be located only in a narrow luminosity range near the turn-off (see Fig 2.8), which disagrees with observations of NGC 330.

Whereas significant uncertainties remain, specifically in reconciling how stars that appear to rotate at 70% of their critical velocity can still form decretion discs and why so few Be stars are observed to rotate near the critical velocity, it appears evident that the observed Be star populations can not be explained by single star evolution alone, and that it may not be the dominant channel for Be star formation. Nevertheless, single star evolution will contribute, most strongly so in the age range from 8 to 20 Myr, at least at sub-solar metallicity.

Furthermore, our single star models predict that the surfaces of rapidly rotating single stars should be contaminated with freshly synthesised nitrogen, the more the faster the rotation. In spun-up mass gainers of binary systems, this is not necessarily so. The observations of non- or weakly nitrogen enriched surfaces in several groups of Be stars therefore strengthens the conclusion that the majority of these objects can not originate from single star evolution.
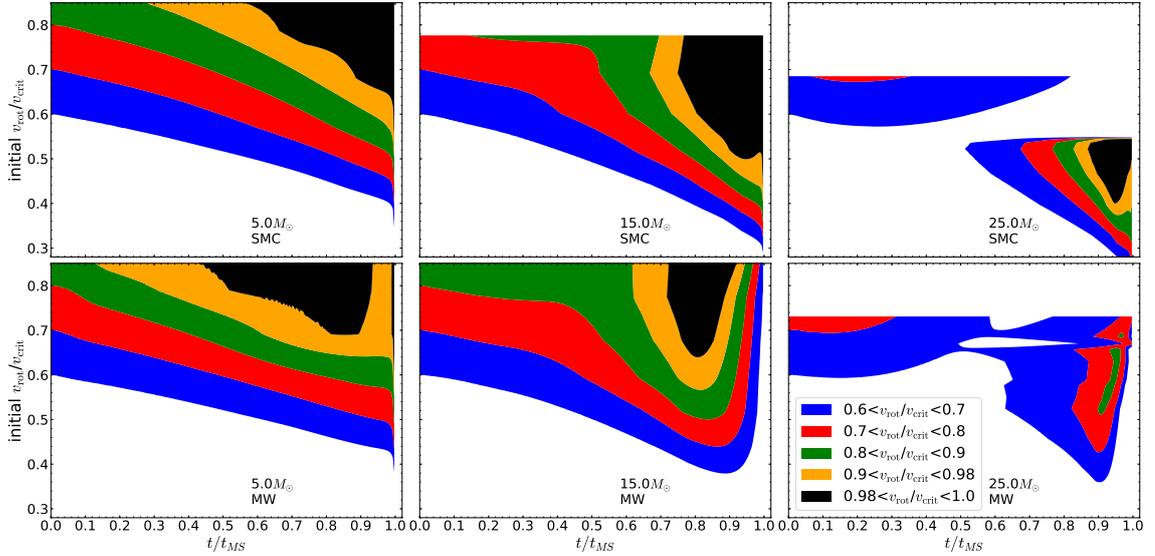
Figure 2.1: Critical velocity fractions, $v_{\rm rot}/v_{\rm crit}$ as a function of fractional hydrogen-burning lifetime, t/t_{MS} and initial critical velocity fractions for models with masses of 5, 15 and 25 $M_\odot$ and SMC (top panels) and MW (bottom panels) metallicities, as indicated in the figure. The colours indicate the critical velocity fraction, $v_{\rm rot}/v_{\rm crit}$ as given in the legend.

Appendix

A Initial conditions required to reach near critical velocities

In Section 2.3.1 we have discussed the evolution of rotational velocities of various models, when the models all have the same relative initial rotation rates. Here we explore how the approach to the critical velocity depends on the initial rotation rate by performing interpolations between the models. Fig. 2.1 shows, for differing stellar masses and metallicities, the critical velocity fraction as a function of time and initial rotation rate. The colour of each point on the plot shows the critical velocity fraction at a particular fractional hydrogen-burning lifetime, t/t_{MS}, and initial critical velocity fraction value. By following horizontal lines in the plot, one traces the evolution of a single model through its evolution.

For 5 $M_\odot$ models at both SMC and MW metallicities, the star evolves generally towards higher critical velocity fractions. This can be seen as one traces a horizontal line, one moves always into regimes of higher critical velocity fractions. The exception is the 5 $M_\odot$ MW models with $v_{\rm rot}/v_{\rm crit} > 0.7$, which at the end of hydrogen burning spin down through increased rotationally enhanced mass-loss. Looking at 15 $M_\odot$ models at SMC metallicity, one sees also that there is a constant evolution towards higher critical velocity fractions. On the other hand 15 $M_\odot$ models with MW metallicity evolve to higher critical velocity fractions until around 80% of the hydrogen-burning lifetime, then they spin down due to angular momentum loss through winds (as discussed in Sec. 2.3.2). The 25 $M_\odot$ models behave in a more complicated way because the initially very fast rotating models can undergo quasi-chemically homogeneous evolution (as discussed in Sec. 2.3.4). In the right panels of Fig. 2.1 one can see the two regimes according to whether or not the critical velocity fraction is increasing or decreasing. We can see that for 25 $M_\odot$ MW models with initial $v_{\rm rot}/v_{\rm crit} \approx 0.7$, they evolve at first to lower critical velocity fractions then after $t/t_{MS} \approx 0.6$ they begin to evolve towards higher critical velocity fractions. This occurs because initially the star is evolving quasi-chemically homogeneously, during which time rotation rates and hence rotationally induced mixing efficiency drops until quasi-chemically homogeneous evolution is shut down, at which point the star begins to evolve with an expanding envelope and approaches the critical velocity. For similarly initially fast rotating SMC models the same behaviour does not occur due to the weaker stellar winds at lower metallicities.

Fig. 2.1 also shows us that the models only reach critical rotation (the black areas in the figure) very near core hydrogen exhaustion. Furthermore, when one looks at the minimum initial rotation rate required to reach near critical rotation, it decreases with increasing mass due to angular momentum transport efficiency (as discussed in Sec. 2.3.3).
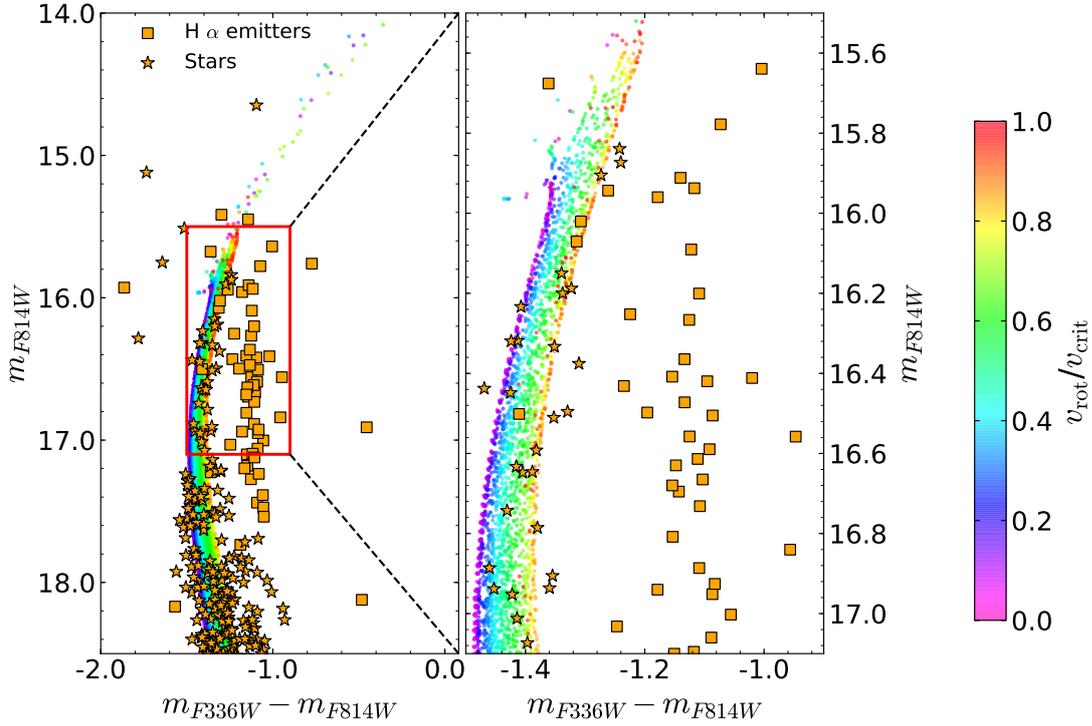
Figure 2.2: Synthetic colour-magnitude diagram of a 35Myr star cluster at SMC metallicity, where each dot represents one single star and the colour gives the critical velocity fraction, $v_{\rm rot}/v_{\rm crit}$ as indicated by the colour bar. Gravity darkening is not included. Over plotted are observations of SMC cluster NGC 330 (Milone, Marino et al., 2018), with H α emitters marked by orange squares and normal stars as orange star symbols. The right panel shows the region indicated by the red box in the left panel. To convert the models to apparent magnitudes a distance modulus of 18.92 mag and a reddening of 0.06 mag were used.

B Synthetic colour-magnitude diagram without gravity darkening

In Fig 2.2 we present the results of our population synthesis to simulate the colour-magnitude diagram of NGC 330 while ignoring the effects of gravity darkening. It is seen that along the main sequence there is a one-to-one relation between current critical velocity fraction and the $m_{F336W} - m_{F814W}$ colour, with faster rotators being redder. Such a relation is destroyed by gravity darkening (see Fig. 2.7).

A stringent upper limit on Be star fractions produced by binary interaction

Ben Hastings[1], Norbert Langer[1,2], Chen Wang[1], Abel Schootemeijer[1], Antonino Milone[3]

[1] Argelander-Institut für Astronomie, Universität Bonn, Auf dem Hügel 71, 53121 Bonn, Germany

[2] Max-Planck-Institut für Radioastronomie, Auf dem Hügel 69, 53121 Bonn, Germany

[3] Dipartimento di Fisica e Astronomia "Galileo Galilei" —Univ. di Padova, Vicolo dell'Osservatorio 3, Padova, I-35122, Italy

Author contributions: B.H and N.L developed the conceptual essence of this work. B.H performed the calculations. C.W and A.S produced the stellar models used in this work. A.M provided the observational data and assisted in its interpretation. B.H wrote the text and produced the figures. All authors reviewed the manuscript.

Summary

The evolution of a star in a binary can be severely altered by mass-transfer from its companion. An example is the accretion of mass, and importantly angular momentum, which can produce an extremely rapidly rotating star, predicted to be observable as a classical emission line star (also known as a Be star). Despite numerous pieces of observational evidence pointing to this possibly being the dominant formation mechanism of such stars, current binary evolution models struggle to produce a satisfactory description of emission line star populations.

The results of binary interaction are very sensitive to uncertain physics such as the mass-transfer efficiency and the occurrence of mergers. Populations of emission line stars predicted by binary evolution calculations can thus differ significantly depending on the initial modeling assumptions.

This work presents a flexible analytic model that aims to circumvent the previously mentioned shortcomings of detailed models. We tested hypothesis that binary evolution alone is responsible for the large numbers of emission line stars residing in young open clusters by deliberately maximising the production of emission line stars in our model. We compared the upper limit given by our model to observations of emission line stars in the Small Magellanic Cloud cluster NGC 330. This provides insights about the likelihood of binary evolution dominating the formation of emission line stars and probes several aspects of binary star physics.

To produce an upper limit, a theoretical population of binary stars was constructed in which every system is assumed to interact stably to produce a rapidly rotating accretor. Other assumptions that were made include that every star is born as a member of a binary. We argued that because determinations of the observed binary fraction cannot account for post-interaction systems, they do not represent the initial binary fraction, which is likely higher than the 70% observed binary fraction. We also assumed that once spun up, a star exhibits emission features for the rest of its lifetime. This assumption is challenged by the fact that the emission line phenomena is known to be transient.

The population is defined by given distributions of initial primary mass, mass-ratio and initial orbital period, which are varied within the observed limits to explore their effects on the population of emission line stars. It was determined that the largest numbers of rapidly rotating accretors are produced when mass-transfer is non-conservative.

Our population is used to predict the fraction of Be stars to all stars as a function of stellar mass relative to the turn-off mass. We found that in coeval populations, binary interaction can at most account for one third of all main-sequence stars being Be stars. A detailed comparison with the cluster NGC 330 showed that near the main-sequence turn-off, our theoretical upper limit appears to be matched. However, away from the turn-off, the model over-produces Be stars.

Applying simple and physically motivated assumptions about which systems are likely to undergo unstable mass-transfer and merge resulted in a good match between the observed and theoretical populations. Binaries with extreme mass-ratios have large discrepancies in the thermal timescales of the components and so are good candidates to merge during thermal timescale mass-transfer. The exact merger criteria is tailored in the plane of mass-ratio and primary mass so that the upper limit fits the Be fraction along the main-sequence of the cluster. The physical validity of the resulting merger criteria may be investigated in future studies.

By assuming distinct physics, binary evolution alone can in principle match the high numbers of Be stars observed in open clusters. However, this demands rather extreme conditions, such as an initial binary fraction of unity, highly non-conservative mass-transfer and a specific merger criteria. While robust evidence of each of these conditions is as yet lacking, they are nonetheless reasonable. Whether the required binary physics is realised in nature remains to be investigated.

3.1 Introduction

Be stars are massive main-sequence stars which display emission features in their spectra. While, since their discovery over 150 years ago (Secchi, 1866), we have advanced our understanding to explain the emission as a result of a decretion-disc which is being ionized by the central star (Struve, 1931), it is still not clear how a Be star gains its disc. Observations conclusively show that Be stars rotate significantly faster than their B counterparts (Struve, 1931; Porter, 1996; Huang, Gies and McSwain, 2010; Zorec, Frémat, Domiciano de Souza et al., 2016), such that potentially, the centripetal force matches the gravitational force at the equator (Collins and Truax, 1995; Townsend, Owocki and Howarth, 2004). However the fundamental origin of this fast rotation is still unknown, although single and binary star channels have been proposed.

One way to achieve such rotation is for a star to be spun up by mass-transfer in a binary system (Kriz and Harmanec, 1975; Pols et al., 1991a; Liu, van Paradijs and van den Heuvel, 2006; Langer, 2012). When a star accretes material, it also accretes angular momentum, which in the absence of tidal forces can lead to critical rotation of the accreting star, allowing material to become unbound and form a disc. The accretion of angular momentum is an efficient process, with a star needing to accrete typically a few percent of its own mass to rotate critically (Packet, 1981).

In wide systems which initiate mass-transfer after the primary has exhausted hydrogen in the core (so-called Case B mass-transfer), tidal forces are generally weak for the accretor star and it can be spun up to near-critical velocities. Furthermore, rapid rotators can also originate from close systems which undergo mass-transfer while the donor is still core hydrogen burning (so-called Case A mass-transfer). Although tides inhibit the spin-up of the accretor during the initial mass-transfer phases, these phases cause a widening of the binary (Petrovic, Langer and van der Hucht, 2005) so that when the donor expands to become a giant star (initiating Case AB mass-transfer), many systems are wide enough to render tides ineffective, allowing the mass-gainer to rotate super-synchronously (Sen et al., in prep.). Therefore rapidly rotating mass-gainers can originate from both short and long period systems. What is common between these cases is that the spun-up star is usually produced after the initially more massive star in the system has exhausted its supply of core hydrogen.

In Be star producing binary systems where the primary star is not massive enough to undergo a supernova explosion, a short-lived helium star or long-lived white-dwarf would be the companion to the Be star. Despite the difficulty of detection, both of these types of systems have been observed (K. L. Li et al., 2012; Schootemeijer, Götberg et al., 2018; Shenar et al., 2020; Coe et al., 2020). Furthermore, studies of Be star discs have found that many are truncated, suggesting that they are acted upon by unseen companions (Klement, Carciofi, Rivinius, Matthews et al., 2017; Klement, Carciofi, Rivinius, Ignace et al., 2019a).

When the mass-donor does explode as a supernova, the majority of systems are expected to become unbound (N. Brandt and Podsiadlowski, 1995) and the Be star will probably have no companion. The fact that this does not occur in every case is evidenced by large numbers of Be-Xray binaries (Raguzova and Popov, 2005), which consist of a neutron star in an eccentric orbit around a Be star such that Xrays are produced when the Be disc and neutron star interact. When the binary is disrupted, the Be star would likely be a runaway star. Boubert and N. W. Evans (2018) and Dorigo Jones et al. (2020) both find the peculiar space-velocities of Be stars in the Gaia catalogue to be consistent with a binary origin of Be stars.

Observations show the Be phenomenon to be more common at lower metallicities (Maeder, Grebel and Mermilliod, 1999; Martayan, Baade and Fabregat, 2010; Iqbal and Keller, 2013), in good agreement with predictions of single star models whereby metal-rich stars suffer stronger angular momentum losses through winds, thus making fast-rotators rarer at higher metallicities (Hastings, C. Wang and Langer, 2020). Naively, this trend is difficult to explain in the binary framework. However, further observational characteristics of Be stars have been uncovered that are difficult to explain with a single star formation channel. Initially fast rotating single stars are expected to exhibit enhanced surface nitrogen abundances, as rotational mixing dredges up CNO processed material to the photosphere. However, there appears to be an incompatibility between models of rotating single stars and measurements of nitrogen abundances in Be stars, with many Be stars showing much lower nitrogen abundances than expected (Lennon et al., 2005; Dunstall et al., 2011; Ahmed and Sigut, 2017; Hastings, C. Wang and Langer, 2020). On the other hand, spun-up mass-gainers might not be rich in surface nitrogen. Although the physics governing the details of mass-transfer remains uncertain, accretion may be limited by the angular momentum content of the gainer, such that accretion becomes non-conservative once critical rotation is achieved (C. Wang, Langer et al., 2020; Langer et al., 2020). Another factor is the strong mean molecular weight barrier established from hydrogen burning which prevents efficient rotational mixing in the critically rotating mass-gainer (R. Kippenhahn, 1974; Pinsonneault et al., 1989).

As demonstrated by Ekström et al. (2008) and Hastings, C. Wang and Langer (2020), single stars may achieve near-critical rotation during the late stages of hydrogen burning, in contrast to observations showing that Be stars have a range of fractional main-sequence ages (Zorec, Frémat and Cidale, 2005; McSwain and Gies, 2005; Milone, Marino et al., 2018). If Be stars are mostly single, one should expect pre-interaction binaries to host Be primaries, as whatever proposed single star mechanism causes the Be phenomenon should work for stars in a pre-interaction binary just as well as for single stars. It is thus telling that almost no Be stars with a main-sequence companion have been detected (Bodensteiner, Shenar and Sana,

2020).

Despite the numerous pieces of evidence to support the dominance of a binary formation channel, several uncertainties in binary evolution prevent a solid and accurate theoretical description of Be star populations. Proof of the difficulty in modelling the production of Be stars is given by the contrasting results of previous authors. It has been concluded that binaries are responsible for either all (Shao and X.-D. Li, 2014), half (Pols et al., 1991a) or only a small minority (van Bever and Vanbeveren, 1997) of galactic Be stars. This difference is mostly due to different assumptions on mass-transfer efficiency and the stability of mass-transfer.

In light of these uncertainties, we find it useful to determine a model free upper-limit to Be star production from mass-transfer in binary systems. Assessment of this limit can provide insight into whether it is at all possible for Be stars to be formed exclusively in binaries, and to what extent other formation mechanisms must be invoked. Under the assumption that binary evolution dominates the production of Be stars, we can also probe uncertain binary physics. We shall use recent high quality observations of Be stars in open clusters (Milone, Marino et al., 2018) to give a stringent test to our simple picture.

In Section 5.3 we explain our procedure for calculating an upper-limit to Be star production from mass-transfer in binary systems, with the results of this endeavour presented in Section 5.4. In Section 3.4 we compare our results to the numbers of Be stars observed in young open clusters. We infer the conditions for stable mass-transfer that are required for our prescription to reproduce the Be fractions along the main-sequences of young open clusters in Section 3.5. Uncertainties and the implications of the upper-limit are discussed in Section 4.7. Concluding remarks are given in Section 3.7.

3.2 Method

3.2.1 A hypothetical population of interacting binary stars

In order to calculate an upper-limit to the numbers of Be stars that may be produced, we take extreme assumptions. The first of which is that the initial binary fraction in the population is 1; that is every star is born as a member of a binary. Nextly, as the hydrogen-burning episode of a massive star makes up around 90% of the star's total lifetime, we shall assume that as soon as a primary star leaves the main-sequence, stable mass-transfer will occur on a very short timescale, instantly producing a Be star. In our model, a Be star shall be produced regardless of the initial period, primary mass, or mass-ratio of the system, so that every secondary star will at some point during its lifetime become a Be star. In this framework, the orbital period distribution becomes irrelevant. Furthermore we shall assume that once a Be star is formed, it remains so for the rest of its lifetime.

For simplicity we ignore the effects of mass-loss through stellar winds, such that every system remains at its initial mass-ratio, q, until mass-transfer occurs (which may be either conservative or non-conservative). Also, given the fact that the stellar mass-luminosity relation is very steep, we define each binary system by its most luminous component, so that each binary can be assigned an equivalent single-star mass. To facilitate comparison with open cluster observations, our synthetic population is assumed to be coeval.

Other properties of our population are not designed to maximise the efficiency of Be star formation, and are more or less standard in binary evolution calculations. We denote the initial masses of the initially more massive star as M_1, the initially less massive as $M_{2,i}$ and define the initial mass-ratio, q, as

$$q = \frac{M_{2,i}}{M_1},$$

(3.1)

such that

$$0 < q \leq 1.$$

(3.2)

We consider a population of binary stars where the distribution of initial primary mass follows a power law like

$$\xi(M_1) = \xi_0 M_1^\alpha,$$

(3.3)

and the distribution of initial mass-ratios is described similarly as

$$f(q) = f_0 q^\kappa,$$

(3.4)

where ξ_0 and f_0 are normalizing constants to ensure that the integral over the whole parameter space is unity (as befitting a

probability-density function). For example, the value of f_0 is easily computed as

$$f_0 = \frac{\kappa + 1}{1 - q_{min}^{\kappa+1}}, \qquad (3.5)$$

where q_{min} is the minimum mass-ratio in our population and will be nominally set to $q_{min} = 0.1$ to match the observing campaigns of Sana, de Mink et al. (2012) and Sana, de Koter et al. (2013). It is assumed that systems born with mass-ratios smaller than this value are likely to be unstable and merge either during their formation or early in their evolution and hence are not considered.

Mass gain of the accretor shall be parameterised by assuming that a total mass of ΔM is accreted, giving the relation between final and initial masses of the accretor as

$$M_{2,f} = M_{2,i}(1 + \Delta M/M_{2,i}), \qquad (3.6)$$

with $\Delta M/M_{2,i}$ being a free parameter.

Our assumptions on the population are summarized in the list below.

1. initial binary fraction is 1

2. every system will undergo stable Case B mass-transfer and form a Be star, irrespective of period or mass ratio

3. once a primary star leaves the main-sequence a Be star is immediately formed

4. once a Be star is formed, it remains so for the rest of its lifetime

5. the accretor star gains mass ΔM, with the relative mass-gain $\Delta M/M_{2,i}$ being a free parameter.

6. the effects of wind mass-loss are ignored so that a system remains at its initial mass-ratio until mass-transfer occurs.

7. the distribution of initial primary masses follows a power law, $\xi(M_1) \propto M_1^{\alpha}$

8. the distribution of initial mass-ratios follows a power law, $f(q) \propto q^{\kappa}$

9. only considered are binaries with a mass-ratio greater than q_{min}, which is set to 0.1.

10. when both stars are hydrogen-burning, the luminosity of a binary system is given by that of the primary. When the primary has evolved off the main-sequence, the luminosity of the system is naturally that of the secondary.

According to our assumptions, every secondary star with a post-main-sequence companion is a Be star, meaning the number of Be stars with given mass M is

$$n(\text{Be}) = n(M_{2,f} = M \,\&\, M_1 > M_{TO}), \qquad (3.7)$$

where M_{TO} is the turn-off mass of our coeval population. In our model the number of non-Be stars is given by the number of primaries at a given mass. The Be fraction, $\phi_{\text{Be}}(M)$ shall be defined as the number fraction of Be stars to all stars at a given mass. In a coeval population this becomes

$$\phi_{\text{Be}}(M) = \frac{n(M_{2,f} = M \,\&\, M_1 > M_{TO})}{n(M_{2,f} = M \,\&\, M_1 > M_{TO}) + n(M_1 = M)} \qquad (3.8)$$

$$= \left[1 + \frac{n(M_1 = M)}{n(M_{2,f} = M \,\&\, M_1 > M_{TO})} \right]^{-1}. \qquad (3.9)$$

In our model, a Be star's mass is related to its initial mass, $M_{2,i}$, and the relative mass-gain, $\Delta M/M_{2,i}$ via Eq. 3.6, such that the expression above becomes

$$\phi_{\text{Be}}(M) = \left[1 + \frac{n(M_1 = M)}{n(M_{2,i} = \frac{M}{1+\Delta M/M_{2,i}} \,\&\, M_1 > M_{TO})} \right]^{-1}. \qquad (3.10)$$

With the aid of Eqs. 3.1 and 3.6, the condition

$$M_1 > M_{TO} \qquad (3.11)$$

can be rewritten as

$$q < \frac{M_{2,i}}{M_{TO}},$$

(3.12)

leading to

$$q < \frac{M_{2,f}}{M_{TO}(1 + \Delta M/M_{2,i})}.$$

(3.13)

This results in

$$\phi_{\text{Be}}(M) = \left[1 + \frac{n(M_1 = M)}{n(M_{2,i} = \frac{M}{1 + \Delta M/M_{2,i}} \; \& \; q < \frac{M}{M_{TO}(1 + \Delta M/M_{2,i})})} \right]^{-1}.$$

(3.14)

To study coeval populations, a more convenient approach is to find the Be fraction as a function of the fractional main-sequence turn-off mass, M/M_{TO}. This produces the expression

$$\phi_{\text{Be}}(M/M_{TO}) = \left[1 + \frac{n(M_1 = M/M_{TO})}{n(M_{2,i} = \frac{M}{M_{TO}(1 + \Delta M/M_{2,i})} \; \& \; q < \frac{M}{M_{TO}(1 + \Delta M/M_{2,i})})} \right]^{-1},$$

(3.15)

which shall be our basis for exploring the Be fraction in coeval populations.

To evaluate the Be fraction, it is necessary to find the relative numbers of primary stars to that of secondary stars at a given mass. We may write that the number of primary stars with a given mass, $n(M_1)$, is the integral of the primary mass distribution across an infinitesimally small mass range, dM_1, multiplied by the total number of stars in the population, n_{tot}, as

$$n(M_1) = n_{tot}\xi(M_1)dM_1 = n_{tot}\xi_0 M_1^\alpha dM_1.$$

(3.16)

To tackle the number of secondary stars at a given mass is sightly more involved as we do not have directly the distribution of secondary masses, instead it is inferred from the primary mass and mass-ratio distributions. First consider a population in which there exists only a single mass-ratio, q_0, i.e. the mass-ratio distribution is a delta-Dirac function. If one is interested in the number of secondary stars with initial mass $M_{2,i}$, one must count the number of primaries with mass $M_{2,i}/q_0$, so we have

$$n(M_{2,i} \; \& \; q_0) = n_{tot}\xi\left(\frac{M_{2,i}}{q_0}\right)d\left(\frac{M_{2,i}}{q_0}\right),$$

(3.17)

with $d\left(\frac{M_{2,i}}{q_0}\right)$ representing an infinitesimally small change in $\frac{M_{2,i}}{q_0}$.

Any distribution may be expressed as an infinite sum of appropriately weighted delta-Dirac distributions, with the weighting coming from the probability-density function. Therefore for the general case we have

$$n(M_{2,i}) = n_{tot}\int_{q_{min}}^{1} f(q)\xi\left(\frac{M_{2,i}}{q}\right)d\left(\frac{M_{2,i}}{q}\right)dq.$$

(3.18)

It is then clear that the limits of the integral above place constraints on the initial mass-ratios counted. The number of systems with a given initial secondary mass $M_{2,i}$ and initial mass-ratios between q_{min} and q_{max} can thus be written as

$$n(M_{2,i} \; \& \; q_{min} < q < q_{max}) = n_{tot}\int_{q_{min}}^{q_{max}} f(q)\xi\left(\frac{M_{2,i}}{q}\right)d\left(\frac{M_{2,i}}{q}\right)dq,$$

(3.19)

The differential $d\left(\frac{M_{2,i}}{q}\right)$ in Eq.3.19 is quite cumbersome so we chose to let

$$r = \frac{M_{2,i}}{q}.$$

(3.20)

We may now write

$$n(M_{2,i} \& q_{min} < q < q_{max}) = n_{tot} \int_{q_{min}}^{q_{max}} f(q)\xi(r)dr dq. \tag{3.21}$$

We have

$$M_{2,i} = qM_1, \tag{3.22}$$

thus

$$dM_{2,i} = q dM_1 + M_1 dq. \tag{3.23}$$

As we are interested in the number of secondary stars at a fixed mass, $dM_{2,i} = 0$, so

$$dq = -\frac{q}{M_1} dM_1. \tag{3.24}$$

Differentiating r gives

$$dr = \frac{-M_{2,i}}{q^2} dq. \tag{3.25}$$

Combining Eqs. 3.24 and 3.25 results in

$$dr = \frac{1}{q} \frac{M_{2,i}}{M_1} dM_1. \tag{3.26}$$

Inserting this into our expression for $n(M_{2,i} \& q_{min} < q < q_{max})$ (Eq. 3.21) gives

$$n(M_{2,i} \& q_{min} < q < q_{max}) = n_{tot} \int_{q_{min}}^{q_{max}} f(q)\xi\left(\frac{M_{2,i}}{q}\right) \frac{1}{q} \frac{M_{2,i}}{M_1} dM_1 dq. \tag{3.27}$$

We now divide Eq. 3.16 by Eq. 3.27 leaving

$$\frac{n(M_1)}{n(M_{2,i} \& q_{min} < q < q_{max})} = \frac{M_1 \xi(M_1)}{M_{2,i} \int_{q_{min}}^{q_{max}} f(q)\xi\left(\frac{M_{2,i}}{q}\right) \frac{1}{q} dq}. \tag{3.28}$$

When the distributions for initial primary mass and mass-ratio, Eqs. 3.3 and 3.4, are inserted, Eq. 3.28 simplifies further to

$$\frac{n(M_1)}{n(M_{2,i} \& q_{min} < q < q_{max})} = \left(\frac{M_1}{M_{2,i}}\right)^{\alpha+1} \frac{1}{\int_{q_{min}}^{q_{max}} f_0 q^{\kappa-\alpha-1} dq}. \tag{3.29}$$

This result may be readily checked against Monte-Carlo sampling of the primary mass and mass-ratio distributions.

Equation 3.29 can be used to directly determine the Be fraction (Eq. 3.15) by setting $M_1 = M/M_{TO}$, $M_{2,i} = \frac{M}{M_{TO}(1+\Delta M/M_{2,i})}$ and $q_{max} = \frac{M}{M_{TO}(1+\Delta M/M_{2,i})}$. This leaves

$$\phi_{Be}(M/M_{TO}) = \left[1 + \frac{(1+\Delta M/M_{2,i})^{(\alpha+1)}}{\int_{q_{min}}^{\frac{M}{(1+\Delta M/M_{2,i})M_{TO}}} f_0 q^{\kappa-\alpha-1} dq} \right]^{-1}, \tag{3.30}$$

where the integral has a simple analytic solution. Eq. 3.30 describes the Be star fraction as a function of the fractional turn-off mass, M/M_{TO} for our model open cluster. As the mass-dependance in Eq. 3.30 is expressed by the fractional turn-off mass, is not necessary to specify the turn-off mass.

3.2.2 Limits for remaining parameters

All that remains is to explore Eq. 3.30 in a suitable parameter space. The parameters we have are α, κ and $\Delta M/M_{2,i}$, the primary mass distribution exponent, initial mass-ratio distribution exponent and relative accretor mass-gain respectively.

The canonical value for the initial-mass-function (IMF) exponent, α, is given by the Salpeter IMF, $\alpha = -2.35$ (Salpeter, 1955). However recent observations of young stars in the 30 Doradus starburst region suggest instead $\alpha = -1.90^{+0.37}_{-0.26}$ (Schneider, Sana et al., 2018). Similarly in the R136 star forming region an exponent of $\alpha = -2.0\pm0.3$ was found (Bestenlehner et al., 2020). On the other hand it has also been proposed that the IMF follows an even steeper law with $\alpha = -2.7$ (Scalo, 1986). Therefore we consider the range $-1.9 < \alpha < -2.7$.

Observations of Galactic O-type stars show that the mass-ratio distribution follows a power law with exponent $\kappa = -0.1 \pm 0.6$ (Sana, de Mink et al., 2012) for $0.1 < q < 1$. In the Large Magellanic Cloud, the mass-ratios of massive binaries appear to be distributed differently with $\kappa = -1.0 \pm 0.4$ again in the range $0.1 < q < 1$ (Sana, de Koter et al., 2013). There are many claims that mass-ratios of binaries favour either low values (Trimble, 1990; Tout, 1991; Hogeveen, 1991) or follow a uniform distribution(Kobulnicky and Fryer, 2007; Kouwenhoven, Brown, Portegies Zwart et al., 2007). In light of these findings we shall consider κ values in the range $-1 < \kappa < 0$.

Estimates of the accretor mass-gain, $\Delta M/M_{2,i}$, obtained by demanding that mass-transfer stops once the mass-gainer reaches critical rotation tell us that $\Delta M/M_{2,i}$ is at the very most 0.1 and in most cases around 0.02, depending on the angular momentum content and physical structure of the mass-gainer before accretion (Packet, 1981; Petrovic, Langer and van der Hucht, 2005; C. Wang, Langer et al., 2020). It has been found that around 70% of the mass leaving the donor must be ejected from the system to explain observed distributions of Be star masses in Be X-ray binaries (Vinciguerra et al., 2020). However it must be noted that because it is expected that up to 90% of massive binary systems are broken apart by a supernova kick (N. Brandt and Podsiadlowski, 1995), Be X-ray binaries represent a small fraction of the population, and hence may well contain strong biases. Furthermore, it is believed that mass-transfer must be highly non-conservative to explain observed populations of Wolf-Rayet O-star binaries (Petrovic, Langer and van der Hucht, 2005; Shao and X.-D. Li, 2016). On the other hand, several systems exist which show evidence of near-conservative mass-transfer having taken place (de Mink, Pols and Hilditch, 2007; Schootemeijer, Götberg et al., 2018; Broz et al., 2021). To fully explore the effects of mass-transfer efficiency on Be star populations, we take the full range $0 < \Delta M/M_{2,i} < 1$.

3.3 Results

The results of Eq. 3.30 are plotted in Fig. 3.1 for the extremal parameters outlined in Sect. 3.2.2. The primary mass distribution affects the absolute numbers of Be stars because for a shallower distribution (α closer to 0), there is an abundance of massive binaries, such that many systems contain post main-sequence primaries and therefore the number of Be stars increases. Conversely when $\alpha << 0$, the population contains fewer primaries of mass greater than the turn-off mass and the Be count decreases.

The effect of the mass-ratio distribution can be understood by considering a population with a high value of κ such that secondary stars have a similar mass to their companion. In this case, when the primary leaves the main-sequence, the secondary will be rather evolved, and hence most Be stars will be found near the turn-off. On the other hand in a population with a low κ, the opposite is true; the secondary stars will have low masses compared to the turn-off mass and Be stars will be more evenly distributed along the main-sequence, as seen in Fig. 3.1.

Figure 3.1 shows how a varying mass-gain changes the Be count, with accretors that gain more mass producing fewer Be stars. This can be understood by considering a Be star of mass $0.9M_{TO}$ that is produced by inefficient mass-transfer. For the primary to exceed the turn-off mass, the initial mass-ratio of the system must be less than 0.9. Now if this star had gained $0.1M_{TO}$, the initial mass would be $0.8M_{TO}$ and the initial mass-ratio must be less than 0.8. Therefore, mass gain restricts the number of systems that are able to produce Be stars of a given mass, and low mass-transfer efficiency leads to higher numbers of Be stars being produced at a given mass.

It is seen in Fig. 3.1 that the largest Be fractions are produced when mass-transfer is inefficient ($\Delta M/M_{2,i} = 0$) and the initial mass function is shallow. The mass-ratio distribution then tunes the distribution of Be stars along the main-sequence. Therefore it is judged that the most Be stars are produced with the parameters $\Delta M/M_{2,i} = 0$, $\alpha = -1.9$ and $-1 < \kappa < 0$. Depending on the chosen parameters, the maximum Be fraction is in the range 0.2-0.35 near the main-sequence turn-off.
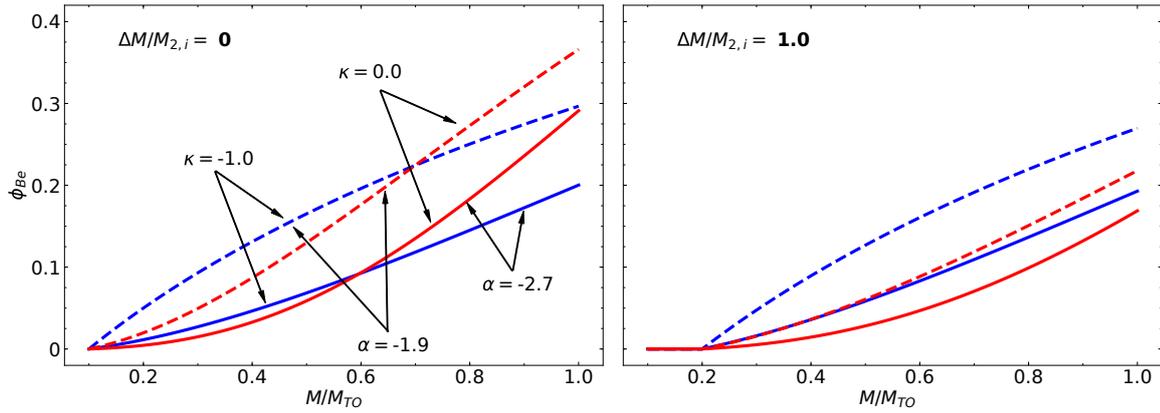
Figure 3.1: The maximum Be fraction, Φ_{Be}, in a coeval population as defined by Eq. 3.30 plotted as a function of fractional main-sequence turn-off mass, M/M_{TO} for varying parameters. The left and right Panels show $\Delta M/M_{2,i} = 0$, and 1 respectively. The colour of the lines represents differing κ values with red being $\kappa = 0$ and blue $\kappa = -1$. Dashed lines show $\alpha = -1.9$ and solid lines $\alpha = -2.7$ as indicated by the annotations.

3.4 Comparison to observations

To contextualise to our results, we attempt here a comparison with observations using high quality Hubble Space Telescope photometry of young Small and Large Magellanic Cloud open clusters in which Be stars are revealed as bright objects in a narrow-band filter centred on Hα (Milone, Marino et al., 2018). Photometry was performed with Hubble wide-band filters $F814W$ and $F336W$ and the narrow band $F656N$ filter, allowing one to produce colour-magnitude diagrams in which Be stars are identified from Hα photometry.

As many spectroscopically confirmed Be stars in NGC 330 are bright in Hα (Bodensteiner, Sana et al., 2020), we judge Hα emission to be a good proxy for Be stars. It is possible for the accretion discs of Algol-type binaries to exhibit Hα emission (Peters, 1989) however, such systems are expected to contribute around 3% to the total population (de Mink, Sana et al. 2014, Sen et al. in prep.). Furthermore, some field stars may be Hα emitters, with Milone, Marino et al. (2018) noting that no more than one-tenth of stars in the cluster field are suspected field stars. Field stars will also contaminate the population of stars not emitting in Hα, therefore their presence is not expected to significantly alter the relative fractions of Hα emitters and non-emitters.

Be star fractions have previously been measured as a function of magnitude (Keller, Wood and Bessell, 1999; Milone, Marino et al., 2018; Bodensteiner, Sana et al., 2020). However we find it worthwhile to repeat this exercise, including several factors which were previously overlooked.

3.4.1 Counting Be stars

Our goal is to measure the observed Be fraction as a function of mass along the main-sequence of an open cluster. To do this we must note the two major differences between a Be star and a "normal" B star; fast rotation and the presence of a decretion disc. Due to the effect of the centrifugal force, a fast-rotating star suffers from reduced effective gravity at the equator, and according to the von Zeipel theorem (von Zeipel, 1924), this results in a lower effective temperature. Therefore fast-rotating stars are cooler and redder than their non-rotating counterparts. Furthermore, light from a Be star consists of radiation from the star itself and also light from the decretion disc. Typically the average temperature of the disc is around 70% that of the star's effective temperature (Sigut, McGill and Jones, 2009), and so the disc is expected to emit mostly in visible and infra-red wavelengths.

In a colour-magnitude diagram, the magnitude in a red filter is plotted on the y-axis and a colour defined by the blue and red filter (B - R) on the x-axis. When a star becomes brighter in the red filter, it will therefore move to the right and upwards in the colour-magnitude diagram. This effect means that to count the Be stars as a function of mass, we must do so in bins that are sloped with respect to the x-axis. The gradient of this slope depends on how much redder a near-critically rotating star is than a slow rotator at the same mass, and on how much light the decretion disc radiates.

As no reliable numerical models exist of stars rotating at the critical velocity, we shall adopt a simple model to relate the luminosity and temperature of a critical rotator to an equivalent non-rotating star. After having been spun up, a star will change its shape, becoming oblate. At the same time we do not expect a great difference in luminosity between a star before and after the spin-up. This is because stars are generally very centrally condensed, such that the centrifugal force is small compared to gravity in the regions where nuclear burning occurs, meaning that (excluding the effects of rotational mixing) central temperatures and thus luminosities are not very sensitive to rotation, in agreement with models (Brott, de Mink et al., 2011; Paxton, Smolec et al., 2019). Following the Steffan-Boltzmann law, because of the increased surface area of a critical rotator, the effective temperature decreases. Using the Roche model (see Appendix A) , one can show that a critically rotating star has a surface area of approximately $1.58 \times 4\pi R_p^2$, with R_p being the polar radius, which corresponds to a decrease in effective temperature by a factor of $1.58^{-\frac{1}{4}} \approx 0.89$. Knowing this, we can construct isochrones describing the intrinsic properties of critically rotating stars from non-rotating isochrones.

A further complication that is brought about by gravity darkening is that a fast rotating star appears cooler and dimmer when viewed equator-on as compared to pole-on. Assuming a random orientation of the inclination axis, the mean value of the sine of the inclination angle is $\pi/4$, corresponding to a mean inclination angle of 51.8 °. To take into account the mean effect of gravity darkening, we employ the model of Espinosa Lara and Rieutord, 2011 as implemented in MESA (Paxton, Smolec et al., 2019). Here, the projected luminosity and effective temperature, L_{proj}, $T_{\mathrm{eff,proj}}$ are related to the intrinsic luminosity and effective temperature, L, T_{eff} by

$$L_{\mathrm{proj}} = C_T(\omega, i)L \tag{3.31}$$

$$T_{\mathrm{eff,proj}} = C_L(\omega, i)T_{\mathrm{eff}}, \tag{3.32}$$

with C_T and C_L depending on the fraction of critical velocity, ω and inclination angle i.

The temperatures and luminosities of critically rotating stars are found by using the coefficients $C_T(\omega = 1, i = 51.8°) = 1.02$ and $C_L(\omega = 1, i = 51.8°) = 1.22$. It is a rather curious feature of the gravity darkening model that at the mean inclination, the coefficients exceed unity, meaning the average effect of gravity darkening is not darkening at all, but brightening. Finally, by interpolating tables of synthetic stellar spectra (Choi et al., 2016) to produce magnitudes in Hubble filters, we are able to produce an isochrone of critical rotators, as shown in Fig. 3.2.

The contribution of a Be star's disc to its total flux is more difficult to assess. It has been noticed that a loss of spectral emission features in certain Be stars coincides with a dimming of around 0.3-0.5 magnitudes in the R and V filters (Carciofi et al., 2012; Labadie-Bartz, Pepper et al., 2017; Rimulo et al., 2018). If the loss of emission features is interpreted as the disappearance of the disc, one can take this change in brightness to equal the flux contribution of the disc. By comparing the colour of our isochrones with the colours of Be stars in NGC 330, we can assess how much the Be disc shines, as in Fig. 3.2. After assuming that the disc shines in the F814W filter but not in the F336W filter, we find a reasonable fit to the Hα emitters when a disc brightness of $0.25m_{\mathrm{F814W}}$ is adopted, as shown by the solid and dashed purple lines in Fig. 3.2.

For NGC 330, in the regions of the colour-magnitude diagram containing Be stars, we find stars of equal mass on the non-rotating and Be star isochrones to be connected by lines of gradient $\frac{-dm_{\mathrm{F814W}}}{d(m_{\mathrm{F336W}} - m_{\mathrm{F814W}})} = 2$. For NGC 2164, again assuming a constant disc magnitude of $0.25m_{\mathrm{F814W}}$, the gradient is found to be 1.8. These differing values are caused by the ways in which stellar spectra, and hence magnitude in a given filter, vary with luminosity and effective temperature.

Figure 3.3 shows the colour-magnitude diagrams of NGC 330 and NGC 2164 with the Be fraction as counted in slanted bins with gradients of 2.0 and 1.8 respectively. It is noted that as compared to counting the Be fraction in bins of constant m_{F814W} magnitude (i.e. horizontal bins) the values measured here are lower because in the horizontal bin case, one is counting B stars with a higher mass than the Be stars in the same bin. According the initial-mass-function, the higher mass stars are less populous and hence the Be fraction increases solely because there are fewer B stars being counted.

We use isochrones of rotating single stars based on an extended model grid of Schootemeijer, Langer et al. (2019) (see Appendix B for a thorough description) with an initial rotation rate of $v_{\mathrm{rot}}/v_{\mathrm{crit}} = 0.6$ to assign mass-ranges to each bin, so that the Be fraction can be evaluated as a function of mass. The bins are placed so that the outer edge of the last bin is at the point where hydrogen has been exhausted in the stellar core. The value of $v_{\mathrm{rot}}/v_{\mathrm{crit}} = 0.6$ is chosen as suggested by Gossage et al. (2019) and Wang et al. (in prep.), and produces equatorial rotation velocities that are in broad agreement with spectroscopic observations (Dufton, Langer et al., 2013; Marino et al., 2018; Sun et al., 2019; Kamann et al., 2020). The redenning and distance modulus values are tailored to give the best fit to the cluster and are in good agreement with previous isochrone fittings for these clusters (Milone, Marino et al., 2018). The isochrone fits are shown in Fig 3.3.

The isochrones allow us to measure the turn-off mass and the masses associated with each bin, thereby a direct comparison between the theory presented in Sec. 5.4 and observations is possible. Figure 3.4 shows this comparison, with counting
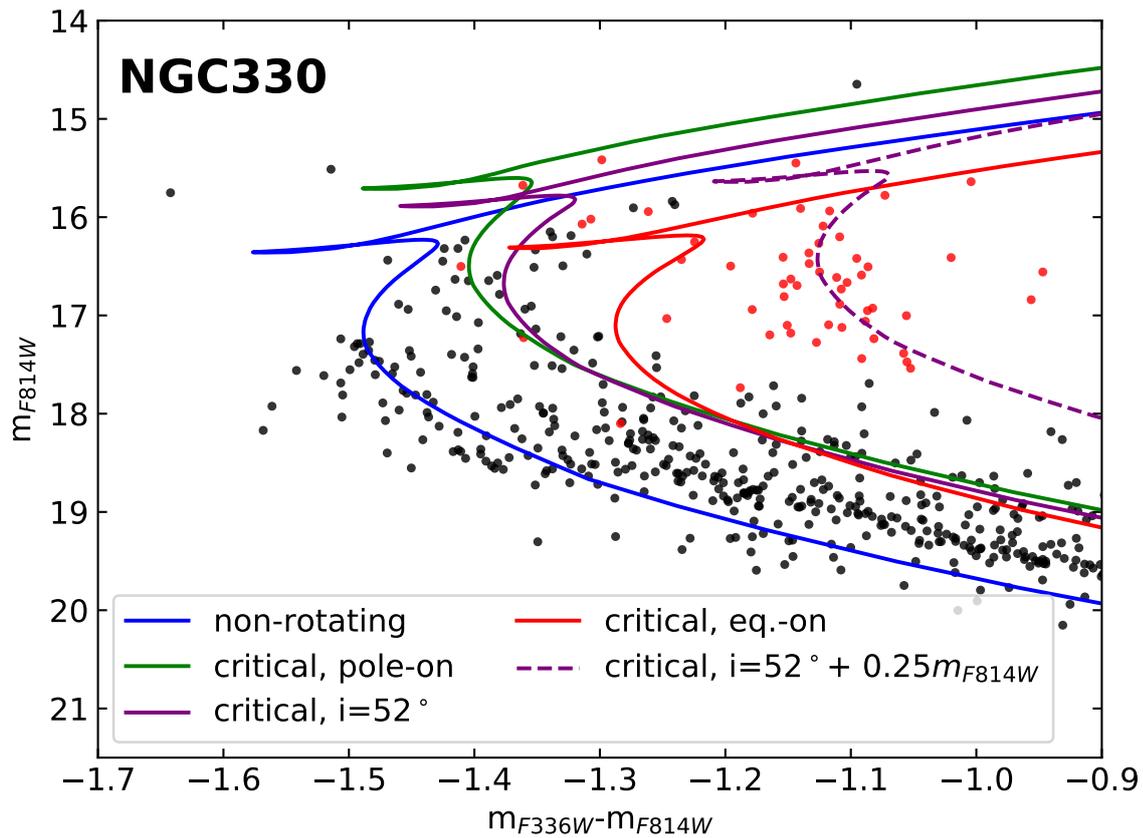
Figure 3.2: Colour-magnitude diagram of NGC 330 focussed on the turn-off region with Hα emitters marked in red. An isochrone of non-rotating stars is plotted in blue (see App. B for model details). Green and red isochrones depict critically rotating stars viewed pole-on and equator-on respectively, as derived from a simple model of critical rotators (see App. A). The solid purple isochrone represents critically rotating stars viewed at the mean inclination angle when the rotation axis is randomly oriented (51.8°) and for the dotted purple $0.25m_{F814W}$ has been added to simulate the decretion disc. The isochrone age is 30 Myr, distance modulus $\mu =$ 18.8 mag and redenning of E(B-V)=0.1 mag. Data from Milone, Marino et al. (2018)
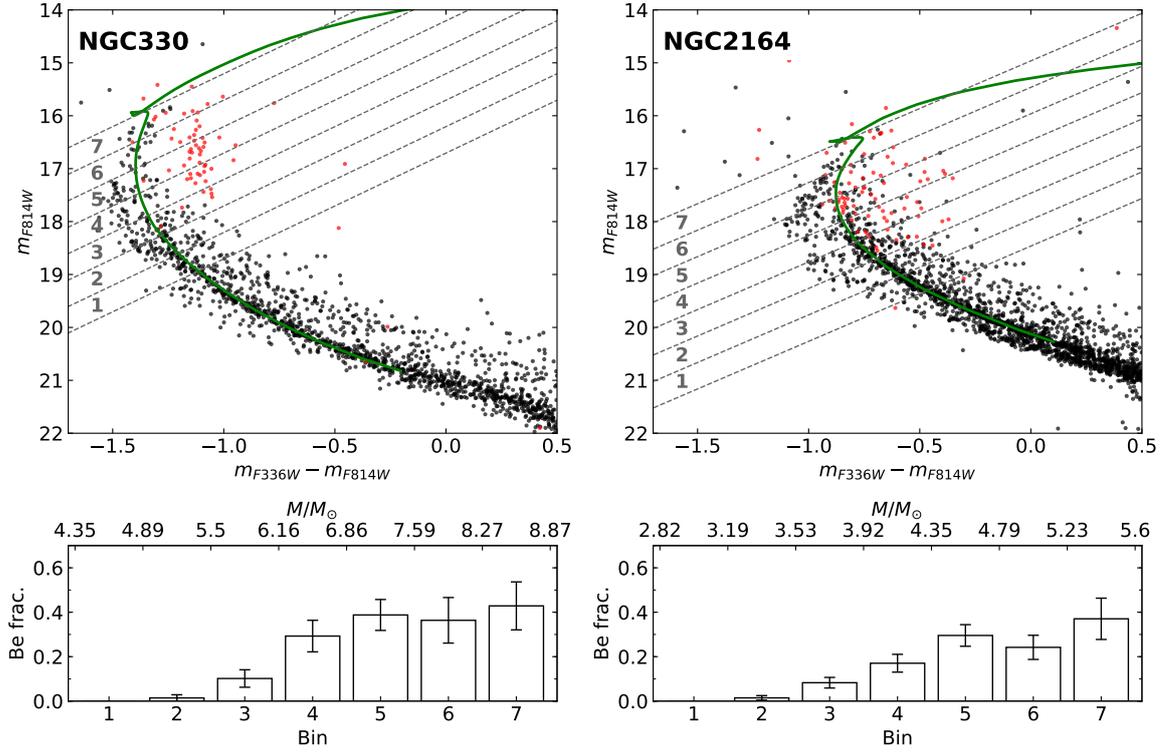
Figure 3.3: Colour-magnitude diagrams with isochrone fits and Be star counts for Small Magellanic Cloud cluster NGC 330 (left) and Large Magellanic Cloud cluster NGC 2164 (right). Hα emitters are marked in red. Bottom panels show the Be fraction counted in bins as defined in the top panels with the errors given by the binomial counting error. The bins have a gradient of 2.0 and 1.8 for NGC 330 and NGC 2164 respectively. Mass values associated with the bins are provided by the isochrone fit. For both clusters the isochrone depicts stars with initial rotation equal to 0.6 $v_{\rm rot}/v_{\rm crit}$. For NGC 330 the isochrone age is 30 Myr, distance modulus μ = 18.8 mag and redenning of E(B-V)=0.1 mag. For NGC 2164 the age is 80 Myr, μ= 18.3 mag and E(B-V)=0.12 mag. Data from Milone, Marino et al. (2018)

uncertainties on the Be fraction given by the standard error, σ, assuming a binomial distribution as

$$\sigma = \sqrt{\Phi(1 - \Phi)/N}, \tag{3.33}$$

with Φ being the measured Be fraction and N the total number of stars in a given bin.

We find that despite the two clusters being of different metallicities and ages, they seem to have similar Be fractions as a function of relative turn-off mass. This may be an indication that whatever the dominant Be production channel is, it is universal.

In both clusters the Be fraction steadily increases from zero to around 0.4 in the range 60-80% of the turn-off mass. Near the turn-off, the Be fraction is found to be approximately 0.4 with significant counting uncertainty due to the relatively small numbers of stars occupying this region. Taking into account these uncertainties, it is seen that our upper limit can describe the numbers of Be stars in the upper part of the main-sequence. It is important to note that because of the difficulty in performing an isochrone fit, the Be fractions near the turn-off are particularly uncertain, with a small change in the isochrone fit resulting in a large change in the measured Be fraction (see Sec. 3.6.1 for a quantitative discussion). Therefore, despite the measured Be fraction in NGC 330 at times exceeding our upper limit, it is reasonable to conclude that the upper limit does provide a reasonable fit to the Be star numbers near the turn-off. However it does fail to explain the lack of Be stars below $M/M_{TO} \approx 0.7$. This may be the result of certain systems not forming Be stars but instead merging, as shall be discussed in the next section.
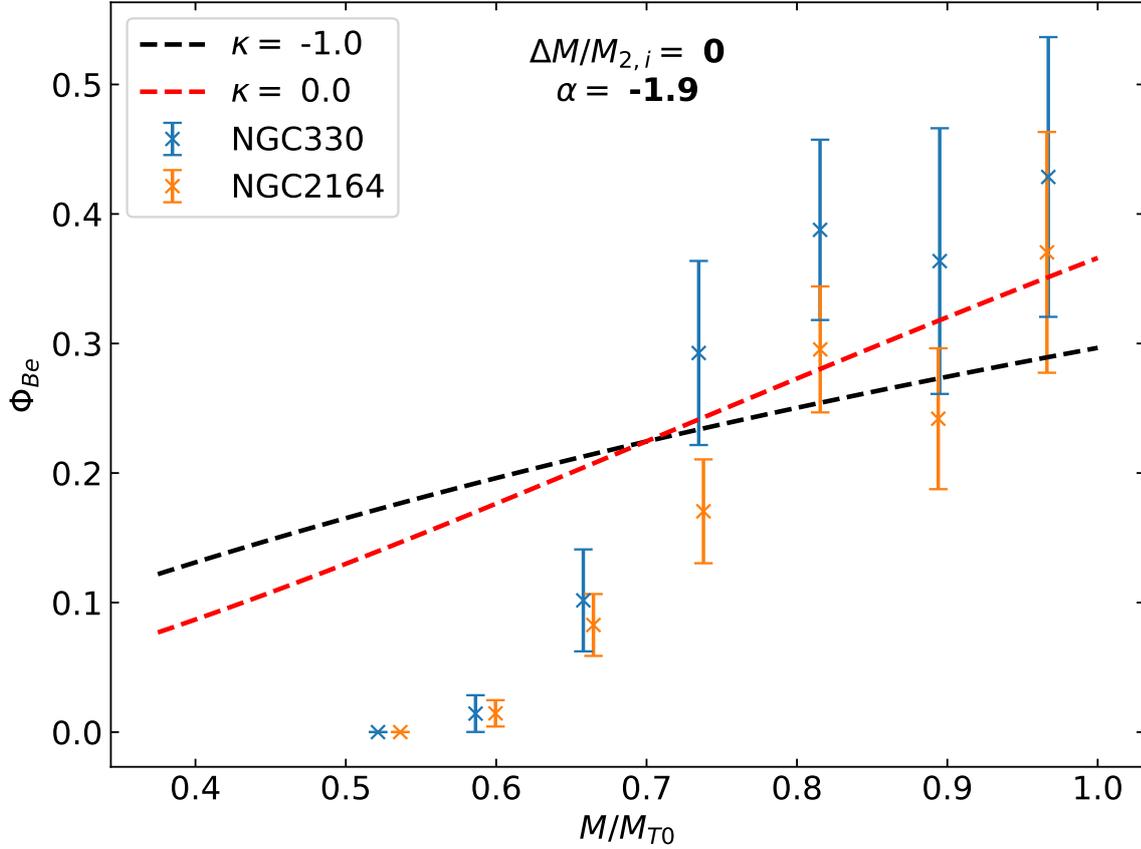
Figure 3.4: Comparison between theory and observations. Be fraction as a function of fractional main-sequence turn-off mass in NGC 330 and NGC 2164 as shown in Fig. 3.3. Dashed lines show theoretical upper limit given by Eq. 3.30 with $\alpha = -1.9$, $\Delta M/M_{2,i} = 0$ and $\kappa = -1.0, 0$ (see Fig. 3.1) as given by legend.

3.5 Inferring the initial conditions for stable mass-transfer

The observations presented in Sec. 3.4 show that our upper limit can approximately describe the numbers of Be stars near the turn off, but fails to reproduce the Be sequence's sharp cut-off. Here, we shall investigate how our prescription will need to be changed in order to reproduce this feature.

In reality, not every binary system will undergo stable mass-transfer to form a Be star. For the specific case of the donor being in the Hertzsprung gap, as it is in Case AB or Case B mass-transfer, the mass-transfer proceeds at the Kelvin-Helmholtz (or thermal) timescale (Tout et al., 1997; Wellstein, Langer and Braun, 2001), meaning that if there is a large discrepancy in the Kelvin-Helmholtz timescales of the donor and accretor, the mass-transfer will become unstable and a common envelope situation will ensue, most likely leading to a stellar merger.

To model the occurrence of mergers, it is often assumed in simplified binary evolution calculations (Pols et al., 1991a; Hurley, Tout and Pols, 2002; Schneider, Izzard et al., 2015) that systems below a certain mass-ratio will merge, however such a simple criterion is unsuitable to reproduce the observations shown in Fig. 3.3. Equation 3.30 gives the Be star fraction as an integral quantity, such that the Be star fraction at the main-sequence turn-off is the accumulation of systems with mass-ratios from q_{min} to 1. This may be understood intuitively by noting that a Be star of mass near the main-sequence turn-off mass can originate from either an extreme mass-ratio system with a very massive primary, or from a system with mass-ratio close to unity. Therefore, when we demand that all systems below a given mass-ratio merge, we will naturally decrease the Be fraction at the turn-off, which we must avoid to retrieve high numbers of Be stars at the turn-off.

To keep the Be fraction near the turn-off high and produce a sharp break in the Be fraction at $M/M_{TO} \approx 0.7$, more

sophisticated criteria are needed, namely with dependence on primary mass and mass-ratio. We propose that the systems most likely to suffer unstable mass-transfer are those with an extreme mass-ratio and low primary mass, as the components of such systems have the largest difference in Kelvin-Helmholtz timescales. This can be visualised in a grid of primary mass against mass-ratio, with the bottom corner consisting of systems that merge. In such a grid, systems with a fixed secondary mass are represented by parabolae, as depicted in Fig. 3.5a. If the parabola representing a secondary with the turn-off mass can avoid the region containing merger progenitors, the Be fraction at the turn-off will remain close to the maximum theoretical prediction. Then as the secondary mass decreases, the parabolae will move into the corner with low mass-ratio and low primary mass and consequently the Be fraction will decrease.

To make a test of our hypothesis, we perform a Monte-Carlo simulation, whereby systems are picked randomly from given distributions of initial primary mass and initial mass-ratio. As before, we shall assume that mass-transfer is completely non-conservative ($\Delta M / M_{2,i} = 0$). By choosing a turn-off mass, we can calculate the masses of Be stars in the simulation and therefore assess the Be fraction. The occurrence of mergers is decided using the stable mass-transfer region depicted in Fig. 3.5 a. The motivation for selecting this region will now be explained. Analysis of mass-transfer from giant donors (Pavlovskii and Ivanova, 2015) has indicated that mass-transfer from Hertzsprung-gap stars is stable at mass-ratios greater than around 0.6. We will therefore assume that all systems with initial mass-ratios greater than 0.6 will undergo stable mass-transfer. The stability of mass-transfer is determined by the donor's reaction to mass-loss, where stars with radiative envelopes generally tend to contract as the envelope is being stripped (Hjellming and Webbink, 1987). This is reversed for convective-envelope stars, which typically expand in response to mass loss (Hjellming and Webbink, 1987). Stellar structure calculations suggest that stars with a mass greater than around $60\,M_\odot$ spend very little time as red-giants, meaning that they mostly have radiative envelopes (Schootemeijer, Langer et al., 2019; Klencki et al., 2021) such that mass-transfer is much more likely to occur when the donor has a radiative envelope. We therefore propose that mass-transfer will be stable for all systems with a primary mass exceeding $60\,M_\odot$. The region of instability is then defined by a linear interpolation between systems with $M_1 = 60\,M_\odot$, $q = 0.1$ and $M_1 = 5\,M_\odot$, $q = 0.6$, as depicted in Fig. 3.5a. We shall again assume that the orbital period plays no role in determining the stability of mass-transfer, hence allowing us to not specify an orbital period distribution.

Merger products change the distribution of masses in a population, hence affect the Be fraction as a function of mass. We will assume that Be stars are not merger products for two reasons. Firstly, it is believed that, although merger products are fast-rotators initially, while thermal equilibrium is returned, internal angular momentum redistribution causes a rapid spin-down (Schneider, Ohlmann et al., 2019). What is more, stellar mergers may produce strongly magnetised stars (Ferrario et al., 2009; Wickramasinghe, Tout and Ferrario, 2014; Schneider, Ohlmann et al., 2019) which would further spin-down due to magnetic braking. Secondly, a merger between a star with a helium core and a main-sequence object will not produce a hydrogen burning star owing to the higher mean molecular weight and lower entropy of the helium-core star (Langer, 2012; Justham, Podsiadlowski and Vink, 2014). As observations (Milone, Marino et al., 2018) show Be stars to be concentrated on the main-sequence, we assume that Be stars are unlikely to be produced from the merging of two stars. For mergers, we assume the fraction of mass lost during the merging process to the total binary mass to be equal to

$$\mu_{loss} = \frac{0.3q}{1 + q^2}, \tag{3.34}$$

(Glebbeek and Pols, 2008) which equates to between 2 and 15% over the range $0.1 < q < 1$. As the mass lost during the merging process is assumed to be low, mergers will always have a mass exceeding the turn-off mass and will not affect the Be fractions on the main-sequence.

Figure 3.5 b shows the results of the simulation for clusters with turn-off masses of 9 and $6\,M_\odot$, which roughly correspond to NGC 330 and NGC 2164, respectively. The chosen criteria have maintained a high Be fraction near the turn-off and also produced a sudden end to the Be-sequence, and provide a reasonable fit to the measured Be fractions in NGC 330 and NGC 2164. It is remarkable that such simple, although physically motivated, stable mass-transfer criteria can successfully reproduce the numbers of Be stars in the open clusters studied. Our empirical mass-transfer stability criteria could be tested in the next generation of detailed binary evolution models.
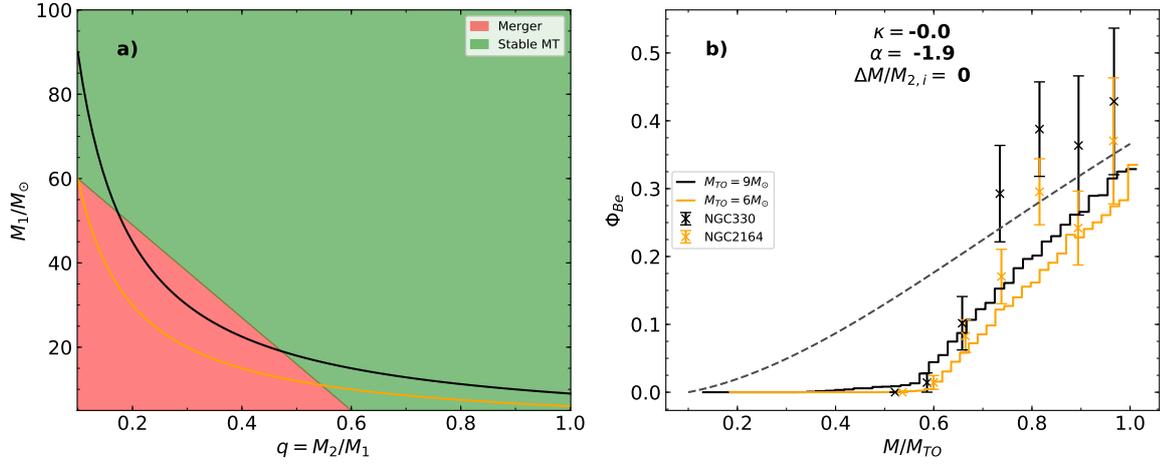
Figure 3.5: **a)** Adopted region of stable mass-transfer in the primary mass-mass-ratio plane. Regions coloured red experience unstable mass-transfer and merge, while for green regions, mass-transfer is stable and a Be star is formed. The black and orange lines show systems with secondary masses of 9 and 6 $M_\odot$ respectively. **b)** Results of a Monte-Carlo simulation showing the Be fraction, Φ_{Be}, when the stable mass-transfer region in a) is applied. Binary systems have a flat mass-ratio distribution ($\kappa = 0$), a primary mass distribution $\xi(M_1) \propto M^{-1.9}$ and we have assumed inefficient accretion ($\Delta M/M_{2,i} = 0$). The black line shows a simulation with a turn-off mass of $9\,\mathrm{M}_\odot$, and the orange line of $6\,\mathrm{M}_\odot$. The dashed grey line shows the theoretical upper limit, as given by Eq. 3.30. Measured Be fractions of NGC 330 and NGC 2164 according to Fig. 3.3 are plotted as black and orange crosses respectively.

3.6 Discussion

3.6.1 Uncertainties

The largest uncertainty in our procedure comes from the isochrone fits. Most, if not all open clusters display an extended main-sequence turn-off, making the choice of a suitable isochrone age difficult. This is illustrated in Fig. 3.6, where isochrones of two different ages are fitted to NGC 330 and the Be fractions are evaluated. It is seen that a small variation in the adopted age can cause the Be count in some bins to vary by up to 0.2, with the end of the Be sequence being particularly affected. A similar sensitivity is also found for small differences in the distance modulus, redenning and isochrone rotation rates. From Fig. 3.6, it is judged that the uncertainty on the measured Be fractions is approximately 0.1 without including the counting error.

To measure the observed Be fraction as a function of mass, we must use slanted bins. In calculating the gradient of these bins, we have assumed that the Be star disc always adds $0.25m_{\mathrm{F814W}}$ to the magnitude of the star. This may be an over-simplification, with Be stars of differing mass or evolutionary status hosting relatively brighter or dimmer discs. Unfortunately this effect is difficult to observe and characterise and is also compounded by the fact that Be stars can display spectral and photometric variability (Porter and Rivinius, 2003). Sigut, McGill and Jones (2009) report that the ratio of stellar effective temperature to mean disc temperature and infrared excess are indeed functions of spectral type.

Far older clusters, such as the 300Myr old NGC 1856 have much lower Be fractions than their younger counterparts (see Milone, Marino et al., 2018, Fig. 17). Our simple model and mass-transfer stability criteria predict that the Be fraction does not vary strongly with turn-off mass and therefore is unable to explain the turn-off Be fraction in NGC 1856 of around 0.2. However this discrepancy may be partly explained by a changing binary fraction with mass, as it is known that more massive stars display a stronger preference for binary companionship (Köhler et al., 2006; Kouwenhoven, Brown, Goodwin et al., 2009), thus older clusters which contain fewer binaries will naturally have fewer Be stars. Another aspect behind the emission line phenomenon is the ionizing power of the star, because to produce an emission line, the central Be star must ionize its decretion disc. Without sufficient ionizing power, even if a decretion disc is present, no emission line will be observable and hence the star will seem ordinary. The ionizing photon emission rate is known to be strongly dependant on
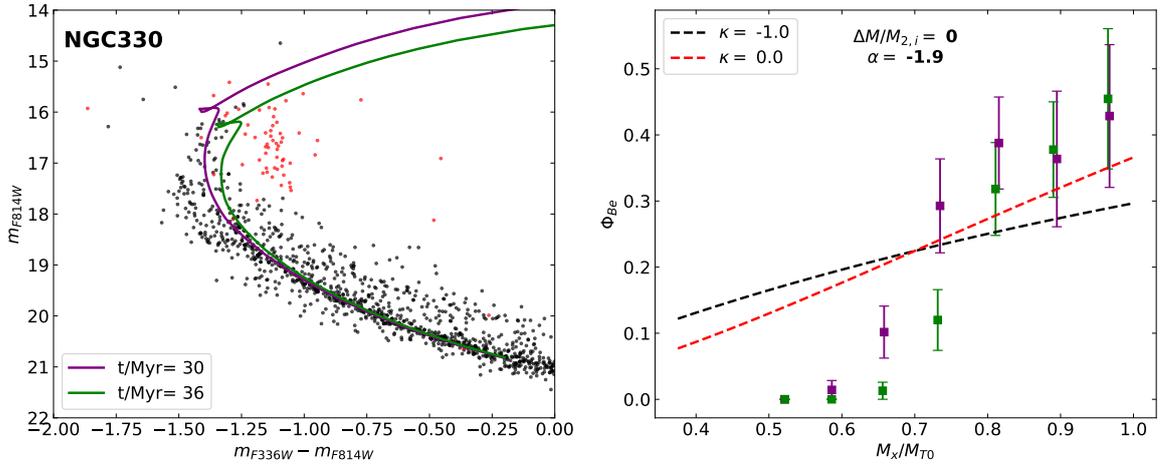
Figure 3.6: Left panel: colour-magnitude diagram of NGC 330 with Hα emitters marked in red. Isochrone fits with ages 30 and 36Myr are plotted in purple and green respectively. Both isochrones have initial rotation of $v_{\mathrm{rot}}/v_{\mathrm{crit}}$ =0.6, a distance modulus of 18.8 mag and redenning of E(B-V)=0.1 mag. Right panel: Be fraction as a function of fractional turn-off mass as measured by the 30Myr isochrone (in purple) and the 36Myr isochrone (in green). Dashed lines show theoretical upper limit given by Eq. 3.30 with $\alpha = -1.9$, $\Delta M/M_{2,i} = 0$ and $\kappa = -1.0, 0$ as given by legend.

effective temperature (Sternberg, Hoffmann and A. W. A. Pauldrach, 2003), so at some limiting mass one would expect the central star to be unable to ionize a disc. This effect may play a role in lowering the Be fraction in older clusters and causing a dearth of Be stars at low magnitudes in the colour-magnitude diagram. Both of the clusters studied here have several stars that are very red, despite not being marked as Hα emitters, which could in fact be such "dormant Be stars".

Lastly we note that in our work we have assumed that the properties of binary systems are distributed according to very simple laws. In reality however, the distributions may well be complex functions of one another, for example the mass-ratio distribution might be a function of the primary mass. The nature of these distributions is set by poorly understood binary star formation mechanisms as outlined by Tokovinin and Moe (2020).

3.6.2 Mass-transfer efficiency

To construct our prediction of Be star fractions, we have assumed that no mass is accreted during mass-transfer and seen that this scenario fits observations reasonably well. It has been demonstrated that for efficient mass-transfer, the Be star fraction decreases, meaning that the theoretical framework presented here would not fit observations if mass-transfer were efficient. This leads us to propose that, if the binary Be formation channel is the dominant one, mass-transfer is, on average, far from conservative.

Binary models with conservative mass-transfer predict Be stars to be blue stragglers, after having gained a lot of mass (van Bever and Vanbeveren, 1997). The observations presented in Fig. 3.3 contradict this prediction, with the vast majority of Be stars lying either on the main-sequence or being slightly redder than it, strengthening our conclusion about mass-transfer being highly non-conservative.

3.6.3 On the initial binary fraction

In obtaining our results we have assumed an initial binary fraction of 1, which could be criticised as too extreme. We have demonstrated that in a coeval population of binary systems, at most 30% of systems are post-interaction binaries (see Sec. 5.4). Pre-interaction systems would therefore make up no less than 70% of this population. Dedicated models show that under the assumption of a constant star formation rate, 30^{+10}_{-15} % of massive stars are the products of binary interaction (de Mink, Sana et al., 2014), in broad agreement with this work.

Post-interaction binaries are either merger products, contain a relatively low mass post-main-sequence object (helium

star, black-hole, neutron star or white-dwarf) with a main-sequence (possibly emission line) star or form a runaway star ejected from the binary orbit after a supernova. Such objects manifest themselves either as single stars, or would be difficult to detect as binaries (de Mink, Langer and Izzard, 2011b; de Mink, Langer and Izzard, 2011a). Thus, even in a population whose initial binary fraction is 1, apparently single stars are present in the proportions described above.

By examining radial velocity variations of very massive stars, one may only measure the pre-interaction binary fraction (as supernova kicks are believed to disrupt almost all binary systems (N. Brandt and Podsiadlowski, 1995)), which has been observed to be around 0.7 for O-type stars (Sana, de Mink et al., 2012). We therefore argue that the initial binary fraction is certainly greater than the observed pre-interaction binary fraction, such that at this stage, we must remain open to the possibility that an initial binary fraction very close to one is indeed realised in nature.

3.7 Conclusions

In light of various uncertainties plaguing binary evolution calculations, we have investigated whether binary evolution can possibly reflect the large numbers of Be stars observed in open clusters. Starting from the premise that any binary system, regardless of primary mass, orbital period or mass-ratio, will undergo stable mass-transfer to form a Be star, we have calculated a rigorous upper limit to the formation of Be stars through this channel. It has been demonstrated that such binary evolution does not allow more than around 30% of stars to have been spun up though binary interaction and become emission line objects.

After using isochrone fits to assign stars in the colour-magnitude diagram masses, a count of the $H\alpha$ emitters in two open clusters reveals that for objects near the turn-off, our upper-limit provides a reasonable description of the numbers of Be stars, especially when uncertainties arising from the counting method are taken into account. The upper limit does however fail to describe the sudden decrease in Be fraction that both clusters exhibit at a mass approximately 70-80% of the turn-off mass.

This problem can be rectified by assuming that systems of low mass-ratio and low primary mass merge. By adopting simple, although physically justified stable mass-transfer criteria, we have shown that a good fit to the observational data is produced by this postulate.

It has been demonstrated in a qualitative way that in coeval populations, a larger mass-gain of the donor results in a smaller Be fraction at a given mass. Given that the observed Be fractions are very close to our upper limit when assuming totally inefficient mass-transfer, it follows that to be able to explain such high Be fractions, mass-transfer must be non-conservative.

We have highlighted the distinction between the initial binary fraction and the binary fraction that one is able to observe, and argued that these two quantities are not equal. This is so because a population of binary stars will always contain post-interaction systems that will appear to be single stars. The calculations outlined in this work provide rough constraints on this discrepancy, suggesting that the initial binary fraction is much higher than previously thought.

In conclusion, our theoretical argument serves to reinforce numerous observational arguments that suggest binary interactions to be responsible for Be stars. We conclude that observations of Be stars in young open clusters (Milone, Marino et al., 2018; Bodensteiner, Sana et al., 2020) do not contradict the hypothesis that Be stars originate exclusively from mass-transfer in binary systems. We have shown that if all Be stars are binary interaction products, somewhat extreme assumptions must be realised such as an initial binary fraction very close to unity, a shallow initial mass function and very non-conservative mass transfer. Whether or not these conditions can be met by the stars in the sky remains to be seen.

Appendix

A Stars at the critical velocity

Here we investigate how critically rotating and slowly rotating stars vary in terms of their effective temperatures and luminosities. Owing to the fact that stable and reliable numerical models of very fast rotating stars are difficult to produce, we shall employ a simple analytical model.

The luminosity of a main-sequence star is generated from nuclear reactions in the central region. As stars are centrally condensed, when a given star is spun up to the critical velocity the centripetal forces acting in the central regions are much weaker than the force of gravity, meaning the structure of the core is largely unchanged. Hence, the intrinsic luminosity is constant to first order.

What does however change when a star is spun up is the outer structure. The equatorial radius increases, and therefore so does the surface area of the star, S. This then causes the effective temperature to decrease, as evidenced by the

Stefan–Boltzmann law

$$L \propto S T_{\text{eff}}^4. \tag{3.35}$$

To characterise this change in effective temperature we use the Roche model, which describes a star with all mass concentrated at the centre, and rotating with constant angular velocity Ω. In this framework, the effective potential, with respect to the radial coordinate r and latitude θ, is

$$\Psi(r, \theta) = -\frac{GM}{r} - \frac{1}{2}\Omega^2 r^2 sin^2(\theta). \tag{3.36}$$

At the critical angular velocity, the polar radius, R_p is equal to the radius of an equivalent non-rotating star of the same mass, whereas the equatorial radius, R_e is given by

$$R_e = \frac{3}{2}R_p. \tag{3.37}$$

Taking the $x - y$ plane to be parallel to the axis of rotation, where y represents the distance along the rotation axis and x the perpendicular distance from the rotation axis, the surface of a critically rotating star is described by

$$\left(\frac{y}{R_e}\right)^2 = \left(\frac{2}{3 - x^2/R_e^2}\right)^2 - \left(\frac{x}{R_e}\right)^2, \tag{3.38}$$

(Zahn, Ranc and Morel, 2010) The surface area of a star is (see Paxton, Smolec et al., 2019, Appendix B) , in general

$$S = 4\pi \int_0^{R_e} x\sqrt{\left(\frac{dy}{dx}\right)^2 + 1}\, dx. \tag{3.39}$$

After choosing units such that $R_e = 1$, Eqs. 3.38 and 3.39 can be solved numerically to give the surface area of a critical rotator, S_c, as

$$S_c \approx 4\pi \times 0.7028. \tag{3.40}$$

Compare this to the surface areas of non-rotating stars with radii R_e and R_p,

$$S_0(r = R_e) = 4\pi \tag{3.41}$$

and

$$S_0(r = R_p) = 4\pi \left(\frac{2}{3}\right)^2 \approx 4\pi \times 0.4444. \tag{3.42}$$

As expected we have

$$S_o(r = R_p) < S_c < S_o(r = R_e). \tag{3.43}$$

We see that the surface area of a critically rotating star is around 1.58 times larger than that of its non-rotating counterpart.

Therefore from Eq. 3.35, the temperature of a star after having been spun up to critical decreases by a factor of 0.89.

B Stellar isochrones

As our model predictions give the Be fraction as a function of mass, to make an effective comparison with observations, we must extract masses from stars in the colour-magnitude diagram. To this end, we employ isochrones of single rotating stars to assign mass ranges to different areas of the colour magnitude diagram.

We use the grid of Schootemeijer, Langer et al. (2019) that has been extended to masses between 2 and $20\,\mathrm{M}_\odot$ with slight changes to internal mixing - see below. The code used was MESA (Paxton, Bildsten et al., 2011; Paxton, Cantiello et al., 2013; Paxton, Marchant et al., 2015; Paxton, Schwab et al., 2018; Paxton, Smolec et al., 2019). Models were computed at initial rotation rates between 0 and 80% of critical velocity in steps of 10%. As is standard in MESA the critical velocity is

defined as

$$v_{\text{crit}} = \sqrt{\frac{GM}{R}(1 - \Gamma)}, \qquad (3.44)$$

where Γ is the ratio of luminosity to Eddington luminosity, and is negligible for the models presented here. During early times, the models undergo a relaxation period, during which the critical velocity fraction can oscillate wildly. To circumvent this, we define the initial critical velocity fraction at the point when the model has burnt 3% of its initial hydrogen content by mass.

The physics employed in the models is mostly identical to that of Brott, de Mink et al. (2011), except for the treatment of two mixing processes. Stepped convective overshooting is adopted that extends the convective zone by α_{OV} times the local pressure scale-height. A dependence of α_{OV} with mass accounts for observational trends (Castro et al., 2014; Claret and Torres, 2016; Schootemeijer, Langer et al., 2019), whereby α_{OV} increases linearly from 0.1 at $1.66\,M_\odot$ Claret and Torres, 2016 to 0.3 at $20\,M_\odot$ Brott, de Mink et al., 2011. Furthermore, time smoothing in rotational mixing is turned off to avoid unrealistically strong mixing.

Isochrones are generated through a series of linear interpolations and are split up into two equivalent-evolutionary-phases (EEPs). The first phase lasts until core hydrogen depletion, and the second phase from core hydrogen depletion until core helium depletion. To compute the parameters of a star in the first EEP with initial mass M_i, initial critical velocity fraction v_i at time t, we first find the time at which this star would experience core hydrogen exhaustion, T_{MS}. In total, four models are used for the interpolation, two models with initial masses M_1 and initial critical velocity fractions $v_{1,a}$ and $v_{1,b}$ and similarly two models with initial masses M_2 and initial critical velocity fractions $v_{2,a}$ and $v_{2,b}$. The models are selected such that $M_1 < M_i < M_2$ and $v_{1,a} < v_i < v_{1,b}$ and similarly for $v_{2,a}, v_{2,b}$. For M_1 and M_2 we interpolate the lifetime when initial $v_{\text{rot}}/v_{\text{crit}} = v_i$ from these models as is shown in Fig. 3.1 a. The hydrogen burning lifetime is then computed as an interpolation in mass between the values of M_1 and M_2, as depicted in Fig. 3.1 b. For this step, the most accurate results are obtained when the logarithm of hydrogen burning lifetime is interpolated against the logarithm of initial mass. Using the interpolated lifetime, T_i, of this star with initial mass M_i and initial critical velocity fraction v_i, we define its fractional lifetime as t/T_i. This fractional lifetime is the value at which all further interpolations will be carried out. Next, a given quantity (for the purposes of making isochrones, the quantities of interest are effective temperature and luminosity), Q, is interpolated at a fractional lifetime of t/T_i for the four selected models, as in 3.1 c. The penultimate step is to calculate the quantities Q_{M_1}, Q_{M_2} which represent the values of Q of a star with mass M_1, M_2, initial critical velocity fraction v_i and fractional lifetime t/T_i by interpolating across initial critical velocity fraction like in Fig. 3.1 d. Finally, an interpolation in initial mass between the quantities Q_{M_1} and Q_{M_2} is done to produce the value of the chosen parameter for a star of given mass, initial rotation rate and age.

To generate the second EEP, the same procedure is used but only with a different fractional lifetime, namely the fractional helium-burning lifetime, t/T_{He} such that at core hydrogen exhaustion $t/T_{He} = 0$ and at core helium exhaustion $t/T_{He} = 1$.

Absolute magnitudes in Hubble Space Telescope filters are computed by interpolating tables of synthetic stellar spectra provided by the MIST project Choi et al. (2016). Apparent magnitudes are then calculated as

$$m_{\text{F814W}} = M_{\text{F814W}} + A_{F814W} + \mu, \qquad (3.45)$$

$$m_{\text{F336W}} = M_{\text{F336W}} + A_{F336W} + \mu, \qquad (3.46)$$

with μ being the distance modulus and absorption coefficients $A_{F814W} = 2.04E(B - V)$ and $A_{F336W} = 5.16E(B - V)$ (Milone, Marino et al., 2018).
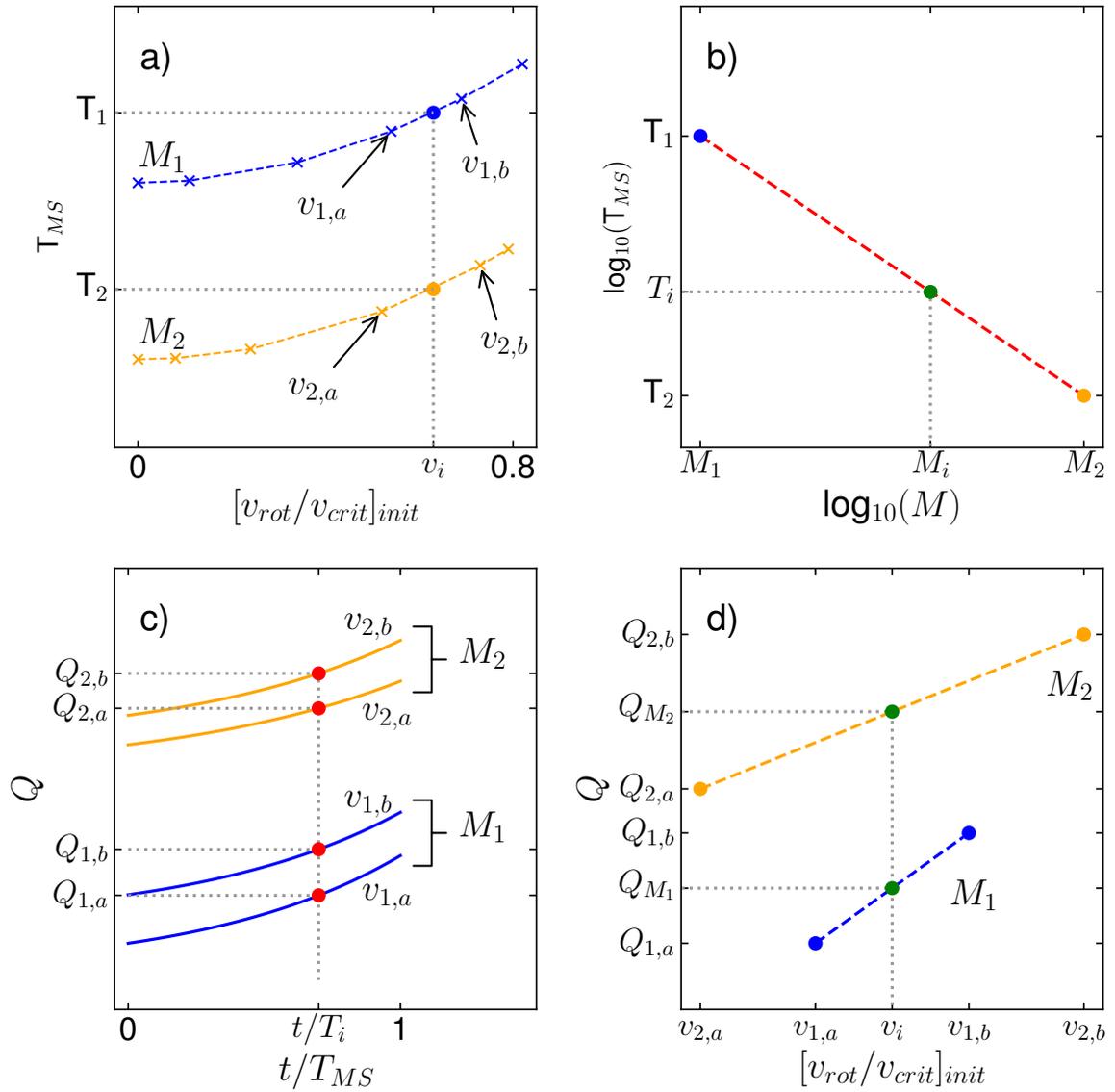
Figure 3.1: Schematic representation of the interpolation procedure employed to produce isochrones. See text for a thorough explanation.

A model of anisotropic winds from rotating stars for evolutionary calculations

Ben Hastings[1], Norbert Langer[1,2], Joachim Puls[3]

[1] Argelander-Institut für Astronomie, Universität Bonn, Auf dem Hügel 71, 53121 Bonn, Germany
[2] Max-Planck-Institut für Radioastronomie, Auf dem Hügel 69, 53121 Bonn, Germany
[3] LMU München, Universitätssternwarte, Scheinerstr. 1, 81679 München, Germany

SUMMARY

The most important quantity that governs the rotation of any object is the conserved quantity angular momentum. A rotating massive star loses both mass and angular momentum through stellar winds. Understanding of the evolution of rotating stars thus requires a detailed knowledge of the stellar winds. This chapter presents a method for self-consistently calculating the mass and angular momentum loss arising from an anisotropic wind of a rotating star that can be employed by any one-dimensional stellar evolution code.

The fundamental aspect of stellar rotation is the centrifugal force. At the pole, there is no such force, while at the equator the centrifugal force is at its maximum. Due to the centrifugal force, the surface gravity varies over the stellar surface, with gravity being weakest at the equator. The local photon flux depends directly on the surface gravity following the von Zeipel theorem (von Zeipel, 1924) and so the local photon flux must also be spatially variable.

Massive stars host radiatively-driven winds, whereby particles are expelled as a wind through the exchange of momentum with photons. The properties of such a wind are thus sensitive to the photon field in the stellar atmosphere. Winds are also sensitive to the surface gravity because ultimately for a wind to be launched, the surface gravity must be overcome. It then follows that because both the surface gravity and photon flux vary over the stellar surface, the wind should also be spatially variable.

Many evolutionary models completely ignore this effect and treat the wind as being isotropic, which may lead to significant errors in the predicted spin evolution of rotating stars. The models analysed in Chapter 2 for example assume

isotropic winds. We aim to improve the physics of stellar winds and assess the discrepancy between isotropic and anisotropic wind models.

To determine the properties of an anisotropic wind, one needs a detailed description of the stellar surface. The required quantities are the surface gravity and effective temperature (which gives the photon flux). The surface gravity profile is given by the Roche model, which assumes that the star is centrally condensed, which is a very good approximation. The effective temperature profile is given by a gravity darkening law, which is a physically justified model of how the effective temperature varies over the surface of a rotating star.

While no general recipe exists to describe the anisotropic wind of a rotating star, one can take advantage mass-loss recipes for non-rotating stars. These are functions that estimate the mass-loss rate of a non-rotating star as a function of various parameters such as luminosity, mass and effective temperature. For a point on the surface of a rotating star, one can assign an equivalent single star with the same surface properties as the chosen point. The mass-loss rate of this equivalent single star is then given by the mass-loss recipe. The surface mass-flux, that is the mass-loss rate per unit area, is found using the equivalent single star's radius. When this process is repeated to every point on the rotating star, a surface mass-flux profile results. Integrating the mass-flux profile over the distorted stellar surface gives the global mass-loss rate of the rotating star. A similar surface integral taking into account the distance from the axis of rotation gives the global angular momentum loss rate.

Evolutionary models were computed which showed that mass-loss rates are largely insensitive to rotation. The exception is when surface temperatures become low enough to enable the recombination of iron that brings about a large increase in opacity, which is predicted to increase the surface mass-flux dramatically. Compared to models that assume an isotropic wind, the anisotropic wind model does not seem to greatly alter the spin evolution of the models presented in this chapter.

The implementation of our scheme in the stellar evolution code MESA is available online: `https://zenodo.org/record/7437006`

4.1 Introduction

All massive stars suffer from the effects of stellar winds. For O-type stars, the winds can be so strong that a significant portion of the star evaporates and the evolutionary pathway is altered dramatically, for example forming a Wolf-Rayet star (Maeder and Meynet, 1987; de Koter, Heap and Hubeny, 1997). In contrast, lower-mass stars typically lose only a negligible fraction of their mass to winds. However even a non-magnetic wind carries angular momentum away from a star, and a star's spin evolution can even be affected by weak winds (Langer, 1998).

In the simplest sense, the density and velocity structure and thus also the mass-loss rate of a radiation-driven wind is determined by the opposing effects of gravity and radiative acceleration. Gravity serves to bind material to the stellar surface, while radiation, through both continuum and line opacities, provides a force to overcome gravity (Castor, Abbott and Klein, 1975; A. Pauldrach, Puls and R. P. Kudritzki, 1986). Rotation directly affects both the gravitational field strength and the radiation field (von Zeipel, 1924), with both varying over the stellar surface, in turn resulting in an anisotropic wind (Poe and Friend, 1986; Cranmer and Owocki, 1995; Curé and Rial, 2004).

For an anisotropic wind, attention needs to be paid to angular momentum loss since mass lost at the equator carries a larger specific angular momentum than mass lost near the poles, especially so for stars that are significantly deformed from sphericity. Owing to internal structural changes, stars born with moderate rotation may evolve to become extremely fast rotators (Hastings, C. Wang and Langer, 2020), so the effects of rotation on stellar winds have the potential to be relevant to a large portion of stars.

For a number of decades, massive star modelling efforts (Heger, Langer and Woosley, 2000; Brott, de Mink et al., 2011; Paxton, Cantiello et al., 2013) have described the effects of rotation on mass loss by increasing the mass-loss rate of an equivalent non-rotating star by a factor that depends on the rotation rate (Friend and Abbott, 1986). Such a formulation is lacking due to two issues. Firstly, it is assumed that, independent of the wind recipe used, rotation always increases mass-loss rates by the same relative amount. This is not a fair assumption because two of the major effects of rotation on the surface of a star are to weaken the gravitational field and to reduce the surface-averaged effective temperature (von Zeipel, 1924). These two effects generally, though not always, serve to counteract each other, with winds being enhanced by weaker gravities but diminished by lower effective temperatures. It is unclear which effect dominates. Both the dependence of the mass-loss rate on temperature and the assumed temperature profile across the stellar surface (gravity darkening law) will govern whether rotation enhances or reduces mass loss, meaning that the enhancement ought to be model dependant (cf. Müller and Vink 2014).

Secondly, some of the mathematical functions used to provide the mass-loss enhancement diverge as the star approaches the critical velocity. While this behaviour is used in stellar evolution calculations merely to prevent models from exceeding critical rotation (Heger, Langer and Woosley, 2000; Petrovic, Langer and van der Hucht, 2005), it is unphysical not least because it is usually[1] only material at the equator which achieves the critical rotation velocity, and strictly the equator covers an infinitesimally small surface, while gravity does manage to keep the star bound over the rest of the surface.

Angular momentum loss from massive stars plays a role in several active research topics such as the study of Be stars (Curé, 2004; Curé, Rial and Cidale, 2005; Ekström et al., 2008; Hastings, C. Wang and Langer, 2020); the occurrence of chemically homogeneous evolution, relevant to double black-hole mergers (Marchant et al., 2016) and gamma-ray burst progenitors (Yoon, Langer and Norman, 2006; Aguilera-Dena et al., 2020); wind-driven orbital evolution in massive binary stars (MacLeod and Loeb, 2020; Sen et al., 2021); and of course the rotation rates of stars in general. Improved modelling of the winds of rotating stars would be beneficial to the advancement our understanding of stellar physics.

Various studies concerning winds from rotating massive stars have been performed (e.g. Poe and Friend 1986; Poe, Friend and Cassinelli 1989; Owocki, Cranmer and Blondin 1994; Cranmer and Owocki 1995; Pelupessy, Lamers and Vink 2000; Petrenz and Puls 2000; Curé, Cidale and Rial 2012; Müller and Vink 2014; Gagnier et al. 2019b), although the results of which have not been adopted for use in stellar evolution codes. Our aim is to provide a simple and easily implementable scheme that improves upon the popular rotationally enhanced mass-loss schemes. We applied our scheme to the one-dimensional stellar evolution code MESA and provide the files necessary to compute models using it [2].

The structure of this paper is as follows. Section 5.3 details the derivation of our stellar wind prescription. In Section 5.4 we compare the results of our new wind model to the commonly used rotationally enhanced mass-loss prescription. A brief discussion of uncertainties is given in Section 4.4. Section 5.5 hosts a comparison of our results to more sophisticated approaches. Lastly, our conclusions are put forward in Section 4.7.

---

[1] In the case of a uniform surface opacity (e.g. electron scattering opacity) and a near-Eddington luminosity, material becomes unbound over the whole surface of the star (Maeder and Meynet, 2000).

[2] `https://zenodo.org/record/7437006`

4.2 Method

4.2.1 Anisotropic wind model

Our basic philosophy is to apply a one-dimensional wind recipe to every point on the surface of a rotating star. For every point on the stellar surface, the given wind recipe uses the local physical conditions to provide a surface mass-flux, which when integrated results in global mass and angular momentum loss rates. We shall now determine the surface properties of a rotating star.

Surface properties of a rotating star

A rotating star with mass M, polar radius R_p, equatorial radius R_e, luminosity L is assumed to be rotating rigidly with angular velocity Ω. In reasonable agreement with detailed stellar models (Maeder, 2009), we assume that the polar radius is not affected by rotation. The contribution of radiative acceleration to the total gravity shall be ignored, as we focus primarily on stars with luminosities below the Eddington luminosity. The critical velocity, or break-up velocity is then the Keplerian angular velocity, at which the gravitational force matches the centrifugal force at the equator and reads

$$\Omega_{\text{Kep}} = \sqrt{\frac{GM}{R_e^3}} \tag{4.1}$$

and the fraction of Keplerian angular velocity is denoted as

$$\omega = \frac{\Omega}{\Omega_{\text{Kep}}}. \tag{4.2}$$

Recent two-dimensional models of rotating stars suggest that the rotation velocity at which material becomes unbound from the stellar surface is very close to the Keplerian velocity (Gagnier et al., 2019a). However, these models only cover two separate values of the stellar mass (15 and $40\,\mathrm{M_\odot}$) at one point in their evolution. Therefore we cannot exclude that for very luminous stars, radiation might play a significant role in unbinding material from the surface and thus reducing the critical rotation velocity. This issue is discussed further in Sec. 4.2.2.

We note that several different working definitions of the critical velocity velocity exist (see discussion in Section 2.3.1 of Rivinius, Carciofi and Martayan 2013 and their Eqns. 3 and 4). Our choice is made to be consistent with the stellar evolution code MESA (Paxton, Smolec et al., 2019).

In the co-rotating frame of a rotating star, the centrifugal force is perpendicular to the rotation axis, which causes the effective surface gravity to to become latitude-dependant. Following from the varying surface gravity , effective temperature also varies across the surface (von Zeipel, 1924). Also effected is the star's shape, evidenced by a bulging equator. These three effects shall now be quantified in order.

As massive stars are centrally condensed, the use of the Roche potential is justified (Collins, 1965; Rieutord, 2016). We define the effective surface gravity as the sum of self-gravitation and centrifugal forces which is

$$\vec{g}_{\text{eff}}(\theta) = \left(-\frac{GM}{r(\theta)^2}\sin(\theta) + \Omega^2 r(\theta)\sin(\theta) \right) \vec{x} - \frac{GM}{r(\theta)^2}\cos(\theta)\,\vec{z}, \tag{4.3}$$

where $\vec{x}$ and $\vec{z}$ are the Cartesian unit vectors, perpendicular and parallel to the rotation axis respectively. The radial co-ordinate is designated r and θ the co-latitude. The magnitude of the surface gravity is then found to be

$$|\vec{g}_{\text{eff}}(\theta)| = \left(\frac{GM}{R_P^2} \right) \delta^{-2} \left[\delta^4 \left(\frac{r(\theta)}{R_P} \right)^{-4} \right.$$
$$\left. + \omega^4 \delta^{-2} \left(\frac{r(\theta)}{R_P} \right)^2 \sin^2(\theta) - 2\omega^2 \sin^2(\theta)\delta \left(\frac{r(\theta)}{R_P} \right)^{-1} \right]^{\frac{1}{2}}, \tag{4.4}$$

where δ is the ratio of equatorial and polar radii, $\delta = \frac{R_e}{R_p}$. Because we assume that every point on the surface can be treated as an equivalent non-rotating star (i.e. we wish to reduce the two-dimensional problem of a rotating star to one dimension), and that the flux vector is nearly perfectly aligned with the gravity vector in a rotating star (Espinosa Lara and Rieutord,

2011), the magnitude of the gravity vector is the quantity of interest, not the gravitational field strength in the radial direction.

The local effective temperature is defined using the local flux, $\vec{F}(\theta)$, and the Stefan-Boltzmann constant, σ as

$$T_{eff}(\theta)^4 = |\vec{F}(\theta)|/\sigma. \tag{4.5}$$

The effective temperature profile is given by the model of Espinosa Lara and Rieutord (2011), which assumes a Roche potential and that the flux at the surface of a star is well approximated by

$$\vec{F}(\theta) = -f(r,\theta)\,\vec{g}_{\text{eff}}, \tag{4.6}$$

which requires the energy flux to be anti-parallel to the effective gravity. This condition is fulfilled in stars with convective envelopes and is also valid to within a very fine tolerance in stars with radiative envelopes (Espinosa Lara and Rieutord, 2011). The function $f(r,\theta)$ is found by demanding that no heat is generated in the envelope (i.e. $\nabla\vec{F} = 0$) and reads

$$f(r,\theta) = \frac{L}{4\pi GM}\frac{\tan^2\vartheta}{\tan^2\theta}, \tag{4.7}$$

where ϑ is the solution to

$$\cos\vartheta + \ln\,\tan\frac{\vartheta}{2} = \frac{1}{3}\omega^2\left(\frac{r}{R_e}\right)^3\cos^3\theta + \cos\theta + \ln\,\tan\frac{\theta}{2}. \tag{4.8}$$

Alternative gravity darkening laws are available (Slettebak, 1949; Lucy, 1967; Lovekin, Deupree and Short, 2006; Lipatov and T. D. Brandt, 2020). We note that the gravity darkening model of Espinosa Lara and Rieutord (2011) predicts that the equatorial flux of a critically rotating star is zero, which might be unphysical.

Lastly, the radial profile can be determined from the Roche equipotential surface (Appendix A) to be

$$\frac{r(\omega,\theta)}{R_p} =$$
$$(2+\omega^2)\sqrt{\frac{2+\omega^2}{3\omega^2\sin^2(\theta)}}\cos\left[\frac{1}{3}\arccos\left(\frac{3}{2+\omega^2}\sqrt{\frac{3\omega^2\sin^2(\theta)}{2+\omega^2}}\right)+\frac{\pi}{3}\right]. \tag{4.9}$$

Mass and angular momentum flux

To quantify the wind over the stellar surface, we shall use the mass-loss rate per unit surface area, or mass-flux, $\dot{m}(\theta)$, which is related to the total mass-loss rate, $\dot{M}$ via

$$\dot{M} = \int \dot{m}(\theta)dS, \tag{4.10}$$

where dS represents the infinitesimal surface element. Knowledge of the star's shape allows us to compute the above integral as (cf. Gagnier et al. (2019b))

$$\dot{M} = 2\pi\int \dot{m}(\theta)r^2(\theta)\sqrt{1+\frac{1}{r^2(\theta)}\left(\frac{\partial r}{\partial\theta}\right)^2}\sin\theta d\theta, \tag{4.11}$$

where $r(\theta)$ is given by Eq. 4.9.

The local angular momentum flux is defined as

$$\dot{\ell}(\theta) = \dot{m}\Omega r^2(\theta)\sin^2\theta \tag{4.12}$$

and the global angular momentum loss rate is found by integrating again over the stellar surface as

$$\dot{\mathcal{L}} = 2\pi\int \dot{\ell}(\theta)r^2(\theta)\sqrt{1+\frac{1}{r^2(\theta)}\left(\frac{\partial r}{\partial\theta}\right)^2}\sin\theta d\theta. \tag{4.13}$$

Determining surface mass flux

Calculating the surface mass flux of a rotating massive star requires not only knowledge of the general mechanics of radiation-driven winds but also of several rotation specific phenomena and their interplay in driving a wind. As of yet, general mass-loss recipes exist only for non-rotating stars, and even those differ significantly depending on methods and assumptions. It is felt that although the use of a non-rotating wind recipe cannot capture the fine details of physical processes in rotating stars, their use in describing rotating star winds is still beneficial and above all represents an improvement over the almost exclusively used rotationally enhanced mass-loss scheme.

Using the effective surface gravity profile, effective temperature profile and surface shape of a rotating star, we may assign an equivalent non-rotating star to each co-latitude of the rotating star, for which the mass-loss rate is given by a chosen recipe. This equivalent non-rotating star is defined to have the same radius, effective temperature and surface gravity as a given latitude on the rotating star. The surface mass-flux is then, in general

$$\dot{m}(\theta) = \frac{\dot{M}\left(|\vec{g}_{\text{eff}}(\theta)|, T_{eff}(\theta), r(\theta), ...\right)}{4\pi r(\theta)^2},$$
(4.14)

where $\dot{M}$ is the function provided by the non-rotating wind recipe. The only requirement for the recipe is that it is a function of, or can be manipulated to be a function of, at least the effective surface gravity, effective temperature and radius.

For the calculations in this work, we shall use the mass-loss recipe of Vink, de Koter and Lamers (2001), although in principle any recipe can be used. Here the mass-loss rate is a function of the stellar mass, effective temperature, luminosity and metallicity, Z. For our purposes, we first need to modify the input parameters of the recipe.

The mass and luminosity of a non-rotating star can be described using the effective surface gravity and effective temperature, provided the radius is known. This means that at each latitude of a rotating star, an equivalent non-rotating star would have a different mass (following from the radius and surface gravity of the rotating star) and a different luminosity (following from the effective temperature and radius). To account for this, the mass-dependence must be expressed instead in terms of the surface gravity and radius. As luminosity is determined by the Stefan-Boltzmann law, an effective luminosity for each colatitude on a rotating star can be defined as

$$L_{\text{eff}}(\theta) = 4\pi\sigma r(\theta)^2 T_{eff}(\theta)^4.$$
(4.15)

This equivalent luminosity represents the luminosity that a non-rotating star, with equal surface properties of a given colatitude, would have. It is therefore this quantity that must be used in place of the luminosity in the mass-loss recipe, which becomes

$$\dot{m}(\theta) = \frac{\dot{M}\left(\frac{|\vec{g}_{\text{eff}}(\theta)|r(\theta)^2}{G}, T_{eff}(\theta), L_{\text{eff}}(\theta), Z\right)}{4\pi r(\theta)^2}.$$
(4.16)

4.2.2 Critical rotation velocity

For a star, there exists a critical (or break-up) rotation velocity at which material becomes unbound from the stellar surface. Although a simple concept, there are several nuances which shall be discussed here. In this work we assume that the critical velocity is attained when the centrifugal and gravitational forces balance, however in general this is likely only an approximation.

In massive stars the force from radiation itself contributes to the force balance, and thus has been proposed to reduce the critical velocity (Langer, 1997). The acceleration produced by radiation is proportional to the flux and opacity, which are both effected by rotation. As first argued by Glatzel (1998), when a luminous star rotates very quickly, gravity darkening causes the equatorial flux to weaken strongly, suggesting that the appropriate limit is the Keplerian one. Although analysis by Maeder and Meynet (2000) determined that below a threshold luminosity (around 60% of the Eddington luminosity), the radiation force indeed plays no role in unbinding material from the surface, the issue is still not clear cut, as discussed in the following.

Gravity darkening is traditionally described by Von Zeipel's Law, which states that effective temperature is proportional to effective gravity to the power of β, with $\beta = 0.25$. Interferometric observations of rapidly rotating stars have demonstrated that gravity darkening is not as strong as predicted by Von Zeipel's Law, with lower β values for faster rotators (Monnier et al., 2007; Zhao et al., 2009; Che et al., 2011; Domiciano de Souza et al., 2014). These observations are generally consistent with two-dimensional numerical models (Espinosa Lara and Rieutord, 2013) and analytic gravity darkening

models (Espinosa Lara and Rieutord, 2011), but one star, β Cassiopeiae, appears to exhibit much weaker gravity darkening than expected (Che et al., 2011), perhaps exposing weaknesses in our understanding of gravity darkening. Weaker gravity darkening would result in a stronger radiative force at the equator, hence helping to reduce the critical velocity.

The surface opacity of a rotating star is also uncertain. Maeder and Meynet (2000) assumed that the region with the highest opacity would be the equator, as this is the coldest part of the surface. However, the centrifugal force also causes a decrease in the matter density at the equator, consequently decreasing the opacity. Two-dimensional numerical models of stars on the zero-age-main-sequence suggest that the effect of decreasing density dominates, thus a fast rotating star is predicted to have a lower equatorial opacity than an equivalent non-rotating star (Gagnier et al., 2019a), meaning that radiative acceleration is unable to contribute to the force balance. However there may be some exceptions. Firstly stars may suffer the effects of opacity bumps caused by recombination of certain species (notably hydrogen, helium and iron; Iglesias and F. J. Rogers 1996), that could drastically alter the opacity profile over the surface of the star. Secondly in very hot stars, where the opacity is dominated by electron scattering, the surface opacity is largely independent of temperature and thus spatially uniform. Such a case would need careful study to determine whether the break-up velocity is affected.

Classical Be stars are fast rotators with a decretion disc, which are believed to be typically rotating at approximately 70% of the Keplerian velocity (Porter, 1996; Rivinius, Carciofi and Martayan, 2013; Zorec, Frémat, Domiciano de Souza et al., 2016; Dufton, Lennon et al., 2022), and in some cases even lower (Huang, Gies and McSwain, 2010; Zorec, Frémat, Domiciano de Souza et al., 2016). It may be reasonably supposed that an outflowing disc will affect the structure of its host star, such that the surface flux and opacities may be different when a disc is present, thus altering the break-up velocity. There is evidence to suggest that the threshold rotation rate for the Be phenomenon, assumed to be the true break-up velocity, varies with effective temperature (Cranmer, 2005; Huang, Gies and McSwain, 2010), with hotter Be stars rotating more slowly than their cool counterparts. It is well understood that hotter stars are closer to the Eddington limit, which may suggest that indeed in the hotter Be stars, radiative acceleration does play a role in unbinding material.

4.2.3 Numerical method

In order to investigate the effect of our prescription on the evolution of both mass and angular momentum loss rates of rotating stars, we employ the one-dimensional detailed stellar evolution code MESA (Paxton, Smolec et al., 2019), version 12115. The files required to compute models presented in this work are available online[3]. The adopted physics is largely identical, except for the stellar winds, to that of Brott, de Mink et al. (2011) and implemented in MESA as by Schootemeijer, Langer et al. (2019). The models include internal angular momentum transport achieved by magnetic torques (Spruit, 2002) which enforce near solid-body rotation during most of the main-sequence evolution.

We run two sets of models, one using the rotationally enhanced mass-loss scheme as it is usually implemented in MESA (named the standard scheme), where the mass-loss rates are first calculated using the recipe of Vink, de Koter and Lamers (2001) and then following Friend and Abbott (1986) [4] increased by a factor of

$$\left(1 - \Omega \sqrt{\frac{R_e^3}{GM(1-\Gamma)}} \right)^{-0.43}. \tag{4.17}$$

The second set uses mass-loss rates set by the method outlined in Sec. 4.2.1 and is named the local scheme. Both sets rely on the wind mass-loss recipe of Vink, de Koter and Lamers (2001). This wind recipe includes the bi-stability jump effect (first found by A. W. A. Pauldrach and Puls 1990), where mass-loss rates are theorised to increase dramatically during the transition to temperatures cooler than approximately 22kK owing to the recombination of Fe IV in the atmosphere (Vink, de Koter and Lamers, 1999). The impact of the bi-stability jump on mass-loss rates is not certain, with Björklund et al. (2022) noting that 'the drastic $\dot{M}$ increase found in earlier models in this region might simply be an artefact of not being dynamically consistent around the sonic point, and not allowing properly for the feedback between radiative and velocity acceleration'. The quantitative behaviour of models near the jump is also contested (Markova and Puls, 2008; Vink, 2018; Krtička, Kubát and Krtičková, 2021). We stress that our method is not confined to a particular mass-loss recipe and that several others could be used, for example those of R. P. Kudritzki et al. (1989), Sundqvist et al. (2019) and Björklund et al. (2022).

---

[3] `https://zenodo.org/record/7437006`

[4] see Lamers and Cassinelli (1999) for a thorough description

For the standard scheme, stellar winds are assumed to be isotropic with the angular momentum loss $\dot{\mathcal{L}}$, given by

$$\dot{\mathcal{L}} = j_{\text{surf}}\dot{\mathcal{M}}, \tag{4.18}$$

where j_{surf} is the specific angular momentum of the distorted surface and $\dot{\mathcal{M}}$ the global mass-loss rate (Paxton, Smolec et al., 2019). The local scheme computes angular momentum loss according to Eqns.4.12 and 4.13, taking into account both the anisotropic wind and surface deformation caused by rotation.

We compute models with a chemical mixture representing the Large Magellanic Cloud as in Brott, de Mink et al. (2011). Two initial masses of $10\,\text{M}_\odot$ and $20\,\text{M}_\odot$ are chosen to straddle the bi-stability jump. We run models with an initial equatorial rotation velocity of $300\,\text{km}\,\text{s}^{-1}$ until core hydrogen depletion, defined as a central hydrogen mass fraction of 1×10^{-4}. The chosen rotation velocity represents the typical value for early B-stars found in the Large Magellanic Cloud (Dufton, Langer et al., 2013) and corresponds to an initial critical rotation fraction of around 0.45 for both masses.

It is also useful to assess numerical models with varying rotation rates at a fixed point in their evolution. To this end we run models with very small timesteps until the model has burnt 3% by mass of its initial supply of hydrogen in the core ($X_c = 0.7169$). This is approximately the earliest point at which the model finds itself in thermal and nuclear equilibrium and hence is a good point in the star's evolution to investigate. We shall term the point when $X_c = 0.7169$ the zero-age-main-sequence.

Our models are numerically stable until initial critical velocity fractions, ω, of around 0.65, so to investigate stars with faster rotation, an extrapolation is performed. The local wind scheme requires as inputs the stellar mass, rotation rate, polar radius and luminosity .

The polar radius is assumed to be invariant to rotation, so this is known from a non-rotating model. For the luminosity, we extrapolate from the slower rotating models as described in Appendix B up to $\omega = 0.9$. Using the four named quantities, the effective gravity and effective temperature profiles can be calculated (as outlined in Sec. 4.2.1), and resultingly the surface mass-flux. Thus we may investigate the behaviour of our scheme for very fast rotating stars on the zero-age-main-sequence despite not having stellar models at these rotations. Stars born with moderate rotation may evolve to rotate at high critical velocity fractions owing to internal structural changes (Hastings, C. Wang and Langer, 2020), so it is important to check the behaviour of our scheme at near critical rotations.

4.3 Results

4.3.1 Mass loss on the zero-age-main-sequence

Figure 4.1 shows the surface mass flux as a function of colatitude for $10\,\text{M}_\odot$ and $20\,\text{M}_\odot$ models rotating at various rates. All models displayed have a central hydrogen mass fraction of 0.7169, equating to 97% of the initial hydrogen mass fraction. It is seen that for slow rotation, mass flux is stronger at the poles and weaker at the equator. This occurs because rotation results in a hotter pole, relative to the non-rotating case, and a cooler equator, and stellar winds are very sensitive to effective temperature changes.

For faster rotating $10\,\text{M}_\odot$ models, mass-flux experiences a jump at colatitudes between 60 and 80°caused by the bi-stability jump. Moving from pole to equator across the stellar surface, effective gravity and hence effective temperature decrease. At some point, the effective temperature subceeds the 'jump temperature' at which Fe IV recombines to Fe III causing a sudden, dramatic increase in the mass flux, as evidenced in the left panel of Fig. 4.1. The $20\,\text{M}_\odot$ model does not undergo the same phenomenon as here the effective temperature always exceeds the jump temperature.

The global mass-loss rate depends on both the surface mass-flux and the stellar surface area. For the wind recipe of Vink, de Koter and Lamers (2001) used in this work, provided the ionisation equilibrium does not change significantly, faster rotation is seen to cause a decreasing surface mass-flux at the equator. Also rotation increases the surface area of the equatorial region due to the equatorial bulge. These two effects can offset one another, causing the global mass-loss rate to be roughly independent of rotation, as exemplified by models shown in Fig. 4.2. We note that because of the relatively small area covered by the polar region, the polar surface mass-flux does not contribute significantly to the global mass-loss rate.

For the $10\,\text{M}_\odot$ model in the local scheme, mass loss decreases slightly with faster rotation, until the bi-stability jump comes into effect at $\omega \approx 0.5$ and drives mass-loss rate up. In contrast, the $20\,\text{M}_\odot$ model displays almost no change in mass-loss rates until $\omega \approx 0.3$ and then a small increase thereafter, due to the effect of the growing surface area of the equator dominating over the diminished equatorial surface mass-flux. We note that, except for models affected by the bi-stability jump, our local scheme produces slightly weaker winds than the standard scheme. Our models show that excluding the effects of the bistability jump, mass-loss rates of a rotating star are not predicted to be significantly different to that of an equivalent non-rotating star.

Figure 4.1: Mass-loss rate per unit surface area as a function of colatitude, θ, for $10\,M_\odot$ (left panel) and $20\,M_\odot$ models (right panel) at various rotation rates. All models have burnt 3% by mass of their initial hydrogen (i.e. $X_c = 0.7169$). Critical velocity fraction, ω, is depicted in the legend.

At very high initial rotation rates, our estimates of the mass-loss rate from extrapolation of the luminosity show that for the $20\,M_\odot$ model, the increase in mass-loss rate is modest, 10% at most. Whereas the cooler $10\,M_\odot$ model displays mass-loss rate enhancement of a factor 9 at $\omega = 0.9$. We are thus confident that our scheme behaves reasonably at near-critical velocities.

4.3.2 Evolutionary models

Our evolutionary models are presented in Fig. 4.3 where panels a) and b) show the evolution of global mass-loss rates. In the standard scheme the bi-stability jump is implemented as a sharp jump, however in the local scheme the jump is more gradual, owing to the fact that as the star cools, the region of the surface affected by the jump grows, causing the mass-loss to also gradually increase.

Panels c) and d) of Fig. 4.3 show the normalised specific angular momentum loss of our evolutionary models, given as

$$\frac{\dot{\mathcal{L}}}{\frac{2}{3}\dot{\mathcal{M}}\Omega R_{\text{eq}}^2}. \tag{4.19}$$

This is a unitless quantity that describes the strength of angular momentum loss independently of the rotation rate and mass-loss rate. A spherical star with an isotropic wind (i.e. a slowly rotating star) has a normalised specific angular momentum loss of 1. Values larger than unity imply that the star is losing more angular momentum per unit mass than the spherically symmetric case and that spin-down will occur more rapidly. This quantity is sensitive to both the anisotropy of the wind and the deformation of the star. We see that away from the bi-stability jump temperatures, models using the local scheme suffer lower angular momentum losses than the standard scheme. This reduced normalised specific angular momentum loss means that stars may be able to maintain faster rotation rates. The opposite is true when mass-flux across the stellar surface is increased due to the bi-stability jump, because the model loses large quantities of mass from the equatorial regions.

Panels e) and f) of Fig. 4.3 show the equatorial velocities of our models. Comparing the velocities near the end of the main-sequence, we see that the local scheme displays larger rotational velocities, due to the generally lower mass-loss and normalised specific angular momentum losses as shown in the upper two panels. The effect is greatest in the $20\,M_\odot$ model, with velocities increased by roughly 10% compared to the standard scheme.
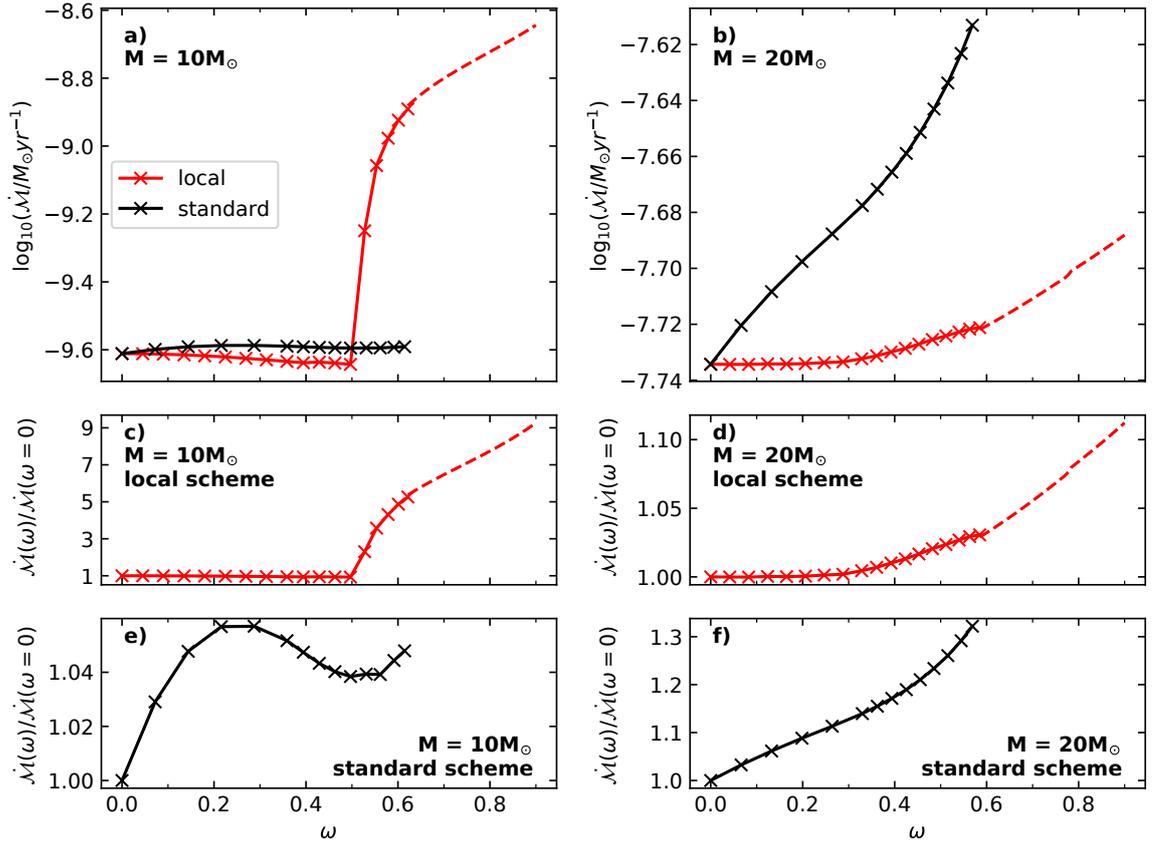
Figure 4.2: *Upper panels:* Global mass-loss rates as a function of critical velocity fraction, ω, for $10\,M_\odot$ (left panel) and $20\,M_\odot$ models (right panel). Predictions of the local scheme, where surface mass flux is determined by Eq. 4.16 and the global mass-loss rate given by Eq. 4.11, are given in red. The standard scheme, where the mass loss rates are increased by Eq. 4.17 is depicted in black. All models have burnt 3% by mass of their initial hydrogen (i.e. $X_c = 0.7169$). Dotted lines represent mass-loss rates calculated from extrapolation (see Sec. 4.2.3). *Lower panels:* Ratios of rotating star mass-loss to non-rotating star mass loss, $\dot{M}(\omega)/\dot{M}(\omega = 0)$, for each combination of mass-loss model and initial mass as given in each panel.
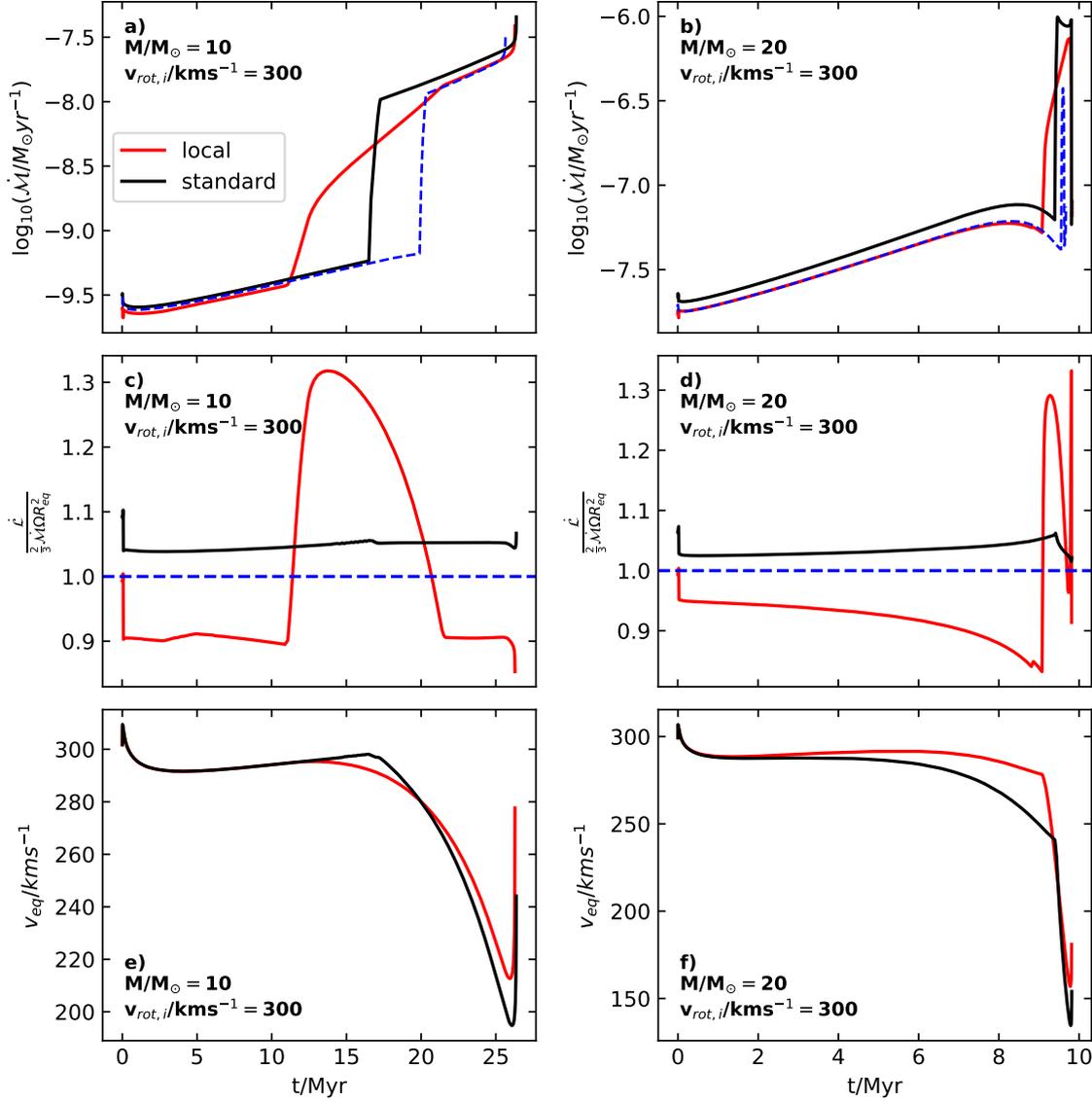
Figure 4.3: *Upper panels:* evolution of global mass-loss rate as a function of time. The blue dashed line shows the mass-loss rate computed from a non-rotating model. *Central panels:* evolution of normalised specific angular momentum loss, as given by Eq. 4.19 (see text for details). In the limit of slow rotation this quantity is equal to unity, shown by the blue dashed line. *Lower panels:* evolution of the equatorial rotational velocity as a function of time. The left panels show a $10\,M_\odot$ model, the right panels a $20\,M_\odot$ model. Predictions of the local scheme, where surface mass flux is determined by Eq. 4.16 and the global mass-loss rate given by Eq. 4.11, are given in red. The standard scheme, where the mass loss rates are increased by Eq. 4.17 is depicted in black. All rotating models have initial equatorial rotational velocities of $300\,\text{km s}^{-1}$.

4.4 Uncertainties

When attempting to describe a two-dimensional phenomenon with a one-dimensional model there are inevitably shortcomings. Most stellar evolution codes compute the structure of a rotating star by applying certain corrections to the stellar structure equations that are designed to produce the average properties along an isobar (for a detailed description see Heger, Langer and Woosley 2000). This approximation may break down under certain conditions, for example when the surface temperature at the equator is cool enough for helium-I to form yet the pole it is not, the opacity will vary greatly over the stellar surface causing different physical conditions at the equator and pole. In such a case, average quantities will not capture this diversity and may lead to different structures as computed by one and two-dimensional models.

A weakness of our wind scheme is that to determine the local mass-flux, we use a mass-loss recipe that was calculated for non-rotating stars. Such a recipe naturally ignores rotational phenomena like non-spherical geometry and the effects of limb-darkening. What is more, the ionisation of the wind is expected to be sensitive to radiation from various latitudes on the stellar surface (Petrenz and Puls, 2000), which could effect the mass-loss rates.

A fundamental assumption of our scheme is that the wind is launched from the stellar surface and moves parallel to the photon flux (which is assumed to correspond to the direction of the effective gravity). In reality, a wind is continually accelerated until it reaches the terminal wind velocity and during this acceleration a wind particle may be influenced by photons streaming at an oblique angle to the stellar surface. This would introduce a non-radial line force (particularly in combination with a polar-angle dependent velocity field), which may alter the wind structure and angular momentum content (Owocki, Cranmer and Gayley, 1996; Gayley and Owocki, 2000). What is more, in our model the effective gravity, and hence flux, have a non-radial direction, while most one-dimensional mass-loss recipes assume a purely radial flux.

When running models at large critical velocity fractions, caution must be exercised, as one may be extrapolating from the non-rotating wind recipe. For any given wind recipe, there are bounds in which the input parameters are valid and it is entirely possible that under extreme rotation the local surface conditions fall outside of the prescribed bounds. Should this occur, a second suitable wind recipe could be used to give the local mass flux for the effected regions, for example a cool star wind recipe may be appropriate for describing the equatorial wind.

4.5 Applicability of the local mass-loss scheme

The pre-requisites for the mass-loss scheme presented here are that the star's shape needs to be well described by the Roche potential and the gravity darkening law of Espinosa Lara and Rieutord (2011) must be valid. This is in general true for both convective and radiative stars that do not have near-Eddington luminosities and are rotating sub-critically (Espinosa Lara and Rieutord, 2011), however there are further cases where these conditions are not met and other special cases which will be discussed here.

For very luminous stars, the radiative acceleration may facilitate the unbinding of material from the stellar surface at lower rotation velocities than the Keplerian velocity. As this effect is ignored in our formalism, our scheme is not appropriate for very luminous objects. In light of the findings of Maeder and Meynet (2000), we would conservatively advise the limit of applicability to be 60% of the Eddington luminosity. Improved gravity darkening laws and a more detailed account of the stellar surface opacity could possibly allow for applying our scheme also at higher Eddington factors, but this still needs to be investigated (see Sec. 4.2.2).

Furthermore, luminous stars may suffer the effects of inflation whereby radiation pressure "inflates" the star, producing a very tenuous, extended envelope (Ishii, Ueno and Kato, 1999; Sanyal, Grassitelli et al., 2015). If the radiation pressure deviates from spherical symmetry, then the strength of inflation will vary according to latitude, suggesting that the star's shape is not well described by the Roche potential. Our mass-loss scheme is therefore not applicable to inflated stellar models. Inflation is expected to occur at masses above $30\,M_{\odot}$ for stars with galactic metallicity, but for much higher masses at lower metallicities (Sanyal, Langer et al., 2017).

A star may suffer the effects of additional forces which can alter the surface effective gravity beyond the Roche potential. Examples include radial pulsations, accelerations from rapid expansion or contraction and a close binary companion. Such cases would need to be dealt with separately, although our scheme could be extended to them.

While our scheme may be applied to rapid rotators, once a star reaches critical velocity, evolutionary models demand that the star lose enough angular momentum to maintain sub-critical rotation. It is not entirely clear how this may happen, there are several possibilities. The star may undergo a "mechanical mass-loss episode", losing the required angular momentum through increased mass loss at the equator only (Granada, Ekström et al., 2013). The other extreme is to lose angular momentum via an isotropic wind, as is currently done in MESA models, but one may also prescribe for mass to be lost from the surface in any configuration. For at least some fast rotating stars in nature, a circumstellar decretion disc forms

that can efficiently drain angular momentum from the star (Krtička, Owocki and Meynet, 2011). For lower-mass stars ($M \lesssim 10 M_\odot$), the required angular momentum loss rates, and correspondingly required mass loss rates are low (Granada, Ekström et al., 2013), hence the evolution of the star is largely insensitive to the mechanics of angular momentum loss at the critical velocity. This is not true for more massive stars, which can lose upwards of 10% of their initial mass from rotating critically (cf. Table 1 of Granada, Ekström et al. 2013), so how exactly angular momentum is drained from a critical rotator becomes important. Therefore we advise caution when stellar models achieve critical rotation.

A crucial aspect of our formulation is that it demands that the wind is sensitive only to the local conditions of where on the surface it was launched from. An example where this condition is violated is the dust-driven winds of asymptotic giant branch stars. Global pulsations may lead to dust formation in the outer atmosphere, which is essential for the wind driving (Winters et al., 2000).

4.6 Comparison to other studies

Several authors have investigated the problem of stellar winds and rotation by directly taking into account rotation specific physics. The prescription presented here is better described as an adaptation of a wind model for non-rotating stars, so it is useful to compare our results to previous studies.

It has been reported that radiation-driven winds are most strongly affected by gravity darkening directly beneath the point from which the wind was launched (Cranmer and Owocki, 1995). This suggests that the wind is only sensitive to the point form which it is launched, justifying our use of a non-rotating wind model as our basis. It is also encouraging as limb-darkening, which is not accounted for in our prescription, is deemed unimportant (Cranmer and Owocki, 1995).

Petrenz and Puls (2000) calculated wind models using the concept of a mean irradiating atmosphere and found the winds to have a prolate structure, with increased mass-flux at the pole. Furthermore, for B-type stars, rotation is predicted to diminish mass-loss rates, with models rotating at around 80% of critical velocity displaying mass-loss rates a few percent lower than corresponding non-rotating models (c.f Table 4 of Petrenz and Puls 2000). Similarly, we predict a very weak rotation dependence on mass-loss rates (away from the bi-stability jump), although our models can show enhanced or reduced winds depending on the stellar parameters. Müller and Vink (2014) also find that mass-loss actually diminishes due to the effects of rotation, in contrast to the rotationally enhanced wind schemes.

Pelupessy, Lamers and Vink (2000) focused on B[e] stars using models including the bi-stability jump effect. They report that rotation, in general, enhances mass-flux from the poles but hardly changes that of the equator. The spatial variation in mass-flux predicted by Pelupessy, Lamers and Vink (2000) shows a discontinuity owing to the bi-stability jump, albeit not as steep as in our results (c.f. Fig. 9 with our Fig. 4.1). Pelupessy, Lamers and Vink (2000) predict the winds of a $20 M_\odot$ star to grow stronger with rotation, with rotation at 60% of critical velocity boosting mass-loss by 16% compared to the non-rotating case (c.f. Table 3).

The works mentioned above computed only stationary models, however different stellar parameters were used in each case. For example the $20 M_\odot$ model of Petrenz and Puls (2000) had a radius of $20 R_\odot$, while that of Pelupessy, Lamers and Vink (2000) was more than twice as large, $47 R_\odot$. The fact that the resulting relationships between rotation and mass-loss rates disagree is therefore not surprising.

The work of Gagnier et al. (2019a) differs from this study twofold. Firstly, the two-dimensional ESTER code (Espinosa Lara and Rieutord, 2013) was used to compute the stellar structure, whereas here we rely on a one-dimensional code. Secondly, the local mass-flux was calculated by calibrating the one-dimensional CAK theory (Castor, Abbott and Klein, 1975) to the wind recipe of Vink, de Koter and Lamers (2001). Given that models presented here and in Gagnier et al. (2019a) are based on the same wind recipe of Vink, de Koter and Lamers (2001), a comparison between the two will highlight differences in the underlying methods.

To compare our scheme to that of Gagnier et al. (2019a), a $15 M_\odot$ model has been computed with solar metallicity as in Brott, de Mink et al. (2011) and initial critical angular velocity fraction, $\omega = 0.5$. Fig 4.4 compares the results of the two methods. Firstly, we see that the equatorial effective temperatures predicted by both models agree to within around 2000K, and to within several hundred Kelvin during the early evolution. This discrepancy can largely be credited to the differences of the structures predicted by two and one-dimensional models and the implementation of rotational mixing.

A disadvantage of the method of Gagnier et al. (2019a) is that the required calibration of the surface mass-flux is sensitive to the strength of surface gravity, meaning that properly, (as stars evolve to lower surface gravities) a new calibration must be made at every timestep (see Sec. 4.2 of Gagnier et al. 2019b). However, as the calibration is onerous, it was only carried out for models on the zero-age-main-sequence, meaning that "the local mass-flux may be underestimated by a factor ~1.7 at most". Our scheme does not suffer from this issue, which may explain partly why our model predicts slightly higher mass-loss rates in panel a of Fig. 4.4. Both models however show the same general trend, with a gradual increase in
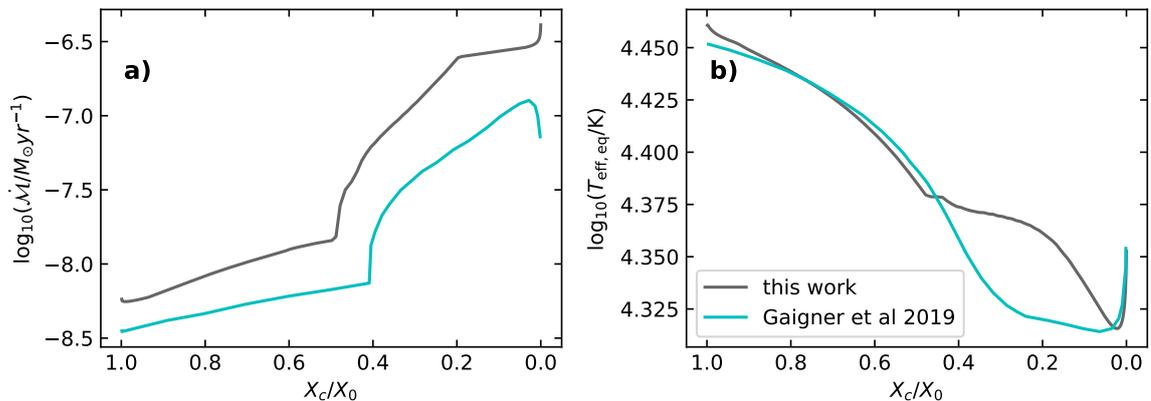
Figure 4.4: Comparison of the global mass-loss rates (left panel) and equatorial effective temperatures (right panel) predicted by this work and that of Gagnier et al. (2019a). Shown are the results of $15\,M_\odot$ models with solar metallicity and initial critical velocity fraction, $\omega = 0.5$. Predictions of this work are plotted as grey lines, and those of Gagnier et al. (2019a) as cyan lines. The x-axis depicts the central hydrogen mass fraction normalised to the initial value. The panels in this figure are directly comparable to Figures 13 and 14 of Gagnier et al. (2019a).

mass-loss rates once the equatorial effective temperature cools below 22-23kK. The relative increase in mass-loss rates brought about by the bistability jump is approximately the same in both models. The jump temperature differs slightly in the two models because the jump temperature is sensitive to the stellar luminosity (see Eq. 16 of Gagnier et al. 2019a). Both models naturally have different luminosities owing to their different structures, as mentioned earlier. We find it encouraging that our relatively simple scheme behaves similarly to a two-dimensional, more advanced model.

4.7 Conclusions

We have presented a new and simple to implement prescription for the mass and angular momentum loss rates of rotating massive stars. This represents an improvement over the widely used rotationally enhanced mass-loss schemes as we calculate the two-dimensional mass-flux over the stellar surface and are able to compute the angular momentum loss resulting from an anisotropic wind originating from a distorted star. Our method involves using a mass-loss recipe for non-rotating stars to determine the local mass-flux across the surface of a rotating star, which is then integrated to give global mass and angular momentum loss rates.

In general we notice that, away from the bi-stability jump temperature, mass-loss rates are slightly diminished compared to the rotationally enhanced mass-loss scheme. The local mass-flux scheme has the effect of smoothing out the bi-stability jump as the increase in mass-loss rate is implemented locally on the star's surface, not globally, also observed in the models of Gagnier et al. (2019a). Our models show that the presence of the bistability-jump causes a strong relationship between rotation and mass-loss. If the bistability-jump does not in fact operate in nature, as suggested by theoretical wind models of Björklund et al. (2022), moderate and even fast rotation is not predicted to strongly alter mass-loss compared to the non-rotating case. We see evidence that the detailed relationship between rotation and wind strength is complex, with mass-loss rates being either decreased or increased depending on the surface properties of the star.

Our aim to provide a scheme for one-dimensional stellar evolution codes will of course mean that simplifications must be made. In spite of our scheme's shortcomings, comparisons with similar, more physically comprehensive works deliver a broad agreement in global mass-loss rates.

Our methods are relevant to several areas of stellar astrophysics where the evolution of angular momentum plays a decisive role. For example, Be stars are known to be fast rotators, so are expected to have strongly anisotropic winds and large distortions. Models such as those presented here may therefore be used to investigate evolutionary properties of Be stars. Secondly, the evolution of models along a chemically homogeneous pathway can be interrupted by spin-down caused by stellar winds (Yoon, Langer and Norman, 2006). The calculations presented here suggest that angular momentum loss

has been generally overestimated in stellar models, suggesting that chemically homogeneous evolution (e.g. Hastings, Langer and Koenigsberger 2020) may be more common or easier to maintain than previously thought. In the future, our wind prescription may be implemented in the next grids of stellar evolution models in order to gain further insights into the physics of rotating massive stars.

Appendix

A Shapes of rotating stars

Here we derive the shape of the surface of a rotating star. We assume that the star is well described as a point mass enclosed by a massless envelope and that the polar radius in unaffected by rotation. The surface of the star is then an equipotential given by the Roche potential and reads

$$\frac{GM}{r(\theta)} + \frac{1}{2}\Omega^2 r(\theta)^2 \sin^2(\theta) = \text{constant}, \tag{4.20}$$

with M representing the stellar mass, Ω the angular velocity (which is assumed to be constant across both the surface and through the interior of the star), $r(\theta)$ the radial co-ordinate and θ the co-latitude. We parametrise the strength of rotation with the Keplerian angular velocity, defined using the equatorial radius R_e as

$$\Omega_{\text{Kep}}^2 = \frac{GM}{R_e^3}. \tag{4.21}$$

We let

$$\omega = \Omega/\Omega_{\text{Kep}}. \tag{4.22}$$

It is important to stress that the derivation that follows is only valid for the above parametrisation of rotation.

Combining Eqns. 4.20, 4.21 and 4.22 gives

$$1 + \frac{1}{2}\omega^2 \frac{r^3}{R_e^3}\sin^2(\theta) = \frac{r}{R_e}(1 + \frac{\omega^2}{2}), \tag{4.23}$$

which after defining

$$\tilde{r} = r/R_e, \tag{4.24}$$

further simplifies to

$$\tilde{r}^3 - \frac{2+\omega^2}{\omega^2 \sin^2(\theta)}\tilde{r} + \frac{2}{\omega^2 \sin^2(\theta)} = 0. \tag{4.25}$$

Eq. 4.25 is a cubic in the form $x^3 + px + q = 0$ (known as a depressed cubic) and has the general solution

$$x_k = 2\sqrt{\frac{-p}{3}}\cos\left[\frac{1}{3}\arccos\left(\frac{3q}{2p}\sqrt{\frac{-3}{p}}\right) - \frac{2\pi k}{3}\right] \tag{4.26}$$

for $k = 0, 1, 2$ corresponding to the 3 cubic roots (Zwillinger, 1996).

Here we have $p = -\frac{2+\omega^2}{\omega^2 \sin^2(\theta)}$ and $q = \frac{2}{\omega^2 \sin^2(\theta)}$ giving

$$\tilde{r}_k = 2\sqrt{\frac{2+\omega^2}{3\omega^2 \sin^2(\theta)}}\cos\left[\frac{1}{3}\arccos\left(-\frac{3}{2+\omega^2}\sqrt{\frac{3\omega^2 \sin^2(\theta)}{2+\omega^2}}\right) - \frac{2\pi k}{3}\right]. \tag{4.27}$$

The periodicity of the cosine function means that if $y = \cos(x)$ then $-y = \cos(x + n\pi)$ where n is an integer so that $\arccos(-y) = x + n\pi$ and $x = \arccos(y) - n\pi$. Thus Eq. 4.27 becomes

$$\tilde{r}_k = 2\sqrt{\frac{2+\omega^2}{3\omega^2 \sin^2(\theta)}}\cos\left[\frac{1}{3}\arccos\left(\frac{3}{2+\omega^2}\sqrt{\frac{3\omega^2 \sin^2(\theta)}{2+\omega^2}}\right) - \frac{2\pi k}{3} - n\pi\right]. \tag{4.28}$$

To be physical, the solution must be independent of n, which is only achieved when $k = 1$. Choosing $n = -1$ results in

$$\tilde{r}_{k=1} = 2\sqrt{\frac{2+\omega^2}{3\omega^2\sin^2(\theta)}}\cos\left[\frac{1}{3}\arccos\left(\frac{3}{2+\omega^2}\sqrt{\frac{3\omega^2\sin^2(\theta)}{2+\omega^2}}\right) + \frac{\pi}{3}\right]. \tag{4.29}$$

From Eqn. 4.23 one can deduce the ratio of equatorial to polar radii, $\frac{R_e}{R_p}$ as

$$\frac{R_e}{R_p} = 1 + \frac{1}{2}\omega^2. \tag{4.30}$$

The final solution is arrived at by combining Eqns. 4.29 and 4.30 and reads

$$\frac{r(\omega,\theta)}{R_p} = (2+\omega^2)\sqrt{\frac{2+\omega^2}{3\omega^2\sin^2(\theta)}}\cos\left[\frac{1}{3}\arccos\left(\frac{3}{2+\omega^2}\sqrt{\frac{3\omega^2\sin^2(\theta)}{2+\omega^2}}\right) + \frac{\pi}{3}\right]. \tag{4.31}$$

As expected, the expression above gives the equatorial radius at critical rotation to be 1.5 times the polar radius ($\frac{r(\omega=1,\theta=\pi/2)}{R_p} = 1.5$). We note that Eq. 4.31 differs from Equation 26 used by Cranmer and Owocki (1995) owing to the use of different definitions of the critical velocity (Cranmer and Owocki (1995) use $\Omega_{\rm crit}^2 \propto M/(1.5R_p)^3$).

B Surface properties of fast rotators close to the zero-age-main-sequence

Our numerical models are unable to compute the structure of a rotating star with initial rotation exceeding around 70% of the critical velocity. However the wind properties of very fast rotating stars on the zero-age-main-sequence may be determined via extrapolation. The wind scheme presented in this paper requires knowledge of the effective gravity and effective temperature profile of a star. To calculate these profiles, only the polar radius, luminosity, mass and rotation rate are required.

To calculate the luminosity of fast rotators on the zero-age-main-sequence, we extrapolate linearly from our models with initial critical fractions between 0.4 and 0.6. We extrapolate the luminosity normalised to the value of the non-rotating model against the intial fraction of critical velocity, where all values are defined at the point when the central hydrogen mass fraction decreases by 3% from its initial value (this we term the zero-age-main-sequence, as it is the earliest point in which the models find themselves in equilibrium). This extrapolation is shown in Fig. 4.1 for 10 and 20 $M_\odot$ models. We find that rotation rate and luminosity are inversely proportional. This effect is rather weak, with luminosity decreasing by approximately 6% at 60% of critical rotation. The extrapolations suggest that at up to 90% of the critical velocity, the luminosity is reduced by no more than 10% compared to the non-rotating case.

In line with the assumptions of the Roche potential, the polar radius is not affected by rotation, so this value may be assumed from a non-rotating MESA model, depicted graphically by the horizontal dashed yellow line in Fig. 4.1. Indeed, as evidenced by Fig. 4.1 the numerical models predict that to within a few percent, the polar radius remains unchanged by rotation.

The results of our extrapolations compare favourably to the computed stellar structures of Ekström et al. (2008). One-dimensional models of a 20 $M_\odot$ star predict that the luminosity decreases by around 8% over the course of being spun up from stationary to critical rotation (Ekström et al., 2008, Fig. 5). While the polar radius is judged to shrink very slightly with increasing rotation, but this is at most a 2% effect (Ekström et al., 2008, Fig. 2), thus justifying the assumption of the Roche potential.
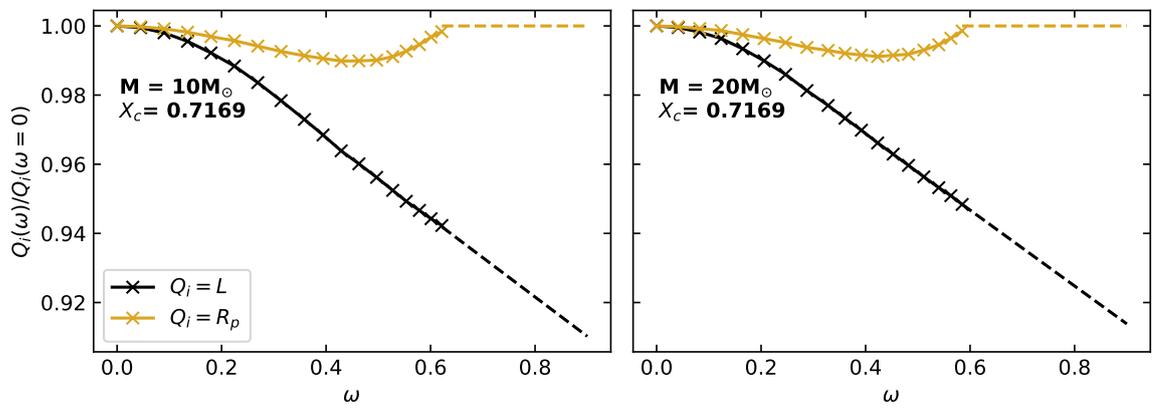
Figure 4.1: Variation of luminosity (black line), L, and polar radius (yellow line), R_p, normalised to the values of a non-rotating star as a function of critical velocity fraction, ω. The left panel shows models with masses $10\,M_\odot$ and the right panel $20\,M_\odot$. All models have burnt 3% by mass of their initial hydrogen (i.e. $X_c = 0.7169$). Each cross represents a value computed by a MESA model. Dashed lines show extrapolated values.

Constraints on mass-transfer from Be + stripped star binaries

Summary

Mass transfer arising from Roche-lobe overflow in a binary star can significantly alter the evolutionary pathway of stars. Several arguments, both observational and theoretical, suggest that not all of the material leaving the donor star is accreted by the accretor star. The exact mechanics of mass-transfer however are poorly understood and the degree of mass-transfer efficiency is not well known. As many binary interaction products undergo at least one mass-transfer phase, a robust understanding of mass-transfer efficiency is crucial for the study of binary stars in general.

This work aims to determine mass-transfer efficiencies by comparing a suite of binary evolution calculations with observations of Be + stripped star binaries. Be + stripped star binaries are in the stage just after mass transfer has terminated and so represent the best chance to deduce the physics of mass transfer, without needing to consider further complications such as supernova kicks. Furthermore, angular momentum loss resulting from non-conservative mass transfer is assessed. The observed component masses and orbital periods of three Be + stripped star systems are compared against a large grid of binary evolution calculations with varying mass-transfer efficiencies and angular momentum loss. A statistical test is performed to determine the favoured mass-transfer parameters. It is seen that mass-transfer efficiencies of around 50% and relatively weak angular momentum losses are preferred. Importantly, these values are significantly different from those adopted in current binary evolution calculations.

5.1 Introduction

Interacting binary stars are believed to be responsible for astrophysical phenomena such as type Ia supernovae, Be X-ray binaries, compact object mergers and many more. Every interacting binary will undergo at least one mass-transfer episode, be it stable or unstable. The detailed mechanics of mass-transfer is in general poorly understood, with one of the greatest uncertainties coming from whether mass leaving the donor star is actually accreted by the accretor star, or whether that mass is ejected from the system. The mass-transfer efficiency affects both the mass-ratio and the orbital evolution of the system, possibly altering the final evolutionary outcome. Thus the properties of nearly all binary interaction products depend heavily on the assumed mass-transfer efficiency.

For binaries which undergo inefficient mass-transfer (other wise known as non-conservative), it is not known how much orbital angular momentum is removed from the binary by the ejected material. Many binary evolution calculations (e.g. de Mink, Pols and Hilditch 2007; Schootemeijer, Götberg et al. 2018; Langer et al. 2020; Sen et al. 2022) rely on the anisotropic fast-wind approximation (sometimes known as Jeans mass-loss), whereby ejected material carries the specific orbital angular momentum of the accretor (Soberman, Phinney and van den Heuvel, 1997). This approximation may be difficult to realise as a large amount of matter must acquire enough kinetic energy to escape the system without interacting with it. The luminosities of typical OB type stars might not always be capable of providing this energy, although another, unknown energy source could be involved. A more likely scenario would be that material floats around the system before eventually being ejected, interacting with both stars and exchanging energy and angular momentum with the orbit (Brookshaw and Tavani, 1993; MacLeod and Loeb, 2020).

Recently, Be-subdwarf binaries have received much attention as they can exhibit similar spectral properties to black-hole binaries (Abdul-Masih, Banyard et al., 2020). Unfortunately for those seeking black-holes, several candidate black-hole binary systems have turned out to contain a subdwarf instead of a black-hole (Shenar et al., 2020; Bodensteiner, Shenar, Mahy et al., 2020). A Be-subdwarf system consists of a more massive main-sequence star which is believed to have accreted mass and angular momentum, becoming a rapid rotator and thus a Be star, in orbit around a stripped, helium-burning companion. As mass-ratios are typically extreme (resulting in low radial velocity variations) and the stripped companions are often dim in visible wavebands, detection of subdwarves orbiting Be stars remains a challenge. Recently, several claims have been made that most Be stars might in fact host a hidden companion (El-Badry and Quataert, 2021) and more systems are being discovered thanks to dedicated searches (L. Wang, Gies and Peters, 2018; L. Wang, Gies, Peters et al., 2021).

In the Be-subdwarf phase, the orbital properties have mostly only been affected by mass-transfer (although stellar winds do remove mass and angular momentum, in B stars, their effects are negligible compared to mass-transfer episodes). During the mass-transfer episode, the accretor can be enveloped in an optically thick cloud (Broz et al., 2021), making direct observation difficult. Thus the Be-subdwarf systems, being the earliest evolutionary stage after mass-transfer in which both stars are visible, offer us an excellent opportunity to determine how the mass-transfer process governs binary evolution.

This work aims to confront observations of Be-subdwarf binaries with binary evolution calculations in order to constrain mass-transfer efficiency and angular momentum loss during mass-transfer episodes. Using parameters to describe mass-transfer efficiency and angular momentum loss, we determine the orbital evolution of binaries, tracking the masses of each component and the orbital periods. Stellar masses and orbital periods are compared to observations via a χ-squared statistic in order to determine the favoured mass-transfer parameters.

The observations are introduced in Section 5.2. Section 5.3 outlines our parametrisation of mass-transfer and explains the binary evolution calculations used. To determine the favoured mass-transfer parameters a comparison is made between the observations and evolutionary calculations in Section 5.4. Section 5.5 hosts a comparison with other studies. Suggestions for further lines of investigation and interpretation of the results are given in Section 5.6.

5.2 Observed systems

A literature review revealed around 25 known or suspected Be-subdwarf systems with determined periods, listed in Table 5.1. This number is increasing rapidly, and we may look forward to uncovering many more objects in the near future. There are several Be stars which are known to have subdwarf companions, but an orbit has not yet been determined (L. Wang, Gies and Peters, 2018; L. Wang, Gies, Peters et al., 2021; Klement, Schaefer et al., 2022).

Table 5.1 contains three stars which are strictly not confirmed Be-subdwarf systems, but are nevertheless interesting. We note that the nature of the companions of the γ Cas stars is unknown, although it has been argued that γ Cas stars are Be + white-dwarf systems (Gies, L. Wang and Klement, 2023). Regulus is a fast rotating B star (not Be) which is conjectured to have accreted material from the currently pre-white-dwarf companion (Gies, Lester et al., 2020). κ Dra. is a single lined spectroscopic binary in which the nature of the $0.8\,M_\odot$ component (Saad et al., 2005) remains unknown, with no hot companion reliably detected (L. Wang, Gies and Peters, 2018) and a white-dwarf companion remaining a possibility. 66 Oph is a B2Ve star in a wide and eccentric orbit with a $3\,M_\odot$ object Hutter et al. (2021) whose nature is poorly understood. The unknown object appears itself to be a double-lined spectroscopic binary with a 10 day period (Stefl, Hadrava et al. 2004 J. Bodensteiner priv. communication). A subdwarf was not detected in the system (L. Wang, Gies and Peters, 2018), leaving two open possibilities: the system contains a black hole, or is a Be star orbiting an inner binary. Both scenarios are indeed exciting. In the case that the companion is itself a close binary (which must consist of two main-sequence stars due to the short period) this system would be one of the first known binaries containing a Be and main-sequence star, providing the "smoking gun" for Be production channels involving single star evolution (Bodensteiner, Shenar and Sana, 2020).

To determine binary component masses, the most common approach takes advantage of periodic Doppler shifts in spectral lines. These shifts are produced by the orbital motion of the stars and yield a velocity semi-amplitude that represents the largest velocity of the star along the line of sight. That Doppler shift only reveals velocities along the line of sight means that only the star's orbital velocity multiplied by the sine of the orbital inclination to the line of sight can be measured. The orbital inclination is generally unknown, meaning that only the ratio of component masses may be determined by radial velocity variations. To circumvent this problem, the mass of the brightest star, ie. the Be star, is often estimated from its spectral type (e.g. Shenar et al. 2020). Be stars are spectrally atypical owing to their fast rotation causing blending of spectral lines, a reduction of the surface gravity and effective temperature (von Zeipel, 1924) and light contribution from the Be disc all resulting in equivalent mass B and Be stars having different spectra. These effects thus make determination of a Be star's mass from its spectral type more complex than has been accounted for.

Another, more quantitative approach is to compare derived effective temperature and luminosity of the Be star with

Name	$M_{Be}/M_\odot$	$M_D/M_\odot$	period/days	Notes	Ref.
SAO 49725	13	0.2-0.5	26.11	γ Cas. star	Nazé et al. (2022)
59 Cyg	6.3-9.4	0.6-0.9	28.2		Peters, Pewett et al. (2013)
O Pup	11-15	0.7-1.0	28.9		Koubský, Kotková, Votruba et al. (2012)
Fy CMa	10-13	1.1-1.5	37.3		Peters, Gies et al. (2008)
Regulus	3.7 ± 1.4	0.31 ± 0.10	40.11	fast rotator, not Be. Donor pre-WD	Gies, Lester et al. (2020)
HR 6819	$6.7^{+1.9}_{-1.5}$	$0.47^{+0.28}_{-0.22}$	40.3		El-Badry and Quataert (2021)
κ Dra	4.8 ± 0.8	0.8	61.52	subdwarf not detected (L. Wang, Gies and Peters, 2018)	Saad et al. (2005)
V2119 Cyg	8.65 ± 0.35	1.62 ± 0.28	63.146	Interferometrically observed	Klement, Schaefer et al. (2022)
V810 Cas	12.5	0.7-0.8	75.8	γ Cas. star	Nazé et al. (2022)
LB-1	7 ± 2	1.5 ± 0.4	78.8		Shenar et al. (2020)
HR 2142	10.5	0.7	80.9		Peters, L. Wang et al. (2016)
V558 Lyr	8	0.7-0.8	83.3	γ Cas. star	Nazé et al. (2022)
π Agr	15	2.4 ± 0.5	84.1	γ Cas. star	K. S. Bjorkman et al. (2002)
HD 55606	6.0-6.6	0.83-0.9	93.8		Chojnowski et al. (2018)
HD 161306	15	0.9	99.9		Koubský, Kotková, Kraus et al. (2014)
HD 45995	10	1.0 ± 0.1	103.1	γ Cas. star	Nazé et al. (2022)
V782 Cas	9	0.6-0.7	122.0	γ Cas. star	Nazé et al. (2022)
V2156 Cyg	11	0.7-0.8	126.6		Nazé et al. (2022)
Φ Per	9.6 ± 0.3	1.2 ± 0.2	126.70	Interferometrically observed	Mourard et al. (2015)
ζ Tau	11	0.9-1.0	133.0		Ruzdjak et al. (2009)
ξ Oph	10	1.7-2.0	138.8		Abt and Levy (1978)
60 Cyg	7.3 ± 1.1	1.2 ± 0.2	147.68	Interferometrically observed	Klement, Schaefer et al. (2022)
γ Cas	13	0.98	203.6	γ Cas. star	Nemravová et al. (2012)
66 Oph	9.6	3.4	23421.1	eccentric orbit	Hutter et al. (2021)
7 Vul	6 ± 1	0.6 ± 0.1	63.42		Harmanec et al. (2020)

Table 5.1: Properties of Be-subdwarf systems with determined orbits in order of increasing period. Note the subdwarf status of some companions is uncertain, see text for details. The orbital periods have negligible uncertainties, typically less than 0.01 days. We note that the nature of the companions of the γ Cas. stars is unknown.

evolutionary models in the Hertzsprung-Russell diagram (e.g. El-Badry and Quataert 2021). However, this is also not without its problems. In addition to those mentioned above, the location of a fast rotating star in the Hertzsprung-Russell diagram depends on the angle at which the rotation axis is oriented to the observer. The centrifugal force is strongest at the stellar equator, causing the equatorial effective surface gravity to be weaker. Weaker gravity results in a cooler local effective temperature, and hence a dimmer equator via the von Zeipel theorem (von Zeipel, 1924). This effect is known as gravity darkening and causes rotating stars viewed pole-on to appear brighter and hotter than those viewed equator-on. At near-critical rotation, the location of a star in the Hertzsprung-Russell diagram (cf. Fig. 38 of Paxton, Smolec et al. (2019) or colour-magnitude diagram (cf. Fig. 4 of D'Antona et al. 2015) is strongly dependant on the inclination angle. Without knowing the inclination angle of a Be star, it becomes very difficult to assign an evolutionary mass. A third method is to use functions which predict mass and radius from effective temperature that have been calibrated using eclipsing binaries (Harmanec, 1988; Koubský, Harmanec et al., 2000). However this also suffers from the issues brought about by fast rotation discussed previously.

Far stronger constraints of stellar masses can be provided by combining spectroscopic and interferometric observations. An interferometer reveals an object's 2-dimensional motion as projected on the sky, whereas spectroscopic observations give the motion perpendicular to the sky. Thus by levering both techniques, the movement of a binary component can be traced in 3-dimensions and dynamical masses can be measured using Kepler's laws. To date, this has been done for 3 Be-subdwarf systems: Φ Per (Mourard et al., 2015), 60 Cyg (Klement, Schaefer et al., 2022) and V2119 Cyg (Klement, Schaefer et al., 2022).

It is telling to note that for 60 Cyg, the Be star's dynamical mass was measured to be $7.3 \pm 1.1\,M_\odot$ (Klement, Schaefer et al., 2022). While Koubský, Harmanec et al. (2000) had found that by using the effective temperature of the star to determine the mass, one arrives at a value of $11.8\,M_\odot$. The discrepancy between these two measurements serves to emphasise the difficulty in estimating a Be star's mass. This work shall therefore focus on the 3 systems which have been observed interferometrically as the resulting masses are deemed to be more accurate than measurements made using surface properties (spectral type, luminosity and effective temperature).

5.3 Method

5.3.1 Mass-transfer parameters

In order to quantify mass-transfer efficiency and angular momentum loss, we define a parameter for each respectively. We term the mass-transfer efficiency β, and let the rate of mass gain of the accretor, $\dot{M}_A$ be related to the rate of mass loss of the donor, $\dot{M}_D$ through

$$\dot{M}_A = -\beta \dot{M}_D. \tag{5.1}$$

Note that by definition the donor's rate of change of mass is negative. Conservative mass-transfer is thus described by $\beta = 1$, while fully non-conservative mass-transfer is given by $\beta = 0$.

In (partly) non-conservative binary evolution, mass is lost from the system, and this mass must also remove orbital angular momentum. To describe the loss of orbital angular momentum, we assume that mass leaving the system carries away the specific angular momentum of a massless particle which is located along the line joining the two centre of masses of the stars and a distance r_{ej} from the system's centre of mass. This geometry is sketched in Fig. 5.1. The specific angular momentum of ejected material, j is then given by

$$j = r_{\text{ej}}^2 \omega, \tag{5.2}$$

where ω is the orbital frequency of the binary.

We define the angular momentum loss parameter γ as the distance r_{ej} normalised by the distance from the binary centre of mass to the accretor centre of mass, r_A, as

$$\gamma = \frac{r_{\text{ej}}}{r_A} = \frac{r_{\text{ej}}(M_D + M_A)}{a M_D}, \tag{5.3}$$

with a representing the orbital separation and M_D, M_A the donor and accretor masses respectively. The parameter γ is designed that $\gamma = 1$ corresponds to the isotropic reemission model, whereby material is ejected as a fast isotropic wind from the surface of the accretor. Using the definition of γ, the specific angular momentum of ejected material becomes

$$j = \gamma^2 a^2 \left(\frac{M_D}{M_D + M_A} \right)^2 \omega. \tag{5.4}$$

For an assumed mass-transfer efficiency, the orbital angular momentum loss rate, $\dot{J}$, after applying Kepler's third law to eliminate the dependency on the orbital period ω becomes

$$\dot{J} = \dot{M}_D (1 - \beta) \gamma^2 (Ga)^{\frac{1}{2}} M_D^2 \left(M_D + M_A \right)^{-\frac{3}{2}}. \tag{5.5}$$

An upper limit for γ is given by considering that a co-rotating particle lying outside of the second Lagrangian point will be ejected from the binary, hence the second Lagrangian point represents the maximum specific angular momentum loss possible. For an equal mass binary, the centre of mass is located halfway between the two stars, i.e. $r_A = 0.5a$ and the second Lagrangian point is approximately $1.7a$ from the donor's centre of mass. This means that the γ value associated with the second Lagrange point is $(1.7 - 0.5)/0.5 = 2.4$. This is taken to be the maximum realistic value of γ. A particle leaving the system must remove some angular momentum, so the lower limit for γ is 0.

5.3.2 Extremely rapid binary evolution

We aim to determine the mass-transfer parameters that best reproduce observed masses and orbital periods of observed Be-subdwarf binaries. To this end, we need only follow the evolution of the binary component masses and orbital angular momentum, which can be done using an "extremely rapid" binary evolution model. An example of an extremely rapid binary evolution calculation is given in Appendix A. The philosophy is that for any binary system with given initial component masses and initial orbital period and assuming fixed mass-transfer parameters, one can calculate the orbital evolution of the system during mass transfer without solving any stellar structure equations. To achieve this, we must make several simplifying assumptions.

Firstly we assume that the donor star loses its entire hydrogen envelope, leaving behind a helium core whose mass is the helium core mass of an equivalent mass single star at the terminal-age-main-sequence. For Case B mass-transfer (where
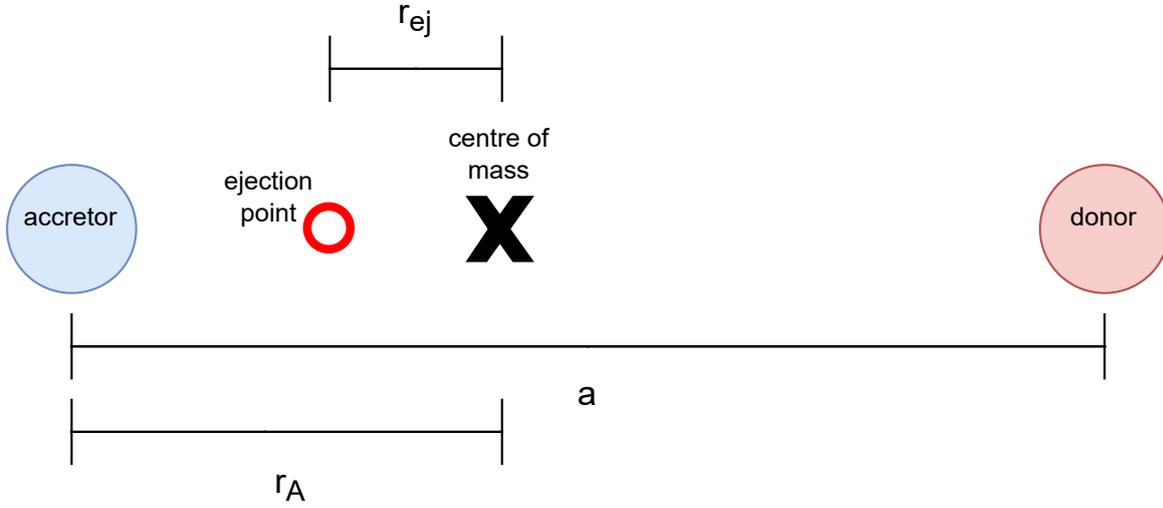
Figure 5.1: Illustration of the geometry of a binary system. The centre of mass is depicted by a black cross, the accretor and donor are shown as discs (labelled respectively). Mass is assumed to be ejected without ineracting with the binary from the ejection point, depicted by a red circle. The orbital separation is marked as a.

the donor has depleted its supply of core hydrogen), this is a good approximation. Whereas for Case A (where the donor is still core hydrogen burning), the core mass may be slightly underestimated, as during the stripping of the donor, the hydrogen burning core recedes. We rely on numerical models calculated using MESA (Paxton, Smolec et al., 2019) to relate a star's initial mass to its terminal-age-main-sequence helium core mass, with the resulting relationship given in Fig. 5.2. The models are identical to those of Schootemeijer, Langer et al. (2019) with overshooting parameter α_{OV}=0.335, semi-convection parameter α_{SC}=1 and no rotation, but computed with galactic metallicity as set out in Brott, de Mink et al. (2011).

Secondly we assume that the both evolution of stellar masses and the orbital period is only affected by the mass-transfer episode. In reality stellar winds also play a role, however for B-type stars, winds are typically weak and the dominating process acting on the binary is certainly mass-transfer. Lastly, the binaries are assumed to have a circular orbit at all times and each star is modelled as a point mass.

For a binary with given initial donor mass $M_{D,i}$, initial accretor mass $M_{A,i}$, initial orbital period p_i and mass-transfer parameters β and γ, the initial orbital angular momentum is

$$J_i = \left(\frac{G^2}{2\pi}\right)^{\frac{1}{3}} M_{A,i} M_{D,i} \left(M_{D,i} + M_{A,i}\right)^{-\frac{1}{3}} p_i^{\frac{1}{3}}. \tag{5.6}$$

From the initial donor mass, the donor mass at the end of mass-transfer is given by Fig. 5.2. A numerical integration is carried out where the donor mass is decreased step-wise by dm, causing the accretor mass to increase by βdm. Consequently the orbital angular momentum decreases by dj,

$$dj = dm(1 - \beta)\gamma^2 (Ga)^{\frac{1}{2}} M_D^2 \left(M_D + M_A\right)^{-\frac{3}{2}}, \tag{5.7}$$

where the orbital separation, a, is found using Kepler's third law.

The process continues until the donor mass prescribed by Fig. 5.2 is attained. For the value of dm, 0.001 $M_\odot$ is chosen. In this way for chosen initial parameters, we can calculate the component masses and the orbital period after mass-transfer has stripped the donor of its hydrogen envelope.
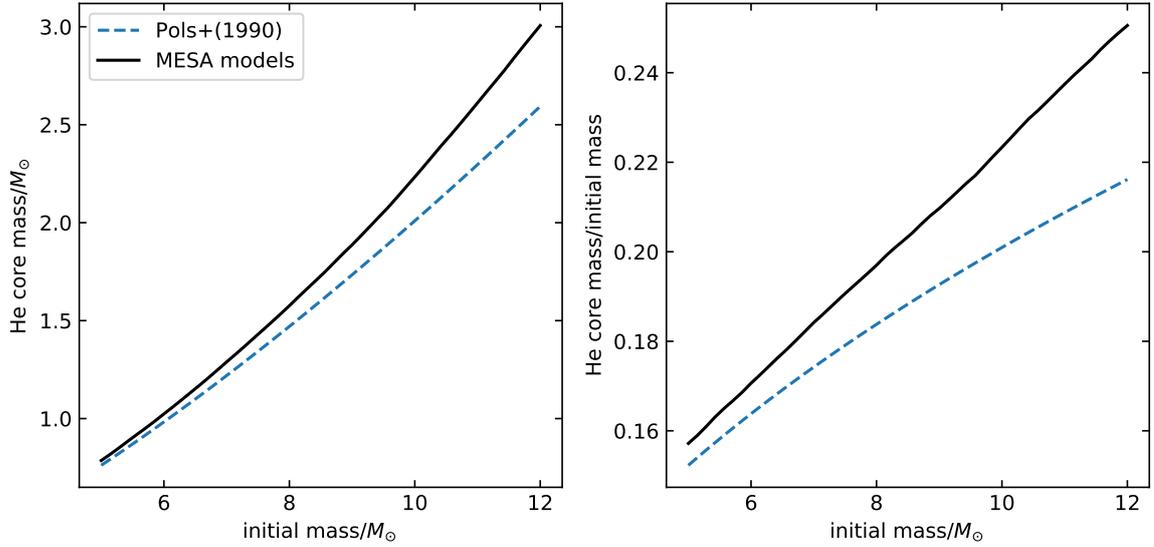
Figure 5.2: Left panel: helium core mass at terminal-age-main-sequence as a function of initial mass for our MESA models (black line) and the relation given by Pols et al. (1991b) with no overshooting (blue dashed line). Right panel: ratio of helium core mass at terminal-age-main-sequence to initial mass as a function of initial mass.

5.3.3 Merger criteria

For mass-transfer to remain stable, the accretor star must remain in thermal equilibrium while accreting. If the mass-transfer rate is too high, the accretor will not be able to accept material and a common envelope situation will ensue. We shall assume that common envelope evolution will always lead to a merging of the two stars. To assess whether stable mass-transfer occurs, we compare the stars' thermal timescales to one another. The thermal timescale for a star of mass M, radius R, luminosity L is

$$\tau_{\rm th} \propto \frac{GM^2}{RL}.$$

(5.8)

We define the thermal mass change rate as

$$\dot{M}_{\rm th} = \frac{M}{\tau_{\rm th}}.$$

(5.9)

To assess the stability of mass-transfer we must compare the thermal mass change rate of the accretor to the rate at which material is deposited onto the accretor. To this end, we define K as the ratio of the donor and accretor thermal mass change rates, factoring in the mass-transfer efficiency like

$$K = \beta \frac{\dot{M}_{\rm th,D}}{\dot{M}_{\rm th,A}}.$$

(5.10)

We assess this ratio at the initiation of mass transfer, ie. the first point at which the donor fills its Roche lobe. For a given binary system, the volume-equivalent radius of the donor's Roche lobe, R_L, is calculated as (Eggleton, 1983)

$$R_L = a \frac{0.49 \left(M_D/M_A\right)^{2/3}}{0.6 \left(M_D/M_A\right)^{2/3} + \ln\left(1 + \left[M_D/M_A\right]^{1/3}\right)}.$$

Using our single star models, we find the properties of both the donor and accretor at the time when the donor's radius is R_L.

94
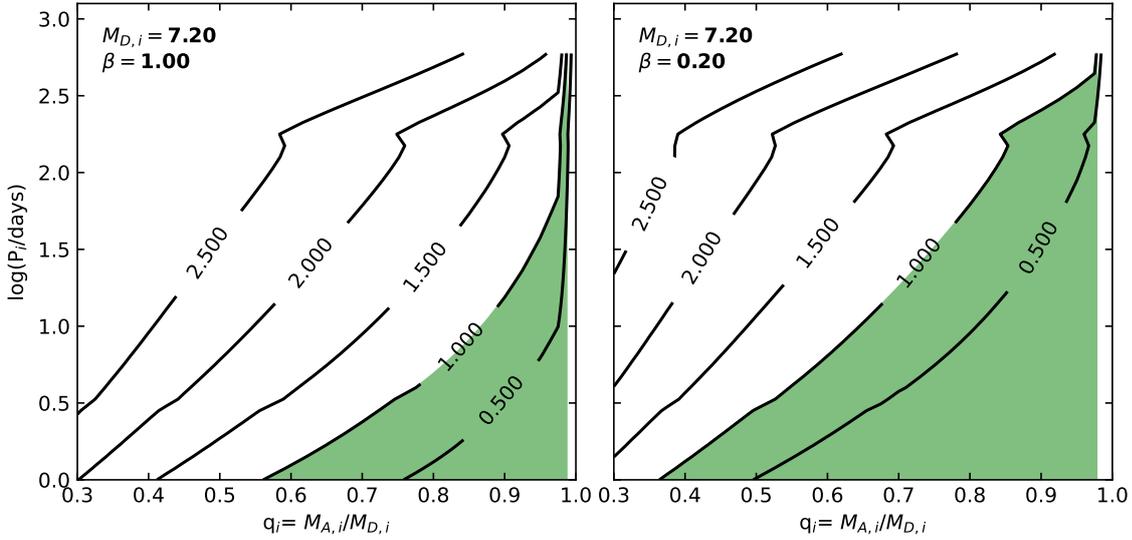
Figure 5.3: Contours of the logarithm of thermal mass change ratio as given by Eq. 5.10 as a function of initial mass-ratio, q_i, and initial period, P_i for systems with initial donor mass of $7.2\,M_\odot$. Contour values are labelled on the plot. Left panel shows conservative mass-transfer ($\beta = 1$). Right panel shows non-conservative mass-transfer ($\beta = 0.2$). The green region shows systems with thermal mass change ratios less than 10, which are assumed to undergo stable mass-transfer.

With these values, we calculate the ratio of thermal mass change rates for the binary. At the onset of mass-transfer, the donor is more luminous and has a larger radius and hence a larger thermal mass change rate than the accretor. Thus the ratio given in Eq.5.10 is greater than unity. We judge a merger to occur when the donor's thermal mass change rate exceeds 10 times that of the accretor's, ie. a merger occurs where $K > 10$.

Figure 5.3 shows contours of constant values of the thermal mass change ratio, with systems assumed to undergo stable mass-transfer marked in green. We see that the region of stability extends towards lower periods and equal mass-ratios. This is because the thermal timescale is inversely proportional to the radius, so for wider binaries, the donor has a larger radius at the start of mass-transfer, meaning the mass-transfer rate is higher meaning the mass-transfer is more likely to be unstable. Similarly equal mass-ratios are preferred due to the steep mass-luminosity relationship causing the accretor's thermal mass change rate to become ever lower as the mass-ratio decreases.

We note that the picture of accretor limited mass-transfer presented here is not the only criteria that can be employed. One may also examine the donor's response to being stripped (Soberman, Phinney and van den Heuvel, 1997; Hurley, Tout and Pols, 2002; Eldridge et al., 2017). A further alternative is to consider whether enough energy exists in the system to eject material during non-conservative mass-transfer (Marchant, 2017b; Langer et al., 2020).

5.3.4 Goodness of fit test

To find the preferred mass-transfer parameters, we use a χ^2 statistic, which measures the deviation of observed parameters, O_i, to expected parameters, E_i, as

$$\chi^2 = \sum^i \frac{(O_i - E_i)^2}{\sigma_i^2},$$ (5.11)

with σ_i being the observational uncertainty. For this work the three observed parameters are the Be star mass, subdwarf mass and orbital period of a Be-subdwarf binary.

The expected values are calculated from a grid of extremely rapid binary evolution models with initial donor masses in range 7-10.5 $M_\odot$ with spacing 0.1 $M_\odot$, initial mass ratios in range 0.1-1 with steps of 0.025 and initial periods in range

1-1000 days with logarithmic steps of 0.075 dex. Mass-transfer parameters considered are β ranging from 0.1 to 0.9 in steps of 0.1 and γ from 0 to 2 in steps of 0.25. This results in a grid of 4.4 million individual systems. Our calculations are compared with three binaries, as justified in Sec. 5.2; V2119 Cyg, Φ Pers and 60 Cyg. To avoid an extreme dependance of our results on the orbital period, we use a relative uncertainty of 10% for the orbital period, in line with the relative uncertainties for the star masses.

5.4 Results

5.4.1 Parameter trends

Figure 5.4 shows χ^2 values for individual systems calculated with the observed parameters of Φ Pers assuming an initial donor mass of $7.0\,M_\odot$ and four combinations of mass-transfer parameters. We see that near-conservative mass-transfer ($\beta = 0.9$) favours more extreme initial mass-ratios, while non-conservative evolution ($\beta = 0.5$) finds the best solutions have larger initial mass-ratios. This is because in conservative evolution, the mass of the accretor increases, so to match the current mass of the Be star in Φ Pers, the accretor must have a lower initial mass, resulting in a low initial mass-ratio value. For non-conservative evolution, the accretor mass does not change (or at least not as much), hence the accretor must be born close to its current mass and the initial mass-ratio must be more equal.

The angular momentum loss parameter, γ, affects only the final periods of systems, and naturally has little to no effect on conservative mass-transfer. When angular momentum loss in increased, the best fitting systems are forced to longer initial periods, as more initial angular momentum is needed to match the observed period. In this way the angular momentum loss tunes the initial period required to explain the observed period of the binary.

In Fig. 5.4 we see that for near-conservative mass-transfer ($\beta = 0.9$), the best fitting systems have initial mass-ratio of approximately 0.6 and initial periods around 10 days, in good agreement with Schootemeijer, Götberg et al. (2018). However, these best fitting systems are not expected to undergo stable mass-transfer, as they have relatively extreme mass-ratios, resulting in a large discrepancy in the thermal timescales of the donor and accretor. Therefore we conclude that for Φ Pers, conservative evolution is unlikely. For non-conservative mass-transfer, systems with larger initial mass-ratios produce better χ^2 statistics. Importantly, the best solutions are now inside the region of stable mass-transfer, and are deemed viable.

In the non-conservative case, angular momentum loss causes a shift in the initial periods of the best solutions, with large angular momentum loss demanding longer initial periods (ie. more initial angular momentum) to match the observed period of the system. Fig. 5.5 shows χ^2 values for V2119 Cyg. For non-conservative evolution ($\beta = 0.4$), we see that when angular momentum loss is high ($\gamma = 2.0$), the best fitting solutions are raised to higher initial periods, outside of the region of stable mass-transfer. While for lower angular momentum loss ($\gamma = 0.5$), the best solutions lie comfortably inside the boundary for stable mass-transfer.

Figures 5.4 and 5.5 show that the merger criteria have a large impact on determining the initial parameters of Be-subdwarf systems. The occurrence of mergers in the parameter space is sensitive to both mass-transfer efficiency and angular momentum loss. It is therefore of crucial importance that the merger criteria are well understood.

5.4.2 Favoured parameters

From our grid of calculations, we would like to uncover the mass-transfer parameters which produce the best fits to the observations. In order to achieve this, we must take care in designing a metric to select the favoured parameters. The simplest metric would be to take the parameters of the best fitting model for each system. However, for each observed system, approximately half of the mass-transfer parameter combinations have a χ^2 value of less than 3 (meaning that, on average, each prediction agrees to the observation within the uncertainty). For each system, the lowest χ^2 value is of the order 10^{-3}, so our results may be over-fitted if we simply select models with the lowest χ^2 values and will certainly depend on the model grid spacings.

Instead, we propose to use the fraction of models which agree with the observed values to within the observational error, such that they have χ^2 values for each individual parameter being less than 1 (ie. $\chi_i^2 < 1$). In an conceptual sense, this metric measures how large the island of good solutions is compared to the parameter space. We do not count any models that are deemed to undergo unstable mass-transfer, as outlined in Sec. 5.3.3, in the fraction of models with a good agreement to the observations. The goodness of fit according to this metric is shown in Fig. 5.6 for each of the three systems.

We shall discuss the results of each system individually, starting with ϕ Pers The current subdwarf mass of $1.2\,M_\odot$ suggests an initial donor mass of around $7\,M_\odot$ (see Fig. 5.2). The current Be star mass of $9.6\,M_\odot$, rules out totally non-conservative mass-transfer as the accretor must be initially less massive than the donor, which is not possible if
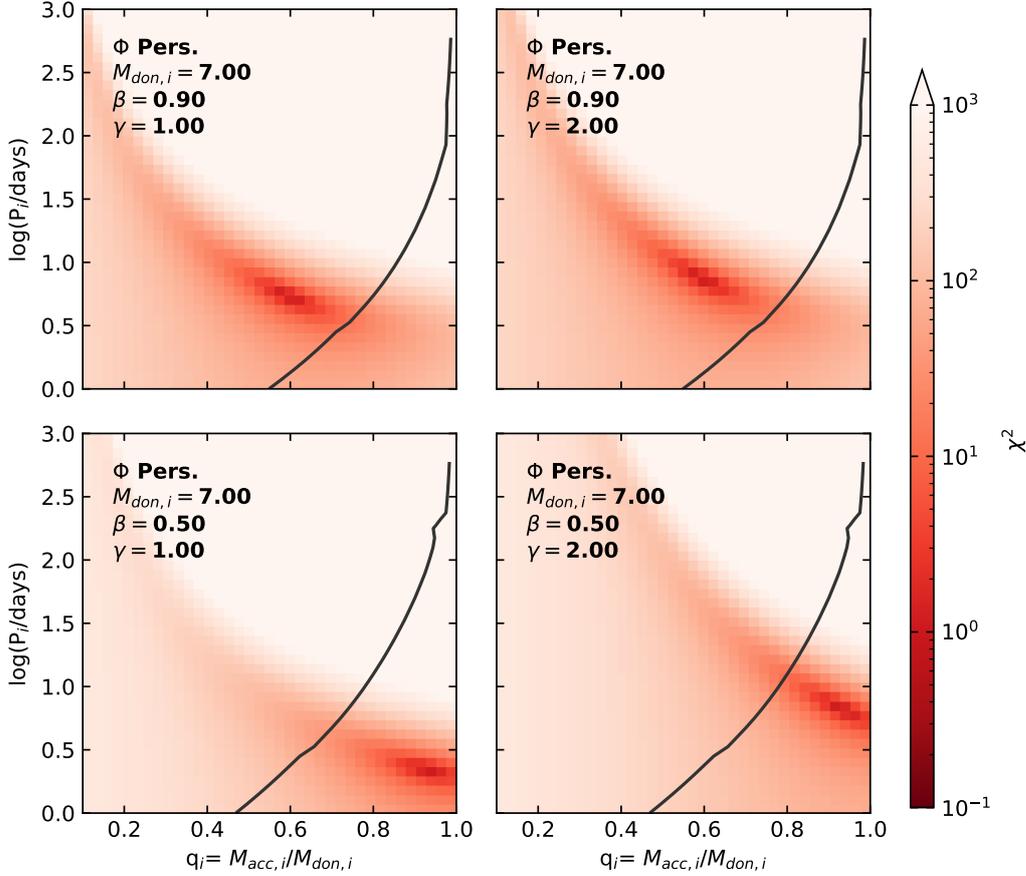
Figure 5.4: χ^2 values for Φ Pers as a function of initial mass ratio, q_i and initial period, P_i, for varying mass-transfer efficiency, β, and angular momentum loss parameter, γ as given in the plots. In all panels the initial donor mass is $7.0\,M_\odot$. The grey line depicts binaries whose thermal mass change ratio as given by Eq. 5.10 is 10. Only systems to the right of this line are assumed to undergo stable mass-transfer.

the Be star had not accreted any material. Thus the rather extreme mass-ratio of ϕ Pers, $M_D/M_{Be} = 0.125$, rules out non-conservative mass-transfer. Fig. 5.6 therefore shows that for ϕ Pers, there are no models that fit the observations well with mass-transfer efficiencies less than 0.3. We find that near conservative mass-transfer is also unlikely, as to match the current binary parameters, the initial mass-ratio must be small (that is the accretor must have a low initial mass), such that the thermal timescales of the donor and accretor have a large discrepency and mass-transfer is unlikely to be stable as argued in Sec. 5.3.3. We thus see that the favoured mass-transfer efficiencies are in the range 0.4-0.6. We see a preference for γ values below 1.0. This is due to the fact that long initial periods are required if angular momentum loss is high and that the parameter space for stable mass-transfer narrows at longer periods (see Fig. 5.3), meaning more systems merge when angular momentum loss is high.

60 Cyg has a similar orbital period and subdwarf mass to ϕ Pers, but a significantly lower Be star mass of $7.2\,M_\odot$, resulting in a mass-ratio $M_D/M_{Be} = 0.164$. This opens the possibility of 60 Cyg having evolved partially non-conservatively. The same arguments as for ϕ Pers disfavour fully conservative evolution. For 60 Cyg we judge the mass-transfer efficiency to be around 0.2-0.3. 60 Cyg shows best fitting γ values of around 0.25.

The final system considered, V2119 Cyg has a Be star mass of $8.65\,M_\odot$ that sits between the two others. The subdwarf residing in V2119 Cyg is the most massive of our systems, with a mass of $1.62\,M_\odot$. The mass-ratio then becomes $M_D/M_{Be} = 0.187$, the largest of the three systems. Again, because of the merger criteria, few good solutions are found for near conservative evolution. The relatively large mass-ratio allows non-conservative evolution. As such the likely
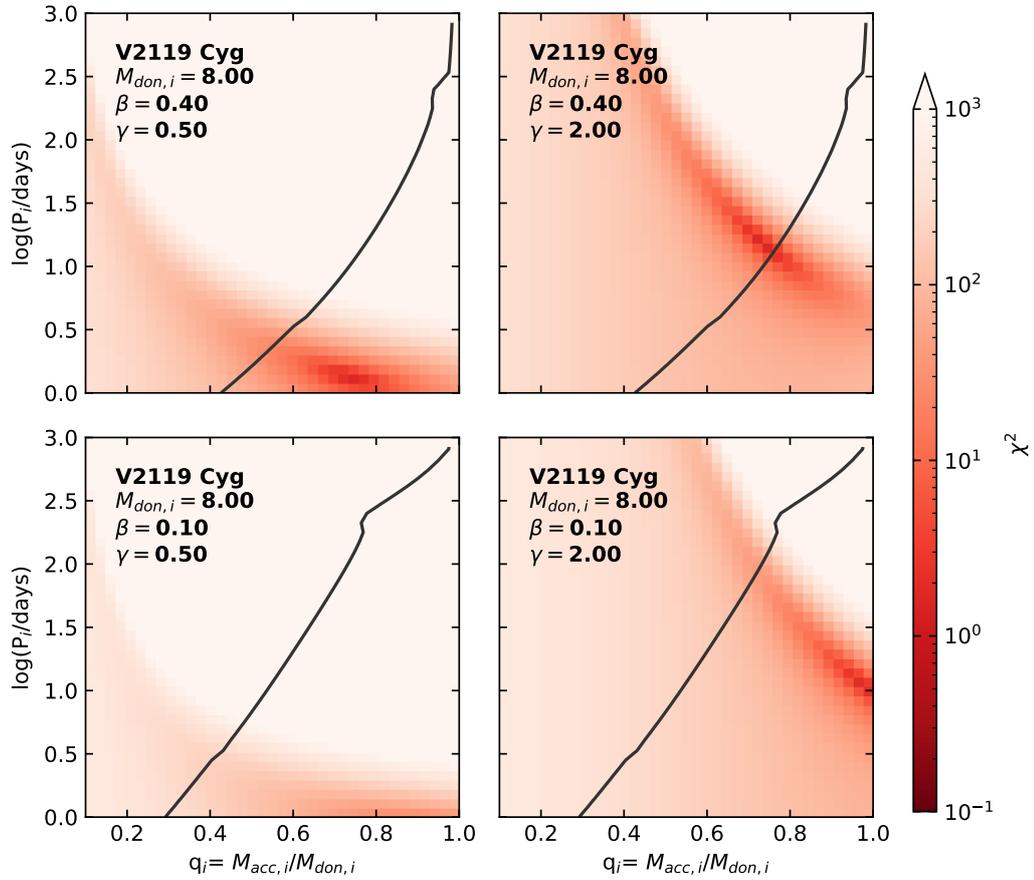
Figure 5.5: χ^2 values for V2119 Cyg as a function of initial mass ratio, q_i and initial period, P_i, for varying mass-transfer efficiency, β, and angular momentum loss parameter, γ as given in the plots. In all panels the initial donor mass is $8.0\,M_\odot$. The grey line depicts binaries whose thermal mass change ratio as given by Eq. 5.10 is 10. Only systems to the right of this line are assumed to undergo stable mass-transfer.
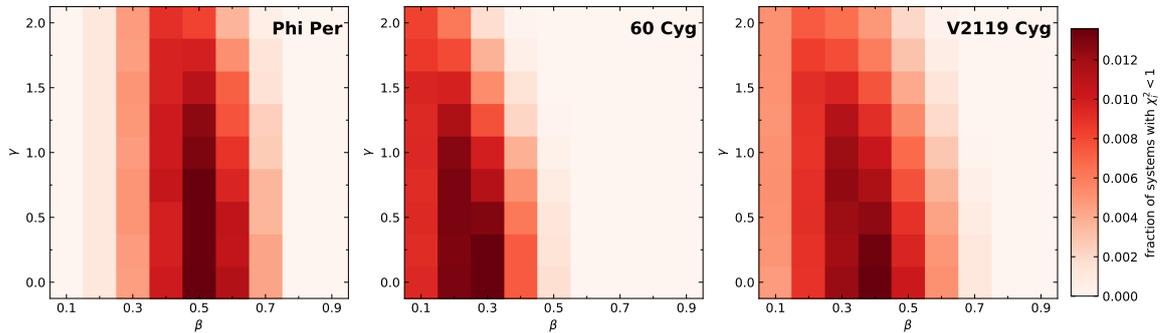
Figure 5.6: Fractions of models that fit the observational parameters to within the observational errors as a function of mass-transfer efficiency, β, and angular momentum loss, γ. Each panel represents a different Be-subdwarf binary as given in the plot.

mass-transfer efficiency values lie in the range 0.3-0.5. Similarly to 60 Cyg, V2119 Cyg displays best fitting γ values below 0.5.

It is interesting to note that our three systems seem to fall into two categories: those who show evidence of more conservative mass-transfer ($\beta \sim 0.5$) and larger angular momentum loss ($\gamma \sim 1.0$), and those with lower mass-transfer efficiencies ($\beta < 0.4$) and lower angular momentum loss ($\gamma < 0.5$). This may be due to physical processes, for example case A and case B mass-transfer. Our limited sample of observed systems prohibits further investigation, but future study may confirm or deny this perceived bimodality.

Generally, we see that moderate mass-transfer efficiencies of around 30-50% are preferred. Angular momentum loss is predicted to be weaker than that of a fast wind blown from the accretor (ie. $\gamma < 1.0$).

5.5 Comparison with other works

Several efforts have been made to determine mass-transfer efficiency by confronting theoretical models to observations. Here, a comparison shall be made between these works and the results presented here.

Petrovic, Langer and van der Hucht (2005) focussed on Wolf-Rayet + O-star binaries, which are significantly more massive than Be + subdwarf binaries but are otherwise in a comparable evolutionary phase as Be + subdwarf systems. The binaries were modelled using three different methods of varying sophistication, each supporting the conclusion that mass-transfer efficiency is about 10%. The third method of Petrovic, Langer and van der Hucht (2005) limited accretion based on the spin of the accretor star. Initially the binaries were modelled assuming efficient mass-transfer and that when the accretor attains critical velocity, mass-transfer effectively becomes totally non-conservative. Material is assumed to be ejected from the surface of the accretor as a fast wind (corresponding to $\gamma = 1$ in this work). This is a parameter-free prescription that can naturally produce a range of mass-transfer efficiencies owing to the effect of tides or strong winds retarding the spin-up of the accretor. For wide systems, where tides have minimal impact, the mass-transfer efficiency is typically less than 10% owing to the efficient accretion of angular momentum (Packet, 1981). Two of the three Wolf-Rayet + O-star systems studied by Petrovic, Langer and van der Hucht (2005) could be explained well by this model of mass-transfer. This same prescription can describe the observed periods and mass-ratios of massive Algol binaries well, but is not so successful with lower mass systems (Sen et al., 2022). It may not be surprising that the mass-transfer efficiencies of very massive systems ($M > 30\,\mathrm{M_\odot}$) differ to the less massive systems ($M \approx 10\,\mathrm{M_\odot}$) considered in this work, owing to the presence of many energetic particles surrounding very massive stars.

Through studying massive contact binaries, with component masses in the range 1-35 $\mathrm{M_\odot}$, de Mink, Pols and Hilditch (2007) conclude that "no single value of mas-transfer efficiency (β) can explain all systems". Concerningly, it is found that "a large fraction of the semi-detached systems cannot be fitted well with any assumption for the mass transfer efficiency". de Mink, Pols and Hilditch (2007) found evidence that initially wider systems tend to fit better to less conservative models, supporting the scenario where accretion is limited by the accretor's spin.

In the Small Magellanic Cloud, the spectral type distribution of Be stars in Be-Xray binaries seems to differ to that of apparently single Be stars. That no Be-Xray components later than around spectral type B5 exist, suggests that these stars have all accreted significant amounts of matter, thus explaining the lack of early stars. A population synthesis study determined that the properties of the Be-Xray binaries are best matched by an accretion efficiency greater than 30% (Vinciguerra et al., 2020). This finding is in broad agreement with this work, which finds mass-transfer efficiencies in the range 30-50%.

Phi Pers was analysed using the rapid binary evolution code binary_c by Schootemeijer, Götberg et al. (2018), who argued that the system must have evolved through near-conservative mass-transfer, in contrast to the results presented here. The difference lies in the merger criteria. In binary_c a system merges when the donor is unable to retreat inside its Roche lobe. We find a good agreement with Schootemeijer, Götberg et al. (2018) if we assume that no systems merge. However, when our merger criteria is applied (see Sec. 5.3.3), many of the conservative models are predicted to merge. This is because to match the current system mass, a conservative model must have a rather unequal mass-ratio, which in turn leads to a large difference between the thermal timescales of accretor and donor, making accretion unstable. This indicates the sensitivity of our results, and of binary evolution in general, on the conditions required for mergers.

5.6 Conclusions

The extremely rapid binary evolution calculations used here are designed to compute the orbital properties of binaries over a very large parameter space, and accordingly are missing some detailed physics such as the effects of tides and stellar

winds on the angular momentum content of the binary and its components. Furthermore, it is assumed that a donor is always stripped to its bare helium core, which may not be accurate for case A systems, where the growth of the helium core is affected by the stripping of the star. Lastly, as the radii of the stars are not computed, our scheme here does not consider systems where the orbit narrows so much during mass-transfer that the stars merge. These shortcomings can be circumvented by the use of a detailed binary evolution code. The extremely rapid calculations provide the approximate behaviour of binary systems, and only certain promising systems need to be followed up with detailed calculations, reducing the parameter space significantly.

For the time being, insights into mass-transfer efficiency and angular momentum loss must be made through direct comparison to observations. In this regard, we may look forward to more Be + stripped star systems being identified, as well as further interferometric observations being made. As discussed in Sec. 5.2, current mass estimates of Be stars suffer from distinct inaccuracies, which may be overcome in the future. The surface properties of a Be star can be very different to the surface properties of a "normal", slowly rotating B star of the same mass due to the effects of gravity darkening, light from the decretion disc and potentially rotational mixing and mass accretion. As all of these effects can at present be modelled, it is entirely possible that the mapping between spectral type and mass may be updated for Be stars, incorporating the mentioned effects. This would allow for more reliable mass estimates for Be stars, as well as fast rotating stars in general.

The results presented in this work favour intermediate mass-transfer efficiencies (around 50%) and weak angular momentum loss compared to a fast wind lost from the accretor ($\gamma < 1.0$). In light of this, current binary evolution models, which typically model non-conservative mass-transfer as a fast wind blown from the accretor (ie. $\gamma = 1$) may need to be refined. Arguments relating the available energy (presumed to be the stellar luminosity) for accelerating a fast wind to the energy required to overcome the gravitational potential of the binary, reveal that it is unlikely that two B stars can eject the amounts of material demanded by binary evolution calculations as a fast wind. A more realistic scenario is that the wind is much slower, and because of that trades energy and angular momentum with the binary before eventually leaving the system. Work on such cases has been made, showing that angular momentum loss can be reduced compared to the fast wind model (Brookshaw and Tavani, 1993; MacLeod and Loeb, 2020).

Current models limit the accretion of material once critical rotation of the accretor is achieved, typically resulting in very low (less than 10%) mass-transfer efficiencies. A key assumption of these models is that material is accreted from a Keplerian accretion disc. For a sub-critically rotating star, there exists a sharp discontinuity in angular velocity between the stellar surface and the inner edge of a Keplerian accretion disc. It may be reasonable to assume that this discontinuity is unphysical in an accreting star, as magnetic interactions could remove angular velocity gradients between the star and the inner disc (just like they do inside the star itself Spruit 2002). Employing a "no slip" boundary condition between angular velocity of the star and inner accretion disc would reduce the specific angular momentum of accreted material, meaning that more mass can be transferred before critical rotation is reached and non-conservative evolution ensues. This would naturally increase the mass-transfer efficiency, perhaps in line with the results presented here.

Appendix

A Extremely rapid binary evolution code example

The Python code below details how an extremely rapid binary evolution code calculates the orbital evolution of a binary system.

```python
from __future__ import division
import numpy as np
import pandas as pd

#some constants in cgs units
G=6.6743e-08
Msun=1.988409870698051e+33 # g
Rsun=69570000000.0 # cm

def Keplers_third_for_a(m1,m2,a):
    """given masses of components and separation of binary system, gives binary
    period
    m1 = primary mass / Msun
    m2= secondary mass / Msun
```

```python
    a = orbital separation / Rsun

    returns T = period / days"""

    T_s_sq = (a*Rsun)**3 / (G*Msun*(m1+m2) / (4 * np.pi**2 ) )
    T_days = np.sqrt(T_s_sq)/(24*60**2)
    return T_days

def Keplers_third(m1,m2,T):
    """given masses of components and binary period, gives separation of binary
    system
    m1 = primary mass / Msun
    m2= secondary mass / Msun
    T = period / days

    returns a = orbital separation / Rsun"""

    T_s = T*24*60**2 # period in seconds
    a_cubed = T_s**2 *G*Msun*(m1+m2)/(4 * np.pi**2 )
    a_m = a_cubed**(1/3.0)
    a= a_m/Rsun
    return a

def calc_J(m1,m2,a):
    """returns orbital angular momentum (in cgs units) for a circular binary
    m1 = primary mass / g
    m2= secondary mass / g
    a = orbital separation / cm"""
    return np.sqrt(G*a/(m1+m2)) * m1*m2

def calc_a(m1,m2,J):
    """returns orbital separation (in cgs units) for a circular binary
    m1 = primary mass / g
    m2= secondary mass / g
    J = orbital angular momentum / cgs units"""
    return ((m1+m2)/G)*(J/(m1*m2))**2

def evolve_system(md_i, ma_i, p_i,md_f, beta, gamma,  dm):
    """evolves binary system with
        md_i = initial donor mass /msun
        ma_i = initial accretor mass /msun
        p_i = initial period / days
        md_f = final donor mass /msun
        beta = mt efficiency
        gamma = angular momentum loss parameter
        dm = amount of mass lost per iteration /msun """

    a_i = Keplers_third(md_i,ma_i,p_i)
    md_i = md_i*Msun
    ma_i = ma_i*Msun
    a_i = a_i*Rsun
    dm = dm*Msun
    md_f = md_f*Msun
    md=md_i
    ma= ma_i
```

```python
    a = a_i
    J = calc_J(md_i, ma_i, a_i)

    res=[pd.DataFrame({'md_Msun':md/Msun,'ma_Msun':ma/Msun,'a_Rsun':a/Rsun,'
    p_days':p_i, 'J':J}, index=[0])]
    i=1
    while md> md_f:
        md= md - dm
        ma = ma+ beta* dm
        dj = dm * (1-beta) * gamma**2 * md**2 * (md+ma)**(-1.5)* np.sqrt(G*a)
        J = J-dj
        a = calc_a(md,ma,J)
        p = Keplers_third_for_a(ma/Msun,md/Msun,a/Rsun)
        res_i = pd.DataFrame({'md_Msun':md/Msun,'ma_Msun':ma/Msun,'a_Rsun':a/Rsun
    ,'p_days':p, 'J':J}, index=[i])
        res.append(res_i)
        i+=1
    #res = pd.concat(res)
    return res_i

if __name__ == '__main__':
    md_i = 8.0 # initial donor mass/Msun
    ma_i = 6.0 # initial accretor mass/Msun
    p_i = 10.0 # initial period/days
    md_f = 1.5 # final donor mass/Msun
    beta = 0.5 # mass transfer efficiency
    gamma = 1.0 # angular momentum loss parameter

    print('Running system with:\ninitial donor mass = 8 Msun\ninitial accretor
    mass = 6 Msun')
    print('initial period = 10 days')
    print('beta = 0.5\ngamma=1.0')
    print('final donor mass = 1.5 Msun')
    print('')
    print('final orbital properites are:')
    r=evolve_system(md_i, ma_i, p_i,md_f, beta, gamma,  dm=0.01)
    print(r)
```

Summary and Outlook

Classical emission line stars make up a significant fraction of the massive star population in environments ranging from young open clusters (Milone, Marino et al., 2018; Bodensteiner, Sana et al., 2020) to dwarf galaxies (Schootemeijer, Lennon et al., 2022). This thesis explores the origin of rapid rotation that is believed to underpin the emission line phenomenon. Two distinct formation channels are investigated: that of single and binary star evolution. Understanding the contribution of each formation channel to emission line star populations allows constraints on several key, but uncertain aspects of stellar physics including stellar winds, internal angular momentum transport and the dynamics of mass-transfer in binary systems. Most importantly, knowledge of the formation channel reveals the future evolution of these stars, allowing insights into the lives of massive stars in general.

The young open cluster NGC 330 is taken as a test bed. This cluster hosts one of the richest populations of massive stars in the Small Magellanic Cloud, including a sizeable collection of emission line stars (Milone, Marino et al., 2018; Bodensteiner, Sana et al., 2020). This thesis investigates the viability of two emission line star formation channels in explaining the populations in NGC 330: that of single star evolution and binary evolution. Furthermore, as both channels suffer from distinct theoretical uncertainties, an attempt is made at constraining these uncertainties.

This thesis is structured as follows. Chapter 2 explores the single star channel and predicts relative numbers of emission line stars. Chapter 3 deals with the binary evolution channel through a simple and flexible toy model that is adapted to fit the emission line star population in NGC 330, thus elucidating the binary channel's effectiveness in producing emission line stars. Chapter 4 develops a model of winds from fast rotating stars that is an improvement upon what current evolutionary models assume. Finally Chapter 5 uses Be + stripped star binaries to constrain the mass-transfer efficiency and angular momentum loss during binary interaction.

Chapter 2 uses the previously published evolutionary models of Brott, de Mink et al. (2011) to assess the spin evolution of single rotating stars. A synthetic population is produced assuming an initial rotational velocity distribution derived from observations. The population is coeval and so represents an open star cluster. The relative fractions of stars rotating faster than a threshold rate is assessed and compared to the numbers of emission line stars in the cluster NGC 330. The models can only explain the high Be star fractions near the main-sequence turn-off when the emission line phenomena threshold is relaxed to 70% or more of the critical velocity. However, at any rotation threshold, the models cannot reproduce the high Be star fractions up to two magnitudes below the main-sequence turn-off, as the spin-up mechanism is predicted by the models to reach high rotation rates only when the star is close to core hydrogen depletion, that is evolved. Recent measurements of young stars in open clusters suggest that the majority of stars are born with slower roation rates than was assumed in this chapter (C. Wang, Hastings et al., 2023), further aggravating the single star channel's difficulty in producing Be stars. The failure of the models to describe the Be star population in NGC 330 leads to the conclusion that the single star channel cannot dominate Be star formation, and must at the very least be complimented by the binary evolution channel.

Motivated by the findings of the previous Chapter, Chapter 3 studies the binary evolution channel. The results of detailed binary evolution calculations are plagued by distinct uncertainties, such as the occurrence of mergers and the mass-transfer efficiency. To allow an assessment of Be star production that encompasses these uncertainties, an analytic toy model of binary evolution is developed. We find that under certain distinct, although extreme conditions, binary evolution can match the Be star population in NGC 330 well. These conditions are that every star is born as a member of a binary, that mass-transfer is inefficient, that approximately one-eighth of the binaries merge and that every binary that does not merge will produce a Be star. We argue that although some of these conditions may appear at first glance unlikely, they might be realised in nature.

The spin evolution of single stars is highly sensitive to the angular momentum budget. Rotating stars lose angular momentum through stellar winds, which is the focus of Chapter 4. Owing to the centrifugal force, a rotating star has a spatially variable surface gravity, and accordingly a spatially variable effective temperature. Such a star ought to host an anisotropic wind; that is the mass-loss of the equatorial regions is different to that of the polar regions. Wind anisotropies can effect the angular momentum loss of a star, possibly altering its spin evolution. Current models, such as those analysed in Chapter 2, do not take these effects into account. In Chapter 4 a simple prescription that can be implemented in one-dimensional stellar evolution codes in developed and explored. The new prescription uses the local surface properties of the star to determine the mass and angular momentum loss rates, fully accounting for both the spatial variations in surface properties and the oblate shape of the star. It is seen that previous less physically accurate prescriptions for the mass and angular momentum loss of rotating stars may have overestimated the angular momentum loss. Therefore the single star Be production channel may be more effective than seen in Chapter 2.

A key uncertainty in binary evolution is the mass-transfer efficiency, which is investigated in Chapter 5. A Be + stripped star system represents a binary just after mass-transfer is completed and thus represents the best possible opportunity to constrain the physics of binary interaction. The observed component masses and orbital periods of three Be + stripped star binaries are compared to a large grid of binary evolution calculations. The mass-transfer efficiency and angular momentum loss associated with non-conservative mass-transfer are treated as free parameters in the evolutionary calculations. It is found that the best fits to the observed systems are given by intermediate mass-transfer efficiencies, in the range 30-50% and with low angular momentum loss, lower than that lost as a fast wind blown from the accretor. This picture of mass-transfer contradicts the physics that is commonly employed in binary evolution calculations; namely either extremely conservative or non-conservative mass-transfer and angular momentum loss modelled as a fast wind originating from the accretor. Suggestions for further work on this topic are given.

Both the single and binary evolution channels may have the potential to dominate the production of emission line stars, although both suffer from considerable uncertainties. It is argued in Chapter 2 that the single star channel cannot dominate Be star production, although it can contribute significantly in the later evolutionary states, if the threshold velocity for the Be phenomenon is low enough. In light of how little is known about winds of rotating stars and specifically the angular momentum loss associated therewith, a population of single stars may spin up very efficiently to near critical velocities. On the other hand, the binary evolution channel can reproduce the population of Be stars in NGC 330 under certain assumptions. It is not at all clear whether these assumptions are met in nature. For example, the requirement that mass-transfer must be very inefficient found in Chapter 3 appears not to be realised, as found in Chapter 5.

At the time of writing (early 2023), much attention is being paid to the binary evolution channel. The fact that many Be-Xray binaries and several Be + stripped star systems are known and that there are no Be stars that have been confirmed to originate from single star evolution provides a strong argument for the dominance of the binary channel. However the results of this thesis cannot fully endorse one channel over the other, with the most probable situation being that both channels co-exist to produce emission line stars.

The field does however remain dynamic and there are several anticipated efforts on both the observational and theoretical sides that promise to advance understanding. Telescopes all over the world, and flying around it, are searching for companions of massive stars. Although detection remains a challenge, emission line stars are being found in increasing numbers to host companions that suggest binary interaction must have occurred, like subdwarves and white dwarves. The true population of Be binaries remains uncovered and will shed light on the Be stars' previous history.

Similarly observational evidence for the single star channel is being unearthed. A hydrogen burning star in orbit around a Be star would provide a strong argument that the single star channel occurs in nature. This is because the presence of a main-sequence companion excludes the possibility of binary interaction occurring, and the Be star must have come into existence through the single star channel. It has been claimed that no such binary systems exist (Bodensteiner, Shenar and Sana, 2020), yet very recently several candidates have been proposed; ν Geminorum (Klement, Hadrava et al., 2021) and Achernar (Kervella et al., 2022).

There are several properties that may distinguish a Be star's formation pathway. The rotation rate is one of them, with Chapter 2 suggesting that if Be stars rotate very close to the critical velocity (> 90%), then it is unlikely that the single star channel can produce significant numbers of Be stars. Measurements of Be star's rotation rates have been made, but they all use one-dimensional techniques that are poorly suited to studying very fast rotators, which are oblate and hence not well described by one-dimensional models (Abdul-Masih, 2023). Once the stars' spatially variable properties are considered, this may alter the measured rotation rates. Several methods for self-consistently calculating the spectra of a fast rotating star exist (Abdul-Masih, Sana et al., 2020; Hennicker et al., 2022; Abdul-Masih, 2023) but they are yet to be applied to a sample of emission line stars.

Our theoretical understanding of emission line stars can be strengthened in several areas. The evolution of rotating stars with anisotropic winds is largely unexplored. The methods set out in Chapter 4 are well suited to studying the spin

evolution of stars hosting anisotropic winds, and may answer the question of how effective the single star spin-up mechanism is. Furthermore, improvements in the theoretical models of massive stars such as the development of two-dimensional evolutionary models can further improve our understanding. An example is defining the threshold rotation velocity at which a decretion disc forms because over the non-uniform surface of a fast rotating star, the surface flux and opacities can vary significantly, resulting in a different force balance compared to the simpler one-dimensional case. These avenues of investigation give hope of a dynamic future for the study of emission line stars.

Bibliography

Abdul-Masih, M. (2023), *Effects of rotation on the spectroscopic observables of massive stars*,
   A&A **669**, L11 L11, arXiv: 2212.10485 [astro-ph.SR].

Abdul-Masih, M., G. Banyard et al. (2020), *On the signature of a 70-solar-mass black hole in LB-1*,
   Nature **580** E11, arXiv: 1912.04092 [astro-ph.SR].

Abdul-Masih, M., H. Sana et al. (2020),
   Spectroscopic patch model for massive stars using PHOEBE II and FASTWIND,
   A&A **636**, A59 A59, arXiv: 2003.09008 [astro-ph.SR].

Abt, H. A. and S. G. Levy (1978), *Binaries among B2 - B5 IV, V absorption and emission stars.*,
   ApJS **36** 241.

Aerts, C., S. Mathis and T. M. Rogers (2019), *Angular Momentum Transport in Stellar Interiors*,
   ARA&A **57** 35, arXiv: 1809.07779 [astro-ph.SR].

Aguilera-Dena, D. R., N. Langer, J. Antoniadis and B. Müller (2020), *Precollapse Properties of
   Superluminous Supernovae and Long Gamma-Ray Burst Progenitor Models*, ApJ **901**, 114 114,
   arXiv: 2008.09132 [astro-ph.SR].

Ahmed, A. and T. A. A. Sigut (2017),
   Rotational mixing in Be stars: nitrogen abundances for a sample of Be stars from the MiMeS survey,
   MNRAS **471** 3398, arXiv: 1707.03009 [astro-ph.SR].

Arcos, C. et al. (2018),
   Stellar parameters and H α line profile variability of Be stars in the BeSOS survey,
   MNRAS **474** 5287, arXiv: 1711.08675 [astro-ph.SR].

Baade, D., T. Rivinius, S. Stefl and A. Kaufer (2002),
   A spectroscopic search for variability of Be stars in the SMC, A&A **383** L31.

El-Badry, K. and K. B. Burdge (2022),
   NGC 1850 BH1 is another stripped-star binary masquerading as a black hole, MNRAS **511** 24,
   arXiv: 2111.07925 [astro-ph.SR].

El-Badry, K. and E. Quataert (2020), *Not so fast: LB-1 is unlikely to contain a 70 $M_\odot$ black hole*,
   MNRAS **493** L22, arXiv: 1912.04185 [astro-ph.SR].

– (2021),
   A stripped-companion origin for Be stars: clues from the putative black holes HR 6819 and LB-1,
   MNRAS **502** 3436, arXiv: 2006.11974 [astro-ph.SR].

Ballereau, D., J. Chauville and J. Zorec (1995),
   Some Fe II emission-line profiles of nine southern Be stars., A&AS **111** 457.

Balona, L. A. and D. Ozuyar (2020), *TESS observations of Be stars: a new interpretation*,
   MNRAS **493** 2528, arXiv: 1911.03068 [astro-ph.SR].

Balona, L. A. and D. Ozuyar (2019), *TESS observations of Be stars: a new interpretation*, arXiv e-prints, arXiv:1911.03068 arXiv:1911.03068, arXiv: `1911.03068 [astro-ph.SR]`.

Batten, A. H. (1989), *Two Centuries of Study of Algol Systems*, Space Sci. Rev. **50** 1.

Bestenlehner, J. M. et al. (2020), *The R136 star cluster dissected with Hubble Space Telescope/STIS. II. Physical properties of the most massive stars in R136*, MNRAS, arXiv: `2009.05136 [astro-ph.SR]`.

Björklund, R., J. O. Sundqvist, S. M. Singh, J. Puls and F. Najarro (2022), *New predictions for radiation-driven, steady-state mass-loss and wind-momentum from hot, massive stars III. Updated mass-loss rates for stellar evolution*, arXiv e-prints, arXiv:2203.08218 arXiv:2203.08218, arXiv: `2203.08218 [astro-ph.SR]`.

Bjorkman, K. S., A. S. Miroshnichenko, D. McDavid and T. M. Pogrosheva (2002), *A Study of π Aquarii during a Quasi-normal Star Phase: Refined Fundamental Parameters and Evidence for Binarity*, ApJ **573** 812, arXiv: `astro-ph/0203357 [astro-ph]`.

Bodensteiner, J., H. Sana et al. (2019), *The young massive SMC cluster NGC 330 seen by MUSE. I. Observations and stellar content*, arXiv e-prints, arXiv:1911.03477 arXiv:1911.03477, arXiv: `1911.03477 [astro-ph.SR]`.

– (2020), *The young massive SMC cluster NGC 330 seen by MUSE. I. Observations and stellar content*, A&A **634**, A51 A51, arXiv: `1911.03477 [astro-ph.SR]`.

Bodensteiner, J., T. Shenar, L. Mahy et al. (2020), *Is HR 6819 a triple system containing a black hole?. An alternative explanation*, A&A **641**, A43 A43, arXiv: `2006.10770 [astro-ph.SR]`.

Bodensteiner, J., T. Shenar and H. Sana (2020), *Investigating the lack of main-sequence companions to massive Be stars*, A&A **641**, A42 A42, arXiv: `2006.13229 [astro-ph.SR]`.

Boubert, D. and N. W. Evans (2018), *On the kinematics of a runaway Be star population*, MNRAS **477** 5261, arXiv: `1804.05849 [astro-ph.SR]`.

Brandt, N. and P. Podsiadlowski (1995), *The effects of high-velocity supernova kicks on the orbital properties and sky distributions of neutron-star binaries*, MNRAS **274** 461.

Brookshaw, L. and M. Tavani (1993), *Wind-driven Angular Momentum Loss in Binary Systems. I. Ballistic Case*, ApJ **410** 719.

Brott, I., S. E. de Mink et al. (2011), *Rotating massive main-sequence stars. I. Grids of evolutionary models and isochrones*, A&A **530**, A115 A115, arXiv: `1102.0530 [astro-ph.SR]`.

Brott, I., C. J. Evans et al. (2011), *Rotating massive main-sequence stars. II. Simulating a population of LMC early B-type stars as a test of rotational mixing*, A&A **530**, A116 A116, arXiv: `1102.0766 [astro-ph.SR]`.

Broz, M. et al. (2021), *Optically thin circumstellar medium in the β Lyr A system*, A&A **645**, A51 A51, arXiv: `2010.05541 [astro-ph.SR]`.

Carciofi, A. C. et al. (2012), *The First Determination of the Viscosity Parameter in the Circumstellar Disk of a Be Star*, ApJ **744**, L15 L15, arXiv: `1112.0053 [astro-ph.SR]`.

Casares, J. et al. (2014), *A Be-type star with a black-hole companion*, Nature **505** 378, arXiv: `1401.3711 [astro-ph.SR]`.

Cassinelli, J. P., J. C. Brown, M. Maheswaran, N. A. Miller and D. C. Telfer (2002),
A Magnetically Torqued Disk Model for Be Stars, ApJ **578** 951,
arXiv: `astro-ph/0207370 [astro-ph]`.

Castor, J. I., D. C. Abbott and R. I. Klein (1975), *Radiation-driven winds in Of stars.*, ApJ **195** 157.

Castro, N. et al. (2014), *The spectroscopic Hertzsprung-Russell diagram of Galactic massive stars*,
A&A **570**, L13 L13, arXiv: `1410.3499 [astro-ph.SR]`.

Che, X. et al. (2011), *Colder and Hotter: Interferometric Imaging of β Cassiopeiae and α Leonis*,
ApJ **732**, 68 68, arXiv: `1105.0740 [astro-ph.SR]`.

Chen, W. et al. (2020),
Close binary evolution affects the main sequence morphology in young star clusters,
ApJL, submitted.

Choi, J. et al. (2016), *Mesa Isochrones and Stellar Tracks (MIST). I. Solar-scaled Models*,
ApJ **823**, 102 102, arXiv: `1604.08592 [astro-ph.SR]`.

Chojnowski, S. D. et al. (2018),
The Remarkable Be+sdOB Binary HD 55606. I. Orbital and Stellar Parameters, ApJ **865**, 76 76,
arXiv: `1806.06843 [astro-ph.SR]`.

Claret, A. and G. Torres (2016), *The dependence of convective core overshooting on stellar mass*,
A&A **592**, A15 A15.

Coe, M. J., J. A. Kennea, P. A. Evans and A. Udalski (2020),
Swift J004427.3−734801 - a probable Be/white dwarf system in the Small Magellanic Cloud,
MNRAS **497** L50, arXiv: `2005.02891 [astro-ph.HE]`.

Collins George W., I. and R. J. Truax (1995), *Classical Rotational Broadening of Spectral Lines*,
ApJ **439** 860.

Collins Geroge W., I. (1965), *Continuum Emission from a Rotating Non-Gray Stellar Atmosphere.*,
ApJ **142** 265.

Cote, J. and M. H. van Kerkwijk (1993), *New bright Be stars and the Be star frequency.*,
A&A **274** 870.

Cotton, D. V. et al. (2017), *Polarization due to rotational distortion in the bright star Regulus*,
Nature Astronomy **1** 690, arXiv: `1804.06576 [astro-ph.SR]`.

Cranmer, S. R. (2005),
A Statistical Study of Threshold Rotation Rates for the Formation of Disks around Be Stars,
ApJ **634** 585, arXiv: `astro-ph/0507718 [astro-ph]`.

– (2009), *A Pulsational Mechanism for Producing Keplerian Disks Around Be Stars*, ApJ **701** 396,
arXiv: `0906.2772 [astro-ph.SR]`.

Cranmer, S. R. and S. P. Owocki (1995), *The Effect of Oblateness and Gravity Darkening on the
Radiation Driving in Winds from Rapidly Rotating B Stars*, ApJ **440** 308.

Curé, M., L. Cidale and D. F. Rial (2012), *Limb-darkened Radiation-driven Winds from Massive Stars*,
ApJ **757**, 142 142, arXiv: `1207.6009 [astro-ph.SR]`.

Curé, M. and D. F. Rial (2004),
The influence of rotation in radiation driven winds from hot stars. II. CAK topological analysis,
A&A **428** 545, arXiv: `astro-ph/0408511 [astro-ph]`.

Curé, M., D. F. Rial and L. Cidale (2005), *Outflowing disk formation in B[e] supergiants due to
rotation and bi-stability in radiation driven winds*, A&A **437** 929,
arXiv: `astro-ph/0503359 [astro-ph]`.

Curé, M. (2004), *The Influence of Rotation in Radiation-driven Wind from Hot Stars: New Solutions and Disk Formation in Be Stars*, ApJ **614** 929, arXiv: `astro-ph/0406490 [astro-ph]`.

D'Antona, F. et al. (2015), *The extended main-sequence turn-off cluster NGC 1856: rotational evolution in a coeval stellar ensemble*, MNRAS **453** 2637, arXiv: `1508.01932 [astro-ph.SR]`.

de Koter, A., S. R. Heap and I. Hubeny (1997),
On the Evolutionary Phase and Mass Loss of the Wolf-Rayet–like Stars in R136a, ApJ **477** 792.

de Mink, S. E., N. Langer and R. G. Izzard (2011a), *Binaries are the best single stars*,
Bulletin de la Societe Royale des Sciences de Liege **80** 543, arXiv: `1010.2200 [astro-ph.SR]`.

de Mink, S. E., N. Langer, R. G. Izzard, H. Sana and A. de Koter (2013), *The Rotation Rates of Massive Stars: The Role of Binary Interaction through Tides, Mass Transfer, and Mergers*, ApJ **764**, 166 166, arXiv: `1211.3742 [astro-ph.SR]`.

de Mink, S. E., O. R. Pols and R. W. Hilditch (2007), *Efficiency of mass transfer in massive close binaries. Tests from double-lined eclipsing binaries in the SMC*, A&A **467** 1181, arXiv: `astro-ph/0703480 [astro-ph]`.

de Mink, S. E., H. Sana, N. Langer, R. G. Izzard and F. R. N. Schneider (2014),
The Incidence of Stellar Mergers and Mass Gainers among Massive Stars, ApJ **782**, 7 7, arXiv: `1312.3650 [astro-ph.SR]`.

de Mink, S. E., N. Langer and R. G. Izzard (2011b),
"Fast rotating stars resulting from binary evolution will often appear to be single",
Active OB Stars: Structure, Evolution, Mass Loss, and Critical Limits,
ed. by C. Neiner, G. Wade, G. Meynet and G. Peters, vol. 272 531,
arXiv: `1009.3937 [astro-ph.SR]`.

Domiciano de Souza, A. et al. (2014), *The environment of the fast rotating star Achernar. III. Photospheric parameters revealed by the VLTI*, A&A **569**, A10 A10.

Donati, J. -F. et al. (2001), *The magnetic field and wind confinement of β Cephei: new clues for interpreting the Be phenomenon?*, MNRAS **326** 1265.

Dorigo Jones, J., M. S. Oey, K. Paggeot, N. Castro and M. Moe (2020),
Runaway OB Stars in the Small Magellanic Cloud: Dynamical versus Supernova Ejections,
ApJ **903**, 43 43, arXiv: `2009.03571 [astro-ph.SR]`.

Dufton, P. L., P. R. Dunstall et al. (2011), *The VLT-FLAMES Tarantula Survey: The Fastest Rotating O-type Star and Shortest Period LMC Pulsar- Remnants of a Supernova Disrupted Binary?*, ApJ **743**, L22 L22, arXiv: `1111.0157 [astro-ph.SR]`.

Dufton, P. L., N. Langer et al. (2013), *The VLT-FLAMES Tarantula Survey. X. Evidence for a bimodal distribution of rotational velocities for the single early B-type stars*, A&A **550**, A109 A109, arXiv: `1212.2424 [astro-ph.SR]`.

Dufton, P. L., D. J. Lennon et al. (2022), *Properties of the Be-type stars in 30 Doradus*,
MNRAS **512** 3331, arXiv: `2203.02440 [astro-ph.SR]`.

Dunstall, P. R. et al. (2011), *The VLT-FLAMES survey of massive stars: Nitrogen abundances for Be-type stars in the Magellanic Clouds*, A&A **536**, A65 A65, arXiv: `1109.6661 [astro-ph.SR]`.

Eggleton, P. P. (1983), *Aproximations to the radii of Roche lobes.*, ApJ **268** 368.

Ekström, S., G. Meynet, A. Maeder and F. Barblan (2008),
Evolution towards the critical limit and the origin of Be stars, A&A **478** 467,
arXiv: `0711.1735 [astro-ph]`.

Eldridge, J. J. et al. (2017), *Binary Population and Spectral Synthesis Version 2.1: Construction, Observational Verification, and New Results*, PASA **34**, e058 e058, arXiv: `1710.02154 [astro-ph.SR]`.

Emden, R. (1907), *Gaskugeln.*

Espinosa Lara, F. and M. Rieutord (2011), *Gravity darkening in rotating stars*, A&A **533**, A43 A43, arXiv: `1109.3038 [astro-ph.SR]`.

– (2013), *Self-consistent 2D models of fast-rotating early-type stars*, A&A **552**, A35 A35, arXiv: `1212.0778 [astro-ph.SR]`.

Ferrario, L., J. E. Pringle, C. A. Tout and D. T. Wickramasinghe (2009), *The origin of magnetism on the upper main sequence*, MNRAS **400** L71.

Friend, D. B. and D. C. Abbott (1986), *The theory of radiatively driven stellar winds. III - Wind models with finite disk correction and rotation*, ApJ **311** 701.

Gagnier, D., M. Rieutord, C. Charbonnel, B. Putigny and F. Espinosa Lara (2019a), *Critical angular velocity and anisotropic mass loss of rotating stars with radiation-driven winds*, A&A **625**, A88 A88, arXiv: `1904.05089 [astro-ph.SR]`.

– (2019b), *Evolution of rotation in rapidly rotating early-type stars during the main sequence with 2D models*, A&A **625**, A89 A89, arXiv: `1904.05219 [astro-ph.SR]`.

Gayley, K. G. and S. P. Owocki (2000), *Radiative Torque and Partial Spin-Down of Winds from Rotating Hot Stars*, ApJ **537** 461.

Ghoreyshi, M. R. et al. (2018), *The life cycles of Be viscous decretion discs: The case of ω CMa*, MNRAS **479** 2214, arXiv: `1806.04301 [astro-ph.SR]`.

Gies, D. R., K. V. Lester et al. (2020), *Spectroscopic Detection of the Pre-White Dwarf Companion of Regulus*, ApJ **902**, 25 25, arXiv: `2009.02409 [astro-ph.SR]`.

Gies, D. R., L. Wang and R. Klement (2023), *Gamma Cas Stars as Be+White Dwarf Binary Systems*, ApJ **942**, L6 L6, arXiv: `2212.06916 [astro-ph.SR]`.

Girardi, L. et al. (2002), *Theoretical isochrones in several photometric systems. I. Johnson-Cousins-Glass, HST/WFPC2, HST/NICMOS, Washington, and ESO Imaging Survey filter sets*, A&A **391** 195, arXiv: `astro-ph/0205080 [astro-ph]`.

Glatzel, W. (1998), *Remarks on the "Omega -limit"*, A&A **339** L5.

Glebbeek, E. and O. R. Pols (2008), *Evolution of stellar collision products in open clusters. II. A grid of low-mass collisions*, A&A **488** 1017, arXiv: `0806.0865 [astro-ph]`.

Golden-Marx, J. B., M. S. Oey, J. B. Lamb, A. S. Graus and A. S. White (2016), *Classical Oe Stars in the Field of the Small Magellanic Cloud*, ApJ **819**, 55 55, arXiv: `1601.03405 [astro-ph.SR]`.

Gossage, S. et al. (2019), *Combined Effects of Rotation and Age Spreads on Extended Main-Sequence Turn Offs*, ApJ **887**, 199 199, arXiv: `1907.11251 [astro-ph.SR]`.

Granada, A., S. Ekström et al. (2013), *Populations of rotating stars. II. Rapid rotators and their link to Be-type stars*, A&A **553**, A25 A25, arXiv: `1303.2393 [astro-ph.SR]`.

Granada, A., C. Georgy, L. Haemmerlé, S. Ekström and G. Meynet (2016),
“Evolution of Intermediate-Mass Rotating Stellar Populations: Rotational Properties, Nitrogen
Surface Abundances, and Their Link to the Be-Phenomenon.”,
Bright Emissaries: Be Stars as Messengers of Star-Disk Physics,
ed. by T. A. A. Sigut and C. E. Jones, vol. 506,
Astronomical Society of the Pacific Conference Series 33.

Hanuschik, R. W. (2000), “Shell Lines in Be Disks”,
IAU Colloq. 175: The Be Phenomenon in Early-Type Stars,
ed. by M. A. Smith, H. F. Henrichs and J. Fabregat, vol. 214,
Astronomical Society of the Pacific Conference Series 518.

Harmanec, P. et al. (2020), *A new study of the spectroscopic binary 7 Vul with a Be star primary*,
A&A **639**, A32 A32, arXiv: `2005.11089 [astro-ph.SR]`.

Harmanec, P. (1988), *Stellar Masses and Radii Based on Modern Binary Data*,
Bulletin of the Astronomical Institutes of Czechoslovakia **39** 329.

Hastings, B., N. Langer and G. Koenigsberger (2020), *Internal circulation in tidally locked massive
binary stars: Consequences for double black hole formation*, A&A **641**, A86 A86,
arXiv: `2007.11299 [astro-ph.SR]`.

Hastings, B., C. Wang and N. Langer (2020), *The single star path to Be stars*, A&A **633**, A165 A165,
arXiv: `1912.05290 [astro-ph.SR]`.

Heger, A. and N. Langer (2000),
Presupernova Evolution of Rotating Massive Stars. II. Evolution of the Surface Properties,
ApJ **544** 1016, arXiv: `astro-ph/0005110 [astro-ph]`.

Heger, A., N. Langer and S. E. Woosley (2000), *Presupernova Evolution of Rotating Massive Stars. I.
Numerical Method and Evolution of the Internal Stellar Structure*, ApJ **528** 368,
eprint: `astro-ph/9904132`.

Heger, A., S. E. Woosley and H. C. Spruit (2005),
Presupernova Evolution of Differentially Rotating Massive Stars Including Magnetic Fields,
ApJ **626** 350, eprint: `astro-ph/0409422`.

Hennicker, L. et al. (2022), *Binary-object spectral-synthesis in 3D (BOSS-3D). Modelling H_α
emission in the enigmatic multiple system LB-1*, A&A **660**, A17 A17,
arXiv: `2111.15345 [astro-ph.SR]`.

Herschel, W. (1803),
*Account of the Changes That Have Happened, during the Last Twenty-Five Years, in the Relative
Situation of Double-Stars; With an Investigation of the Cause to Which They Are Owing*,
Philosophical Transactions of the Royal Society of London **93** 339, ISSN: 02610523,
URL: `http://www.jstor.org/stable/107080` (visited on 09/09/2022).

Hirata, K. et al. (1987), *Observation of a neutrino burst from the supernova SN1987A*,
Phys. Rev. Lett. **58** 1490.

Hjellming, M. S. and R. F. Webbink (1987),
Thresholds for Rapid Mass Transfer in Binary System. I. Polytropic Models, ApJ **318** 794.

Hoffleit, D. (1997), *History of the Discovery of Mira Stars*,
The Journal of the American Association of Variable Star Observers **25** 115.

Hogeveen, S. J. (1991), *The mass-ratio distribution of binary stars*, PhD thesis: -.

Hoogerwerf, R., J. H. J. de Bruijne and P. T. de Zeeuw (2001), *On the origin of the O and B-type stars with high velocities. II. Runaway stars and pulsars ejected from the nearby young stellar groups*, A&A **365** 49, arXiv: `astro-ph/0010057 [astro-ph]`.

Huang, W., D. R. Gies and M. V. McSwain (2010), *A Stellar Rotation Census of B Stars: From ZAMS to TAMS*, ApJ **722** 605, arXiv: `1008.1761 [astro-ph.SR]`.

Huat, A.-L. et al. (2009), *The B0.5IVe CoRoT target HD 49330. I. Photometric analysis from CoRoT data*, A&A **506** 95.

Hunter, I. et al. (2008), *The VLT-FLAMES survey of massive stars: atmospheric parameters and rotational velocity distributions for B-type stars in the Magellanic Clouds*, A&A **479** 541, arXiv: `0711.2264 [astro-ph]`.

Hurley, J. R., C. A. Tout and O. R. Pols (2002), *Evolution of binary stars and the effect of tides on binary populations*, MNRAS **329** 897, arXiv: `astro-ph/0201220 [astro-ph]`.

Hutter, D. J. et al. (2021), *Surveying the Bright Stars by Optical Interferometry. III. A Magnitude-limited Multiplicity Survey of Classical Be Stars*, ApJS **257**, 69 69, arXiv: `2109.06839 [astro-ph.SR]`.

Iben Icko, J. and M. Livio (1993), *Common Envelopes in Binary Star Evolution*, PASP **105** 1373.

Iglesias, C. A. and F. J. Rogers (1996), *Updated Opal Opacities*, ApJ **464** 943.

Iqbal, S. and S. C. Keller (2013), *A study of Be stars in the Magellanic Clouds*, MNRAS **435** 3103, arXiv: `1309.1224`.

Ishii, M., M. Ueno and M. Kato (1999), *Core-Halo Structure of a Chemically Homogeneous Massive Star and Bending of the Zero-Age Main Sequence*, PASJ **51** 417, arXiv: `astro-ph/9907154 [astro-ph]`.

Jetsu, L. et al. (2013), *Did the Ancient Egyptians Record the Period of the Eclipsing Binary Algol—The Raging One?*, ApJ **773**, 1 1, arXiv: `1204.6206 [astro-ph.SR]`.

Jiang, Y.-F., M. Cantiello, L. Bildsten, E. Quataert and O. Blaes (2015), *Local Radiation Hydrodynamic Simulations of Massive Star Envelopes at the Iron Opacity Peak*, ApJ **813**, 74 74, arXiv: `1509.05417 [astro-ph.SR]`.

Justesen, A. B. and S. Albrecht (2021), *Temperature and Distance Dependence of Tidal Circularization in Close Binaries: A Catalog of Eclipsing Binaries in the Southern Hemisphere Observed by the TESS Satellite*, ApJ **912**, 123 123, arXiv: `2103.09216 [astro-ph.SR]`.

Justham, S., P. Podsiadlowski and J. S. Vink (2014), *Luminous Blue Variables and Superluminous Supernovae from Binary Mergers*, ApJ **796**, 121 121, arXiv: `1410.2426 [astro-ph.SR]`.

Kamann, S. et al. (2020), *How stellar rotation shapes the colour-magnitude diagram of the massive intermediate-age star cluster NGC 1846*, MNRAS **492** 2177, arXiv: `2001.01731 [astro-ph.SR]`.

Keller, S. C. (2004), *Rotation of Early B-type Stars in the Large Magellanic Cloud: The Role of Evolution and Metallicity*, PASA **21** 310, eprint: `astro-ph/0405129`.

Keller, S. C., P. R. Wood and M. S. Bessell (1999), *Be stars in and around young clusters in the Magellanic Clouds*, A&AS **134** 489, arXiv: `astro-ph/9809072 [astro-ph]`.

Kervella, P. et al. (2022), *The binary system of the spinning-top Be star Achernar*,
arXiv e-prints, arXiv:2209.07537 arXiv:2209.07537, arXiv: `2209.07537 [astro-ph.SR]`.

Kippenhahn, R. (1974), "Circulation and Mixing", *Late Stages of Stellar Evolution*,
ed. by R. J. Tayler and J. E. Hesser, vol. 66 20.

Kippenhahn and Weigert (1990), *Stellar Structure and Evolution*, Springer-Verlag.

Kirchhoff, G. and R. Bunsen (1860), *Chemische Analyse durch Spectralbeobachtungen*,
Annalen der Physik **186** 161.

Kjurkchieva, D., D. Marchev, T. A. A. Sigut and D. Dimitrov (2016),
The B and Be States of the Star EM Cepheus, AJ **152**, 56 56,
arXiv: `1606.04815 [astro-ph.SR]`.

Klement, R., A. C. Carciofi, T. Rivinius, L. D. Matthews et al. (2017),
Revealing the structure of the outer disks of Be stars, A&A **601**, A74 A74,
arXiv: `1703.07321 [astro-ph.SR]`.

Klement, R., A. C. Carciofi, T. Rivinius, R. Ignace et al. (2019a),
Prevalence of SED Turndown among Classical Be Stars: Are All Be Stars Close Binaries?,
ApJ **885**, 147 147, arXiv: `1909.12413 [astro-ph.SR]`.

– (2019b), *Prevalence of SED turndown among classical Be stars: Are all Be stars close binaries?*,
arXiv e-prints, arXiv:1909.12413 arXiv:1909.12413, arXiv: `1909.12413 [astro-ph.SR]`.

Klement, R., P. Hadrava et al. (2021), *ν Gem: A Hierarchical Triple System with an Outer Be Star*,
ApJ **916**, 24 24, arXiv: `2105.13437 [astro-ph.SR]`.

Klement, R., G. H. Schaefer et al. (2022),
Interferometric Detections of sdO Companions Orbiting Three Classical Be Stars,
ApJ **926**, 213 213, arXiv: `2112.05073 [astro-ph.SR]`.

Klencki, J., G. Nelemans, A. G. Istrate and M. Chruslinska (2021), *It has to be cool: Supergiant
progenitors of binary black hole mergers from common-envelope evolution*, A&A **645**, A54 A54,
arXiv: `2006.11286 [astro-ph.SR]`.

Kobulnicky, H. A. and C. L. Fryer (2007), *A New Look at the Binary Characteristics of Massive Stars*,
ApJ **670** 747.

Köhler, R. et al. (2006), *Binary stars in the Orion Nebula Cluster*, A&A **458** 461,
arXiv: `astro-ph/0607670 [astro-ph]`.

Koubský, P., P. Harmanec et al. (2000),
Properties and nature of Be stars. XIX. Spectral and light variability of 60 Cygni, A&A **356** 913.

Koubský, P., L. Kotková, M. Kraus et al. (2014), *HD 161306: a radiatively interacting Be binary?*,
A&A **567**, A57 A57.

Koubský, P., L. Kotková, V. Votruba, M. Slechta and S. Dvořáková (2012),
o Puppis: another Be+sdO binary?, A&A **545**, A121 A121.

Kouwenhoven, M. B. N., A. G. A. Brown, S. P. Goodwin, S. F. Portegies Zwart and L. Kaper (2009),
Exploring the consequences of pairing algorithms for binary stars, A&A **493** 979,
arXiv: `0811.2859 [astro-ph]`.

Kouwenhoven, M. B. N., A. G. A. Brown, S. F. Portegies Zwart and L. Kaper (2007),
*The primordial binary population. II.. Recovering the binary population for intermediate mass
stars in Scorpius OB2*, A&A **474** 77, arXiv: `0707.2746 [astro-ph]`.

Kriz, S. and P. Harmanec (1975), *A Hypothesis of the Binary Origin of Be Stars*,
Bulletin of the Astronomical Institutes of Czechoslovakia **26** 65.

Krtička, J., J. Kubát and I. Krtičková (2021),
New mass-loss rates of B supergiants from global wind models, A&A **647**, A28 A28,
arXiv: `2101.04973 [astro-ph.SR]`.

Krtička, J., P. Kurfürst and I. Krtičková (2015), *Magnetorotational instability in decretion disks of critically rotating stars and the outer structure of Be and Be/X-ray disks*, A&A **573**, A20 A20,
arXiv: `1410.7831 [astro-ph.SR]`.

Krtička, J., S. P. Owocki and G. Meynet (2011), *Mass and angular momentum loss via decretion disks*,
A&A **527**, A84 A84, arXiv: `1101.1732 [astro-ph.SR]`.

Kudritzki, R. P., A. Pauldrach, J. Puls and D. C. Abbott (1989), *Radiation-driven winds of hot stars. VI. Analytical solutions for wind models including the finite cone angle effect.*, A&A **219** 205.

Kudritzki, R.-P. and J. Puls (2000), *Winds from Hot Stars*, ARA&A **38** 613.

Kulkarni, S. R. et al. (2007), *An unusually brilliant transient in the galaxy M85*, Nature **447** 458,
arXiv: `0705.3668 [astro-ph]`.

Labadie-Bartz, J., A. C. Carciofi et al. (2022),
Classifying Be Star Variability With TESS. I. The Southern Ecliptic, AJ **163**, 226 226.

Labadie-Bartz, J., J. Pepper et al. (2017), *Photometric Variability of the Be Star Population*,
AJ **153**, 252 252, arXiv: `1609.08449 [astro-ph.SR]`.

Lamers, H. J. G. L. M. and J. P. Cassinelli (1999), *Introduction to Stellar Winds*.

Lamers, H. J. G. L. M., T. P. Snow and D. M. Lindholm (1995),
Terminal Velocities and the Bistability of Stellar Winds, ApJ **455** 269.

Lane, H. J. (1870),
On the theoretical temperature of the Sun, under the hypothesis of a gaseous mass maintaining its volume by its internal heat, and depending on the laws of gases as known to terrestrial experiment,
American Journal of Science **50** 57.

Langer, N. (1997), "The Eddington Limit in Rotating Massive Stars",
Luminous Blue Variables: Massive Stars in Transition, ed. by A. Nota and H. Lamers, vol. 120,
Astronomical Society of the Pacific Conference Series 83.

– (1998), *Coupled mass and angular momentum loss of massive main sequence stars*, A&A **329** 551.

– (2012), *Presupernova Evolution of Massive Single and Binary Stars*, ARA&A **50** 107,
arXiv: `1206.5443 [astro-ph.SR]`.

Langer, N. et al. (2020),
Properties of OB star-black hole systems derived from detailed binary evolution models,
A&A **638**, A39 A39, arXiv: `1912.09826 [astro-ph.SR]`.

Lee, U., Y. Osaki and H. Saio (1991), *Viscous excretion discs around Be stars*, MNRAS **250** 432.

Lennon, D. J., J. .-K. Lee, P. L. Dufton and R. S. I. Ryans (2005),
A Be star with a low nitrogen abundance in the SMC cluster NGC 330, A&A **438** 265,
arXiv: `astro-ph/0407258 [astro-ph]`.

Li, G.-W. et al. (2018), *New Oe Stars in LAMOST DR5*, ApJ **863**, 70 70,
arXiv: `1807.00574 [astro-ph.SR]`.

Li, K. L. et al. (2012),
A Luminous Be+White Dwarf Supersoft Source in the Wing of the SMC: MAXI J0158-744,
ApJ **761**, 99 99, arXiv: `1207.5023 [astro-ph.HE]`.

Lipatov, M. and T. D. Brandt (2020), *Synthetic Spectra of Rotating Stars*, ApJ **901**, 100 100,
arXiv: `2007.12779 [astro-ph.SR]`.

Liu, Q. Z., J. van Paradijs and E. P. J. van den Heuvel (2006),
  Catalogue of high-mass X-ray binaries in the Galaxy (4th edition), A&A **455** 1165,
  arXiv: `0707.0549` [`astro-ph`].

Lovekin, C. C., R. G. Deupree and C. I. Short (2006),
  Surface Temperature and Synthetic Spectral Energy Distributions for Rotationally Deformed Stars,
  ApJ **643** 460, arXiv: `astro-ph/0602084` [`astro-ph`].

Lucy, L. B. (1967), *Gravity-Darkening for Stars with Convective Envelopes*, ZAp **65** 89.

MacLeod, M. and A. Loeb (2020), *Hydrodynamic Winds from Twin-star Binaries*, ApJ **902**, 85 85,
  arXiv: `2007.07252` [`astro-ph.SR`].

Maeder, A. (1987), *Evidences for a bifurcation in massive star evolution. The ON-blue stragglers*,
  A&A **178** 159.

– (1997), *Stellar evolution with rotation. II. A new approach for shear mixing.*, A&A **321** 134.

Maeder, A., E. K. Grebel and J.-C. Mermilliod (1999),
  Differences in the fractions of Be stars in galaxies, A&A **346** 459, eprint: `astro-ph/9904008`.

Maeder, A. and G. Meynet (1987), *Grids of evolutionary models of massive stars with mass loss and
  overshooting - Properties of Wolf-Rayet stars sensitive to overshooting.*, A&A **182** 243.

– (2000), *Stellar evolution with rotation. VI. The Eddington and Omega -limits, the rotational mass
  loss for OB and LBV stars*, A&A **361** 159, arXiv: `astro-ph/0006405` [`astro-ph`].

– (2001), *Stellar evolution with rotation. VII. . Low metallicity models and the blue to red supergiant
  ratio in the SMC*, A&A **373** 555, arXiv: `astro-ph/0105051` [`astro-ph`].

Maeder, A. (2009), *Physics, Formation and Evolution of Rotating Stars.*

Marchant, P. (2017a),
  The impact of tides and mass transfer on the evolution of metal-poor massive binary stars,
  PhD thesis: Rheinische Friedrich-Wilhelms-Universität Bonn.

– (2017b), *The impact of tides and mass transfer on the evolution of metal-poor massive binary stars*,
  PhD thesis: Rheinische Friedrich Wilhelms University of Bonn, Germany.

Marchant, P., N. Langer, P. Podsiadlowski, T. M. Tauris and T. J. Moriya (2016),
  A new route towards merging massive black holes, A&A **588**, A50 A50,
  arXiv: `1601.03718` [`astro-ph.SR`].

Marino, A. F. et al. (2018), *Different Stellar Rotations in the Two Main Sequences of the Young
  Globular Cluster NGC 1818: The First Direct Spectroscopic Evidence*, AJ **156**, 116 116,
  arXiv: `1807.04493` [`astro-ph.SR`].

Markova, N. and J. Puls (2008),
  Bright OB stars in the Galaxy. IV. Stellar and wind parameters of early to late B supergiants,
  A&A **478** 823, arXiv: `0711.1110` [`astro-ph`].

Marr, K. C. et al. (2021), *The Be Star 66 Ophiuchi: 60 Years of Disk Evolution*, ApJ **912**, 76 76,
  arXiv: `2103.06948` [`astro-ph.SR`].

Martayan, C., D. Baade and J. Fabregat (2010),
  A slitless spectroscopic survey for Hα emission-line objects in SMC clusters, A&A **509**, A11 A11,
  arXiv: `0909.2303`.

Martayan, C., Y. Frémat et al. (2006), *Effects of metallicity, star-formation conditions, and evolution
  in B and Be stars. I. Large Magellanic Cloud, field of NGC 2004*, A&A **452** 273,
  arXiv: `astro-ph/0601240` [`astro-ph`].

Martins, F. and A. Palacios (2013),
A comparison of evolutionary tracks for single Galactic massive stars, A&A **560**, A16 A16,
arXiv: `1310.7218 [astro-ph.SR]`.

Mateo, M., H. C. Harris, J. Nemec and E. W. Olszewski (1990),
Blue Stragglers as Remnants of Stellar Mergers: The Discovery of Short-Period Eclipsing Binaries in the Globular Cluster NGC 5466, AJ **100** 469.

McSwain, M. V. and D. R. Gies (2005),
The Evolutionary Status of Be Stars: Results from a Photometric Study of Southern Open Clusters,
ApJS **161** 118, arXiv: `astro-ph/0505032 [astro-ph]`.

McSwain, M. V., W. Huang, D. R. Gies, E. D. Grundstrom and R. H. D. Townsend (2008),
The B and Be Star Population of NGC 3766, ApJ **672** 590, arXiv: `0710.0137 [astro-ph]`.

Meilland, A., O. Delaa et al. (2011), *The binary Be star δ Scorpii at high spectral and spatial resolution. I. Disk geometry and kinematics before the 2011 periastron*, A&A **532**, A80 A80,
arXiv: `1106.1746 [astro-ph.SR]`.

Meilland, A., F. Millour et al. (2012), *First spectro-interferometric survey of Be stars. I. Observations and constraints on the disk geometry and kinematics*, A&A **538**, A110 A110,
arXiv: `1111.2487 [astro-ph.SR]`.

Meilland, A., P. Stee et al. (2007),
First direct detection of a Keplerian rotating disk around the Be star α Arae using AMBER/VLTI,
A&A **464** 59, arXiv: `astro-ph/0606404 [astro-ph]`.

Michell, J. (1767), *An Inquiry into the Probable Parallax, and Magnitude of the Fixed Stars, from the Quantity of Light Which They Afford us, and the Particular Circumstances of Their Situation, by the Rev. John Michell, B. D. F. R. S.*,
Philosophical Transactions of the Royal Society of London Series I **57** 234.

Milone, A. P., L. R. Bedin, G. Piotto and J. Anderson (2009), *Multiple stellar populations in Magellanic Cloud clusters. I. An ordinary feature for intermediate age globulars in the LMC?*,
A&A **497** 755, arXiv: `0810.2558 [astro-ph]`.

Milone, A. P., A. F. Marino et al. (2018), *Multiple stellar populations in Magellanic Cloud clusters - VI. A survey of multiple sequences and Be stars in young clusters*, MNRAS **477** 2640,
arXiv: `1802.10538 [astro-ph.SR]`.

Miroshnichenko, A. S. et al. (2001),
Spectroscopic observations of the δ Scorpii binary during its recent periastron passage,
A&A **377** 485, arXiv: `astro-ph/0106492 [astro-ph]`.

Monnier, J. D. et al. (2007), *Imaging the Surface of Altair*, Science **317** 342,
arXiv: `0706.0867 [astro-ph]`.

Mourard, D. et al. (2015),
Spectral and spatial imaging of the Be+sdO binary <ASTROBJ>φ Persei</ASTROBJ>,
A&A **577**, A51 A51, arXiv: `1503.03423 [astro-ph.SR]`.

Müller, P. E. and J. S. Vink (2014), *Rotating massive O stars with non-spherical 2D winds*,
A&A **564**, A57 A57, arXiv: `1402.5929 [astro-ph.SR]`.

Nazé, Y., G. Rauw, S. Czesla, M. A. Smith and J. Robrade (2022),
Velocity monitoring of γ Cas stars reveals their binarity status, MNRAS **510** 2286,
arXiv: `2111.09579 [astro-ph.SR]`.

Neiner, C. and S. Mathis (2014), "Making a Be star: the role of rotation and pulsations",
Precision Asteroseismology, ed. by J. A. Guzik, W. J. Chaplin, G. Handler and A. Pigulski, vol. 301,
IAU Symposium 465, arXiv: 1311.2261 [astro-ph.SR].

Nemravová, J. et al. (2012),
Properties and nature of Be stars. 29. Orbital and long-term spectral variations of γ Cassiopeiae,
A&A **537**, A59 A59, arXiv: 1111.3761 [astro-ph.SR].

Owocki, S. P., S. R. Cranmer and K. G. Gayley (1996), *Inhibition FO Wind Compressed Disk
Formation by Nonradial Line-Forces in Rotating Hot-Star Winds*, ApJ **472** L115.

Owocki, S. P., S. R. Cranmer and J. M. Blondin (1994), *Two-dimensional Hydrodynamical
Simulations of Wind-compressed Disks around Rapidly Rotating B Stars*, ApJ **424** 887.

Packet, W. (1981), *On the spin-up of the mass accreting component in a close binary system*,
A&A **102** 17.

Pastorello, A. et al. (2019), *Luminous red novae: Stellar mergers or giant eruptions?*,
A&A **630**, A75 A75, arXiv: 1906.00812 [astro-ph.SR].

Pauldrach, A., J. Puls and R. P. Kudritzki (1986),
Radiation-driven winds of hot luminous stars. Improvements of the theory and first results.,
A&A **164** 86.

Pauldrach, A. W. A. and J. Puls (1990), *Radiation-driven winds of hot luminous stars. VIII. The
bistable wind of the luminous blue variable P Cygni (B1 Ia+).*, A&A **237** 409.

Pavlovskii, K. and N. Ivanova (2015), *Mass transfer from giant donors*, MNRAS **449** 4415,
arXiv: 1410.5109 [astro-ph.SR].

Paxton, B., L. Bildsten et al. (2011), *Modules for Experiments in Stellar Astrophysics (MESA)*,
ApJS **192**, 3 3, arXiv: 1009.1622 [astro-ph.SR].

Paxton, B., M. Cantiello et al. (2013), *Modules for Experiments in Stellar Astrophysics (MESA):
Planets, Oscillations, Rotation, and Massive Stars*, ApJS **208**, 4 4,
arXiv: 1301.0319 [astro-ph.SR].

Paxton, B., P. Marchant et al. (2015),
Modules for Experiments in Stellar Astrophysics (MESA): Binaries, Pulsations, and Explosions,
ApJS **220**, 15 15, arXiv: 1506.03146 [astro-ph.SR].

Paxton, B., J. Schwab et al. (2018), *Modules for Experiments in Stellar Astrophysics (MESA):
Convective Boundaries, Element Diffusion, and Massive Star Explosions*, ApJS **234**, 34 34,
arXiv: 1710.08424 [astro-ph.SR].

Paxton, B., R. Smolec et al. (2019), *Modules for Experiments in Stellar Astrophysics (MESA):
Pulsating Variable Stars, Rotation, Convective Boundaries, and Energy Conservation*,
ApJS **243**, 10 10, arXiv: 1903.01426 [astro-ph.SR].

Pelupessy, I., H. J. G. L. M. Lamers and J. S. Vink (2000),
The radiation driven winds of rotating B[e] supergiants, A&A **359** 695,
arXiv: astro-ph/0005300 [astro-ph].

Penny, L. R., A. J. Sprague, G. Seago and D. R. Gies (2004),
Effects of Metallicity on the Rotational Velocities of Massive Stars, ApJ **617** 1316,
eprint: astro-ph/0409757.

Peters, G. J. (1989), *The Hα Emitting Regions of the Accretion Disks in ALGOLS*,
Space Sci. Rev. **50** 9.

Peters, G. J., D. R. Gies, E. D. Grundstrom and M. V. McSwain (2008),
Detection of a Hot Subdwarf Companion to the Be Star FY Canis Majoris, ApJ **686** 1280,
arXiv: `0806.3004 [astro-ph]`.

Peters, G. J., T. D. Pewett, D. R. Gies, Y. N. Touhami and E. D. Grundstrom (2013),
Far-ultraviolet Detection of the Suspected Subdwarf Companion to the Be Star 59 Cygni,
ApJ **765**, 2 2, arXiv: `1301.0257 [astro-ph.SR]`.

Peters, G. J., L. Wang, D. R. Gies and E. D. Grundstrom (2016),
The Hot Companion and Circumbinary Disk of the Be Star HR 2142, ApJ **828**, 47 47,
arXiv: `1607.01829 [astro-ph.SR]`.

Petrenz, P. and J. Puls (2000), *2-D non-LTE models of radiation driven winds from rotating early-type stars. I. Winds with an optically thin continuum*, A&A **358** 956.

Petrovic, J., N. Langer and K. A. van der Hucht (2005), *Constraining the mass transfer in massive binaries through progenitor evolution models of Wolf-Rayet+O binaries*, A&A **435** 1013,
arXiv: `astro-ph/0504242 [astro-ph]`.

Pickering, E. C. (1881), *Reviews.*, Astronomical register **19** 253.

– (1890), *The Draper Catalogue of stellar spectra photographed with the 8-inch Bache telescope as a part of the Henry Draper memorial*, Annals of Harvard College Observatory **27** 1.

Pinsonneault, M. H., S. D. Kawaler, S. Sofia and P. Demarque (1989),
Evolutionary Models of the Rotating Sun, ApJ **338** 424.

Poe, C. H. and D. B. Friend (1986),
A Rotating, Magnetic, Radiation-driven Wind Model Applied to Be Stars, ApJ **311** 317.

Poe, C. H., D. B. Friend and J. P. Cassinelli (1989),
A Rotating, Magnetic, Radiation-driven Wind Model for Wolf-Rayet Stars, ApJ **337** 888.

Pols, O. R., J. Cote, L. B. F. M. Waters and J. Heise (1991a),
The formation of Be stars through close binary evolution, A&A **241** 419.

– (1991b), *The formation of Be stars through close binary evolution.*, A&A **241** 419.

Porter, J. M. (1996), *On the rotational velocities of Be and Be-shell stars*, MNRAS **280** L31.

Porter, J. M. and T. Rivinius (2003), *Classical Be Stars*, PASP **115** 1153.

Quirrenbach, A., K. S. Bjorkman et al. (1997), *Constraints on the Geometry of Circumstellar Envelopes: Optical Interferometric and Spectropolarimetric Observations of Seven Be Stars*,
ApJ **479** 477.

Quirrenbach, A., D. F. Buscher, D. Mozurkewich, C. A. Hummel and J. T. Armstrong (1994),
Maximum-entropy maps of the Be shell star dzeta Tauri from optical long-baseline interferometry.,
A&A **283** L13.

Raguzova, N. V. and S. B. Popov (2005), *Be X-ray binaries and candidates*,
Astronomical and Astrophysical Transactions **24** 151, arXiv: `astro-ph/0505275 [astro-ph]`.

Ramirez-Agudelo, O. H., H. Sana et al. (2015),
The VLT-FLAMES Tarantula Survey. XXI. Stellar spin rates of O-type spectroscopic binaries,
A&A **580**, A92 A92, arXiv: `1507.02286 [astro-ph.SR]`.

Ramirez-Agudelo, O. H., S. Simón-Diaz et al. (2013),
The VLT-FLAMES Tarantula Survey. XII. Rotational velocities of the single O-type stars,
A&A **560**, A29 A29, arXiv: `1309.2929 [astro-ph.SR]`.

Reig, P. (2011), *Be/X-ray binaries*, Ap&SS **332** 1, arXiv: `1101.5036 [astro-ph.HE]`.

Rieutord, M. (2016), "Physical Processes Leading to Surface Inhomogeneities: The Case of Rotation",
Lecture Notes in Physics, Berlin Springer Verlag, ed. by J.-P. Rozelot and C. Neiner, vol. 914 101.

Rimulo, L. R. et al. (2018),
   The life cycles of Be viscous decretion discs: fundamental disc parameters of 54 SMC Be stars,
   MNRAS **476** 3555, arXiv: 1802.07641 [astro-ph.SR].

Rivinius, T., D. Baade, S. Stefl, R. H. D. Townsend et al. (2001), *Stellar and circumstellar activity of the Be star mu Centauri. III. Multiline nonradial pulsation modeling*, A&A **369** 1058.

Rivinius, T., D. Baade, S. Stefl, O. Stahl et al. (1998),
   Stellar and circumstellar activity of the Be star MU Centauri. I. Line emission outbursts,
   A&A **333** 125.

Rivinius, T., S. Stefl and D. Baade (2006), *Bright Be-shell stars*, A&A **459** 137.

Rivinius, T., A. C. Carciofi and C. Martayan (2013),
   Classical Be stars. Rapidly rotating B stars with viscous Keplerian decretion disks,
   A&A Rev. **21**, 69 69, arXiv: 1310.3962 [astro-ph.SR].

Ruzdjak, D. et al. (2009),
   Properties and nature of Be stars. 26. Long-term and orbital changes of ζ Tauri, A&A **506** 1319.

Saad, S. M. et al. (2005), *Spectrum Disentangling and Orbital Solution for κ Dra*, Ap&SS **296** 173.

Salpeter, E. E. (1955), *The Luminosity Function and Stellar Evolution.*, ApJ **121** 161.

Sana, H., A. de Koter et al. (2013),
   The VLT-FLAMES Tarantula Survey. VIII. Multiplicity properties of the O-type star population,
   A&A **550**, A107 A107, arXiv: 1209.4638 [astro-ph.SR].

Sana, H., S. E. de Mink et al. (2012), *Binary Interaction Dominates the Evolution of Massive Stars*,
   Science **337** 444, arXiv: 1207.6397 [astro-ph.SR].

Sanyal, D., L. Grassitelli, N. Langer and J. M. Bestenlehner (2015),
   Massive main-sequence stars evolving at the Eddington limit, A&A **580**, A20 A20,
   arXiv: 1506.02997 [astro-ph.SR].

Sanyal, D., N. Langer, D. Szécsi, S. -C Yoon and L. Grassitelli (2017),
   Metallicity dependence of envelope inflation in massive stars, A&A **597**, A71 A71,
   arXiv: 1611.07280 [astro-ph.SR].

Scalo, J. M. (1986), *The Stellar Initial Mass Function*, Fund. Cosmic Phys. **11** 1.

Schneider, F. R. N., R. G. Izzard, N. Langer and S. E. de Mink (2015),
   Evolution of Mass Functions of Coeval Stars through Wind Mass Loss and Binary Interactions,
   ApJ **805**, 20 20, arXiv: 1504.01735 [astro-ph.SR].

Schneider, F. R. N., H. Sana et al. (2018), *An excess of massive stars in the local 30 Doradus starburst*,
   Science **359** 69, arXiv: 1801.03107 [astro-ph.SR].

Schneider, F. R. N., S. T. Ohlmann et al. (2019),
   Stellar mergers as the origin of magnetic massive stars, Nature **574** 211,
   arXiv: 1910.14058 [astro-ph.SR].

Schootemeijer, A., Y. Götberg, S. E. de Mink, D. Gies and E. Zapartas (2018),
   Clues about the scarcity of stripped-envelope stars from the evolutionary state of the sdO+Be binary system φ Persei, A&A **615**, A30 A30, arXiv: 1803.02379 [astro-ph.SR].

Schootemeijer, A., N. Langer, N. J. Grin and C. Wang (2019),
   Constraining mixing in massive stars in the Small Magellanic Cloud, A&A **625**, A132 A132,
   arXiv: 1903.10423 [astro-ph.SR].

Schootemeijer, A., D. J. Lennon et al. (2022),
   Massive stars in metal-poor dwarf galaxies are often extreme rotators,
   arXiv e-prints, arXiv:2210.01453 arXiv:2210.01453, arXiv: 2210.01453 [astro-ph.SR].

Secchi, A. (1866), *Schreiben des Herrn Prof. Secchi, Directors der Sternwarte des Collegio Romano, an den Herausgeber*, Astronomische Nachrichten **68** 63.

Sen, K. et al. (2021), *Detailed models of interacting short-period massive binary stars*, arXiv e-prints, arXiv:2111.03329 arXiv:2111.03329, arXiv: `2111.03329 [astro-ph.SR]`.

– (2022), *Detailed models of interacting short-period massive binary stars*, A&A **659**, A98 A98, arXiv: `2111.03329 [astro-ph.SR]`.

Shao, Y. and X.-D. Li (2014), *On the Formation of Be Stars through Binary Interaction*, ApJ **796**, 37 37, arXiv: `1410.0100 [astro-ph.HE]`.

Shao, Y. and X.-D. Li (2016), *Nonconservative Mass Transfer in Massive Binaries and the Formation of Wolf-Rayet+O Binaries*, ApJ **833**, 108 108, arXiv: `1610.04307 [astro-ph.SR]`.

Shenar, T. et al. (2020), *The "hidden" companion in LB-1 unveiled by spectral disentangling*, A&A **639**, L6 L6, arXiv: `2004.12882 [astro-ph.SR]`.

Sigut, T. A. A., M. A. McGill and C. E. Jones (2009), *Be Star Disk Models in Consistent Vertical Hydrostatic Equilibrium*, ApJ **699** 1973, arXiv: `0905.1295 [astro-ph.SR]`.

Slettebak, A. (1979), *The Be Stars*, Space Sci. Rev. **23** 541.

Slettebak, A. (1949), *On the Axial Rotation of the Brighter O and B Stars.*, ApJ **110** 498.

Soberman, G. E., E. S. Phinney and E. P. J. van den Heuvel (1997), *Stability criteria for mass transfer in binary stellar evolution.*, A&A **327** 620, arXiv: `astro-ph/9703016 [astro-ph]`.

Spruit, H. C. (2002), *Dynamo action by differential rotation in a stably stratified stellar interior*, A&A **381** 923, arXiv: `astro-ph/0108207 [astro-ph]`.

Stefl, S., D. Baade et al. (2003), *Stellar and circumstellar activity of the Be star omega CMa. I. Line and continuum emission in 1996-2002*, A&A **402** 253.

Stefl, S., P. Hadrava et al. (2004), "A 10-Day Binary System Orbiting the Be Star 66 Oph", *Stellar Rotation*, ed. by A. Maeder and P. Eenens, vol. 215 166.

Sternberg, A., T. L. Hoffmann and A. W. A. Pauldrach (2003), *Ionizing Photon Emission Rates from O- and Early B-Type Stars and Clusters*, ApJ **599** 1333, arXiv: `astro-ph/0312232 [astro-ph]`.

Struve, O. (1931), *On the Origin of Bright Lines in Spectra of Stars of Class B*, ApJ **73** 94.

Suijs, M. P. L. et al. (2008), *White dwarf spins from low-mass stellar evolution models*, A&A **481** L87, arXiv: `0802.3286`.

Sun, W., R. de Grijs, L. Deng and M. D. Albrow (2019), *Stellar Rotation and the Extended Main-sequence Turnoff in the Open Cluster NGC 5822*, ApJ **876**, 113 113, arXiv: `1904.03547 [astro-ph.SR]`.

Sundqvist, J. O., R. Björklund, J. Puls and F. Najarro (2019), *New predictions for radiation-driven, steady-state mass-loss and wind-momentum from hot, massive stars. I. Method and first results*, A&A **632**, A126 A126, arXiv: `1910.06586 [astro-ph.SR]`.

Sweet, P. A. (1950), *The importance of rotation in stellar evolution*, MNRAS **110** 548.

Tarasov, A. E. (2017), "Be Stars in Open Clusters", *Stars: From Collapse to Collapse*, ed. by Y. Y. Balega, D. O. Kudryavtsev, I. I. Romanyuk and I. A. Yakunin, vol. 510, Astronomical Society of the Pacific Conference Series 132.

Tauris, T. M. and E. P. J. van den Heuvel (2006),
  "Formation and evolution of compact stellar X-ray sources", *Compact stellar X-ray sources*, vol. 39
  623.

Telting, J. H. et al. (1998), *The equatorial disc of the Be star X Persei*, MNRAS **296** 785.

Tokovinin, A. and M. Moe (2020),
  Formation of close binaries by disc fragmentation and migration, and its statistical modelling,
  MNRAS **491** 5158, arXiv: 1910.01522 [astro-ph.SR].

Tout, C. A. (1991), *On the relation between the mass-ratio distribution in binary stars and the mass
  function for single stars.*, MNRAS **250** 701.

Tout, C. A., S. J. Aarseth, O. R. Pols and P. P. Eggleton (1997),
  Rapid binary star evolution for N-body simulations and population synthesis, MNRAS **291** 732.

Townsend, R. H. D., S. P. Owocki and I. D. Howarth (2004), *Be-star rotation: how close to critical?*,
  MNRAS **350** 189, arXiv: astro-ph/0312113 [astro-ph].

Trimble, V. (1990), *The distributions of binary system mass ratios - A less biased sample.*,
  MNRAS **242** 79.

van Bever, J. and D. Vanbeveren (1997), *The number of B-type binary mass gainers in general, binary
  Be stars in particular, predicted by close binary evolution.*, A&A **322** 116.

Vinciguerra, S. et al. (2020), *Be X-ray binaries in the SMC as indicators of mass-transfer efficiency*,
  MNRAS **498** 4705, arXiv: 2003.00195 [astro-ph.HE].

Vink, J. S., A. de Koter and H. J. G. L. M. Lamers (1999),
  On the nature of the bi-stability jump in the winds of early-type supergiants, A&A **350** 181,
  arXiv: astro-ph/9908196 [astro-ph].

– (2000), *New theoretical mass-loss rates of O and B stars*, A&A **362** 295,
  eprint: astro-ph/0008183.

Vink, J. S. (2018), *Fast and slow winds from supergiants and luminous blue variables*,
  A&A **619**, A54 A54, arXiv: 1808.06612 [astro-ph.SR].

Vink, J. S., A. de Koter and H. J. G. L. M. Lamers (2001),
  Mass-loss predictions for O and B stars as a function of metallicity, A&A **369** 574,
  arXiv: astro-ph/0101509 [astro-ph].

von Zeipel, H. (1924), *The radiative equilibrium of a rotating system of gaseous masses*,
  MNRAS **84** 665.

Wang, C., B. Hastings et al. (2023), *The initial spin distribution of B-type stars revealed by the split
  main sequences of young star clusters*, A&A **670**, A43 A43,
  arXiv: 2211.15794 [astro-ph.SR].

Wang, C., N. Langer et al. (2020),
  Effects of Close Binary Evolution on the Main-sequence Morphology of Young Star Clusters,
  ApJ **888**, L12 L12, arXiv: 1912.07294 [astro-ph.SR].

Wang, L., D. R. Gies and G. J. Peters (2018),
  Detection of Additional Be+sdO Systems from IUE Spectroscopy, ApJ **853**, 156 156,
  arXiv: 1801.01066 [astro-ph.SR].

Wang, L., D. R. Gies, G. J. Peters et al. (2021),
  The Detection and Characterization of Be+sdO Binaries from HST/STIS FUV Spectroscopy,
  AJ **161**, 248 248, arXiv: 2103.13642 [astro-ph.SR].

Wellstein, S., N. Langer and H. Braun (2001), *Formation of contact in massive close binaries*,
  A&A **369** 939, arXiv: astro-ph/0102244 [astro-ph].

Wheelwright, H. E., J. E. Bjorkman et al. (2012), *Probing the properties of Be star discs with spectroastrometry and NLTE radiative transfer modelling: β CMi*, MNRAS **423** L11, arXiv: `1202.4561 [astro-ph.SR]`.

Wheelwright, H. E., R. D. Oudmaijer and R. S. Schnerr (2009), *The close Be star companion of β Cephei*, A&A **497** 487, arXiv: `0902.4356 [astro-ph.SR]`.

Wickramasinghe, D. T., C. A. Tout and L. Ferrario (2014), *The most magnetic stars*, MNRAS **437** 675, arXiv: `1310.2696 [astro-ph.SR]`.

Winters, J. M., T. Le Bertre, K. S. Jeong, C. Helling and E. Sedlmayr (2000), *A systematic investigation of the mass loss mechanism in dust forming long-period variable stars*, A&A **361** 641.

Yoon, S. .-C., N. Langer and C. Norman (2006), *Single star progenitors of long gamma-ray bursts. I. Model grids and redshift dependent GRB rate*, A&A **460** 199, arXiv: `astro-ph/0606637 [astro-ph]`.

Yoon, S.-C. and N. Langer (2005), *Evolution of rapidly rotating metal-poor massive stars towards gamma-ray bursts*, A&A **443** 643, eprint: `astro-ph/0508242`.

Zahn, J. .-P., C. Ranc and P. Morel (2010), *On the shape of rapidly rotating stars*, A&A **517**, A7 A7.

Zhao, M. et al. (2009), *Imaging and Modeling Rapidly Rotating Stars: α Cephei and α Ophiuchi*, ApJ **701** 209, arXiv: `0906.2241 [astro-ph.SR]`.

Zorec, J. and D. Briot (1997), *Critical study of the frequency of Be stars taking into account their outstanding characteristics.*, A&A **318** 443.

Zorec, J., L. Cidale et al. (2009), *Fundamental parameters of B supergiants from the BCD system. I. Calibration of the (λ_1, D) parameters into T_{eff}*, A&A **501** 297, arXiv: `0903.5134 [astro-ph.SR]`.

Zorec, J., Y. Frémat and L. Cidale (2005), *On the evolutionary status of Be stars. I. Field Be stars near the Sun*, A&A **441** 235, arXiv: `astro-ph/0509119 [astro-ph]`.

Zorec, J., Y. Frémat, A. Domiciano de Souza et al. (2016), *Critical study of the distribution of rotational velocities of Be stars. I. Deconvolution methods, effects due to gravity darkening, macroturbulence, and binarity*, A&A **595**, A132 A132.

Zwillinger, D. (1996), *CRC standard mathematical tables and formulae*, Chapman and Hall/CRC.

Appendix

Appendix to Chapter 2

A full reproduction of the publication resulting from work described in Chapter 2 is given on the next page.

The single star path to Be stars

Ben Hastings, Chen Wang, and Norbert Langer

Argelander-Institut für Astronomie, Universität Bonn, Auf dem Hügel 71, 53121 Bonn, Germany
e-mail: bhastings@astro.uni-bonn.de

ABSTRACT

Context. Be stars are rapidly rotating B main sequence stars that show line emission due to an outflowing disc. By studying the evolution of rotating single star models, we can assess their contribution to the observed Be star populations.

Aims. We identify the main effects that cause single stars to approach critical rotation as functions of initial mass and metallicity, and predict the properties of populations of rotating single stars.

Methods. We perform population synthesis with single-star models of initial masses ranging between 3 and 30 $M_\odot$ and initial equatorial rotation velocities between 0 and 600 km s^{-1} at compositions representing the Milky Way and the Large and Small Magellanic Clouds. These models include efficient core–envelope coupling mediated by internal magnetic fields and correspond to the maximum efficiency of Be star production. We predict Be star fractions and the positions of fast-rotating stars in the colour–magnitude diagram.

Results. We identify stellar wind mass-loss and the convective core mass fraction as the key parameters determining the time dependance of the stellar rotation rates. Using empirical distributions of initial rotational velocities, our single-star models can reproduce the trends observed in Be star fractions with mass and metallicity. However, they fail to produce a significant number of stars rotating very close to the critical velocity. We also find that rapidly rotating Be stars in the Magellanic Clouds should have significant surface nitrogen enrichment, which may be in conflict with abundance determinations of Be stars.

Conclusions. Single-star evolution might explain the high number of Be stars if 70 to 80% of critical rotation would be sufficient to produce the Be phenomenon. However, even in this case, the unexplained presence of many Be stars far below the cluster turn-off indicates the importance of the binary channel for Be star production.

Key words. stars: emission-line, Be – stars: rotation – stars: evolution

1. Introduction

Ever since their discovery over 150 years ago (Secchi 1866), Be stars have offered a promising, albeit misted window into massive star evolution and structure. It was proposed by Struve (1931) that Be stars are fast rotators, whose emission lines originate from a circumstellar decretion disc, a picture which has been maintained until today (Rivinius et al. 2013). Nevertheless, it is still not clear how fast a B-type star must rotate in order to become a Be star.

For a decretion disc to form, the equatorial rotation velocity $v_{\rm rot}$ is expected to be a significant fraction of the critical rotation velocity, $v_{\rm crit}$, defined as the rotation velocity at which material at the equator becomes unbound from the star. Observational evidence suggests that the threshold rotation rate for the Be phenomenon is mass dependant, and could be as low as $v_{\rm rot}/v_{\rm crit} = 0.6$ for stars more massive than 8.6 $M_\odot$ and as high as $v_{\rm rot}/v_{\rm crit} = 0.96$ for stars with $M < 4\,M_\odot$ (Huang et al. 2010). Similarly, Zorec et al. (2016) find that the Be phenomenon is characterised by a wide range of true velocity ratios (0.3 < $v_{\rm rot}/v_{\rm crit}$ < 0.95) and that the probability that Be stars are critical rotators is small. In this case one must look for an additional mechanism to feed the Be disc. Pulsations seem promising as they can serve to kick matter away from the surface of a star, however it is found that not all Be stars pulsate (Baade et al. 2002) and that among those that do there is a wide range of pulsation frequencies and types (Rivinius et al. 2013). Another possibility is that the disc is fed through outbursts of magnetically active starspots, similar to coronal mass ejections as seen

in the Sun, as suggested by Balona & Ozuyar (2019) based on recent TESS results.

On the other hand, Townsend et al. (2004) have argued that all Be stars in fact rotate very close ($v_{\rm rot}/v_{\rm crit} > 0.95$) to the critical velocity, with those which have low measured rotation rates being strongly affected by gravity darkening. Following the Von Zeipel law (von Zeipel 1924), gravity darkening in a fast-rotating star makes the stellar pole, which has a low rotational velocity, more luminous than the equator which has a high rotational velocity, resulting in the star appearing as though it is rotating slower than in reality.

Further questions surrounding Be stars pertain to why the phenomenon seems to be restricted mostly to B-type stars and why Be stars are more common in certain spectral classes than others. Observations in the Milky Way show that the fraction of Be stars in a certain spectral class varies across spectral type with Be-stars being most common in the B1–B2 classification, where the Be fraction is 34%. In comparison, the fraction of Be stars in the B9 classification is 8% and the total fraction of B stars that are Be stars was measured to be 17% (Zorec & Briot 1997). Furthermore, Oe stars seem to be rather rare, with less than 20 having been detected in the Milky Way (Li et al. 2018). It is not clear whether this is caused by processes within O stars themselves, the mechanisms responsible for forming a disc around a fast rotating star, or the conditions under which very massive stars form.

The existence of around 150 (Raguzova & Popov 2005) detected binary systems consisting of a Be star and a compact object (so called Be/X-ray binaries) demonstrates that binary interactions can spin up a star significantly (Kriz & Harmanec 1975;

Pols et al. 1991; Liu et al. 2006; Langer 2012). In order to build a full model of the Be phenomenon, binary evolution must be as well understood as the channels for forming single Be stars.

van Bever & Vanbeveren (1997) used binary star evolution calculations to predict that at most 20% of the Be star population results from binary interactions. Despite this, observations of surface nitrogen abundances in Magellanic Cloud Be stars are in disagreement with fast-rotating single star models (Dunstall et al. 2011). Therefore, the dominant Be star formation channel and the differences between the single and binary Be population remain to be identified.

Considerable efforts have been made to predict the relative fractions of Be stars through single star modelling, most notably by Ekström et al. (2008). These models include coupling between core and envelope by hydrodynamic viscosities through the shear instability. However, a stronger coupling may be produced by internal magnetic fields known as the Tayler-Spruit dynamo (Spruit 2002) which produces very efficient angular momentum transport throughout the star that causes near-solid-body rotation to occur. The models analysed here include such effects, and therefore employ the maximum efficiency of spinning up the surface layers due to the core contraction during hydrogen burning, which is a key factor in the production of single Be stars. At present, the Tayler-Spruit dynamo is used to explain relatively slow rotation rates in white dwarfs (Suijs et al. 2008) and young pulsars (Heger et al. 2005).

In Sect. 2 the models are introduced and our approaches are outlined. In Sect. 3, models from the grid are analysed under conditions of fast and slow rotation for Milky Way and Small Magellanic Cloud metallicities, the factors governing the approach to the critical velocity are investigated, and the expected surface nitrogen abundances of Be stars are investigated. In Sect. 4, population synthesis is performed to calculate the expected fractions of single Be stars in clusters of differing ages and metallicities and predict the positions of fast rotating stars in the colour–magnitude diagram.

2. Method

2.1. Stellar models

We analyse the single star evolutionary models of Brott et al. (2011) to predict the properties of rotating single stars throughout their main sequence evolution. We consider masses from $3\,M_\odot$ to $30\,M_\odot$ at various initial rotation velocities ranging from zero to approximately $600\,\mathrm{km\,s^{-1}}$. Because the model grid is spaced in initial rotational velocities, but the initial critical rotation velocity increases with mass, our grid does not contain models with initial values of $v_{\mathrm{rot}}/v_{\mathrm{crit}}$ greater than around 0.7 for initial masses greater than $25\,M_\odot$.

Three initial chemical compositions represent metallicities of the Milky Way (MW), Large Magellanic Could (LMC) and Small Magellanic Cloud (SMC). The models include internal transport of angular momentum via the Tayler-Spruit dynamo (Spruit 2002) which has the effect of enforcing near-solid-body rotation throughout most of the main sequence evolution. The adopted mass-loss scheme is given by Vink et al. (2000). An enhancement of the mass loss due to rotation is used as outlined in Yoon & Langer (2005), whereby the mass-loss rates are increased by a factor depending on the ratio of the rotation velocity to the critical velocity like

$$\dot{M}(\Omega) = \dot{M}(0)\left(\frac{1}{1 - \frac{v_{\mathrm{rot}}}{v_{\mathrm{crit}}}}\right)^{0.43} \tag{1}$$

where

$$v_{\mathrm{crit}} = \sqrt{\frac{GM}{R}(1 - \Gamma)}\,;\ \Gamma = \frac{\kappa L}{4\pi c GM}. \tag{2}$$

For a detailed description of the models see Brott et al. (2011).

2.2. Population synthesis

To predict properties of populations of rotating stars we use population synthesis to model open star clusters (i.e. collections of coeval stars without any continuous star formation) at various ages. For a cluster age t, we select pairs of random values from a Salpeter initial mass distribution (with exponent 2.35) and a distribution of initial critical velocity fraction, M_i and $v_{\mathrm{rot}}/v_{\mathrm{crit}\,i}$. We then find the masses, M_1, M_2 on the model grid that are straddling the chosen mass value, such that $M_1 < M_i < M_2$. For M_1 and M_2 we interpolate the hydrogen burning lifetimes, t_{MS} as a function of initial critical velocity fraction to obtain the hydrogen-burning lifetimes at the chosen value, $v_{\mathrm{rot}}/v_{\mathrm{crit}\,i}$. The hydrogen-burning lifetime, $t_{\mathrm{MS},i}$, of a model with mass M_i and initial rotation $v_{\mathrm{rot}}/v_{\mathrm{crit}\,i}$ is then found by interpolating between the hydrogen-burning lifetimes of M_1 and M_2. The fractional lifetime is then given by $t/t_{\mathrm{MS},i}$. If the fractional lifetime is greater than 1, the star will no longer be hydrogen burning and so the process is abandoned and new samples are drawn. We then select models with masses M_1 and M_2 at fractional hydrogen-burning times $t/t_{\mathrm{MS},i}$. An interpolation of the quantity of interest, Q across initial critical velocity fraction gives the values of Q for masses M_1, M_2 with initial rotation $v_{\mathrm{rot}}/v_{\mathrm{crit}\,i}$ and fractional hydrogen-burning time $t/t_{\mathrm{MS},i}$. One final interpolation between M_1 and M_2 gives the predicted quantity of the selected mass M_i at the given cluster age. The quantities of interest are luminosity, critical velocity fraction at the current time, and effective temperature.

The initial rotational velocity distribution used was taken from VLT-FLAMES observations of early B stars in the 30 Doradus region of the LMC (Dufton et al. 2013) and is shown in Fig. 1. The deconvolved distribution of equatorial rotational velocities was converted to a distribution in critical velocity fraction by applying a mapping between the two as determined from the $15\,M_\odot$ LMC models at ZAMS and then normalising such that the integral over the whole probability density function equals unity. It is noted that for the heaviest masses on the grid, the distribution extends beyond its limits. When such a massive, very-fast-rotating star is chosen from the distributions, instead the fastest rotator in the grid is used. Observations in 30 Doradus show that no O stars are observed to rotate with deconvolved equatorial velocities much greater than $500\,\mathrm{km\,s^{-1}}$ (Ramírez-Agudelo et al. 2013; Dufton et al. 2011). For a $25\,M_\odot$ star to rotate at a critical velocity fraction of 0.7, = an equatorial rotation velocity of the order $700\,\mathrm{km\,s^{-1}}$ would be required. It is therefore safe to assume that O stars do not enter the ZAMS with initial critical velocity fractions much greater than 0.65, or that if they do, they spin down very quickly.

We note that adopting the observed distribution of rotational velocities of Dufton et al. (2013) as the initial velocity distribution for stars in our synthetic populations may introduce an inconsistency, since the sample of Dufton et al. (2013) consists of field stars of all ages. However, as discussed in textbf Dufton et al. (2013) and Sect. 3.1 below, the rotational velocities of the considered single stars are expected to change very little during their main sequence evolution. If binary evolution affects
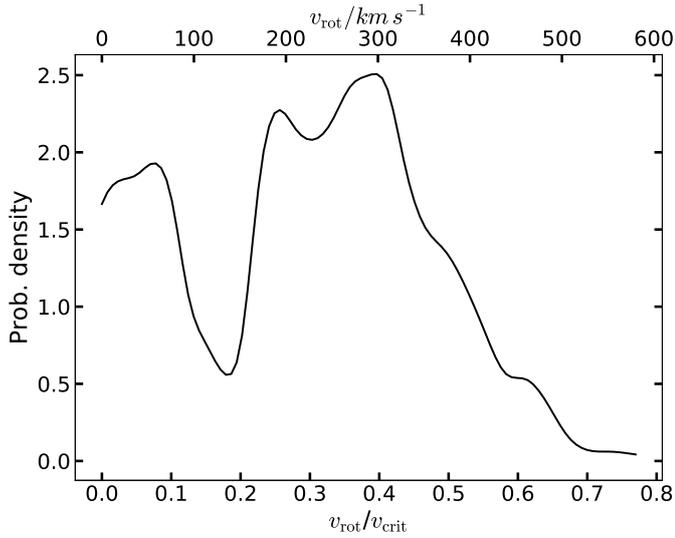
Fig. 1. Deconvolved rotation distribution of early B stars as observed by VLT-FLAMES Survey (Dufton et al. 2013). The distribution was converted to v_{rot}/v_{crit} using 15 $M_\odot$ LMC models at ZAMS. The upper scale shows how the critical velocity fraction values, v_{rot}/v_{crit}, match the equatorial velocities, v_{rot}.

this distribution de Mink et al. (2013), then we would overestimate the number of stars which are born rotating very rapidly. In this case, the predicted number of Be stars from our models may be considered as upper limits.

To compare the models with observations of the SMC open cluster NCG 330 (Milone et al. 2018) in the colour–magnitude diagram, the bolometric luminosities and effective temperature are converted to absolute magnitudes in the *Hubble* Space Telescope Wide-Field Camera 3 filters $F814W$ and $F336W$ by interpolating tables based on synthetic stellar spectra (Girardi et al. 2002). The values of distance modulus and reddening adopted are $(m - M) = 18.92$ and $E(B - V) = 0.06$ respectively. The absorption coefficients used are $A_{F814W} = 2.04E(B - V)$ and $A_{F336W} = 5.16E(B - V)$ (Milone et al. 2009). The effects of gravity darkening are included as described by Espinosa Lara & Rieutord (2011), whereby the effective temperature and luminosity of a star are multiplied by parameters that depend on the inclination angle and fraction of angular critical velocity. Using these corrected effective temperature and luminosity values, we then calculate the absolute magnitudes as described above. The inclination angles, i, in our synthetic population are chosen such that $\cos(i)$ is uniformly distributed between 0 and 1, meaning that one is more likely to observe any given star equator-on than pole-on. Such a distribution describes a random orientation of the rotation axis.

3. Results

3.1. Spin evolution

During the evolution of a slowly rotating star during core hydrogen burning, a strong chemical gradient develops between the convective core and the radiative envelope. The core density increases, and as a reaction the envelope must expand in order to maintain hydrostatic and thermal equilibrium. Equation (2) shows that as the stellar radius increases, the critical velocity decreases, and therefore during main sequence evolution, the critical velocity will fall.

In the absence of internal angular momentum transport, as core density increases, the local conservation of angular momentum demands that the angular velocity of the core increases. Likewise, as the envelope expands, the angular velocity of the envelope decreases. This results in an angular velocity gradient developing between the convective core and radiative envelope. However when the core and envelope are coupled via angular momentum transport, angular momentum is transported from the core to the envelope, decreasing the angular velocity gradient throughout the star. The physical processes responsible for the angular momentum transport in the models studied here are magnetic torques arising from the Tayler-Spruit dynamo (Spruit 2002), which leads to near solid body rotation. While the envelope is expanding and the star is rotating as a solid body, the critical rotation velocity decreases while the equatorial rotation velocity drops only slowly or even increases (see Sect. 3.3).

Figure 2 gives examples of the evolution of critical velocity, equatorial velocity, and the fraction of critical velocity during main sequence evolution for MW and SMC models with initial masses of 5, 15, and 25 $M_\odot$. All models in the plot have an initial critical velocity fraction of approximately 0.6. Although the less massive models have slower equatorial velocities, they also have lower critical velocities (because of a relatively weak dependance on radius with mass), making the critical velocity fraction nearly the same for all models in the plot. It is seen that for the 5 $M_\odot$ models the equatorial rotation velocity remains nearly constant, while the critical velocity decreases. For the 15 $M_\odot$ models, the equatorial rotation velocity increases due to the effects of angular momentum transport. As a result, the critical velocity fraction is generally increasing during hydrogen burning such that the stars are evolving closer to critical rotation, unless angular momentum is drained at a high rate due to mass loss (see Sect. 3.2).

3.2. The effect of mass-loss

The dominating effect of mass-loss through stellar winds is to remove angular momentum, not mass. This is because even in the absence of magnetic fields, the rate of angular momentum loss relative to the total angular momentum is about ten times higher than the rate of mass loss relative to the stellar mass (Langer 1998). Thus, the mass-loss of a given star may strongly affect its spin evolution.

Panels a, c, and e of Fig. 2 show that models at MW metallicity experience a turn-over in the evolution of their critical velocity fraction. This is because in the late stages of hydrogen burning, the mass-loss rate of a given star increases significantly which has the effect of removing angular momentum from the surface at a rate that cannot be compensated by internal angular momentum transport mechanisms, meaning that solid body rotation is no longer a good approximation and the equatorial velocity decreases. This period of strong mass loss is caused by the iron opacity bistability in which partial recombination of Fe ions at effective temperatures of around 22 kK causes a sharp increase in opacity and hence mass loss (Lamers et al. 1995). This behaviour is strongly dependent on metallicity and is therefore weaker in the SMC or LMC models. Comparing panels c and d of Fig. 2, it can be seen that despite both MW and SMC models starting with approximately equal critical velocity fractions, the SMC model achieves a much larger critical velocity fraction at the end of the main sequence. This comparison between MW and SMC models illustrates the effect of mass-loss on the approach to the critical velocity.
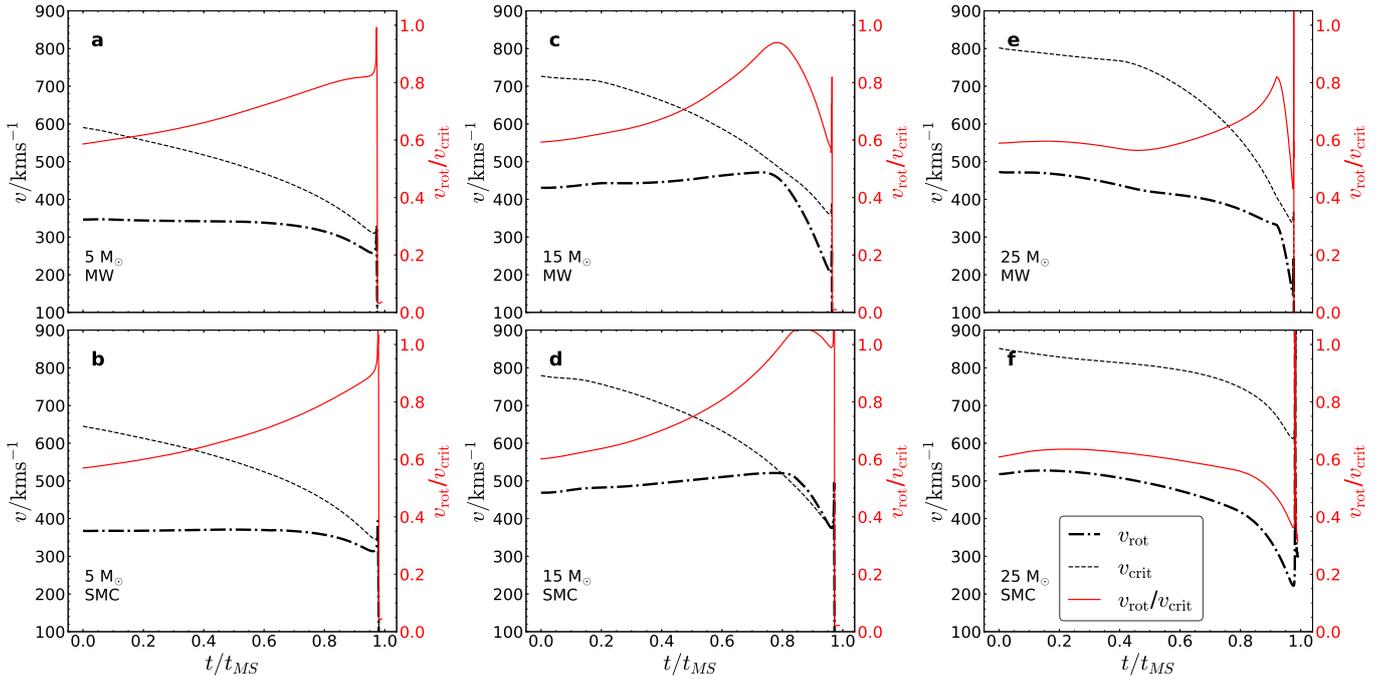
Fig. 2. Evolution of equatorial rotational velocity $v_{\rm rot}$ (thick dot-dashed), critical velocity $v_{\rm crit}$ (dashed), and the critical velocity fraction $v_{\rm rot}/v_{\rm crit}$ (solid red) for 5 $M_\odot$ (*panels a, b*), 15 $M_\odot$ (*panels c, d*), and 25 $M_\odot$ (*panels e, f*) models at MW metallicity (*panels a, c, e*) and SMC metallicity (*panels b, d, f*). The initial critical velocity fraction values are all approximately 0.6. The *X*-axis indicates the fractional main sequence lifetime, $t/t_{\rm MS}$.

Figure 3 shows the ratio of angular momentum at the end of hydrogen burning to the initial angular momentum for models of varying mass and initial critical velocity fraction for MW and SMC models. It is clear that almost every SMC model loses much less angular momentum than the corresponding model at MW metallicity. The exceptions are fast rotating massive SMC models which undergo quasi-chemically homogeneous evolution, and during so become very luminous which leads to increased mass-loss rates. For SMC models, one may judge that mass-loss becomes irrelevant to the angular-momentum budget below masses of around 10 $M_\odot$, where most models (except very fast initial rotators, e.g. with $v_{\rm rot}/v_{\rm crit} > 0.7$) retain more than 90% of their angular momentum. For MW models, we see that only slowly rotating models less massive than 5 $M_\odot$ retain more than 90% of their angular momentum. As expected, the effect of mass loss is strongly metallicity dependent. It is also seen that below 15 . . . 20 $M_\odot$, angular momentum loss becomes less dependent on mass.

Figure 3 shows that for any given mass the fraction of angular momentum lost is a strong function of the initial rotation. For example, a 5 $M_\odot$ model at MW metallicity can lose between 2 and 30% of its initial angular momentum. One contributing factor is the lifetime effect, whereby under the effects of rotation, rotational mixing causes hydrogen to be mixed into the centre of the star and so hydrogen burning can continue for a longer time. For all of our models, the hydrogen-burning lifetime enhancement between the non-rotating model and that with an initial rotation velocity of 600 km s^{-1} never exceeds a factor of 1.5. Therefore, for models losing only small fractions of their total angular momentum as slow rotators (such as low-mass MW metallicity models and all SMC metallicity models), the lifetime effect cannot fully explain the increase in angular momentum loss.

Another effect is rotationally enhanced mass loss. As a star approaches the critical rotation velocity, material at the equator becomes less tightly bound due to the centrifugal force, and therefore one would expect angular momentum lost through winds to increase with rotation velocity. In the models this is governed by Eq. (1). With $v_{\rm rot}/v_{\rm crit} = 0.8$, the mass-loss rates are doubled, so rotationally enhanced mass loss plays only a large role when very high critical rotation fractions are achieved. As an example, the 5 $M_\odot$ models at MW metallicity in Fig. 3 show that in the range of initial $v_{\rm rot}/v_{\rm crit}$ from 0 to 0.4, the total angular momentum lost is almost the same. However, when approaching critical rotation, the enhancement factor becomes divergent, so models rotating near the critical velocity experience tremendous mass loss.

A further effect of rotationally induced mixing is to increase the overall mean molecular weight in the star, μ, compared to models with no rotationally induced mixing. Homologous models suggest a strong dependence on luminosity with mean molecular weight such that $L \propto \mu^4$ (Kippenhahn & Weigert 1990). In turn, mass-loss rates are dependant on luminosity; for the wind prescription used in the models the dependance is approximately $\dot{M} \propto L^2$ (Vink et al. 2000). Therefore, rotationally induced mixing leads to higher mass loss and angular momentum loss. For models which experience quasi-chemical homogeneous evolution where the star can become a helium star, this effect becomes very apparent. Models which undergo quasi-chemical homogeneous evolution for the duration of hydrogen burning (defined by a monotonically increasing surface helium mass fraction) are marked with black circles in Fig. 3. Similarly, models which undergo a phase of quasi-chemical homogeneous evolution (defined by having a slowly increasing difference between surface and central helium mass fraction for longer than one-third of the hydrogen-burning lifetime) are marked by a red circle. Although these models do not have high initial critical rotation fractions, they still lose large fractions of their angular momentum. Quasi-homogeneous evolution
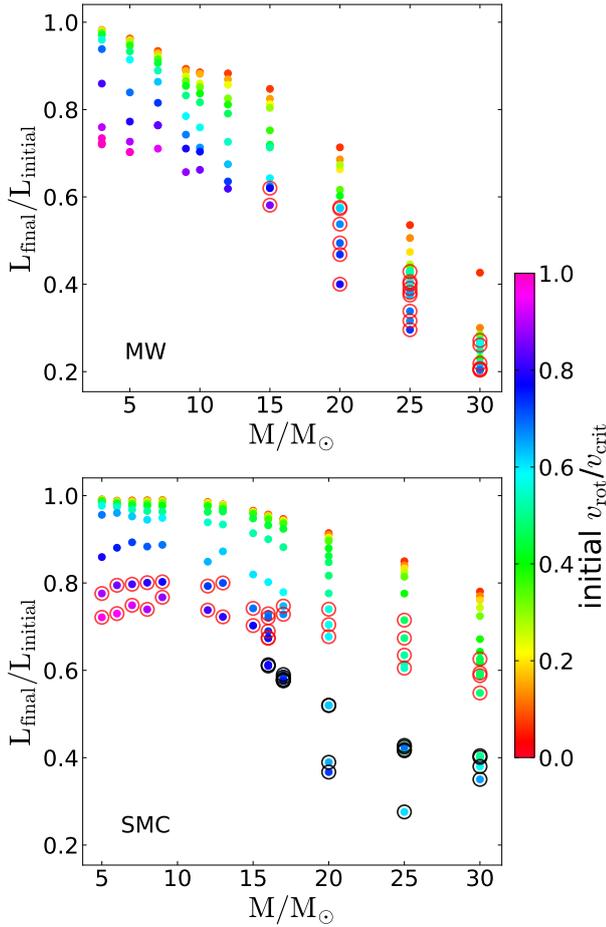
Fig. 3. Ratio of angular momentum at the end of hydrogen burning L_{final} to angular momentum at the start of hydrogen burning $L_{initial}$, as a function of mass for MW (*top*) and SMC (*bottom*) metallicities. The colour of the points represents the initial critical velocity fraction v_{rot}/v_{crit}. Models with a growing helium surface abundance throughout the duration of their evolution are marked by a black circle. Models with a growing helium surface abundance for part of their evolution are marked by a red circle.

occurs more readily in the lower metallicity models because as mass loss is a strong function of metallicity, the MW metallicity models slow down relatively quickly, causing rotational mixing to become less effective, and the homogeneous evolution stops (Yoon et al. 2006).

3.3. The effect of convective core mass

During the main sequence evolution of a massive star, the convective core contracts while the radiative envelope expands. The conservation of angular momentum therefore demands that in the absence of any internal angular momentum transport, the convective core and radiative envelope increase and decrease, respectively, their overall angular velocity (i.e. the core "spins up" while the envelope "spins down"). This tells us that to enforce solid body rotation during core contraction and envelope expansion, angular momentum must be transported from the core to the envelope. This is achieved by magnetic interactions which transport angular momentum along the angular velocity gradient within the star.

Let us now consider two extreme examples. In a rotating star with a negligible envelope mass, the core will dominate the angular momentum budget. Therefore, to maintain a constant

rotational velocity during envelope expansion, a relatively low angular momentum transport rate is required. On the other hand, for an envelope-dominated star to rotate at a constant velocity while the envelope is expanding, the angular momentum transport rate from core to envelope must be high. It is thus likely that internal angular momentum transport mechanisms are unable to meet this demand, and as a result the rotational velocity of the stellar surface will decrease due to the effect of local angular momentum conservation.

In our models, there is an inner region of the star from which angular momentum is being transported and there is an outer region which the angular momentum is being transported to. In between these regions there must be a point which neither gains nor loses any specific angular momentum. The location of this angular momentum "valve" will give an indication as to the strength of the core mass effect as discussed above. Figures 4a and b show the specific angular momentum profiles of a 5 and 15 $M_\odot$ model at one time early in their evolution and one time near the end of hydrogen burning. Hydrogen mass fraction profiles are plotted to indicate the stage of evolution. The models shown are the same as in Figs. 2b and d and have equal initial critical velocity fractions of 0.6. It can be seen that there is a point for each mass at which the specific angular momentum does not change.

Figure 4c shows this more clearly, where the difference in angular momentum at both times, divided by the angular momentum at the earlier time, $\Delta j/j_1$, is plotted. Here, regions where angular momentum is gained have a positive value, whereas regions where angular momentum is lost have a negative value. For the more massive model, the point with a constant specific angular momentum is closer to the edge of the star than for the less massive model. For the 15 $M_\odot$ model, approximately 90% of the total mass is acting as a donor of angular momentum, while for the 5 $M_\odot$ model this figure is 80%. Using the arguments above, the 15 $M_\odot$ model will therefore approach the critical rotation velocity more easily. Furthermore, by inspecting the area under the curves in the region where $\Delta j/j_1$ is positive in Fig. 4c one can determine how much relative angular momentum is gained. For example, if a region from $\frac{m}{M} = m_i$ to $\frac{m}{M} = 1$ had doubled its total angular momentum, the integral $\int_{m_i}^{1} \Delta j/j_1 \mathrm{d}(\frac{m}{M})$ would be equal to $(2-1)(1-m_i)$. Figure 4c shows that the relative angular momentum gain of the matter in the envelope of the 5 $M_\odot$ model is greater than that of the 15 $M_\odot$ model. This tells us that to maintain near-solid-body rotation, a relatively small amount of angular momentum must be transported in the more massive model.

3.4. The effect of efficient rotational mixing

When a star rotates initially at high velocities, quasi-chemically homogeneous evolution can occur. During such evolution, rotational mixing is so efficient that any chemical gradient between core and envelope cannot develop, meaning that the radiative envelope does not expand and the radius of the star remains roughly constant (Maeder 1987; Yoon et al. 2006). However, because the luminosity of a quasi-chemically homogeneously evolving star approaches the Eddington limit, the critical velocity of such a star decreases (through Eq. (2)). Furthermore, the increased luminosity causes a strong increase in the mass-loss rate, meaning that the equatorial velocities of stars undergoing quasi-chemically homogeneous evolution are likely to decrease with time. Such stars therefore evolve with a decreasing critical velocity fraction while quasi-chemically homogeneous evolution occurs.
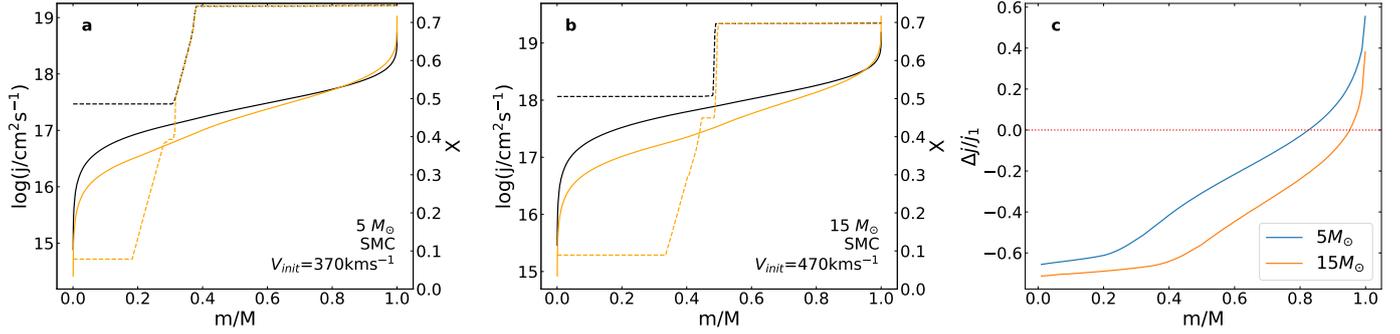
Fig. 4. *a* and *b*: specific angular momentum (solid lines) and hydrogen mass fraction (dotted lines) profiles for two SMC models of masses 5 and 15 $M_\odot$ and initial equatorial velocities of 370 and 470 km s^{-1} respectively. These are the same models plotted in *panels b* and *d* of Fig. 2 and both models have initial critical velocity fractions of around 0.6. Profiles are plotted for models where central helium mass fraction is 0.45 (black), and 0.91 (orange). *c*: for each model in *panels a* and *b* the fractional difference in specific angular momentum is plotted between the two times. The blue line represents the 5 $M_\odot$ model,the orange the 15 $M_\odot$ model. The dotted red line gives a reference for no angular momentum transport. The *X*-axis in all plots indicates the fractional mass co-ordinate.

This behaviour is shown for 25 $M_\odot$ models in Figs. 2e and f. It can be seen that the highest critical velocity fractions occur during the early part of the stars' lifetime because the critical velocities (dashed lines) decrease relatively slowly while the equatorial velocities (dot-dashed lines) fall due to angular momentum loss. In the MW model, quasi-chemically homogeneous evolution is shutdown when the star reaches an age of around 80% of the hydrogen burning lifetime and from this point on the star evolves normally and advances towards the critical velocity. The phase of quasi-chemically homogeneous evolution ends because as the rotational velocity decreases, rotational mixing processes become less efficient and a chemical gradient eventually develops in the star which provides a barrier to mixing through buoyancy forces (Heger et al. 2000) and effectively "turns off" quasi-chemically homogeneous evolution.

For a star to evolve to a high critical velocity fraction, it must have a significant initial rotation velocity but also be rotating slowly enough to avoid quasi-chemically homogeneous evolution. As the minimum rotation rate required for quasi-chemically homogeneous evolution decreases with increasing mass (Yoon et al. 2006), very massive stars rotate at high critical velocity fractions for only very short fractions of their lifetimes, thus explaining the rarity of Oe stars.

3.5. Nitrogen enrichment

Here we address the question of whether or not Be stars formed through a single star evolving towards the critical velocity are expected to show significant surface nitrogen enrichment, where nitrogen is the product of hydrogen burning and is brought to the stellar surface through rotationally induced mixing. Figure 5 shows the evolution of both surface nitrogen abundance and critical velocity fraction as a function of the fractional hydrogen-burning lifetime. Displayed are models with initial masses of 5, 15, and 25 $M_\odot$ with SMC, LMC, and MW metallicities. As discussed by Brott et al. (2011) the relative increase of the surface nitrogen abundance decreases with increasing metallicity, and this is why we see weaker nitrogen enrichment in the MW models than in the LMC and SMC models. It is also clear that rotationally induced mixing is more efficient in more massive stars, owing to the effects of increased radiation pressure in these latter objects (Maeder 1987; Yoon et al. 2006).

In light of the results shown in the bottom panels of Fig. 5, we expect that in the Milky Way, nitrogen is never enhanced

by much more than a factor of ten for models that rotate near critical velocity. On the other hand, the LMC and SMC models that attain near critical rotation velocities show surface nitrogen enhancements of at least a factor of 10 and up to approximately a factor of 30.

We therefore judge that single Be stars in the LMC should have surface nitrogen abundances $\epsilon = 12 + \log(N/H)$ no smaller than around 7.7, and in the SMC no smaller than around 7.4. In the Milky Way, we do not expect the single Be stars to have outstanding nitrogen surface abundances.

4. Population synthesis results

4.1. Predicted fractions of Be stars

In this section, we discuss synthetic populations of coeval, rotating single stars as described in Sect. 2.2. These results can then be compared to the number of Be stars observed in young star clusters of various ages. From our models, we derive the fraction of Be stars within one bolometric magnitude (assumed to be equal to one visual magnitude) of the turn-off. We consider a stellar model to correspond to a Be star when its rotational velocity exceeds a predefined fraction of critical rotation. Figure 6 shows the result as a function of age for various threshold critical velocity fractions and metallicities.

A striking feature of this plot is the maximum in Be fraction for all metallicities near 10 Myr. At $t = 0$ there are no Be stars because, as discussed earlier, the initial rotation distribution prevents O stars entering the ZAMS with v_{rot}/v_{crit} fractions greater than around 0.7. The 30 $M_\odot$ models take approximately 5 Myr to evolve towards critical rotation, and shortly after which they leave the main sequence. From 5 to 10 Myr the Be fraction grows sharply as angular momentum loss from winds diminishes. From 10 to 20 Myr the Be fraction falls because of the core-mass effect as discussed in Sect. 3.3. Comparing the hydrogen-burning lifetimes of non-rotating MW models, it is found that populations with ages from 10 to 20 Myr have a main sequence turn-off mass of around 17 $M_\odot$. These models are in a "Goldilocks" situation where they are massive enough to have an appreciable convective core but not so massive as to lose large amounts of angular momentum.

Furthermore, we see that the Be fraction increases at earlier times for the lower metallicity models and that there is a clear trend in metallicity which shows that single Be stars become more common with decreasing metallicity. Both of these
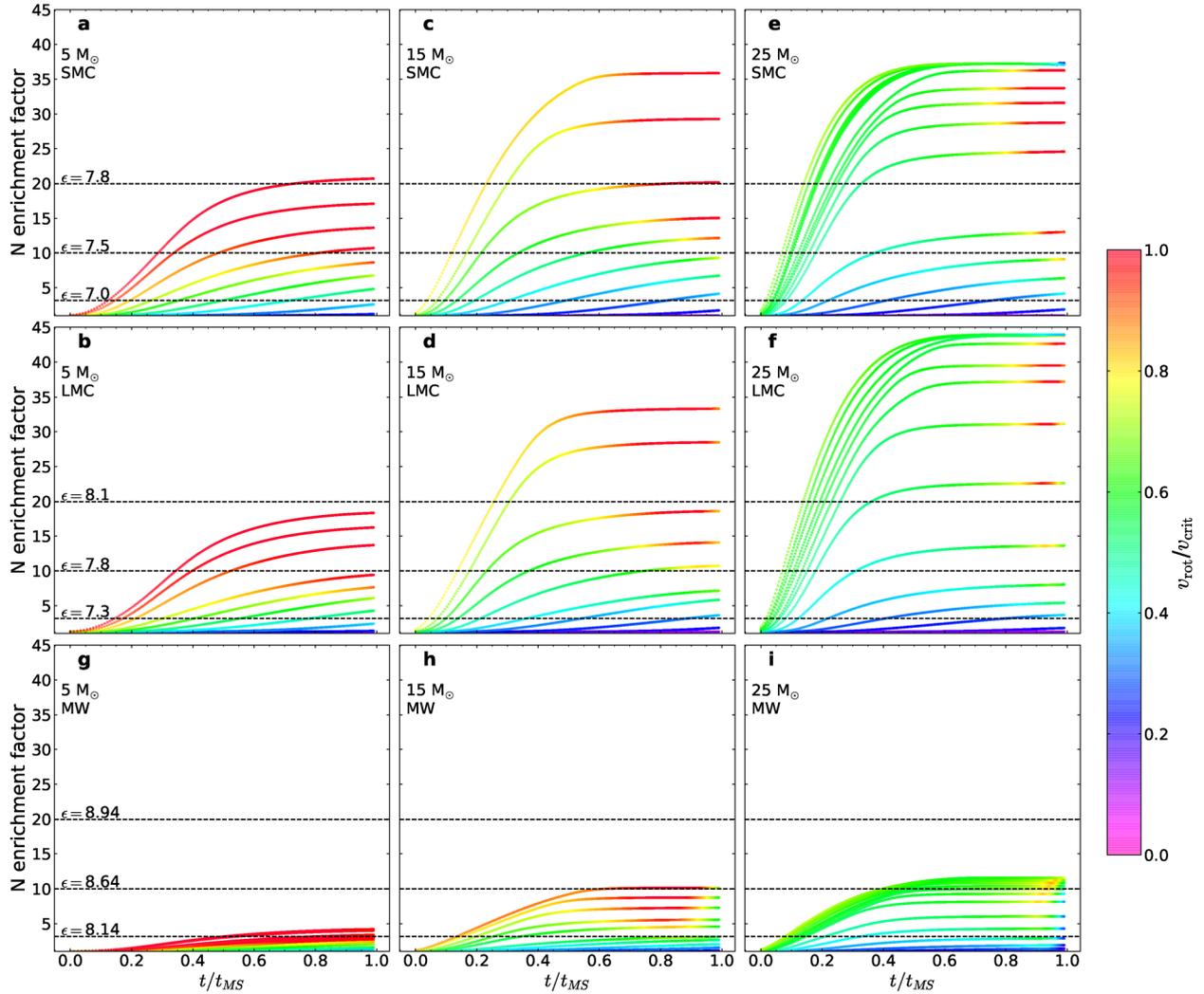
Fig. 5. Surface nitrogen enrichment factor, computed as the nitrogen mass fraction divided by the initial nitrogen mass fraction as a function of the fractional hydrogen-burning lifetime, t/t_{MS}, for models with initial rotational velocities between 0 and 600 km s^{-1} and initial masses of 5, 15, and 25 $M_\odot$ as marked in the plot. *Top, middle, and bottom panels*: SMC, LMC, and MW compositions, respectively. The colour scale corresponds to the critical rotation fraction, $v_{\rm rot}/v_{\rm crit}$. For each metallicity, various nitrogen abundances, $\epsilon = 12 + \log(N/H)$, are displayed as dotted black lines with the value given in the plots of the *left column*.

features are a result of the fact that the strength of angular momentum loss is metallicity dependant as discussed in Sect. 3.2.

It is also found that the Be fraction is strongly dependant on the chosen Be criterion. When a critical velocity fraction, $v_{\rm rot}/v_{\rm crit}$, of 0.7 is chosen as the Be criterion, we predict Be fractions in the Magellanic Clouds in the range 15−35%. Conversely, when we restrict Be stars to being nearly critical rotators ($v_{\rm rot}/v_{\rm crit} > 0.98$), the Magellanic Cloud Be fraction lies in the range of 0−10% and is almost zero for population ages greater than 50 Myr.

4.2. Fast rotators in the colour–magnitude diagram

Using the procedure outlined in Sect. 2.2 we built synthetic colour–magnitude diagrams to indicate the expected positions of fast rotators. Figure 7 shows the colour–magnitude diagram positions and critical velocity fractions of our SMC models with a coeval age of 35 Myr. Over-plotted on our theoretical predictions are *Hubble* Space Telescope observations of the SMC cluster NGC 330 (Milone et al. 2009), We see that the nearly critically

rotating stars are located very close to the turn-off, as can be expected by the fact that our models only achieve high fractions of critical rotation near core hydrogen exhaustion (see Figs. 2 and A.1). Figure 7 also shows the effects of gravity darkening, with the slowly rotating models almost confined to a single isochrone while the fast rotators suffer strong gravity darkening and display a wider range of colours due to a relatively large spread in effective temperatures. Appendix B shows the same colour–magnitude diagram but ignoring the effects of gravity darkening for comparison.

In the following analysis we assume that the Hα emitters in NGC 330 are Be stars. The observations in Fig. 7 show that most of the observed Hα emitters are redder than the ordinary main sequence stars. This segregation is not a unique feature to NGC 330, with many LMC and SMC clusters exhibiting the same trait (Milone et al. 2018). Telting et al. (1998) have suggested through observations of Be stars, the spectra of which spectra show rapid switching between containing emission lines and not, that the decretion disc can contribute up to 40% of a Be star's flux. Because our models do not include the contribution of a Be star's decretion disc to the observed fluxes, it is not
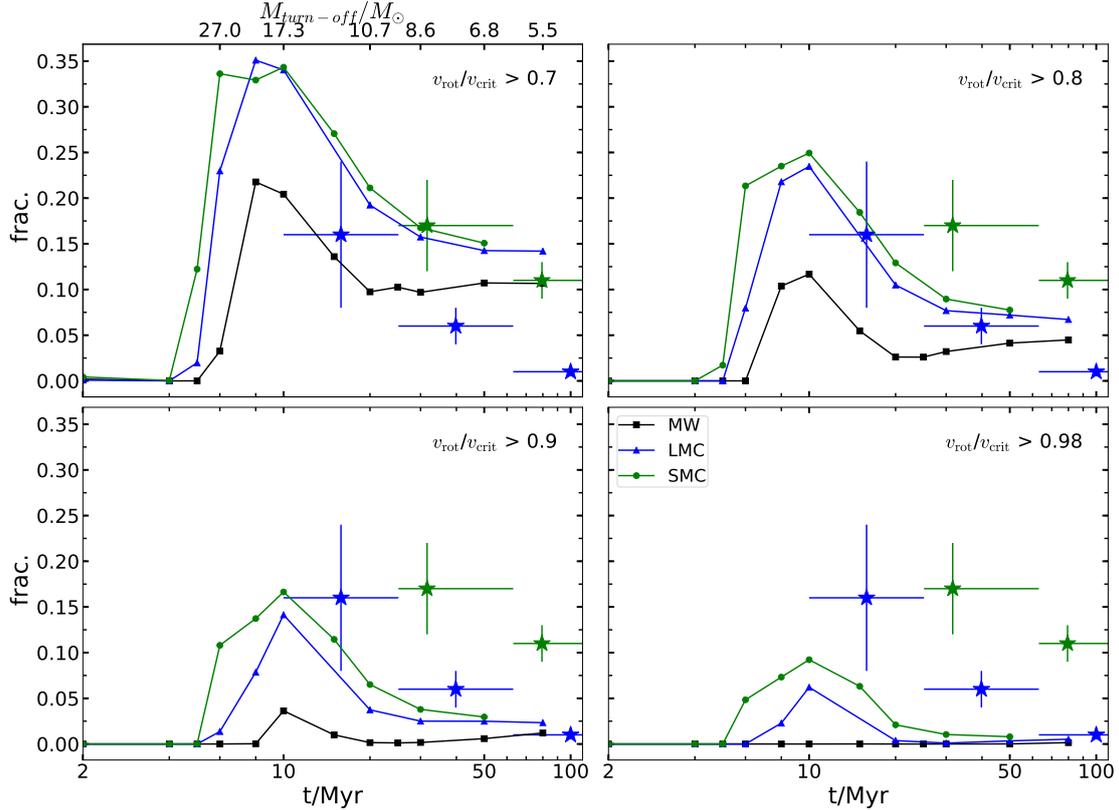
Fig. 6. Fractions of stars rotating faster than various values of the critical rotation fraction, $v_{\rm rot}/v_{\rm crit}$, as given in the *top left corner* of each plot, in our synthetic coeval single star populations as function of their age. Considered only are stars brighter than one bolometric magnitude below the main-sequence turn-off. Metallicities are displayed as MW (black), LMC (blue) and SMC (green). *For the top left panel*: top scale gives the main-sequence turn off mass for non-rotating MW models. Observations with error bars from Iqbal & Keller (2013) are shown as green and blue stars for SMC and LMC observations respectively.

meaningful to compare the colours of our fast-rotating models with those of observed Be stars. However, assuming that the error on the magnitudes of our synthetic Be stars is at most 0.35 mag, we may consider the relationship between the relative number of Be stars and apparent magnitude.

Figure 8 shows the Be fraction of our model predictions in $F814W$ apparent magnitude bins for various threshold rotation rates for stellar models to be considered a Be star. We see that our model Be stars are strongly biased to being located near the main sequence turn-off, around $m_{F814W} = 15.4$ mag, where depending on how fast we require a Be star to rotate, the Be fraction is between 30 and 90%. Figure 8 compares our model predictions to Be star counts in NGC 330 (Milone et al. 2018). The observations show that in NGC 330 the Be fraction is approximately 0.6, and it remains rather constant within a wide magnitude range of 17.0−15.6 mag. This result is quantitatively confirmed by a recent study of Bodensteiner et al. (2020), who used MUSE spectroscopy to identify Be stars in the core of NGC 330.

Comparing our models with the observations, Fig. 8 reveals that when assuming that Be stars are required to rotate only at 70% or more of the critical rotation velocity, our single star models agree with the observed Be star count in NGC 330 at the turn off region. However, they strikingly fail in two respects. Firstly, even adopting the least stringent threshold value for Be stars, our models fail to produce the large number of observed Be stars. Secondly, our models cannot reproduce the fact that the Be star fraction in NGC 330 is constant over a range of 1.5 mag.

Here, the second failure appears to have the greatest consequences. The total number of Be star can in principle be boosted

by lowering the rotation threshold for considering the models a Be star, or by adopting larger initial rotation velocities. However, it is an intrinsic feature of the rotating single star models to increase the ratio of rotation to critical rotation velocity with time (Fig. 5; see also Ekström et al. 2008). Thus, it appears quite unlikely that the observed population of Be stars in NGC 330 can be explained solely by single star evolution.

5. Discussion

5.1. Uncertainties

It is important to keep in mind that models are simply that and at some point they must fail to reflect the behaviour of real stars. Martins & Palacios (2013) found that the hydrogen-burning lifetimes given by models studied here differ from those of MESA models by approximately 15%. As this is merely a discrepancy in the clock, but not in the physical behaviour of the models (Marchant 2017), this is concerning, but should not change the main results presented here.

Another issue is the treatment of mass loss, which is a strong factor in determining the evolution of a model towards the critical velocity. The mass-loss prescription used (Vink et al. 2000) was calibrated for models in the range $15-20\,M_\odot$, so it may be questionable whether this scheme is accurate for models outside this range. Furthermore, the correct treatment of a star rotating close to the critical velocity is complex. Near the critical velocity, two distinct winds are expected to form, a cold equatorial wind (which carries away angular momentum) and a warm
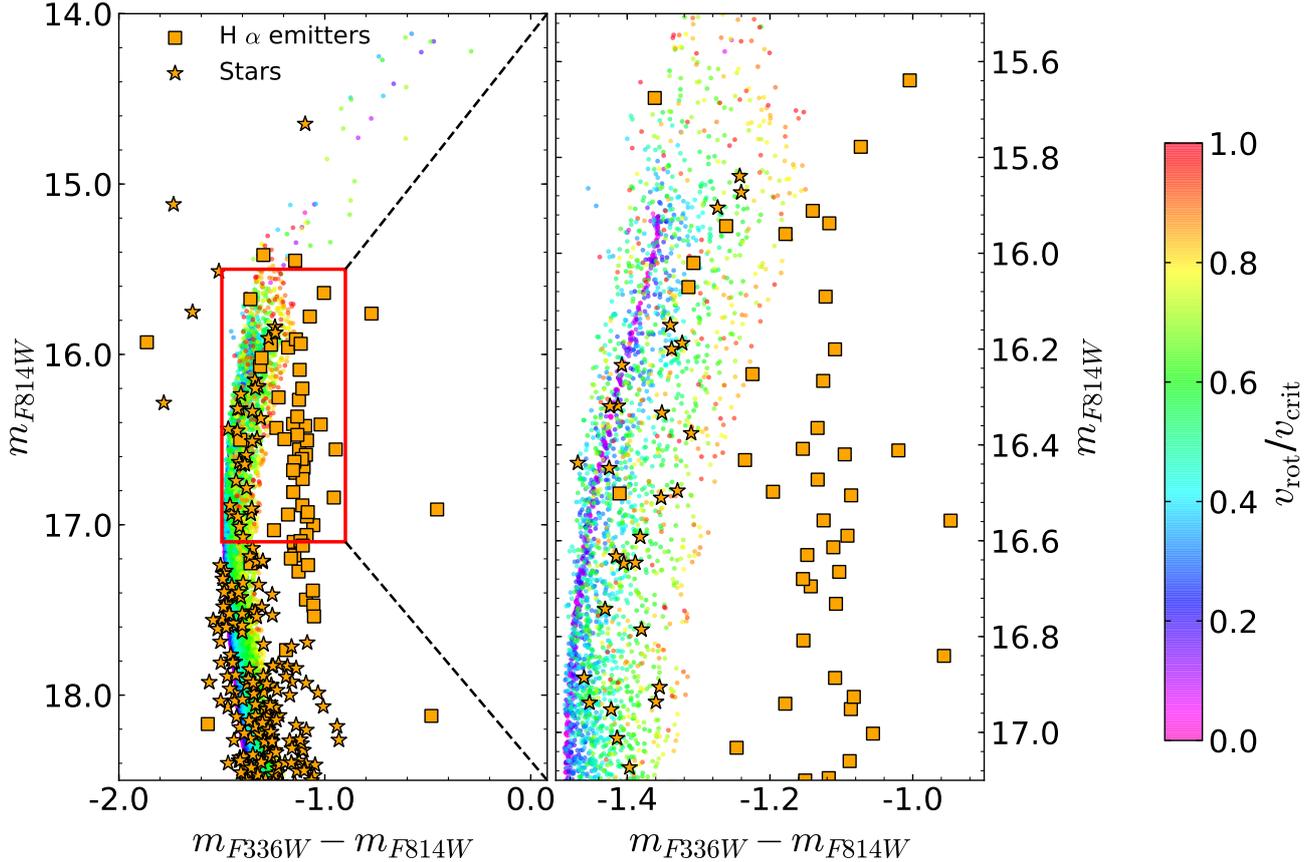
Fig. 7. Synthetic colour–magnitude diagram of a 35 Myr star cluster at SMC metallicity, where each dot represents one single star and the colour gives the critical velocity fraction, v_{rot}/v_{crit} as indicated by the colour bar. Gravity darkening is included assuming a random orientation of the rotation axis. Over plotted are observations of SMC cluster NGC 330 (Milone et al. 2018), with Hα emitters marked by orange squares and normal stars as orange star symbols. *Right panel*: region indicated by the red box in the *left panel*. To convert the models to apparent magnitudes a distance modulus of 18.92 mag and a reddening of 0.06 mag were used.
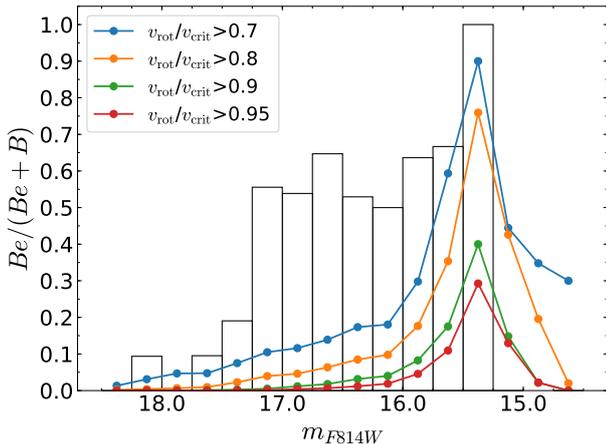
Fig. 8. Histogram of the Be fraction of stars in SMC cluster NGC 330 (Milone et al. 2018) as a function of apparent magnitude in the *Hubble* Space Telescope Wide-field Camera 3 filter *F814W*, m_{F814W} plotted as white columns. It is assumed that Hα emitters are Be stars. Over plotted as coloured lines are our model predictions in the same magnitude bins for various minimum rotation rates to be counted as a Be star, as given in the legend.

polar wind (which carries away less angular momentum). It is not apparent which wind has the dominating effect, although the winds of models presented here always carry away angular

momentum. Equation (1) demands that as a star approaches the critical rotation velocity, the mass-loss rate becomes infinite. It is also questionable whether or not this is correct treatment of the mass loss of a critically rotating star.

In the SMC, Rímulo et al. (2018) matched light-curve models to observations of 54 Be stars and determined that the typical mass-loss rate of a Be star in the mass range $10-20\,M_\odot$ is of the order $10^{-10}\,M_\odot\,yr^{-1}$. Our models predict that only stars with initial masses of less than around $10\,M_\odot$ have such mass-loss rates on the main sequence. This discrepancy highlights the fact that the models studied here are one-dimensional and hence may struggle to accurately represent the mass loss of a rotating star (which is a two-dimensional problem).

Our definition of a Be star is a B star that is rotating close to the critical velocity. However it would appear that nature has a slightly different definition, with pulsations perhaps playing a role (Rivinius et al. 2001; Neiner & Mathis 2014). Pulsations could serve to kick matter off of the stellar surface and aid the formation of a circumstellar disc. Observations with the CoRoT space telescope show that Be stars display pulsations that can transport angular momentum through the star (Huat et al. 2009), thus affecting the evolution of rotation velocities. The interaction of rotation and pulsations is out of the scope of this work and the results of such endeavours are eagerly awaited. Furthermore, recent observations with the TESS space telescope imply that the Be star disc could be fed by mass ejections from starspots (Balona & Ozuyar 2019). Be stars are complex objects,

with rotation being a key ingredient of the Be phenomenon, but perhaps not the only one.

Our population synthesis results are dependant on the initial rotation distribution that is assumed. Whereas Dufton et al. (2013) used high quality data, a large and unbiased sample of stars, and corrected for effects such as macro-turbulence, other rotational velocity distributions are available (Martayan et al. 2006; Hunter et al. 2008; Huang et al. 2010). While our quantitative results might change using one of these other distributions, we do not expect a change in the qualitative behaviour of our results, which appears to be determined by the evolutionary factors discussed in Sect. 3.

5.2. Comparison with previous models

The frequencies of single Be stars have been predicted from models by Ekström et al. (2008) and Granada et al. (2013, 2016). A major difference between these sets of models and the models studied here is the inclusion of the effects of an internal magnetic field which strongly couples the core and envelope, and may increase the predicted numbers of critically rotating stars.

Ekström et al. (2008) predict at solar metallicity and an age of 25 Myr the fraction of stars with a brightness of up to two magnitudes below the turn-off and rotating at the critical velocity is 5%, compared to 0% found here. However when one looks at the fraction of stars rotating faster than $v_{rot}/v_{crit} = 0.7$ at 20 Myr, Ekström et al. (2008) finds a Be fraction of around 15%, compared to 8% found here. Both sets of models agree that at ages greater than around 40 Myr, almost no stars rotate at the critical velocity. Ekström et al. (2008) used a Gaussian-like initial rotation distribution with a peak at $\Omega/\Omega_{crit} = 0.6$, which in the Roche model corresponds to $v_{rot}/v_{crit} \approx 0.4$, and therefore is judged to be a similar initial rotation distribution to the one used in this work. As demonstrated by Ekström et al. (2008) mass-loss rates play a crucial role in the evolution of the surface rotation. In our models above $10 M_\odot$, a turnover in v_{rot}/v_{crit} is caused by strong mass loss at late times (see Fig. 2). When using the Kudritzki & Puls (2000) mass-loss scheme, Ekström et al. (2008) found this turnover not to occur, and so those models spend more time at high v_{rot}/v_{crit} values and so Be stars become more common. It is therefore concluded that mass loss is equally as important as angular momentum transport in producing stars which rotate close to the critical velocity at galactic metallicity. At $Z = 0.002$ (a metallicity similar to our SMC models), Ekström et al. (2008) calculate a maximum in Be fraction at an age of 10 Myr of around 10%, in good agreement with the results presented here.

Both Ekström et al. (2008) and Granada et al. (2013) find that Be stars should become rarer at lower metallicities, which is in contradiction to the results presented here and the general trend seen by observers (Iqbal & Keller 2013; Maeder et al. 1999; Martayan et al. 2010).

5.3. Comparison with further observations

Iqbal & Keller (2013) observed Be star fractions within 1 visual magnitude of the turnoff in LMC and SMC clusters. Such observations are directly comparable with Fig. 6, with the data overplotted on our predictions. In clusters of ages from 7 to 8 Myr the Be fraction decreases from 15% to 0%. When defining the Be criterion to be 0.9 v_{rot}/v_{crit}, a similar behaviour is found albeit at later ages. Iqbal & Keller (2013) also find that Be fractions increase with decreasing metallicity, in agreement with our models.

Both Maeder et al. (1999) and Martayan et al. (2010) found that Be stars are three to five times more frequent in the SMC than the galaxy, again in fairly good agreement with the model predictions. Martayan et al. (2010) reported that the distribution of Be star frequency across spectral types does not depend on metallicity. As Fig. 6 shows similar trends for all metallicities, this behaviour is confirmed by our models.

Observations from Tarasov (2017) show that Be stars become most common in clusters with ages of 12−20 Myr, in relatively good agreement to the model predictions. Golden-Marx et al. (2016) found that in the SMC the frequency of Oe stars is strongly peaked around O9 spectral types. Furthermore, the Oe to O star fraction was measured as 0.26, compared to 0.03 for the MW. This measurement supports our result that very few stars with high critical velocity fractions and ages of less than 10 Myr should be found in the MW, but are found at lower metallicities (see lower panels of Fig. 6).

Owing to the fact that the results of our population synthesis rely strongly on the adopted initial rotation distribution, one may question whether it is appropriate to assume that stars in the MW and Magellanic Clouds have equivalent initial critical rotation fractions. Whether the observed trends in Be fraction with metallicity are due to stellar evolution or a metallicity-dependant rotation distribution is not clear. If lower metallicity stars were to rotate significantly faster, rotationally enhanced mass loss would hinder the formation of Be stars at lower metallicities, therefore there is a limit to how much faster stars at lower metallicities can rotate. Even though Penny et al. (2004) found no significant difference between rotational velocities of O-type stars in the Milky Way and Magellanic Clouds, Keller (2004) concludes that LMC stars are more rapidly rotating than stars in the Milky Way. It is curious to consider that even if LMC stars have faster equatorial velocities, due to their compactness they have larger critical velocities, and hence perhaps the same initial v_{rot}/v_{crit} as galactic stars.

5.4. Comparing the single and binary star formation channels of Be stars

Whereas in this work we focus on the single star formation channel for Be stars, it is evident that Be stars can also be formed through close binary evolution. The main mechanism is spin-up by accretion, which is expected to occur as a consequence of mass transfer (Langer 2012). The class of Be/X-ray binaries (Reig 2011) provides strong support for this picture. Pols et al. (1991) showed through detailed models that Be stars may be produced by mass accretion from a companion star in the course of close binary evolution. Using simplified binary evolution calculations, Shao & Li (2014) demonstrated that potentially a large enough number of them could emerge from binary evolution to explain the currently observed Be star populations. In the following, we discuss several basic differences which can be expected between Be stars formed through binary interaction and those formed through the single star channel.

As we have seen above, when using the rotational velocity distribution of Dufton et al. (2013), it is difficult for single star models to achieve very-close-to-critical rotation (lower right panel of Fig. 6). To remedy this would require that a significant fraction of stars be born with near critical rotation. For low enough mass or metallicity, this group of stars would the remain rapidly rotating throughout their main sequence lifetime. Such a picture appears not to be supported by observations (McSwain & Gies 2005). Accordingly, single star evolution only appears to be able to explain significant Be star populations if

decretion discs are also able to form in stars rotating significantly below critical.

In mass-transferring binary evolution models, this is different. The angular-momentum of the mass-gainer increases quickly, such that critical rotation can be achieved after a relative mass increase of the mass-gainer of 10% or less (Packet 1981). During mass transfer there is no fine-tuning mechanism that switches off accretion when a given rotation rate is reached; instead the only limit is critical rotation. Therefore, all mass-transferring binaries where tides do not limit the spin-up of the mass-gainer – which is the vast majority – are expected to produce a critically rotating main sequence star (Langer 2012). After the accretion phase, the two mechanisms that affect the single stars, namely, spin-down by mass loss and spin-up due to core contraction, will also affect the spun-up mass-gainer. Whereas the wind-induced drainage of angular momentum may spin down some of the most massive mass-gainers, the core contraction accompanying central hydrogen burning ensures that most of them remain at critical rotation for the rest of their main sequence evolution.

Consequently, whereas single star evolution leads to an increase of the rotation velocity relative to its critical value in many cases, the binary channel can produce a much larger number of stars living at critical rotation for a long time. Furthermore, Wang et al. (2020) find that the initial mass ratio limit for stable mass transfer leads naturally to a restriction of binary-produced Be stars to within about two magnitudes of the cluster turn-off, which compares well with observations when interpreting the Hα emitting stars in NGC 330 as Be stars (Milone et al. 2018).

A further important difference between the Be stars produced via single and binary evolution concerns their expected surface abundances. As discussed above, the mass-gainer of a binary system may only accrete a small amount of mass to spin up. In this case, only material from the outer envelope of the donor star is incorporated into the mass-gainer. As this material is generally not enriched in hydrogen-burning products, one would expect Be stars formed through the binary channel to not be significantly polluted by accretion. Detailed binary evolution models with LMC metallicity (Langer et al., in prep.) suggest that the surface nitrogen mass fraction of spun-up mass gainers is at most tripled compared to the baseline nitrogen abundance. Additionally, the spun-up mass-gainers in the models of Langer et al. (in prep.) had ordinary rotation rates before the mass-transfer episode. As such, they established a strong mean molecular weight barrier between core and envelope, which prevents any significant rotationally induced mixing after their spin-up.

In Sect. 3.5 we argue that single Be stars ought to have much larger surface nitrogen enhancements (by as much as a factor 30; cf., Fig. 5). A diagnostic to discriminate single and binary Be stars would then be their surface nitrogen abundances. Dunstall et al. (2011) find that in the LMC cluster NGC 2004, only two Be stars from a sample of 11 were measured to have a nitrogen abundance of $\epsilon = 12 + \log(\text{N/H})$ greater than 7.8, while the other 9 Be stars had ϵ of less than 7.4. This observed bimodal distribution supports the idea of the binary and single Be star formation channels producing populations with different nitrogen enrichments, and would suggest that in NGC 2004 the binary formation channel dominates. Also, Dunstall et al. (2011) found that the nitrogen abundances of the majority of the LMC Be stars observed in the VLT-FLAMES Survey of Massive Stars are not consistent with single star evolution. Moreover, the Be star NGC 330-B 12 was found to be almost devoid of nitrogen lines and to possess a spectrum inconsistent with single star

evolution models (Lennon et al. 2005), providing further evidence that Be stars can be formed by binary interactions.

Finally, we note that a key difference between Be stars produced by the two channels concerns their potential binary companions. Since the initial rotational velocity distribution for single stars and stars in binaries appears to be similar (Ramírez-Agudelo et al. 2015), we would expect a significant fraction of Be stars formed through the single star channel (i.e. without accretion-induced spin-up) to have unevolved main sequence companions. However, essentially no such stars are known. Vice versa, whereas massive binary-produced Be stars may be single since they lost their companion when it produced a supernova explosion, the lower mass binary-produced Be stars should all have evolved companions: subdwarfs or white dwarfs. While those are very hard to detect (Schootemeijer et al. 2018), recent studies of disc truncation of apparently single Be stars suggest that unseen companions are indeed present in the majority of cases (Klement et al. 2019).

6. Conclusions

We have identified and discussed three factors which affect a star's evolution towards the critical velocity throughout main sequence evolution. Mass loss through stellar winds has the effect of removing angular momentum from a star, and thus hinders its approach to critical velocity. The ratio of convective core mass to the total stellar mass strongly affects the internal angular momentum transport, which is crucial for an expanding envelope to maintain a fast rotational velocity. Lastly, the occurrence of quasi-chemically homogeneous evolution prevents the stellar envelope from expanding, thus preventing the critical velocity from decreasing, and also increases the angular momentum lost through stellar winds.

When using an observed distribution of B star rotational velocities to construct synthetic stellar populations, we find that our single star models predict few stars rotating at near-critical velocities, although we do predict as many as 35% of OB stars to rotate at more than 70% of their critical velocity. We therefore conclude that if Be stars are near-critical rotators, then single star models cannot explain the observed numbers of Be stars. In this case, most Be stars must be the product of mass-transfer in binary systems.

If Be stars instead only rotate at 70−80% of their critical velocity, then the observed Be star fractions can be reasonably described by single star evolution (see Fig. 6). However, in the ~40 Myr old SMC cluster NGC 330, Be stars are observed in significant numbers down to almost two magnitudes below the main sequence turn-off. Independent of the rotation threshold for the Be phenomenon, our single star models predict that Be stars should be located only in a narrow luminosity range near the turn-off (see Fig. 8), which disagrees with observations of NGC 330.

Whereas significant uncertainties remain, specifically in reconciling how stars that appear to rotate at 70% of their critical velocity can still form decretion discs and why so few Be stars are observed to rotate near their critical velocity, it appears evident that the observed Be star populations cannot be explained by single star evolution alone, and that it may not be the dominant channel for Be star formation. Nevertheless, single star evolution will contribute, most strongly so in the age range from 8 to 20 Myr, at least at subsolar metallicity.

Furthermore, our single star models predict that the surfaces of rapidly rotating single stars should be contaminated with freshly synthesised nitrogen, the more so the faster the rotation.

In spun-up mass-gainers of binary systems, this is not necessarily so. The observations of non- or weakly nitrogen-enriched surfaces in several groups of Be stars therefore strengthens the conclusion that the majority of these objects cannot originate from single star evolution.

References

Baade, D., Rivinius, T., Štefl, S., & Kaufer, A. 2002, A&A, 383, L31
Balona, L. A., & Ozuyar, D. 2019, ArXiv e-prints [arXiv:1911.03068]
Bodensteiner, J., Sana, H., Mahy, L., et al. 2020, A&A, in press, https://doi.org/10.1051/0004-6361/201936743
Brott, I., de Mink, S. E., Cantiello, M., et al. 2011, A&A, 530, A115
de Mink, S. E., Langer, N., Izzard, R. G., Sana, H., & de Koter, A. 2013, ApJ, 764, 166
Dufton, P. L., Dunstall, P. R., Evans, C. J., et al. 2011, ApJ, 743, L22
Dufton, P. L., Langer, N., Dunstall, P. R., et al. 2013, A&A, 550, A109
Dunstall, P. R., Brott, I., Dufton, P. L., et al. 2011, A&A, 536, A65
Ekström, S., Meynet, G., Maeder, A., & Barblan, F. 2008, A&A, 478, 467
Espinosa Lara, F., & Rieutord, M. 2011, A&A, 533, A43
Girardi, L., Bertelli, G., Bressan, A., et al. 2002, A&A, 391, 195
Golden-Marx, J. B., Oey, M. S., Lamb, J. B., Graus, A. S., & White, A. S. 2016, ApJ, 819, 55
Granada, A., Ekström, S., Georgy, C., et al. 2013, A&A, 553, A25
Granada, A., Georgy, C., Haemmerlé, L., Ekström, S., & Meynet, G. 2016, in Bright Emissaries: Be Stars as Messengers of Star-Disk Physics, eds. T. A. A. Sigut, & C. E. Jones, ASP Conf. Ser., 506, 33
Heger, A., Langer, N., & Woosley, S. E. 2000, ApJ, 528, 368
Heger, A., Woosley, S. E., & Spruit, H. C. 2005, ApJ, 626, 350
Huang, W., Gies, D. R., & McSwain, M. V. 2010, ApJ, 722, 605
Huat, A.-L., Hubert, A.-M., Baudin, F., et al. 2009, A&A, 506, 95
Hunter, I., Lennon, D. J., Dufton, P. L., et al. 2008, A&A, 479, 541
Iqbal, S., & Keller, S. C. 2013, MNRAS, 435, 3103
Keller, S. C. 2004, PASA, 21, 310
Kippenhahn, R., & Weigert, A. 1990, Stellar Structure and Evolution (Springer-Verlag)
Klement, R., Carciofi, A. C., Rivinius, T., et al. 2019, ApJ, 885, 147
Kriz, S., & Harmanec, P. 1975, Bull. Astron. Inst. Czechoslov., 26, 65
Kudritzki, R.-P., & Puls, J. 2000, ARA&A, 38, 613
Lamers, H. J. G. L. M., Snow, T. P., & Lindholm, D. M. 1995, ApJ, 455, 269
Langer, N. 1998, A&A, 329, 551
Langer, N. 2012, ARA&A, 50, 107
Lennon, D. J., Lee, J. K., Dufton, P. L., & Ryans, R. S. I. 2005, A&A, 438, 265
Li, G.-W., Shi, J.-R., Yanny, B., et al. 2018, ApJ, 863, 70
Liu, Q. Z., van Paradijs, J., & van den Heuvel, E. P. J. 2006, A&A, 455, 1165
Maeder, A. 1987, A&A, 178, 159
Maeder, A., Grebel, E. K., & Mermilliod, J.-C. 1999, A&A, 346, 459
Marchant, P. 2017, PhD Thesis, Rheinische Friedrich-Wilhelms-Universität Bonn
Martayan, C., Frémat, Y., Hubert, A. M., et al. 2006, A&A, 452, 273
Martayan, C., Baade, D., & Fabregat, J. 2010, A&A, 509, A11
Martins, F., & Palacios, A. 2013, A&A, 560, A16
McSwain, M. V., & Gies, D. R. 2005, ApJS, 161, 118
Milone, A. P., Bedin, L. R., Piotto, G., & Anderson, J. 2009, A&A, 497, 755
Milone, A. P., Marino, A. F., Di Criscienzo, M., et al. 2018, MNRAS, 477, 2640
Neiner, C., & Mathis, S. 2014, in Precision Asteroseismology, eds. J. A. Guzik, W. J. Chaplin, G. Handler, & A. Pigulski, IAU Symp., 301, 465
Packet, W. 1981, A&A, 102, 17
Penny, L. R., Sprague, A. J., Seago, G., & Gies, D. R. 2004, ApJ, 617, 1316
Pols, O. R., Cote, J., Waters, L. B. F. M., & Heise, J. 1991, A&A, 241, 419
Raguzova, N. V., & Popov, S. B. 2005, Astron. Astrophys. Trans., 24, 151
Ramírez-Agudelo, O. H., Simón-Díaz, S., Sana, H., et al. 2013, A&A, 560, A29
Ramírez-Agudelo, O. H., Sana, H., de Mink, S. E., et al. 2015, A&A, 580, A92
Reig, P. 2011, Ap&SS, 332, 1
Rímulo, L. R., Carciofi, A. C., Vieira, R. G., et al. 2018, MNRAS, 476, 3555
Rivinius, T., Baade, D., Štefl, S., et al. 2001, A&A, 369, 1058
Rivinius, T., Carciofi, A. C., & Martayan, C. 2013, A&ARv, 21, 69
Schootemeijer, A., Götberg, Y., de Mink, S. E., Gies, D., & Zapartas, E. 2018, A&A, 615, A30
Secchi, A. 1866, Astron. Nachr., 68, 63
Shao, Y., & Li, X.-D. 2014, ApJ, 796, 37
Spruit, H. C. 2002, A&A, 381, 923
Struve, O. 1931, ApJ, 73, 94
Suijs, M. P. L., Langer, N., Poelarends, A.-J., et al. 2008, A&A, 481, L87
Tarasov, A. E. 2017, in Stars: From Collapse to Collapse, eds. Y. Y. Balega, D. O. Kudryavtsev, I. I. Romanyuk, & I. A. Yakunin, ASP Conf. Ser., 510, 132
Telting, J. H., Waters, L. B. F. M., Roche, P., et al. 1998, MNRAS, 296, 785
Townsend, R. H. D., Owocki, S. P., & Howarth, I. D. 2004, MNRAS, 350, 189
van Bever, J., & Vanbeveren, D. 1997, A&A, 322, 116
Vink, J. S., de Koter, A., & Lamers, H. J. G. L. M. 2000, A&A, 362, 295
von Zeipel, H. 1924, MNRAS, 84, 665
Wang, C., Langer, N., Schootemaijer, A., et al. 2020, ApJ, 888, L12
Yoon, S.-C., & Langer, N. 2005, A&A, 443, 643
Yoon, S.-C., Langer, N., & Norman, C. 2006, A&A, 460, 199
Zorec, J., & Briot, D. 1997, A&A, 318, 443
Zorec, J., Frémat, Y., Domiciano de Souza, A., et al. 2016, A&A, 595, A132

Appendix A: Initial conditions required to reach near-critical velocities

In Sect. 3.1 we discuss the evolution of rotational velocities of various models, when the models all have the same relative initial rotation rates. Here we explore how the approach to the critical velocity depends on the initial rotation rate by performing interpolations between the models. Figure A.1 shows the critical velocity fraction as a function of time and initial rotation rate for differing stellar masses and metallicities. The colour of each point on the plot shows the critical velocity fraction at a particular fractional hydrogen-burning lifetime, t/t_{MS}, and initial critical velocity fraction value. By following horizontal lines in the plot, one traces the evolution of a single model through its evolution.

For $5\,M_\odot$ models at both SMC and MW metallicities, the star evolves generally towards higher critical velocity fractions; as one traces a horizontal line, one moves always into regimes of higher critical velocity fractions. The exception is the $5\,M_\odot$ MW models with $v_{rot}/v_{crit} > 0.7$, which at the end of hydrogen burning spin down through increased rotationally enhanced mass loss. Looking at $15\,M_\odot$ models at SMC metallicity, one sees also that there is a constant evolution towards higher critical velocity fractions. On the other hand, $15\,M_\odot$ models with MW metallicity evolve to higher critical velocity fractions until

around 80% of the hydrogen-burning lifetime, at which point they spin down due to angular momentum loss through winds (as discussed in Sect. 3.2). The $25\,M_\odot$ models behave in a more complicated way because the initially very fast-rotating models can undergo quasi-chemically homogeneous evolution (as discussed in Sect. 3.4). In the right panels of Fig. A.1 one can see the two regimes according to whether or not the critical velocity fraction is increasing or decreasing. We can see that for $25\,M_\odot$ MW models with initial $v_{rot}/v_{crit} \approx 0.7$, they evolve at first to lower critical velocity fractions then after $t/t_{MS} \approx 0.6$ they begin to evolve towards higher critical velocity fractions. This occurs because initially the star is evolving quasi-chemically homogeneously, during which time rotation rates and hence rotationally induced mixing efficiency drops until quasi-chemically homogeneous evolution is shut down, at which point the star begins to evolve with an expanding envelope and approaches the critical velocity. For similarly initially fast-rotating SMC models the same behaviour does not occur, which is due to the weaker stellar winds at lower metallicities.

Figure A.1 also shows us that the models only reach critical rotation (the black areas in the figure) very near core hydrogen exhaustion. Furthermore, the minimum initial rotation rate required to reach near critical rotation decreases with increasing mass due to angular momentum transport efficiency (as discussed in Sect. 3.3).
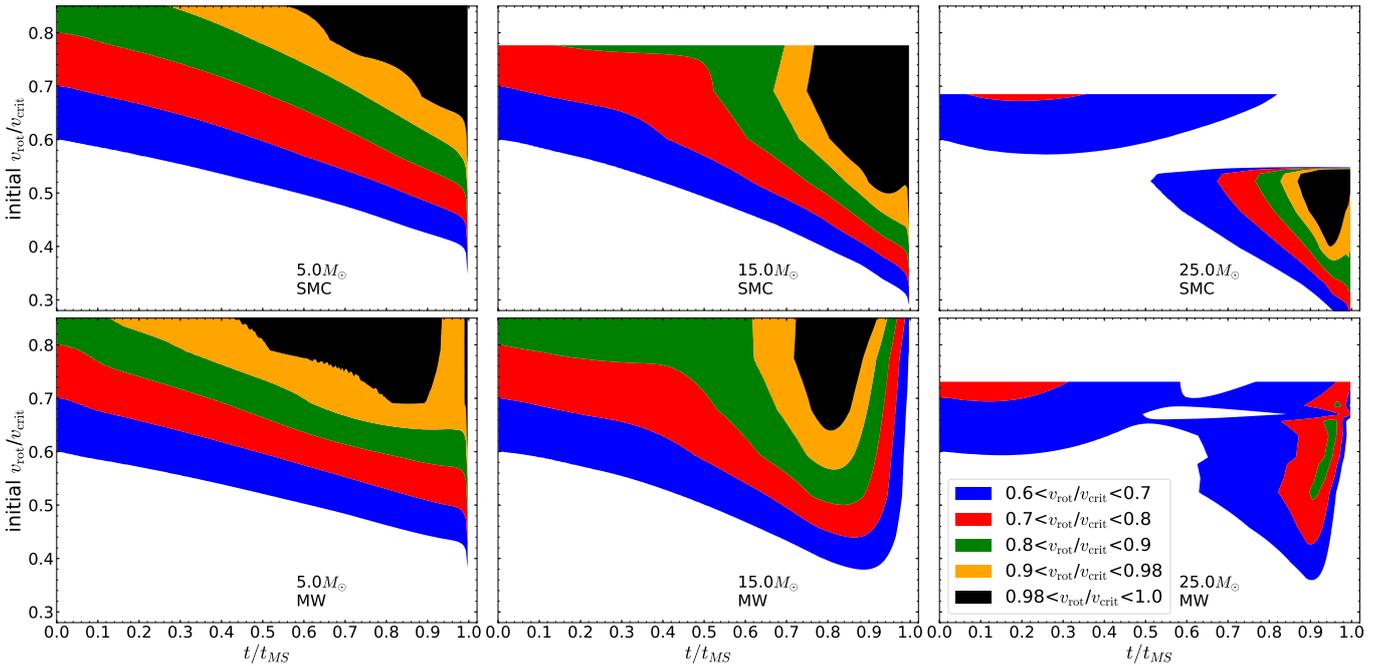
Fig. A.1. Critical velocity fractions, v_{rot}/v_{crit} as a function of fractional hydrogen-burning lifetime, t/t_{MS} and initial critical velocity fractions for models with masses of 5, 15, and $25\,M_\odot$ and SMC (*top panels*) and MW (*bottom panels*) metallicities, as indicated in the figure. The colours indicate the critical velocity fraction, v_{rot}/v_{crit} as given in the legend.

Appendix B: Synthetic colour–magnitude diagram without gravity darkening

In Fig. B.1 we present the results of our population synthesis to simulate the colour–magnitude diagram of NGC 330 while ignoring the effects of gravity darkening. It is seen that along the main sequence there is a one-to-one relation between the current critical velocity fraction and the $m_{F336W} - m_{F814W}$ colour, with faster rotators being redder. Such a relation is destroyed by gravity darkening (see Fig. 7).
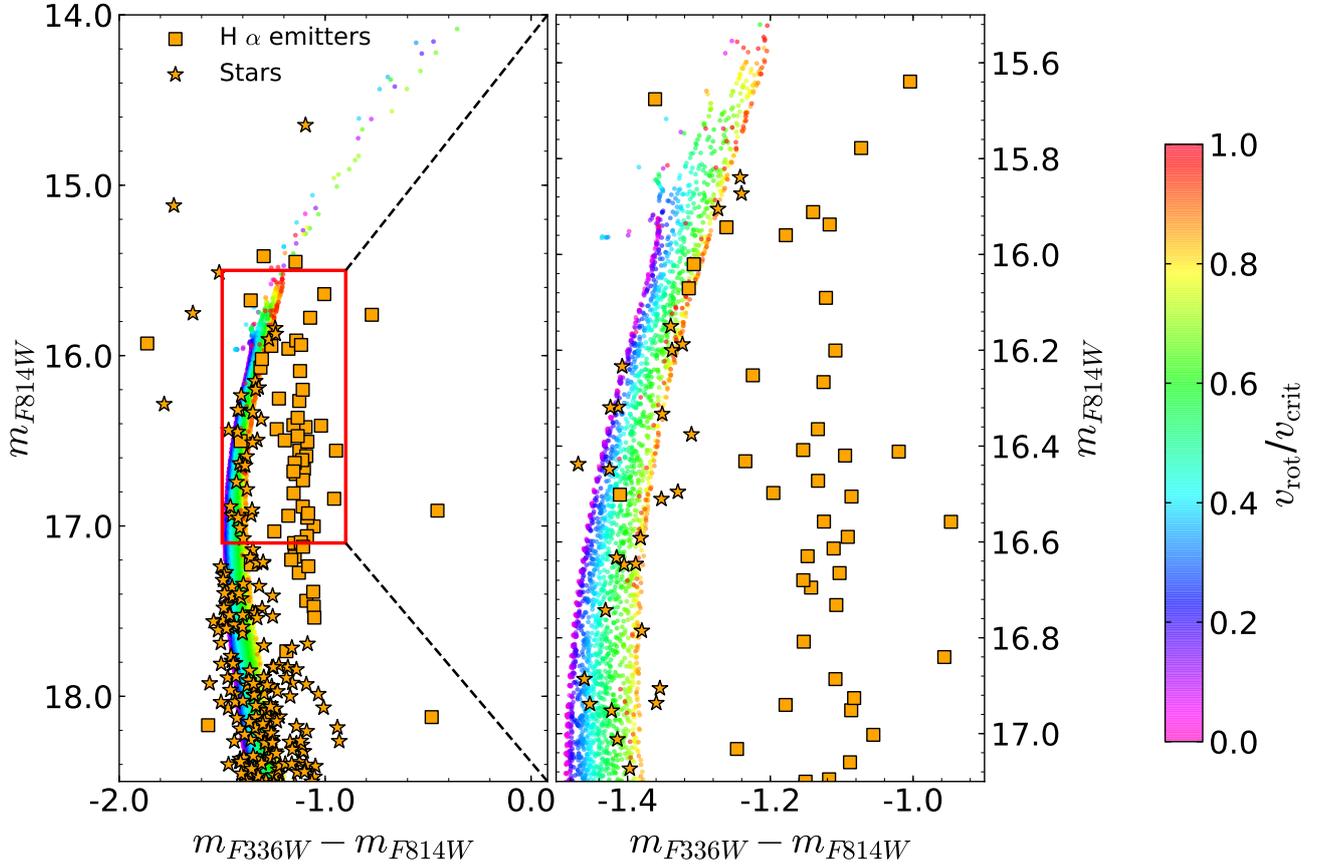
Fig. B.1. Synthetic colour–magnitude diagram of a 35 Myr star cluster at SMC metallicity, where each dot represents one single star and the colour gives the critical velocity fraction, v_{rot}/v_{crit} as indicated by the colour bar. Gravity darkening is not included. Over plotted are observations of SMC cluster NGC 330 (Milone et al. 2018), with Hα emitters marked by orange squares and normal stars as orange star symbols. *Right panel*: region indicated by the red box in the *left panel*. To convert the models to apparent magnitudes a distance modulus of 18.92 mag and a reddening of 0.06 mag were used.

Appendix to Chapter 3

A full reproduction of the publication resulting from work described in Chapter 3 is given on the next page.

Stringent upper limit on Be star fractions produced by binary interaction

B. Hastings[1,2], N. Langer[1,2], C. Wang[1], A. Schootemeijer[1], and A. P. Milone[3]

[1] Argelander-Institut für Astronomie, Universität Bonn, Auf dem Hügel 71, 53121 Bonn, Germany
  e-mail: bhastings@astro.uni-bonn.de
[2] Max-Planck-Institut für Radioastronomie, Auf dem Hügel 69, 53121 Bonn, Germany
[3] Dipartimento di Fisica e Astronomia "Galileo Galilei" Univ. di Padova, Vicolo dell'Osservatorio 3, Padova 35122, Italy

ABSTRACT

Context. Binary evolution can result in fast-rotating stars through accretion of angular momentum during mass-transfer phases. These fast-rotating stars are predicted to be observable as Be stars. Current models struggle to produce a satisfactory description of Be star populations, even though numerous pieces of observational evidence indicate that the accretion process might be the dominant Be formation channel.
Aims. Given the distinct uncertainties in detailed binary evolution calculations, we investigate a rigorous and model-independent upper limit for the production of Be stars through binary interaction and aim to confront this limit with observations of Be stars in young star clusters.
Methods. Using extreme assumptions, we calculate the number ratio of post-interaction to pre-interaction binary systems in a coeval population. This ratio describes an upper limit to Be star formation through mass transfer. A detailed comparison is made between our derived upper limit and relevant observations of Be stars, which allows us to probe several aspects of binary star physics.
Results. We find that in coeval populations, binary interaction can at most account for one-third of all main-sequence stars being Be stars. Near the cluster turn-off region, this limit appears to be realised in the clusters studied. Away from the turn-off, a good fit to the observed Be fraction as a function of mass is obtained by applying simple assumptions about which systems undergo unstable mass-transfer produces.
Conclusions. We find that assuming distinct physics, binary evolution alone can in principle match the high numbers of Be stars that are observed in open clusters. Whether the required binary physics is realised in nature remains to be investigated.

Key words. stars: emission-line, Be – binaries: general – stars: evolution – stars: massive – stars: rotation

1. Introduction

Be stars are massive main-sequence stars that display emission features in their spectra. Since their discovery more than 150 years ago (Secchi 1866), we have advanced our understanding to explain the emission as a result of a decretion-disc, which is being ionised by the central star (Struve 1931), but it is still unclear how a Be star gains its disc. Observations conclusively show that Be stars rotate significantly faster than their B counterparts (Struve 1931; Porter 1996; Huang et al. 2010; Zorec et al. 2016), such that the centripetal force potentially matches the gravitational force at the equator (Collins & Truax 1995; Townsend et al. 2004). However, the fundamental origin of this fast rotation is still unknown with both single and binary star channels having been proposed to play a role.

One way to achieve such rotation is for a star to be spun up by mass transfer in a binary system (Kriz & Harmanec 1975; Pols et al. 1991; Liu et al. 2006; Langer 2012). When a star accretes material, it also accretes angular momentum, which in the absence of tidal forces can lead to critical rotation of the accreting star, allowing material to become unbound and form a disc. The accretion of angular momentum is an efficient process, with a star needing to accrete typically a few percent of its own mass to rotate critically (Packet 1981).

In wide systems that initiate mass-transfer after the primary has exhausted hydrogen in the core (so-called Case B mass transfer), tidal forces are generally weak for the accretor star,

and it can be spun up to near-critical velocities. Furthermore, rapid rotators can also originate from close systems that undergo mass transfer while the donor is still core hydrogen-burning(so-called Case A mass transfer). Although tides inhibit the spin-up of the accretor during the initial mass-transfer phases, these phases cause a widening of the binary (Petrovic et al. 2005) so that when the donor expands to become a giant star (initiating Case AB mass transfer), many systems are wide enough to render tides ineffective, allowing the mass gainer to rotate super-synchronously (Sen et al., in prep.). Therefore rapidly rotating mass gainers can originate from both short- and long-period systems. What is common between these cases is that the spun-up star is usually produced after the initially more massive star in the system has exhausted its central supply of hydrogen.

In binary systems that produce a Be star and in which the primary star is not massive enough to undergo a supernova explosion, a short-lived helium star or long-lived white dwarf would be the companion to the Be star. Despite the difficulty of detection, both of these types of systems have been observed (Li et al. 2012; Schootemeijer et al. 2018; Shenar et al. 2020; Coe et al. 2020). Furthermore, studies of Be star discs have found that many are truncated, suggesting that they are acted upon by unseen companions (Klement et al. 2017, 2019).

When the mass donor does explode as a supernova, the majority of systems are expected to become unbound(due to a supernova kick) (Brandt & Podsiadlowski 1995) and the Be star will probably have no companion. The fact that this does not

occur in every case is evidenced by large numbers of Be-Xray binaries (Raguzova & Popov 2005), which consist of a neutron star in an eccentric orbit around a Be star such that Xrays are produced when the Be disc and neutron star interact. When the binary is disrupted, the Be star would likely be a runaway star. Boubert & Evans (2018) and Dorigo Jones et al. (2020) both found the peculiar space velocities of Be stars in the *Gaia* catalogue to be consistent with a binary origin of Be stars.

Observations show the Be phenomenon to be more common at lower metallicities (Maeder et al. 1999; Martayan et al. 2010; Iqbal & Keller 2013), in good agreement with predictions of single star models whereby metal-rich stars suffer stronger angular momentum losses through winds, thus making fast-rotators rarer at higher metallicities (Hastings et al. 2020). Naively, this trend is difficult to explain in the binary framework. However, further observational characteristics of Be stars have been uncovered that are difficult to explain with a single-star formation channel. Initially fast-rotating single stars are expected to exhibit enhanced surface nitrogen abundances, as rotational mixing dredges up CNO-processed material to the photosphere. However, there appears to be an incompatibility between models of rotating single stars and measurements of nitrogen abundances in Be stars, with many Be stars showing much lower nitrogen abundances than expected (Lennon et al. 2005; Dunstall et al. 2011; Ahmed & Sigut 2017; Hastings et al. 2020). On the other hand, spun-up mass gainers might not be rich in surface nitrogen. Although the physics governing the details of mass transfer remains uncertain, accretion may be limited by the angular momentum content of the gainer, such that accretion becomes non-conservative once critical rotation is achieved (Wang et al. 2020; Langer et al. 2020). Another factor is the strong mean molecular weight barrier established from hydrogen burning, which prevents efficient rotational mixing in the critically rotating mass gainer (Kippenhahn et al. 1974; Pinsonneault et al. 1989).

As demonstrated by Ekström et al. (2008) and Hastings et al. (2020), single stars may achieve near-critical rotation during the late stages of hydrogen burning, in contrast to observations showing that Be stars have a range of fractional main-sequence ages (Zorec et al. 2005; McSwain & Gies 2005; Milone et al. 2018). If Be stars are mostly single, we would expect pre-interaction binaries to host Be primaries because regardless of which proposed single-star mechanism causes the Be phenomenon, it should work for stars in a pre-interaction binary just as well as for single stars. It is thus telling that almost no Be stars with a main-sequence companion have been detected (Bodensteiner et al. 2020b).

Despite the numerous pieces of evidence that support the dominance of a binary formation channel, several uncertainties in binary evolution prevent a solid and accurate theoretical description of Be star populations. Proof of the difficulty of modelling the production of Be stars is given by the contrasting results of previous authors. It has been concluded that binaries are responsible for either all (Shao & Li 2014), half (Pols et al. 1991) or only a small minority (van Bever & Vanbeveren 1997) of galactic Be stars. This difference is mostly due to different assumptions on mass-transfer efficiency and the stability of mass transfer.

In light of these uncertainties, we find it useful to determine a model-free upper limit to Be star production from mass transfer in binary systems. Assessment of this limit can provide insight into whether it is at all possible for Be stars to be formed exclusively in binaries, and to which extent other formation mechanisms must be invoked. Under the assumption that binary evolution dominates the production of Be stars, we can also probe uncertain binary physics. We use recent high-quality observations of Be stars in open clusters (Milone et al. 2018) to rigorously test our simple picture.

In Sect. 2 we explain the procedure with which we calculated an upper limit to Be star production from mass transfer in binary systems. The results of this endeavour are presented in Sect. 3. In Sect. 4 we compare our results to the numbers of Be stars observed in young open clusters. We infer the conditions for stable mass transfer that are required for our prescription to reproduce the Be fractions along the main sequences of young open clusters in Sect. 5. Uncertainties and the implications of the upper limit are discussed in Sect. 6. Concluding remarks are given in Sect. 7.

2. Method

2.1. Hypothetical population of interacting binary stars

In order to calculate an upper limit to the numbers of Be stars that may be produced, we take extreme assumptions. The of which is that the initial binary fraction in the population is 1; that is, every star is born as a member of a binary. Nextly, as the hydrogen-burning episode of a massive star comprises about 90% of the total lifetime of a star, we then assumed that as soon as a primary star leaves the main sequence, stable mass transfer occurs on a very short timescale, instantly producing a Be star. In our model, a Be star is produced regardless of the initial period, primary mass, or mass ratio of the system, so that every secondary star will at some point during its lifetime become a Be star. In this framework, the orbital period distribution becomes irrelevant. Furthermore, we shall assume that once a Be star is formed, it remains so for the rest of its lifetime.

For simplicity, we ignore the effects of mass loss through stellar winds, such that every system remains at its initial mass ratio, q, until mass transfer occurs (which may be either conservative or non-conservative). Moreover, because the stellar mass-luminosity relation is very steep, we define each binary system by its most luminous component, so that each binary can be assigned an equivalent single-star mass. To facilitate comparison with open cluster observations, our synthetic population is assumed to be coeval.

Other properties of our population are not designed to maximise the efficiency of Be star formation, and are more or less standard in binary evolution calculations. We denote the initial masses of the initially more massive star as M_1 and the initial mass of the initially less massive star as $M_{2,i}$ and define the initial mass ratio, q, as

$$q = \frac{M_{2,i}}{M_1}, \tag{1}$$

such that

$$0 < q \leq 1. \tag{2}$$

We considered a population of binary stars in which the distribution of initial primary mass follows a power law like

$$\xi(M_1) = \xi_0 M_1^{\alpha}, \tag{3}$$

and the distribution of initial mass ratios is described similarly as

$$f(q) = f_0 q^{\kappa}, \tag{4}$$

where ξ_0 and f_0 are normalising constants to ensure that the integral over the whole parameter space is unity (as befitting

a probability-density function). For example, the value of f_0 is easily computed as

$$f_0 = \frac{\kappa + 1}{1 - q_{min}^{\kappa+1}}, \tag{5}$$

where q_{min} is the minimum mass-ratio in our population and is nominally set to $q_{min} = 0.1$ to match the observing campaigns of Sana et al. (2012, 2013). It is assumed that systems born with mass ratios lower than this value are likely to be unstable and merge either during their formation or early in their evolution and hence are not considered.

Mass gain of the accretor shall be parametrised by assuming that a total mass of ΔM is accreted, giving the relation between final and initial masses of the accretor as

$$M_{2,f} = M_{2,i}(1 + \Delta M/M_{2,i}), \tag{6}$$

with $\Delta M/M_{2,i}$ being a free parameter.

Our assumptions on the population are summarised in the list below.

1. initial binary fraction is 1
2. every system will undergo stable Case B mass transfer and form a Be star, regardless of period or mass ratio
3. once a primary star leaves the main sequence, a Be star is immediately formed
4. once a Be star is formed, it remains so for the rest of its lifetime
5. the accretor star gains mass ΔM, with the relative mass gain $\Delta M/M_{2,i}$ being a free parameter.
6. the effects of wind mass loss are ignored so that a system remains at its initial mass ratio until mass transfer occurs.
7. the distribution of initial primary masses follows a power law, $\xi(M_1) \propto M_1^\alpha$
8. the distribution of initial mass ratios follows a power law, $f(q) \propto q^\kappa$
9. only considered are binaries with a mass ratio greater than q_{min}, which is set to 0.1.
10. when both stars are burning hydrogen, the luminosity of a binary system is given by that of the primary. When the primary has evolved off the main sequence, the luminosity of the system is naturally that of the secondary.

According to our assumptions, every secondary star with a post-main-sequence companion is a Be star, meaning that the number of Be stars with a given mass M is

$$n(Be) = n(M_{2,f} = M \,\&\, M_1 > M_{TO}), \tag{7}$$

where M_{TO} is the turn-off mass of our coeval population. In our model the number of non-Be stars is given by the number of primaries at a given mass. The Be fraction, $\phi_{Be}(M)$ is defined as the number fraction of Be stars to all stars at a given mass. In a coeval population, this becomes

$$\phi_{Be}(M) = \frac{n(M_{2,f} = M \,\&\, M_1 > M_{TO})}{n(M_{2,f} = M \,\&\, M_1 > M_{TO}) + n(M_1 = M)} \tag{8}$$

$$= \left[1 + \frac{n(M_1 = M)}{n(M_{2,f} = M \,\&\, M_1 > M_{TO})}\right]^{-1}. \tag{9}$$

In our model, the mass of a Be star is related to its initial mass, $M_{2,i}$, and the relative mass gain, $\Delta M/M_{2,i}$ via Eq. (6), such that the expression above becomes

$$\phi_{Be}(M) = \left[1 + \frac{n(M_1 = M)}{n(M_{2,i} = \frac{M}{1+\Delta M/M_{2,i}} \,\&\, M_1 > M_{TO})}\right]^{-1}. \tag{10}$$

With the aid of Eqs. (1) and (6), the condition

$$M_1 > M_{TO} \tag{11}$$

can be rewritten as

$$q < \frac{M_{2,i}}{M_{TO}}, \tag{12}$$

leading to

$$q < \frac{M_{2,f}}{M_{TO}(1 + \Delta M/M_{2,i})}. \tag{13}$$

This results in

$$\phi_{Be}(M) = \left[1 + \frac{n(M_1 = M)}{n(M_{2,i} = \frac{M}{1+\Delta M/M_{2,i}} \,\&\, q < \frac{M}{M_{TO}(1+\Delta M/M_{2,i})})}\right]^{-1}. \tag{14}$$

To study coeval populations, a more convenient approach is to find the Be fraction as a function of the fractional main-sequence turn-off mass, M/M_{TO}. This produces the expression

$$\phi_{Be}(M/M_{TO})$$
$$= \left[1 + \frac{n(M_1 = M/M_{TO})}{n(M_{2,i} = \frac{M}{M_{TO}(1+\Delta M/M_{2,i})} \,\&\, q < \frac{M}{M_{TO}(1+\Delta M/M_{2,i})})}\right]^{-1}, \tag{15}$$

which shall be our basis for exploring the Be fraction in coeval populations.

To evaluate the Be fraction, it is necessary to determine the relative numbers of primary stars to the number of secondary stars at a given mass. We may write that the number of primary stars with a given mass, $n(M_1)$, is the integral of the primary mass distribution across an infinitesimally small mass range, dM_1, multiplied by the total number of stars in the population, n_{tot}, as

$$n(M_1) = n_{tot}\xi(M_1)dM_1 = n_{tot}\xi_0 M_1^\alpha dM_1. \tag{16}$$

To tackle the number of secondary stars at a given mass is sightly more involved as we do not have directly the distribution of secondary masses, instead it is inferred from the primary mass and mass-ratio distributions. First consider a population in which there exists only a single mass-ratio, q_0, i.e. the mass-ratio distribution is a delta-Dirac function. If one is interested in the number of secondary stars with initial mass $M_{2,i}$, one must count the number of primaries with mass $M_{2,i}/q_0$, so we have

$$n(M_{2,i} \,\&\, q_0) = n_{tot}\xi\left(\frac{M_{2,i}}{q_0}\right)d\left(\frac{M_{2,i}}{q_0}\right), \tag{17}$$

with $d\left(\frac{M_{2,i}}{q_0}\right)$ representing an infinitesimally small change in $\frac{M_{2,i}}{q_0}$.

Any distribution may be expressed as an infinite sum of appropriately weighted delta-Dirac distributions, with the weighting coming from the probability-density function. For the general case, we therefore have

$$n(M_{2,i}) = n_{tot}\int_{q_{min}}^1 f(q)\xi\left(\frac{M_{2,i}}{q}\right)d\left(\frac{M_{2,i}}{q}\right)dq. \tag{18}$$

It is then clear that the limits of the integral above place constraints on the initial mass ratios counted. The number of systems with a given initial secondary mass $M_{2,i}$ and initial mass ratios between q_{min} and q_{max} can thus be written as

$$n(M_{2,i} \,\&\, q_{min} < q < q_{max}) = n_{tot}\int_{q_{min}}^{q_{max}} f(q)\xi\left(\frac{M_{2,i}}{q}\right)d\left(\frac{M_{2,i}}{q}\right)dq. \tag{19}$$

The differential $d\left(\frac{M_{2,i}}{q}\right)$ in Eq. (19) is quite cumbersome, therefore we chose to let

$$r = \frac{M_{2,i}}{q}. \tag{20}$$

We may now write

$$n(M_{2,i} \,\&\, q_{min} < q < q_{max}) = n_{tot} \int_{q_{min}}^{q_{max}} f(q)\xi(r)\mathrm{d}r\mathrm{d}q. \tag{21}$$

We have

$$M_{2,i} = qM_1, \tag{22}$$

thus

$$\mathrm{d}M_{2,i} = q\mathrm{d}M_1 + M_1\mathrm{d}q. \tag{23}$$

As we are interested in the number of secondary stars at a fixed mass, $dM_{2,i} = 0$,

$$\mathrm{d}q = -\frac{q}{M_1}\mathrm{d}M_1. \tag{24}$$

Differentiating r gives

$$\mathrm{d}r = \frac{-M_{2,i}}{q^2}\mathrm{d}q. \tag{25}$$

Combining Eqs. (24) and (25) results in

$$\mathrm{d}r = \frac{1}{q}\frac{M_{2,i}}{M_1}\mathrm{d}M_1. \tag{26}$$

Inserting this into our expression for $n(M_{2,i} \,\&\, q_{min} < q < q_{max})$ (Eq. (21)) gives

$$n(M_{2,i} \,\&\, q_{min} < q < q_{max}) = n_{tot} \int_{q_{min}}^{q_{max}} f(q)\xi\left(\frac{M_{2,i}}{q}\right)\frac{1}{q}\frac{M_{2,i}}{M_1}\mathrm{d}M_1\mathrm{d}q. \tag{27}$$

We now divide Eq. (16) by Eq. (27), leaving

$$\frac{n(M_1)}{n(M_{2,i} \,\&\, q_{min} < q < q_{max})} = \frac{M_1\xi(M_1)}{M_{2,i} \int_{q_{min}}^{q_{max}} f(q)\xi\left(\frac{M_{2,i}}{q}\right)\frac{1}{q}\mathrm{d}q}. \tag{28}$$

When the distributions for initial primary mass and mass ratio, Eqs. (3) and (4), are inserted, Eq. (28) simplifies further to

$$\frac{n(M_1)}{n(M_{2,i} \,\&\, q_{min} < q < q_{max})} = \left(\frac{M_1}{M_{2,i}}\right)^{\alpha+1} \frac{1}{\int_{q_{min}}^{q_{max}} f_0 q^{\kappa-\alpha-1}\mathrm{d}q}. \tag{29}$$

This result may be readily checked against Monte Carlo sampling of the primary mass and mass-ratio distributions.

Equation (29) can be used to directly determine the Be fraction (Eq. (15)) by setting $M_1 = M/M_{TO}$, $M_{2,i} = \frac{M}{M_{TO}(1+\Delta M/M_{2,i})}$ and $q_{max} = \frac{M}{M_{TO}(1+\Delta M/M_{2,i})}$. This leaves

$$\phi_{Be}(M/M_{TO}) = \left[1 + \frac{(1 + \Delta M/M_{2,i})^{(\alpha+1)}}{\int_{q_{min}}^{\frac{M}{(1+\Delta M/M_{2,i})M_{TO}}} f_0 q^{\kappa-\alpha-1}\mathrm{d}q}\right]^{-1}, \tag{30}$$

where the integral has a simple analytic solution. Equation (30) describes the Be star fraction as a function of the fractional turn-off mass, M/M_{TO}, for our model open cluster. As the mass dependence in Eq. (30) is expressed by the fractional turn-off mass, is not necessary to specify the turn-off mass.

2.2. Limits for the remaining parameters

All that remains is to explore Eq. (30) in a suitable parameter space. The parameters we have are α, κ, and $\Delta M/M_{2,i}$, which are the primary mass distribution exponent, the initial mass-ratio distribution exponent, and the relative accretor mass gain, respectively.

The canonical value for the exponent of the initial mass function (IMF), α, is given by the Salpeter IMF, $\alpha = -2.35$ (Salpeter 1955). However, recent observations of young stars in the 30 Doradus starburst region instead suggest $\alpha = -1.90^{+0.37}_{-0.26}$ (Schneider et al. 2018). Similarly, in the R136 star-forming region, an exponent of $\alpha = -2.0 \pm 0.3$ was found (Bestenlehner et al. 2020). On the other hand, it has also been proposed that the IMF follows an even steeper law with $\alpha = -2.7$ (Scalo 1986). Therefore we consider the range $-1.9 < \alpha < -2.7$.

Observations of Galactic O-type stars show that the mass-ratio distribution follows a power law with exponent $\kappa = -0.1 \pm 0.6$ (Sana et al. 2012) for $0.1 < q < 1$. In the Large Magellanic Cloud, the mass ratios of massive binaries appear to be distributed differently, with $\kappa = -1.0 \pm 0.4$ again in the range $0.1 < q < 1$ (Sana et al. 2013). There are many claims that mass ratios of binaries favour either low values (Trimble 1990; Tout 1991; Hogeveen 1991) or follow a uniform distribution (Kobulnicky & Fryer 2007; Kouwenhoven et al. 2007). In light of these findings, we consider κ values in the range $-1 < \kappa < 0$.

Estimates of the accretor mass gain, $\Delta M/M_{2,i}$, obtained by demanding that mass transfer stops when the mass gainer reaches critical rotation, tell us that $\Delta M/M_{2,i}$ is 0.1 at most and in most cases is about 0.02, depending on the angular momentum content and physical structure of the mass gainer before accretion (Packet 1981; Petrovic et al. 2005; Wang et al. 2020). It has been found that around 70% of the mass leaving the donor must be ejected from the system to explain the observed distributions of Be star masses in Be X-ray binaries (Vinciguerra et al. 2020). However, it must be noted that because it is expected that up to 90% of massive binary systems are broken apart by a supernova kick (Brandt & Podsiadlowski 1995), Be X-ray binaries represent a small fraction of the population and may therefore well contain strong biases. Furthermore, it is thought that mass transfer must be highly non-conservative to explain the observed populations of Wolf-Rayet O-star binaries (Petrovic et al. 2005; Shao & Li 2016). On the other hand, several systems show evidence that near-conservative mass transfer has taken place (de Mink et al. 2007; Schootemeijer et al. 2018; Brož et al. 2021). To fully explore the effects of mass-transfer efficiency on Be star populations, we consider the full range $0 < \Delta M/M_{2,i} < 1$.

3. Results

The results of Eq. (30) are plotted in Fig. 1 for the extremal parameters outlined in Sect. 2.2. The primary mass distribution affects the absolute numbers of Be stars because for a shallower distribution (α closer to 0), there is an abundance of massive binaries, such that many systems contain post-main-sequence primaries, and therefore the number of Be stars increases. Conversely, when $\alpha \ll 0$, the population contains fewer primaries of mass greater than the turn-off mass, and the Be count decreases.

The effect of the mass-ratio distribution can be understood by considering a population with a high value of κ such that secondary stars have a similar mass to their companion. In this case, when the primary leaves the main sequence, the secondary will be rather evolved, and hence most Be stars will be found near

Fig. 1. Maximum Be fraction, Φ_{Be}, in a coeval population as defined by Eq. (30) plotted as a function of fractional main-sequence turn-off mass, M/M_{TO}, for varying parameters. *Left and right panels*: $\Delta M/M_{2,i} = 0$ and 1, respectively. The colour of the lines represents differing κ values. Red is $\kappa = 0$ and blue is $\kappa = -1$. Dashed lines show $\alpha = -1.9$ and solid lines show $\alpha = -2.7$, as indicated by the annotations.

the turn-off. On the other hand, in a population with a low κ, the opposite is true; the secondary stars will have lower masses compared to the turn-off mass, and Be stars will be more evenly distributed along the main sequence, as shown in Fig. 1.

Figure 1 shows how a varying mass gain changes the Be count, with accretors that gain more mass producing fewer Be stars. This can be understood by considering a Be star of mass $0.9 M_{\text{TO}}$ that is produced by inefficient mass transfer. For the primary to exceed the turn-off mass, the initial mass ratio of the system must be lower than 0.9. If this star had gained $0.1 M_{\text{TO}}$, the initial mass would be $0.8 M_{\text{TO}}$ and the initial mass ratio must be lower than 0.8. This shows that mass gain restricts the number of systems that are able to produce Be stars of a given mass, and a low mass-transfer efficiency leads to higher numbers of Be stars being produced at a given mass.

Figure 1 shows that the largest Be fractions are produced when mass transfer is inefficient ($\Delta M/M_{2,i} = 0$) and the IMF is shallow. The mass-ratio distribution then tunes the distribution of Be stars along the main sequence. Therefore it is judged that most Be stars are produced with the parameters $\Delta M/M_{2,i} = 0$, $\alpha = -1.9$ and $-1 < \kappa < 0$. Depending on the chosen parameters, the maximum Be fraction is in the range 0.2–0.35 near the main-sequence turn-off.

4. Comparison to observations

To contextualise to our results, we attempt here a comparison with observations using high-quality *Hubble* Space Telescope photometry of young Small and Large Magellanic Cloud open clusters in which Be stars are revealed as bright objects in a narrow-band filter centred on Hα (Milone et al. 2018). Photometry was performed with *Hubble* wide-band filters $F814W$ and $F336W$ and the narrow-band $F656N$ filter, allowing colour-magnitude diagrams in which Be stars are identified from Hα photometry to be produced.

As many spectroscopically confirmed Be stars in NGC 330 are bright in Hα (Bodensteiner et al. 2020a), we judge Hα emission to be a good proxy for Be stars. It is possible for the accretion discs of Algol-type binaries to exhibit Hα emission (Peters 1989), but these systems are expected to make up only about 3% of the total population (de Mink et al. 2014; Sen et al., in prep.). Furthermore, some field stars may be Hα emitters. Milone et al.

(2018) noted that no more than one-tenth of the stars in the cluster field are suspected field stars. Field stars will also contaminate the population of stars that do not emit in Hα, therefore their presence is not expected to significantly alter the relative fractions of Hα emitters and non-emitters.

Be star fractions have previously been measured as a function of magnitude (Keller et al. 1999; Milone et al. 2018; Bodensteiner et al. 2020a). We find it worthwhile to repeat this exercise, including several factors that were previously overlooked.

Our goal is to measure the observed Be fraction as a function of mass along the main sequence of an open cluster. To do this, we must note the two major differences between a Be star and a "normal" B star: fast rotation, and the presence of a decretion disc. The effect of the centrifugal force means that a fast-rotating star has a reduced effective gravity at the equator. According to the von Zeipel theorem (von Zeipel 1924), this results in a lower effective temperature. Therefore fast-rotating stars are cooler and redder than their non-rotating counterparts. Furthermore, light from a Be star consists of radiation from the star itself and also of light from the decretion disc. Typically, the average temperature of the disc is about 70% of the effective temperature of the star itself (Sigut et al. 2009), and so the disc is expected to emit mostly in visible and infrared wavelengths.

In a colour-magnitude diagram, the magnitude in a red filter is plotted on the y-axis, and a colour defined by the blue and red filter ($B-R$) on the x-axis. When a star becomes brighter in the red filter, it therefore moves to the right and upwards in the colour-magnitude diagram. This effect means that to count the Be stars as a function of mass, we must do so in bins that are sloped with respect to the x-axis. The gradient of this slope depends on how much redder a near-critically rotating star is than a slow rotator at the same mass, and on how much light the decretion disc radiates.

As no reliable numerical models exist of stars rotating at the critical velocity, we shall adopt a simple model to relate the luminosity and temperature of a critical rotator to an equivalent non-rotating star. After having been spun up, a star will change its shape, becoming oblate. At the same time, we do not expect a great difference in luminosity between a star before and after the spin-up. This is because stars are generally very centrally condensed, such that the centrifugal force is small compared

to gravity in the regions where nuclear burning occurs, meaning that (excluding the effects of rotational mixing) central temperatures and thus luminosities are not very sensitive to rotation, in agreement with models (Brott et al. 2011; Paxton et al. 2019). Following the Stefan-Boltzmann law, because of the increased surface area of a critical rotator, the effective temperature decreases. Using the Roche model (see Appendix A), one can show that a critically rotating star has a surface area of approximately $1.58 \times 4\pi R_p^2$, with R_p being the polar radius. This corresponds to a decrease in effective temperature by a factor of $1.58^{-\frac{1}{4}} \approx 0.89$. Knowing this, we can construct isochrones describing the intrinsic properties of critically rotating stars from non-rotating isochrones.

A further complication that is brought about by gravity darkening is that a fast-rotating star appears cooler and dimmer when viewed equator-on as compared to pole-on. Assuming a random orientation of the inclination axis, the mean value of the sine of the inclination angle is $\pi/4$, corresponding to a mean inclination angle of 51.8°. To take the mean effect of gravity darkening into account, we employed the model of Espinosa Lara & Rieutord (2011) as implemented in MESA (Paxton et al. 2019). Here, the projected luminosity and effective temperature, L_{proj}, $T_{eff,proj}$ are related to the intrinsic luminosity and effective temperature, L, T_{eff} by

$$L_{proj} = C_T(\omega, i)L \tag{31}$$
$$T_{eff,proj} = C_L(\omega, i)T_{eff}, \tag{32}$$

with C_T and C_L depending on the fraction of critical velocity, ω, and inclination angle i.

The temperatures and luminosities of critically rotating stars are found by using the coefficients $C_T(\omega = 1, i = 51.8°) = 1.02$ and $C_L(\omega = 1, i = 51.8°) = 1.22$. It is a rather curious feature of the gravity darkening model that at the mean inclination, the coefficients exceed unity, meaning the average effect of gravity darkening is not darkening at all, but brightening. Finally, by interpolating tables of synthetic stellar spectra (Choi et al. 2016) to produce magnitudes in *Hubble* filters, we are able to produce an isochrone of critical rotators, as shown in Fig. 2.

The contribution of a Be star's disc to its total flux is more difficult to assess. It has been noted that a loss of spectral emission features in certain Be stars coincides with a dimming of about 0.3–0.5 magnitudes in the R and V filters (Carciofi et al. 2012; Labadie-Bartz et al. 2017; Rímulo et al. 2018). If the loss of emission features is interpreted as the disappearance of the disc, one can take this change in brightness to equal the flux contribution of the disc. By comparing the colour of our isochrones with the colours of Be stars in NGC 330, we can assess how much the Be disc shines, as in Fig. 2. After assuming that the disc shines in the $F814W$ filter but not in the $F336W$ filter, we find a reasonable fit to the Hα emitters when a disc brightness of $0.25m_{F814W}$ is adopted, as shown by the solid and dashed purple lines in Fig. 2.

For NGC 330, we find that in the regions of the colour-magnitude diagram containing Be stars, stars of equal mass on the non-rotating and Be star isochrones are connected by lines of gradient $\frac{-dm_{F814W}}{d(m_{F336W} - m_{F814W})} = 2$. For NGC 2164, again assuming a constant disc magnitude of $0.25m_{F814W}$, the gradient is found to be 1.8. These differing values are caused by the ways in which stellar spectra, and hence magnitude in a given filter, vary with luminosity and effective temperature.

Figure 3 shows the colour-magnitude diagrams of NGC 330 and NGC 2164 with the Be fraction as counted in slanted bins with gradients of 2.0 and 1.8, respectively. It is noted that as
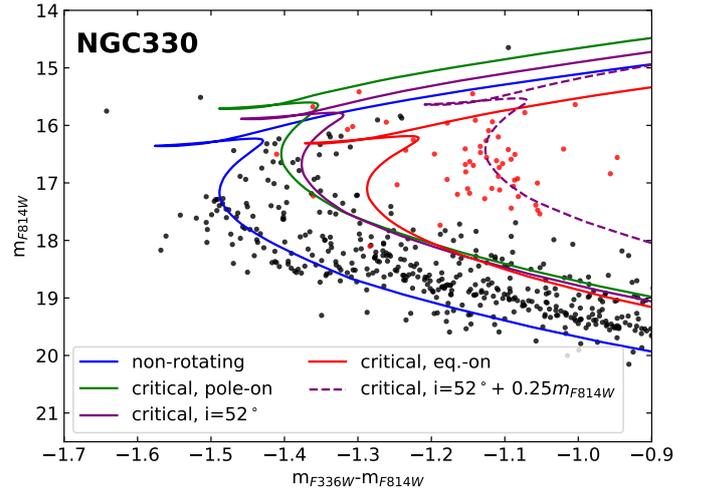
Fig. 2. Colour-magnitude diagram of NGC 330 focused on the turn-off region. Hα emitters are marked in red. An isochrone of non-rotating stars is plotted in blue (see Appendix B for model details). Green and red isochrones depict critically rotating stars viewed pole-on and equator-on, respectively, as derived from a simple model of critical rotators (see Appendix A). The solid purple isochrone represents critically rotating stars viewed at the mean inclination angle when the rotation axis is randomly oriented (51.8°), and for the dotted purple isochrone, $0.25m_{F814W}$ has been added to simulate the decretion disc. The isochrone age is 30 Myr, the distance modulus is $\mu = 18.8$ mag, and the reddening of $E(B-V) = 0.1$ mag. Data are from Milone et al. (2018).

compared to counting the Be fraction in bins of constant m_{F814W} magnitude (i.e. horizontal bins), the values measured here are lower. This is because due to the effects described above, the sequence of Be stars is brighter than the sequence of B stars with the same mass. Therefore a horizontal bin contains relatively massive B stars and relatively low mass Be stars. According to the initial mass function, higher-mass stars are less populous, and hence the Be fraction is higher when horizontal bins are used solely because fewer B stars are counted.

We used isochrones of rotating single stars based on an extended model grid of Schootemeijer et al. (2019) (see Appendix B for a thorough description) with an initial rotation rate of $v_{rot}/v_{crit} = 0.6$ to assign mass ranges to each bin, so that the Be fraction can be evaluated as a function of mass. The bins were placed so that the outer edge of the last bin was at the point at which hydrogen has been exhausted in the stellar core. We chose a value of $v_{rot}/v_{crit} = 0.6$, as suggested by Gossage et al. (2019) and Wang et al. (in prep.). This produced equatorial rotation velocities that broadly agree with spectroscopic observations (Dufton et al. 2013; Marino et al. 2018; Sun et al. 2019; Kamann et al. 2020). The reddening and distance modulus values were tailored to give the best fit to the cluster and agree well with previous isochrone fittings for these clusters (Milone et al. 2018). The isochrone fits are shown in Fig. 3.

The isochrones allowed us to measure the turn-off mass and the masses associated with each bin. This enables a direct comparison between the theory presented in Sect. 3 and observations. Figure 4 shows this comparison. Uncertainties on the Be fraction are given by the standard error, σ, assuming a binomial distribution as

$$\sigma = \sqrt{\Phi(1 - \Phi)/N}, \tag{33}$$

with Φ being the measured Be fraction and N the total number of stars in a given bin.
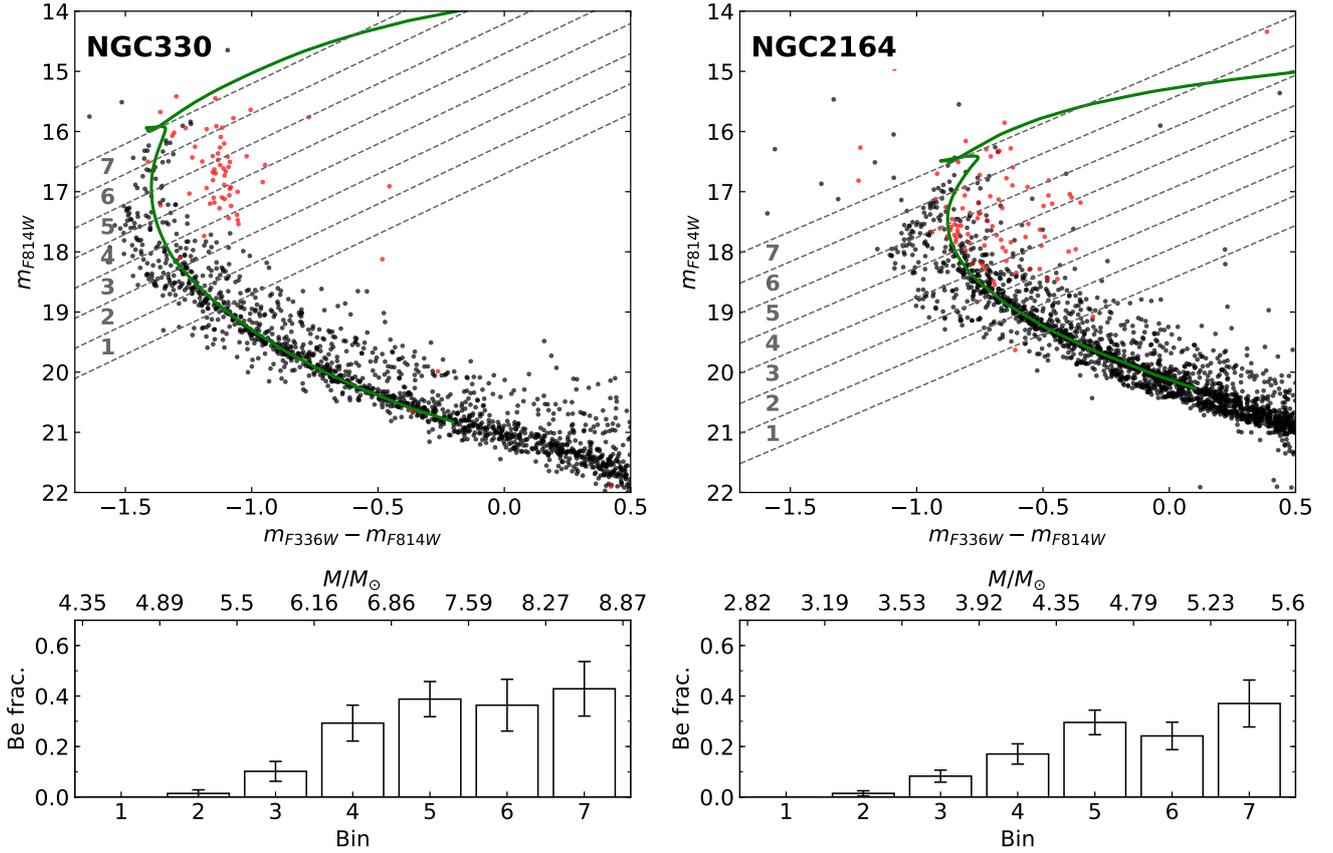
Fig. 3. Colour-magnitude diagrams with isochrone fits and Be star counts for the Small Magellanic Cloud cluster NGC 330 (*left*) and Large Magellanic Cloud cluster NGC 2164 (*right*). Hα emitters are marked in red. *Bottom panels*: Be fraction counted in bins as defined in the top panels. The errors are given by the binomial counting error. The bins have a gradient of 2.0 and 1.8 for NGC 330 and NGC 2164, respectively. Mass values associated with the bins are provided by the isochrone fit. For both clusters, the isochrone depicts stars with initial rotation equal to $0.6 v_{\rm rot}/v_{\rm crit}$. For NGC 330, the isochrone age is 30 Myr, the distance modulus $\mu = 18.8$ mag, and the reddening is $E(B-V) = 0.1$ mag. For NGC 2164, the age is 80 Myr, $\mu = 18.3$ mag, and $E(B-V) = 0.12$ mag. Data are from Milone et al. (2018).
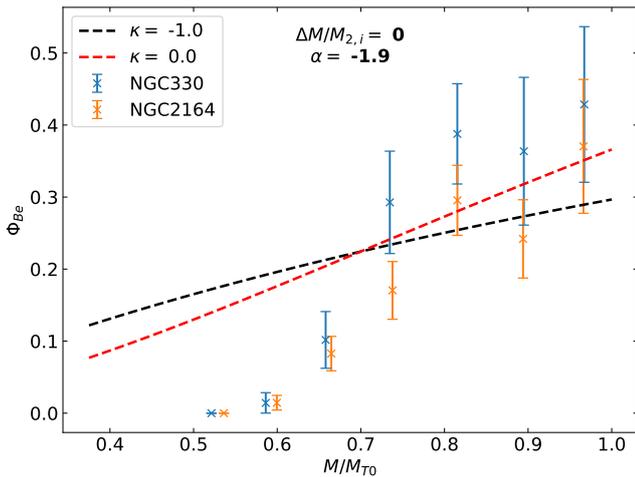
Fig. 4. Comparison of theory and observations. Be fraction as a function of fractional main-sequence turn-off mass in NGC 330 and NGC 2164, as shown in Fig. 3. Dashed lines show the theoretical upper limit given by Eq. (30) with $\alpha = -1.9$, $\Delta M/M_{2,i} = 0$, and $\kappa = -1.0, 0$ (see Fig. 1), as given by the legend.

We find that although the two clusters have different metallicities and ages, they appear to have similar Be fractions as a function of relative turn-off mass. This may be an indication that the dominant Be production channel is universal, regardless of its nature.

In both clusters the Be fraction steadily increases from zero to about 0.4 in the range 60–80% of the turn-off mass. Near the turn-off, the Be fraction is found to be approximately 0.4, with a significant counting uncertainty because relatively few stars occupy this region. When these uncertainties are taken into account, our upper limit can describe the numbers of Be stars in the upper part of the main-sequence. It is important to note that because it is difficult to perform an isochrone fit, the Be fractions near the turn-off are particularly uncertain. A small change in the isochrone fit results in a large change in the measured Be fraction (see Sect. 6.1 for a quantitative discussion). Even though the measured Be fraction in NGC 330 at times exceeds our upper limit, it is therefore reasonable to conclude that the upper limit does provide a reasonable fit to the Be star numbers near the turn-off. However, it fails to explain the lack of Be stars below $M/M_{\rm TO} \approx 0.7$. The reason may be that certain systems do not form Be stars but merge instead, as we discuss in the next section.

5. Inferring the initial conditions for stable mass transfer

The observations presented in Sect. 4 show that our upper limit can approximately describe the numbers of Be stars near the
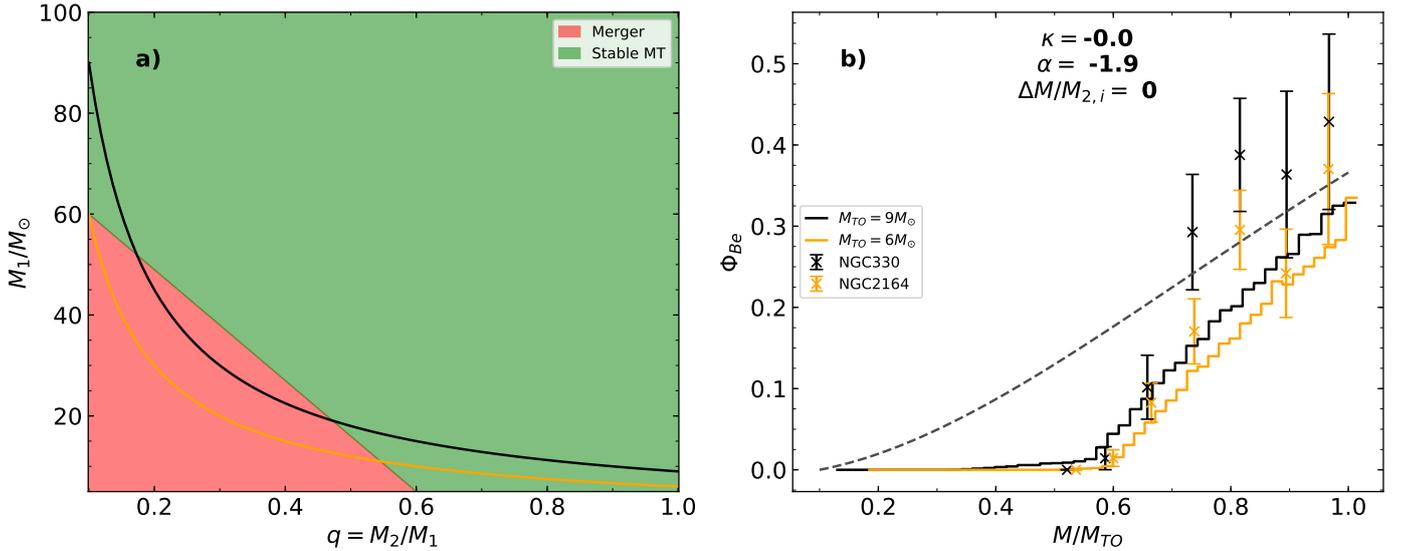
Fig. 5. (*a*) Adopted region of stable mass transfer in the primary mass-mass ratio plane. Regions coloured red experience unstable mass transfer and merge. For green regions, mass transfer is stable, and a Be star is formed. The black and orange lines show systems with secondary masses of 9 and 6 $M_\odot$, respectively. (*b*) Results of a Monte Carlo simulation showing the Be fraction, Φ_{Be}, when the stable mass-transfer region in (a) is applied. Binary systems have a flat mass-ratio distribution ($\kappa = 0$), a primary mass distribution $\xi(M_1) \propto M^{-1.9}$, and we have assumed inefficient accretion ($\Delta M/M_{2,i} = 0$). The black line shows a simulation with a turn-off mass of 9 $M_\odot$, and the orange line a turn-off mass of 6 $M_\odot$. The dashed grey line shows the theoretical upper limit, as given by Eq. (30). Measured Be fractions of NGC 330 and NGC 2164 according to Fig. 3 are plotted as black and orange crosses, respectively.

turn off, but fails to reproduce the sharp cut-off in the Be star sequence We investigate the change required in our prescription to reproduce this feature.

In reality, not every binary system undergoes stable mass transfer to form a Be star. For the specific case when the donor is in the Hertzsprung gap, as for Case AB or Case B mass transfer, the mass transfer proceeds at the Kelvin-Helmholtz (or thermal) timescale (Tout et al. 1997; Wellstein et al. 2001), meaning that if there is a large discrepancy in the Kelvin-Helmholtz timescales of the donor and accretor, the mass transfer will become unstable and a common-envelope situation will ensue, most likely leading to a stellar merger.

To model the occurrence of mergers, it is often assumed in simplified binary evolution calculations (Pols et al. 1991; Hurley et al. 2002; Schneider et al. 2015) that systems below a certain mass ratio will merge. This simple criterion is unsuitable to reproduce the observations shown in Fig. 3, however. Equation (30) gives the Be star fraction as an integral quantity, such that the Be star fraction at the main-sequence turn-off is the accumulation of systems with mass ratios from q_{min} to 1. This may be understood intuitively by noting that a Be star of mass near the main-sequence turn-off mass can originate from either an extreme mass-ratio system with a very massive primary or from a system with mass ratio close to unity. When we demand that all systems below a given mass-ratio merge, we therefore naturally decrease the Be fraction at the turn-off, which we must avoid to retrieve high numbers of Be stars at the turn-off.

To keep the Be fraction near the turn-off high and produce a sharp break in the Be fraction at $M/M_{TO} \approx 0.7$, more sophisticated criteria are needed, namely that depend on primary mass and mass ratio. We propose that the systems most likely to suffer unstable mass transfer are those with an extreme mass-ratio and low primary mass because the components of these systems have the largest difference in Kelvin-Helmholtz timescales. This can be visualised in a grid of primary mass against mass ratio, in which the bottom corner consists of systems that merge. In

this grid, systems with a fixed secondary mass are represented by parabolae, as depicted in Fig. 5a. If the parabola representing a secondary with the turn-off mass can avoid the region containing merger progenitors, the Be fraction at the turn-off will remain close to the maximum theoretical prediction. Then as the secondary mass decreases, the parabolae will move into the corner with low mass ratio and low primary mass, and consequently, the Be fraction will decrease.

To test our hypothesis, we performed a Monte Carlo simulation in which systems were selected randomly from given distributions of initial primary mass and initial mass ratio. As before, we assumed that mass transfer is completely non-conservative ($\Delta M/M_{2,i} = 0$). By choosing a turn-off mass, we can calculate the masses of Be stars in the simulation and thus assess the Be fraction. The occurrence of mergers is decided using the stable mass-transfer region depicted in Fig. 5a. The motivation for selecting this region is explained next. Analysis of mass transfer from giant donors (Pavlovskii & Ivanova 2015) has indicated that mass transfer from Hertzsprung-gap stars is stable at mass ratios greater than around 0.6. We therefore assumed that all systems with initial mass ratios greater than 0.6 undergo stable mass transfer. The stability of mass transfer is determined by the donor's reaction to mass loss, where stars with radiative envelopes generally tend to contract as the envelope is being stripped (Hjellming & Webbink 1987). This is reversed for convective-envelope stars, which typically expand in response to mass loss (Hjellming & Webbink 1987). Stellar structure calculations suggest that stars with a mass greater than around 60 $M_\odot$ spend very little time as red giants, meaning that they mostly have radiative envelopes (Schootemeijer et al. 2019; Klencki et al. 2021) such that mass-transfer is much more likely to occur when the donor has a radiative envelope. We therefore propose that mass transfer is stable for all systems with a primary mass exceeding 60 $M_\odot$. The region of instability is then defined by a linear interpolation between systems with $M_1 = 60 M_\odot, q = 0.1$ and $M_1 = 5 M_\odot, q = 0.6$, as depicted in Fig. 5a. We again
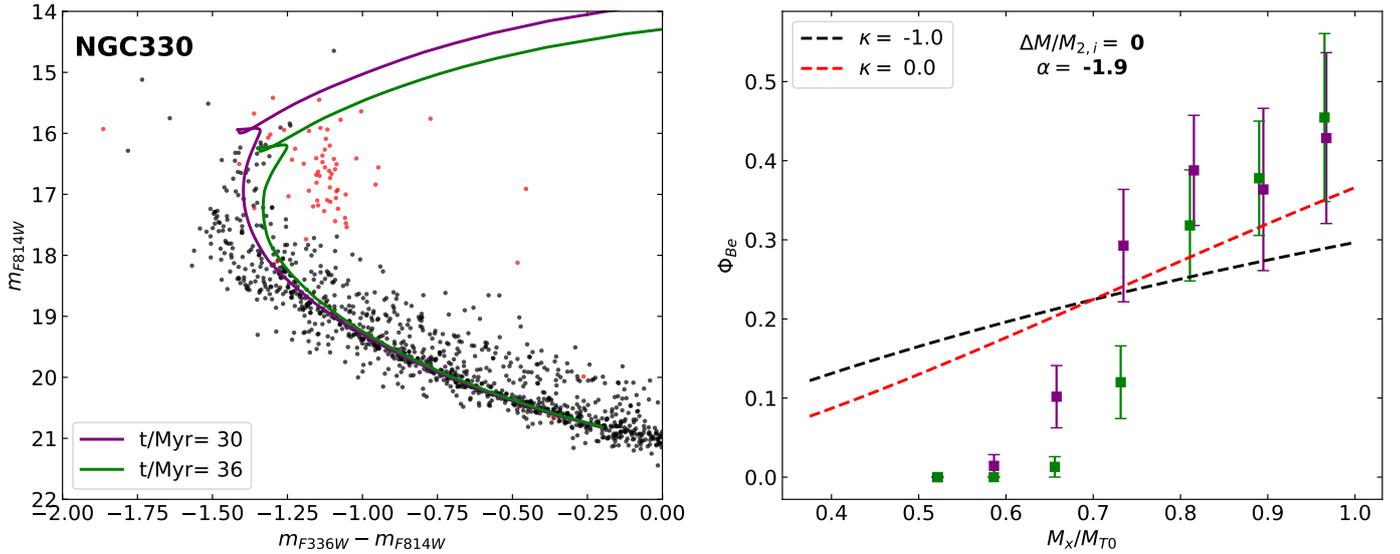
Fig. 6. Colour-magnitude diagram of NGC 330 with Hα emitters marked in red (*left*). Isochrone fits with ages 30 and 36 Myr are plotted in purple and green, respectively. Both isochrones have an initial rotation of $v_{rot}/v_{crit} = 0.6$, a distance modulus of 18.8 mag, and a reddening of $E(B–V) = 0.1$ mag. Be fraction as a function of fractional turn-off mass as measured by the 30 Myr isochrone (in purple) and the 36 Myr isochrone (in green; *right*). Dashed lines show theoretical upper limit given by Eq. (30) with $\alpha = -1.9$, $\Delta M/M_{2,i} = 0$, and $\kappa = -1.0, 0$, as given by the legend.

assumed that the orbital period plays no role in determining the stability of mass transfer, which allows us to avoid specifying an orbital period distribution.

Merger products change the distribution of masses in a population and thus affect the Be fraction as a function of mass. We assumed that Be stars are not merger products for two reasons. Firstly, it is thought that although merger products are initially fast-rotators, while thermal equilibrium is returned, internal angular momentum redistribution causes a rapid spin-down (Schneider et al. 2019). What is more, stellar mergers may produce strongly magnetised stars (Ferrario et al. 2009; Wickramasinghe et al. 2014; Schneider et al. 2019) that would further spin down due to magnetic braking. Secondly, a merger of a star with a helium core and a main-sequence object does not produce a hydrogen-burning star owing to the higher mean molecular weight and lower entropy of the helium-core star (Langer 2012; Justham et al. 2014). As observations (Milone et al. 2018) show Be stars to be concentrated on the main sequence, we assumed that Be stars are unlikely to be produced from the merging of two stars. For mergers, we assumed that the fraction of mass lost during the merging process to the total binary mass is equal to

$$\mu_{loss} = \frac{0.3q}{1 + q^2} \tag{34}$$

(Glebbeek & Pols 2008), which equates to between 2 and 15% over the range $0.1 < q < 1$. As the mass lost during the merging process is assumed to be low, mergers always have a mass exceeding the turn-off mass and do not affect the Be fractions on the main sequence.

Figure 5b shows the results of the simulation for clusters with turn-off masses of 9 and 6 $M_\odot$, which roughly correspond to NGC 330 and NGC 2164, respectively. The chosen criteria have maintained a high Be fraction near the turn-off and also produced a sudden end to the Be-sequence. They provide a reasonable fit to the measured Be fractions in NGC 330 and NGC 2164. It is remarkable that these simple, although physically motivated, stable mass-transfer criteria can successfully reproduce the numbers of Be stars in the open clusters studied here. Our empirical

mass-transfer stability criteria could be tested in the next generation of detailed binary evolution models.

6. Discussion

6.1. Uncertainties

The largest uncertainty in our procedure comes from the isochrone fits. Most if not all open clusters display an extended main-sequence turn-off, making the choice of a suitable isochrone age difficult. This is illustrated in Fig. 6, where isochrones of two different ages are fitted to NGC 330 and the Be fractions are evaluated. A small variation in the adopted age can cause the Be count in some bins to vary by up to 0.2. The end of the Be sequence is particularly affected. A similar sensitivity is also found for small differences in the distance modulus, reddening, and isochrone rotation rates. Based on Fig. 6, we judge that the uncertainty on the measured Be fractions is approximately 0.1 without the counting error.

To measure the observed Be fraction as a function of mass, we must use slanted bins. In calculating the gradient of these bins, we have assumed that the Be star disc always adds $0.25m_{F814W}$ to the magnitude of the star. This may be an over-simplification, with Be stars of differing mass or evolutionary status hosting relatively brighter or dimmer discs. Unfortunately, this effect is difficult to observe and characterise and is also compounded by the fact that Be stars can display spectral and photometric variability (Porter & Rivinius 2003). Sigut et al. (2009) reported that the ratios of stellar effective temperature to mean disc temperature and infrared excess are indeed functions of spectral type.

Far older clusters, such as the 300 Myr old NGC 1856, have much lower Be fractions than their younger counterparts (see Milone et al. 2018, Fig. 17). Our simple model and mass-transfer stability criteria predict that the Be fraction does not vary strongly with turn-off mass and therefore is unable to explain the turn-off Be fraction in NGC 1856 of about 0.2. However, this discrepancy may be partly explained by a changing binary fraction with mass because it is known that more massive

stars display a stronger preference for binary companionship (Köhler et al. 2006; Kouwenhoven et al. 2009). Older clusters that contain fewer binaries therefore naturally have fewer Be stars produced from binary interaction. Another aspect behind the emission line phenomenon is the ionising power of the star. To produce an emission line, the central Be star must ionise its decretion disc. Without sufficient ionising power, no emission line will be observable even if a disc is present, and hence the star will seem ordinary. The ionising photon emission rate is known to be strongly dependent on effective temperature (Sternberg et al. 2003). At some limiting mass, we therefore expect the central star to be unable to ionise a disc. This effect may play a role in lowering the Be fraction in older clusters and causing a dearth of Be stars at low magnitudes in the colour-magnitude diagram. The two clusters studied here have several stars that are very red, even though they are not marked as Hα emitters. They might be such "dormant Be stars".

Lastly, we note that we assumed that the properties of binary systems are distributed according to very simple laws. In reality, however, the distributions may well be complex functions of one another, for example the mass-ratio distribution might be a function of the primary mass. The nature of these distributions is set by poorly understood binary star formation mechanisms, as outlined by Tokovinin & Moe (2020).

6.2. Mass-transfer efficiency

To construct our prediction of Be star fractions, we assumed that no mass is accreted during mass transfer. This scenario fits the observations reasonably well. It has been demonstrated that for efficient mass transfer, the Be star fraction decreases, meaning that the theoretical framework presented here would not fit observations if mass transfer were efficient. This leads us to propose that if the binary Be formation channel is the dominant one, mass transfer is far from conservative on average.

Binary models with conservative mass transfer predict Be stars to be blue stragglers after having gained a lot of mass (van Bever & Vanbeveren 1997). The observations presented in Fig. 3 contradict this prediction. The vast majority of Be stars lie either on the main sequence or are slightly redder than it. This strengthens our conclusion that mass transfer is highly non-conservative.

6.3. Initial binary fraction

To obtain our results, we assumed an initial binary fraction of 1, which might be thought too extreme. We have demonstrated that in a coeval population of binary systems, 30% of the systems at most are post-interaction binaries (see Sect. 3). Pre-interaction systems would therefore comprise not less than 70% of this population. Dedicated models show that under the assumption of a constant star formation rate, $30^{+10}_{-15}\%$ of the massive stars are the products of binary interaction (de Mink et al. 2014), in broad agreement with this work.

Post-interaction binaries are either merger products, contain a relatively low-mass post-main-sequence object (helium star, black hole, neutron star, or white dwarf) with a main-sequence (possibly emission-line) star or form a runaway star ejected from the binary orbit after a supernova. These objects manifest themselves either as single stars or would be difficult to detect as binaries (de Mink et al. 2011b,a). Even in a population whose initial binary fraction is 1, apparently single stars are therefore present in the proportions described above.

By examining radial velocity variations of very massive stars, we may only measure the pre-interaction binary fraction (as supernova kicks are believed to disrupt almost all binary systems (Brandt & Podsiadlowski 1995)), which has been observed to be about 0.7 for O-type stars (Sana et al. 2012). We therefore argue that the initial binary fraction is certainly greater than the observed pre-interaction binary fraction. At this stage, we therefore must remain open to the possibility that an initial binary fraction very close to one is indeed realised in nature.

7. Conclusions

In light of various uncertainties plaguing binary evolution calculations, we have investigated whether binary evolution can possibly reflect the large numbers of Be stars observed in open clusters. Starting from the premise that any binary system, regardless of primary mass, orbital period, or mass-ratio, will undergo stable mass transfer to form a Be star, we have calculated a rigorous upper limit to the formation of Be stars through this channel. It has been demonstrated that this binary evolution does not allow more than about 30% of stars to have been spun up through binary interaction and become emission-line objects.

After using isochrone fits to assign stars in the colour-magnitude diagram masses, a count of the Hα emitters in two open clusters revealed that for objects near the turn-off, our upper limit provides a reasonable description of the numbers of Be stars, especially when uncertainties arising from the counting method are taken into account. The upper limit, however fails to describe the sudden decrease in Be fraction that both clusters exhibit at a mass approximately 70–80% of the turn-off mass.

This problem can be rectified by assuming that systems with a low mass ratio and low primary mass merge. By adopting simple, although physically justified, stable mass-transfer criteria, we have shown that a good fit to the observational data is produced by this postulate.

It has been demonstrated in a qualitative way that in coeval populations, a larger mass gain of the donor results in a smaller Be fraction at a given mass. Because the observed Be fractions are very close to our upper limit when totally inefficient mass transfer is assumed, it follows that to be able to explain such high Be fractions, mass transfer must be non-conservative.

We have highlighted the distinction between the initial binary fraction and the binary fraction that can be observed, and we argued that these two quantities are not equal. This is so because a population of binary stars will always contain post-interaction systems that will appear to be single stars. The calculations outlined in this work provide rough constraints on this discrepancy, suggesting that the initial binary fraction is much higher than previously thought.

In conclusion, our theoretical argument serves to reinforce numerous observational arguments that suggest binary interactions to be responsible for Be stars. We conclude that observations of Be stars in young open clusters (Milone et al. 2018; Bodensteiner et al. 2020a) do not contradict the hypothesis that Be stars originate exclusively from mass transfer in binary systems. We have shown that if all Be stars are binary interaction products, somewhat extreme assumptions must be realised, such as an initial binary fraction very close to unity, a shallow initial mass function, and very non-conservative mass transfer. Whether these conditions can be met by the stars in the sky remains to be determined.

References

Ahmed, A., & Sigut, T. A. A. 2017, MNRAS, 471, 3398
Bestenlehner, J. M., Crowther, P. A., Caballero-Nieves, S. M., et al. 2020, MNRAS, 499, 1918
Bodensteiner, J., Sana, H., Mahy, L., et al. 2020a, A&A, 634, A51
Bodensteiner, J., Shenar, T., & Sana, H. 2020b, A&A, 641, A42
Boubert, D., & Evans, N. W. 2018, MNRAS, 477, 5261
Brandt, N., & Podsiadlowski, P. 1995, MNRAS, 274, 461
Brott, I., de Mink, S. E., Cantiello, M., et al. 2011, A&A, 530, A115
Brož, M., Mourard, D., Budaj, J., et al. 2021, A&A, 645, A51
Carciofi, A. C., Bjorkman, J. E., Otero, S. A., et al. 2012, ApJ, 744, L15
Castro, N., Fossati, L., Langer, N., et al. 2014, A&A, 570, L13
Choi, J., Dotter, A., Conroy, C., et al. 2016, ApJ, 823, 102
Claret, A., & Torres, G. 2016, A&A, 592, A15
Coe, M. J., Kennea, J. A., Evans, P. A., & Udalski, A. 2020, MNRAS, 497, L50
Collins, G. W., II, & Truax, R. J. 1995, ApJ, 439, 860
de Mink, S. E., Pols, O. R., & Hilditch, R. W. 2007, A&A, 467, 1181
de Mink, S. E., Langer, N., & Izzard, R. G. 2011a, Bull. de la Soc. Royale des Sci. de Liege, 80, 543
de Mink, S. E., Langer, N., & Izzard, R. G. 2011b, in Active OB Stars: Structure, Evolution, Mass Loss, and Critical Limits, eds. C. Neiner, G. Wade, G. Meynet, G. Peters, 272, 531
de Mink, S. E., Sana, H., Langer, N., Izzard, R. G., & Schneider, F. R. N. 2014, ApJ, 782, 7
Dorigo Jones, J., Oey, M. S., Paggeot, K., Castro, N., & Moe, M. 2020, ApJ, 903, 43
Dufton, P. L., Langer, N., Dunstall, P. R., et al. 2013, A&A, 550, A109
Dunstall, P. R., Brott, I., Dufton, P. L., et al. 2011, A&A, 536, A65
Ekström, S., Meynet, G., Maeder, A., & Barblan, F. 2008, A&A, 478, 467
Espinosa Lara, F., & Rieutord, M. 2011, A&A, 533, A43
Ferrario, L., Pringle, J. E., Tout, C. A., & Wickramasinghe, D. T. 2009, MNRAS, 400, L71
Glebbeek, E., & Pols, O. R. 2008, A&A, 488, 1017
Gossage, S., Conroy, C., Dotter, A., et al. 2019, ApJ, 887, 199
Hastings, B., Wang, C., & Langer, N. 2020, A&A, 633, A165
Hjellming, M. S., & Webbink, R. F. 1987, ApJ, 318, 794
Hogeveen, S. J. 1991, The mass-ratio distribution of binary stars, PhD Thesis
Huang, W., Gies, D. R., & McSwain, M. V. 2010, ApJ, 722, 605
Hurley, J. R., Tout, C. A., & Pols, O. R. 2002, MNRAS, 329, 897
Iqbal, S., & Keller, S. C. 2013, MNRAS, 435, 3103
Justham, S., Podsiadlowski, P., & Vink, J. S. 2014, ApJ, 796, 121
Kamann, S., Bastian, N., Gossage, S., et al. 2020, MNRAS, 492, 2177
Keller, S. C., Wood, P. R., & Bessell, M. S. 1999, A&AS, 134, 489
Kippenhahn, R. 1974, in Late Stages of Stellar Evolution, eds. R. J. Tayler, & J. E. Hesser, 66, 20
Klement, R., Carciofi, A. C., Rivinius, T., et al. 2017, A&A, 601, A74
Klement, R., Carciofi, A. C., Rivinius, T., et al. 2019, ApJ, 885, 147
Klencki, J., Nelemans, G., Istrate, A. G., & Chruslinska, M. 2021, A&A, 645, A54
Kobulnicky, H. A., & Fryer, C. L. 2007, ApJ, 670, 747
Köhler, R., Petr-Gotzens, M. G., McCaughrean, M. J., et al. 2006, A&A, 458, 461
Kouwenhoven, M. B. N., Brown, A. G. A., Portegies Zwart, S. F., & Kaper, L. 2007, A&A, 474, 77
Kouwenhoven, M. B. N., Brown, A. G. A., Goodwin, S. P., Portegies Zwart, S. F., & Kaper, L. 2009, A&A, 493, 979
Kriz, S., & Harmanec, P. 1975, Bull. Astr. Inst. Czechosl., 26, 65
Labadie-Bartz, J., Pepper, J., McSwain, M. V., et al. 2017, AJ, 153, 252
Langer, N. 2012, ARA&A, 50, 107
Langer, N., Schürmann, C., Stoll, K., et al. 2020, A&A, 638, A39

Lennon, D. J., Lee, J. K., Dufton, P. L., & Ryans, R. S. I. 2005, A&A, 438, 265
Li, K. L., Kong, A. K. H., Charles, P. A., et al. 2012, ApJ, 761, 99
Liu, Q. Z., van Paradijs, J., & van den Heuvel, E. P. J. 2006, A&A, 455, 1165
Maeder, A., Grebel, E. K., & Mermilliod, J.-C. 1999, A&A, 346, 459
Marino, A. F., Przybilla, N., Milone, A. P., et al. 2018, AJ, 156, 116
Martayan, C., Baade, D., & Fabregat, J. 2010, A&A, 511, A11
McSwain, M. V., & Gies, D. R. 2005, ApJS, 161, 118
Milone, A. P., Marino, A. F., Di Criscienzo, M., et al. 2018, MNRAS, 477, 2640
Packet, W. 1981, A&A, 102, 17
Pavlovskii, K., & Ivanova, N. 2015, MNRAS, 449, 4415
Paxton, B., Bildsten, L., Dotter, A., et al. 2011, ApJS, 192, 3
Paxton, B., Cantiello, M., Arras, P., et al. 2013, ApJS, 208, 4
Paxton, B., Marchant, P., Schwab, J., et al. 2015, ApJS, 220, 15
Paxton, B., Schwab, J., Bauer, E. B., et al. 2018, ApJS, 234, 34
Paxton, B., Smolec, R., Schwab, J., et al. 2019, ApJS, 243, 10
Peters, G. J. 1989, Space Sci. Rev., 50, 9
Petrovic, J., Langer, N., & van der Hucht, K. A. 2005, A&A, 435, 1013
Pinsonneault, M. H., Kawaler, S. D., Sofia, S., & Demarque, P. 1989, ApJ, 338, 424
Pols, O. R., Cote, J., Waters, L. B. F. M., & Heise, J. 1991, A&A, 241, 419
Porter, J. M. 1996, MNRAS, 280, L31
Porter, J. M., & Rivinius, T. 2003, PASP, 115, 1153
Raguzova, N. V., & Popov, S. B. 2005, Astron. Astrophys. Trans., 24, 151
Rímulo, L. R., Carciofi, A. C., Vieira, R. G., et al. 2018, MNRAS, 476, 3555
Salpeter, E. E. 1955, ApJ, 121, 161
Sana, H., de Mink, S. E., de Koter, A., et al. 2012, Science, 337, 444
Sana, H., de Koter, A., de Mink, S. E., et al. 2013, A&A, 550, A107
Scalo, J. M. 1986, Fund. Cosmic Phys., 11, 1
Schneider, F. R. N., Izzard, R. G., Langer, N., & de Mink, S. E. 2015, ApJ, 805, 20
Schneider, F. R. N., Sana, H., Evans, C. J., et al. 2018, Science, 359, 69
Schneider, F. R. N., Ohlmann, S. T., Podsiadlowski, P., et al. 2019, Nature, 574, 211
Schootemeijer, A., Götberg, Y., de Mink, S. E., Gies, D., & Zapartas, E. 2018, A&A, 615, A30
Schootemeijer, A., Langer, N., Grin, N. J., & Wang, C. 2019, A&A, 625, A132
Secchi, A. 1866, Astron. Nachr., 68, 63
Shao, Y., & Li, X.-D. 2014, ApJ, 796, 37
Shao, Y., & Li, X.-D. 2016, ApJ, 833, 108
Shenar, T., Bodensteiner, J., Abdul-Masih, M., et al. 2020, A&A, 639, L6
Sigut, T. A. A., McGill, M. A., & Jones, C. E. 2009, ApJ, 699, 1973
Sternberg, A., Hoffmann, T. L., & Pauldrach, A. W. A. 2003, ApJ, 599, 1333
Struve, O. 1931, ApJ, 73, 94
Sun, W., de Grijs, R., Deng, L., & Albrow, M. D. 2019, ApJ, 876, 113
Tokovinin, A., & Moe, M. 2020, MNRAS, 491, 5158
Tout, C. A. 1991, MNRAS, 250, 701
Tout, C. A., Aarseth, S. J., Pols, O. R., & Eggleton, P. P. 1997, MNRAS, 291, 732
Townsend, R. H. D., Owocki, S. P., & Howarth, I. D. 2004, MNRAS, 350, 189
Trimble, V. 1990, MNRAS, 242, 79
van Bever, J., & Vanbeveren, D. 1997, A&A, 322, 116
Vinciguerra, S., Neijssel, C. J., Vigna-Gómez, A., et al. 2020, MNRAS, 498, 4705
von Zeipel, H. 1924, MNRAS, 84, 665
Wang, C., Langer, N., Schootemeijer, A., et al. 2020, ApJ, 888, L12
Wellstein, S., Langer, N., & Braun, H. 2001, A&A, 369, 939
Wickramasinghe, D. T., Tout, C. A., & Ferrario, L. 2014, MNRAS, 437, 675
Zahn, J. P., Ranc, C., & Morel, P. 2010, A&A, 517, A7
Zorec, J., Frémat, Y., Domiciano de Souza, A., et al. 2016, A&A, 595, A132
Zorec, J., Frémat, Y., & Cidale, L. 2005, A&A, 441, 235

Appendix A: Stars at the critical velocity

Here we investigate how critically rotating and slowly rotating stars vary in terms of their effective temperatures and luminosities. Because stable and reliable numerical models of very fast rotating stars are difficult to produce, we employ a simple analytic model.

The luminosity of a main-sequence star is generated from nuclear reactions in the central region. As stars are centrally condensed, when a given star is spun up to the critical velocity, the centripetal forces acting in the central regions are much weaker than the force of gravity, meaning the structure of the core is largely unchanged. Hence, the intrinsic luminosity is constant to first order.

When a star is spun up, the outer structure changes, however. The equatorial radius increases, and therefore so does the surface area of the star, S. This then causes the effective temperature to decrease, as evidenced by the Stefan-Boltzmann law,

$$L \propto S T_{\text{eff}}^4. \tag{A.1}$$

To characterise this change in effective temperature, we used the Roche model, which describes a star in which all mass is concentrated at the centre, and that rotates with constant angular velocity Ω. In this framework, the effective potential with respect to the radial coordinate r and latitude θ is

$$\Psi(r, \theta) = -\frac{GM}{r} - \frac{1}{2}\Omega^2 r^2 sin^2(\theta). \tag{A.2}$$

At the critical angular velocity, the polar radius, R_p, is equal to the radius of an equivalent non-rotating star of the same mass, whereas the equatorial radius, R_e, is given by

$$R_e = \frac{3}{2}R_p. \tag{A.3}$$

Taking the $x - y$ plane to be parallel to the axis of rotation, where y represents the distance along the rotation axis and x the perpendicular distance from the rotation axis, the surface of a critically rotating star is described by

$$\left(\frac{y}{R_e}\right)^2 = \left(\frac{2}{3 - x^2/R_e^2}\right)^2 - \left(\frac{x}{R_e}\right)^2, \tag{A.4}$$

(Zahn et al. 2010). The surface area of a star is (see Paxton et al. 2019, Appendix B) in general

$$S = 4\pi \int_0^{R_e} x \sqrt{\left(\frac{dy}{dx}\right)^2 + 1} \, dx. \tag{A.5}$$

After choosing units such that $R_e = 1$, Eqs. (A.4) and (A.5) can be solved numerically to give the surface area of a critical rotator, S_c, as

$$S_c \approx 4\pi \times 0.7028. \tag{A.6}$$

Compare this to the surface areas of non-rotating stars with radii R_e and R_p,

$$S_0(r = R_e) = 4\pi \tag{A.7}$$

and

$$S_0(r = R_p) = 4\pi \left(\frac{2}{3}\right)^2 \approx 4\pi \times 0.4444. \tag{A.8}$$

As expected, we have

$$S_o(r = R_p) < S_c < S_o(r = R_e). \tag{A.9}$$

The surface area of a critically rotating star is about 1.58 times larger than that of its non-rotating counterpart.

According to Eq. (A.1), the temperature of a star after it is spun up to critical therefore decreases by a factor of 0.89.

Appendix B: Stellar isochrones

As our model predictions give the Be fraction as a function of mass, we must extract masses from stars in the colour-magnitude diagram to make an effective comparison with observations. To this end, we employed isochrones of single rotating stars to assign mass ranges to different areas of the colour-magnitude diagram.

We used the grid of Schootemeijer et al. (2019), which was extended to masses between 2 and 20 $M_\odot$ with slight changes to internal mixing (see below).The code used was MESA (Paxton et al. 2011, 2013, 2015, 2018, 2019). Models were computed at initial rotation rates between 0 and 80% of the critical velocity in steps of 10%. As is standard in MESA, the critical velocity is defined as

$$v_{\text{crit}} = \sqrt{\frac{GM}{R}(1 - \Gamma)}, \tag{B.1}$$

where Γ is the ratio of the luminosity to the Eddington luminosity, and is negligible for the models presented here. At early times, the models undergo a relaxation period, during which the critical velocity fraction can oscillate wildly. To circumvent this, we defined the initial critical velocity fraction at the point when the model has burnt 3% of its initial hydrogen content by mass.

The physics employed in the models is mostly identical to that of Brott et al. (2011), except for the treatment of two mixing processes. Stepped convective overshooting was adopted, which extends the convective zone by α_{OV} times the local pressure scale height. A dependence of α_{OV} on mass accounts for observational trends (Castro et al. 2014; Claret & Torres 2016; Schootemeijer et al. 2019), whereby α_{OV} increases linearly from 0.1 at 1.66 $M_\odot$ Claret & Torres (2016) to 0.3 at 20 $M_\odot$ Brott et al. (2011). Furthermore, time smoothing in rotational mixing was turned off to avoid unrealistically strong mixing.

Isochrones were generated through a series of linear interpolations and were split up into two equivalent evolutionary phases (EEPs). The first phase lasts until core-hydrogen depletion, and the second phase lasts from core-hydrogen depletion until core-helium depletion. To compute the parameters of a star in the first EEP with initial mass M_i and initial critical velocity fraction v_i at time t, we first determined the time at which this star would experience core-hydrogen exhaustion, T_{MS}. Four models were used for the interpolation: two models with initial masses M_1 and initial critical velocity fractions $v_{1,a}$ and $v_{1,b}$, and similarly, two models with initial masses M_2 and initial critical velocity fractions $v_{2,a}$ and $v_{2,b}$. The models were selected such that $M_1 < M_i < M_2$ and $v_{1,a} < v_i < v_{1,b}$ and similarly for $v_{2,a}, v_{2,b}$. For M_1 and M_2, we interpolated the lifetime when initial $v_{\text{rot}}/v_{\text{crit}} = v_i$ from these models, as shown in Fig. B.1a. The hydrogen-burning lifetime was then computed as an interpolation in mass between the values of M_1 and M_2, as depicted in Fig. B.1 b. For this step, the most accurate results are obtained when the logarithm of the hydrogen-burning lifetime is interpolated against the logarithm of initial mass. Using the interpolated lifetime, T_i, of this star with initial mass M_i and initial critical velocity fraction v_i, we defined its fractional lifetime as t/T_i. This fractional lifetime is the value at which all further interpolations were carried out. Next, a given quantity (for the purposes of making isochrones, the quantities of interest are effective temperature and luminosity), Q, was interpolated at a fractional lifetime of t/T_i for the four selected models, as in B.1 c. The penultimate step was to calculate the quantities Q_{M_1}, Q_{M_2}, which represent the values of Q of a star with mass M_1, M_2, initial critical velocity fraction v_i, and fractional lifetime t/T_i by interpolating across the initial

critical velocity fraction like in Fig. B.1 d. Finally, an interpolation in initial mass between the quantities Q_{M_1} and Q_{M_2} was made to produce the value of the chosen parameter for a star of given mass, initial rotation rate, and age.

To generate the second EEP, the same procedure was used, but only with a different fractional lifetime, namely the fractional helium-burning lifetime, t/T_{He}, such that at core-hydrogen exhaustion $t/T_{He} = 0$ and at core helium exhaustion $t/T_{He} = 1$.

Absolute magnitudes in Hubble Space Telescope filters were computed by interpolating tables of synthetic stellar spectra provided by the MIST project of Choi et al. (2016). Apparent magnitudes were then calculated as

$$m_{\text{F814W}} = M_{\text{F814W}} + A_{\text{F814W}} + \mu, \tag{B.2}$$

$$m_{\text{F336W}} = M_{\text{F336W}} + A_{\text{F336W}} + \mu, \tag{B.3}$$

with μ being the distance modulus, and absorption coefficients $A_{F814W} = 2.04E(B - V)$ and $A_{F336W} = 5.16E(B - V)$ (Milone et al. 2018).
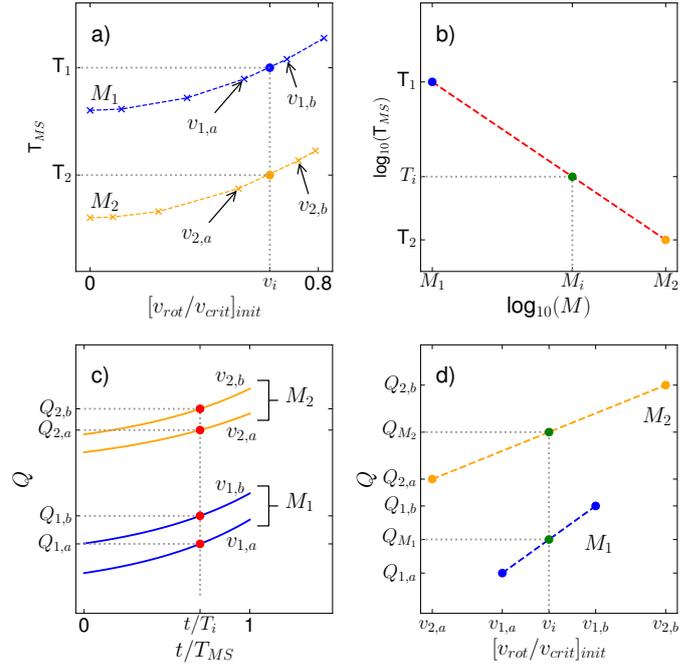
Fig. B.1. Schematic representation of the interpolation procedure employed to produce isochrones. See text for a thorough explanation.

Appendix to Chapter 4

A full reproduction of the publication resulting from work described in Chapter 4 is given on the next page.

This work is reproduced under a CC-BY 4.0 license.

Astronomy
&
Astrophysics

A model of anisotropic winds from rotating stars for evolutionary calculations[*]

B. Hastings[1], N. Langer[1,2], and J. Puls[3]

[1] Argelander-Institut für Astronomie, Universität Bonn, Auf dem Hügel 71, 53121 Bonn, Germany
   e-mail: bhastings@astro.uni-bonn.de
[2] Max-Planck-Institut für Radioastronomie, Auf dem Hügel 69, 53121 Bonn, Germany
[3] LMU München, Universitätssternwarte, Scheinerstr. 1, 81679 München, Germany

ABSTRACT

Context. The surface properties of rotating stars can vary from pole to equator, resulting in anisotropic stellar winds which are not included in the currently available evolutionary models.
Aims. We developed a formalism to describe the mass and angular momentum loss of rotating stars which takes into account both the varying surface properties and distortion due to rotation.
Methods. Adopting the mass-loss recipe for non-rotating stars, we assigned to each point on the surface of a rotating star an equivalent non-rotating star, for which the surface mass flux is given by the recipe. The global mass-loss and angular momentum loss rates are then given by integrating over the deformed stellar surface as appropriate. Evolutionary models were computed and our prescription is compared to the currently used simple mass-loss enhancement recipes for rotating stars.
Results. We find that mass-loss rates are largely insensitive to rotation for models not affected by the bi-stability jump. For those affected by the bi-stability jump, the increase in mass-loss rates with respect to time is smoothed. As our prescription considers the variation of physical conditions over the stellar surface, the region affected by the bi-stability jump is able to grow gradually instead of the whole star suddenly being affected.
Conclusions. We have provided an easy to implement and flexible, yet physically meaningful prescription for calculating mass and angular momentum loss rates of rotating stars in a one-dimensional stellar evolution code which compares favourably to more physically comprehensive models

Key words. stars: evolution – stars: massive – stars: mass-loss – stars: winds, outflows – stars: rotation

1. Introduction

All massive stars suffer from the effects of stellar winds. For O-type stars, the winds can be so strong that a significant portion of the star evaporates and the evolutionary pathway is altered dramatically, for example forming a Wolf-Rayet star (Maeder & Meynet 1987; de Koter et al. 1997). In contrast, lower-mass stars typically lose only a negligible fraction of their mass to winds. However even a non-magnetic wind carries angular momentum away from a star, and a star's spin evolution can even be affected by weak winds (Langer 1998).

In the simplest sense, the density and velocity structure and thus also the mass-loss rate of a radiation-driven wind is determined by the opposing effects of gravity and radiative acceleration. Gravity serves to bind material to the stellar surface, while radiation, through both continuum and line opacities, provides a force to overcome gravity (Castor et al. 1975; Pauldrach et al. 1986). Rotation directly affects both the gravitational field strength and the radiation field (von Zeipel 1924), with both varying over the stellar surface, in turn resulting in an anisotropic wind (Poe & Friend 1986; Cranmer & Owocki 1995; Curé & Rial 2004).

For an anisotropic wind, attention needs to be paid to angular momentum loss since mass lost at the equator carries a larger specific angular momentum than mass lost near the poles, especially so for stars that are significantly deformed from sphericity. Owing to internal structural changes, stars born with moderate rotation may evolve to become extremely fast rotators (Hastings et al. 2020b), so the effects of rotation on stellar winds have the potential to be relevant to a large portion of stars.

For a number of decades, massive star modelling efforts (Heger et al. 2000; Brott et al. 2011; Paxton et al. 2013) have described the effects of rotation on mass loss by increasing the mass-loss rate of an equivalent non-rotating star by a factor that depends on the rotation rate (Friend & Abbott 1986). Such a formulation is lacking due to two issues. Firstly, it is assumed that, independent of the wind recipe used, rotation always increases mass-loss rates by the same relative amount. This is not a fair assumption because two of the major effects of rotation on the surface of a star are to weaken the gravitational field and to reduce the surface-averaged effective temperature (von Zeipel 1924). These two effects generally, though not always, serve to counteract each other, with winds being enhanced by weaker gravities but diminished by lower effective temperatures. It is unclear which effect dominates. Both the dependence of the mass-loss rate on temperature and the assumed temperature profile across the stellar surface (gravity darkening law) will govern whether rotation enhances or reduces mass loss, meaning that the

---

enhancement ought to be model dependant (cf. Müller & Vink 2014).

Secondly, some of the mathematical functions used to provide the mass-loss enhancement diverge as the star approaches the critical velocity. While this behaviour is used in stellar evolution calculations merely to prevent models from exceeding critical rotation (Heger et al. 2000; Petrovic et al. 2005), it is unphysical not least because it is usually[1] only material at the equator which achieves the critical rotation velocity, and strictly the equator covers an infinitesimally small surface, while gravity does manage to keep the star bound over the rest of the surface.

Angular momentum loss from massive stars plays a role in several active research topics such as the study of Be stars (Curé 2004; Curé et al. 2005; Ekström et al. 2008; Hastings et al. 2020b); the occurrence of chemically homogeneous evolution, relevant to double black-hole mergers (Marchant et al. 2016) and gamma-ray burst progenitors (Yoon et al. 2006; Aguilera-Dena et al. 2020); wind-driven orbital evolution in massive binary stars (MacLeod & Loeb 2020; Sen et al. 2022); and of course the rotation rates of stars in general. Improved modelling of the winds of rotating stars would be beneficial to the advancement our understanding of stellar physics.

Various studies concerning winds from rotating massive stars have been performed (e.g., Poe & Friend 1986; Poe et al. 1989; Owocki et al. 1994; Cranmer & Owocki 1995; Pelupessy et al. 2000; Petrenz & Puls 2000; Curé et al. 2012; Müller & Vink 2014; Gagnier et al. 2019b), although the results of which have not been adopted for use in stellar evolution codes. Our aim is to provide a simple and easily implementable scheme that improves upon the popular rotationally enhanced mass-loss schemes. We applied our scheme to the one-dimensional stellar evolution code MESA and provide the files necessary to compute models using it[2].

The structure of this paper is as follows. Section 2 details the derivation of our stellar wind prescription. In Sect. 3 we compare the results of our new wind model to the commonly used rotationally enhanced mass-loss prescription. A brief discussion of uncertainties is given in Sect. 4. Section 6 hosts a comparison of our results to more sophisticated approaches. Lastly, our conclusions are put forward in Sect. 7.

2. Method

2.1. Anisotropic wind model

Our basic philosophy is to apply a one-dimensional wind recipe to every point on the surface of a rotating star. For every point on the stellar surface, the given wind recipe uses the local physical conditions to provide a surface mass-flux, which when integrated results in global mass and angular momentum loss rates. We shall now determine the surface properties of a rotating star.

2.1.1. Surface properties of a rotating star

A rotating star with mass M, polar radius R_p, equatorial radius R_e, luminosity L is assumed to be rotating rigidly with angular velocity Ω. In reasonable agreement with detailed stellar models (Maeder 2009), we assume that the polar radius is not affected

---

by rotation. The contribution of radiative acceleration to the total gravity shall be ignored, as we focus primarily on stars with luminosities below the Eddington luminosity. The critical velocity, or break-up velocity is then the Keplerian angular velocity, at which the gravitational force matches the centrifugal force at the equator and reads

$$\Omega_{Kep} = \sqrt{\frac{GM}{R_e^3}} \tag{1}$$

and the fraction of Keplerian angular velocity is denoted as

$$\omega = \frac{\Omega}{\Omega_{Kep}}. \tag{2}$$

Recent two-dimensional models of rotating stars suggest that the rotation velocity at which material becomes unbound from the stellar surface is very close to the Keplerian velocity (Gagnier et al. 2019a). However, these models only cover two separate values of the stellar mass (15 and 40 $M_\odot$) at one point in their evolution. Therefore we cannot exclude that for very luminous stars, radiation might play a significant role in unbinding material from the surface and thus reducing the critical rotation velocity. This issue is discussed further in Sect. 2.2.

We note that several different working definitions of the critical velocity velocity exist (see discussion in Sect. 2.3.1 of Rivinius et al. 2013 and their Eqs. (3) and (4)). Our choice is made to be consistent with the stellar evolution code MESA (Paxton et al. 2019).

In the co-rotating frame of a rotating star, the centrifugal force is perpendicular to the rotation axis, which causes the effective surface gravity to to become latitude-dependant. Following from the varying surface gravity, effective temperature also varies across the surface (von Zeipel 1924). Also effected is the star's shape, evidenced by a bulging equator. These three effects shall now be quantified in order.

As massive stars are centrally condensed, the use of the Roche potential is justified (Collins 1965; Rieutord 2016). We define the effective surface gravity as the sum of self-gravitation and centrifugal forces which is

$$\mathbf{g}_{eff}(\theta) = \left(-\frac{GM}{r(\theta)^2}\sin(\theta) + \Omega^2 r(\theta)\sin(\theta)\right)\mathbf{x} - \frac{GM}{r(\theta)^2}\cos(\theta)\mathbf{z}, \tag{3}$$

where $\mathbf{x}$ and $\mathbf{z}$ are the Cartesian unit vectors, perpendicular and parallel to the rotation axis respectively. The radial co-ordinate is designated r and θ the co-latitude. The magnitude of the surface gravity is then found to be

$$|\mathbf{g}_{eff}(\theta)| = \left(\frac{GM}{R_p^2}\right)\delta^{-2}\left[\delta^4\left(\frac{r(\theta)}{R_p}\right)^{-4}\right.$$
$$\left. + \omega^4\delta^{-2}\left(\frac{r(\theta)}{R_p}\right)^2\sin^2(\theta) - 2\omega^2\sin^2(\theta)\delta\left(\frac{r(\theta)}{R_p}\right)^{-1}\right]^{\frac{1}{2}}, \tag{4}$$

where δ is the ratio of equatorial and polar radii, $\delta = \frac{R_e}{R_p}$. Because we assume that every point on the surface can be treated as an equivalent non-rotating star (i.e., we wish to reduce the two-dimensional problem of a rotating star to one dimension), and that the flux vector is nearly perfectly aligned with the gravity vector in a rotating star (Espinosa Lara & Rieutord 2011), the magnitude of the gravity vector is the quantity of interest, not the gravitational field strength in the radial direction.

The local effective temperature is defined using the local flux, $\boldsymbol{F}(\theta)$, and the Stefan-Boltzmann constant, σ as

$$T_{\text{eff}}(\theta)^4 = |\boldsymbol{F}(\theta)|/\sigma. \tag{5}$$

The effective temperature profile is given by the model of Espinosa Lara & Rieutord (2011), which assumes a Roche potential and that the flux at the surface of a star is well approximated by

$$\boldsymbol{F}(\theta) = -f(r, \theta)\boldsymbol{g}_{\text{eff}}, \tag{6}$$

which requires the energy flux to be anti-parallel to the effective gravity. This condition is fulfilled in stars with convective envelopes and is also valid to within a very fine tolerance in stars with radiative envelopes (Espinosa Lara & Rieutord 2011). The function $f(r, \theta)$ is found by demanding that no heat is generated in the envelope (i.e., $\nabla \boldsymbol{F} = 0$) and reads

$$f(r, \theta) = \frac{L}{4\pi GM} \frac{\tan^2\vartheta}{\tan^2\theta}, \tag{7}$$

where ϑ is the solution to

$$\cos\vartheta + \ln\tan\frac{\vartheta}{2} = \frac{1}{3}\omega^2 \left(\frac{r}{R_{\text{e}}}\right)^3 \cos^3\theta + \cos\theta + \ln\tan\frac{\theta}{2}. \tag{8}$$

Alternative gravity darkening laws are available (Slettebak 1949; Lucy 1967; Lovekin et al. 2006; Lipatov & Brandt 2020). We note that the gravity darkening model of Espinosa Lara & Rieutord (2011) predicts that the equatorial flux of a critically rotating star is zero, which might be unphysical.

Lastly, the radial profile can be determined from the Roche equipotential surface (Appendix A) to be

$$\frac{r(\omega, \theta)}{R_{\text{p}}} = (2 + \omega^2)\sqrt{\frac{2 + \omega^2}{3\omega^2\sin^2(\theta)}}\cos\left[\frac{1}{3}\arccos\left(\frac{3}{2 + \omega^2}\sqrt{\frac{3\omega^2\sin^2(\theta)}{2 + \omega^2}}\right) + \frac{\pi}{3}\right]. \tag{9}$$

2.1.2. Mass and angular momentum flux

To quantify the wind over the stellar surface, we shall use the mass-loss rate per unit surface area, or mass-flux, $\dot{m}(\theta)$, which is related to the total mass-loss rate, $\dot{\mathcal{M}}$ via

$$\dot{\mathcal{M}} = \int \dot{m}(\theta)\text{d}S, \tag{10}$$

where dS represents the infinitesimal surface element. Knowledge of the star's shape allows us to compute the above integral as (cf. Gagnier et al. 2019b)

$$\dot{\mathcal{M}} = 2\pi \int \dot{m}(\theta)r^2(\theta)\sqrt{1 + \frac{1}{r^2(\theta)}\left(\frac{\partial r}{\partial \theta}\right)^2}\sin\theta\text{d}\theta, \tag{11}$$

where $r(\theta)$ is given by Eq. (9).

The local angular momentum flux is defined as

$$\dot{\ell}(\theta) = \dot{m}\Omega r^2(\theta)\sin^2\theta \tag{12}$$

and the global angular momentum loss rate is found by integrating again over the stellar surface as

$$\dot{\mathcal{L}} = 2\pi \int \dot{\ell}(\theta)r^2(\theta)\sqrt{1 + \frac{1}{r^2(\theta)}\left(\frac{\partial r}{\partial \theta}\right)^2}\sin\theta\text{d}\theta. \tag{13}$$

2.1.3. Determining surface mass flux

Calculating the surface mass flux of a rotating massive star requires not only knowledge of the general mechanics of radiation-driven winds but also of several rotation specific phenomena and their interplay in driving a wind. As of yet, general mass-loss recipes exist only for non-rotating stars, and even those differ significantly depending on methods and assumptions. It is felt that although the use of a non-rotating wind recipe cannot capture the fine details of physical processes in rotating stars, their use in describing rotating star winds is still beneficial and above all represents an improvement over the almost exclusively used rotationally enhanced mass-loss scheme.

Using the effective surface gravity profile, effective temperature profile and surface shape of a rotating star, we may assign an equivalent non-rotating star to each co-latitude of the rotating star, for which the mass-loss rate is given by a chosen recipe. This equivalent non-rotating star is defined to have the same radius, effective temperature and surface gravity as a given latitude on the rotating star. The surface mass-flux is then, in general

$$\dot{m}(\theta) = \frac{\dot{M}\left(|\boldsymbol{g}_{\text{eff}}(\theta)|, T_{\text{eff}}(\theta), r(\theta), \ldots\right)}{4\pi r(\theta)^2}, \tag{14}$$

where $\dot{M}$ is the function provided by the non-rotating wind recipe. The only requirement for the recipe is that it is a function of, or can be manipulated to be a function of, at least the effective surface gravity, effective temperature and radius.

For the calculations in this work, we shall use the mass-loss recipe of Vink et al. (2001), although in principle any recipe can be used. Here the mass-loss rate is a function of the stellar mass, effective temperature, luminosity and metallicity, Z. For our purposes, we first need to modify the input parameters of the recipe.

The mass and luminosity of a non-rotating star can be described using the effective surface gravity and effective temperature, provided the radius is known. This means that at each latitude of a rotating star, an equivalent non-rotating star would have a different mass (following from the radius and surface gravity of the rotating star) and a different luminosity (following from the effective temperature and radius). To account for this, the mass-dependence must be expressed instead in terms of the surface gravity and radius. As luminosity is determined by the Stefan-Boltzmann law, an effective luminosity for each colatitude on a rotating star can be defined as

$$L_{\text{eff}}(\theta) = 4\pi\sigma r(\theta)^2 T_{\text{eff}}(\theta)^4. \tag{15}$$

This equivalent luminosity represents the luminosity that a non-rotating star, with equal surface properties of a given colatitude, would have. It is therefore this quantity that must be used in place of the luminosity in the mass-loss recipe, which becomes

$$\dot{m}(\theta) = \frac{\dot{M}\left(\frac{|\boldsymbol{g}_{\text{eff}}(\theta)|r(\theta)^2}{G}, T_{\text{eff}}(\theta), L_{\text{eff}}(\theta), Z\right)}{4\pi r(\theta)^2}. \tag{16}$$

2.2. Critical rotation velocity

For a star, there exists a critical (or break-up) rotation velocity at which material becomes unbound from the stellar surface. Although a simple concept, there are several nuances which shall be discussed here. In this work we assume that the critical velocity is attained when the centrifugal and gravitational forces balance, however in general this is likely only an approximation.

In massive stars the force from radiation itself contributes to the force balance, and thus has been proposed to reduce

the critical velocity (Langer 1997). The acceleration produced by radiation is proportional to the flux and opacity, which are both effected by rotation. As first argued by Glatzel (1998), when a luminous star rotates very quickly, gravity darkening causes the equatorial flux to weaken strongly, suggesting that the appropriate limit is the Keplerian one. Although analysis by Maeder & Meynet (2000) determined that below a threshold luminosity (around 60% of the Eddington luminosity), the radiation force indeed plays no role in unbinding material from the surface, the issue is still not clear cut, as discussed in the following.

Gravity darkening is traditionally described by Von Zeipel's Law, which states that effective temperature is proportional to effective gravity to the power of β, with $\beta = 0.25$. Interferometric observations of rapidly rotating stars have demonstrated that gravity darkening is not as strong as predicted by Von Zeipel's Law, with lower β values for faster rotators (Monnier et al. 2007; Zhao et al. 2009; Che et al. 2011; Domiciano de Souza et al. 2014). These observations are generally consistent with two-dimensional numerical models (Espinosa Lara & Rieutord 2013) and analytic gravity darkening models (Espinosa Lara & Rieutord 2011), but one star, β Cassiopeiae, appears to exhibit much weaker gravity darkening than expected (Che et al. 2011), perhaps exposing weaknesses in our understanding of gravity darkening. Weaker gravity darkening would result in a stronger radiative force at the equator, hence helping to reduce the critical velocity.

The surface opacity of a rotating star is also uncertain. Maeder & Meynet (2000) assumed that the region with the highest opacity would be the equator, as this is the coldest part of the surface. However, the centrifugal force also causes a decrease in the matter density at the equator, consequently decreasing the opacity. Two-dimensional numerical models of stars on the zero-age-main-sequence suggest that the effect of decreasing density dominates, thus a fast rotating star is predicted to have a lower equatorial opacity than an equivalent non-rotating star (Gagnier et al. 2019a), meaning that radiative acceleration is unable to contribute to the force balance. However there may be some exceptions. Firstly stars may suffer the effects of opacity bumps caused by recombination of certain species (notably hydrogen, helium and iron; Iglesias & Rogers 1996), that could drastically alter the opacity profile over the surface of the star. Secondly in very hot stars, where the opacity is dominated by electron scattering, the surface opacity is largely independent of temperature and thus spatially uniform. Such a case would need careful study to determine whether the break-up velocity is affected.

Classical Be stars are fast rotators with a decretion disc, which are believed to be typically rotating at approximately 70% of the Keplerian velocity (Porter 1996; Rivinius et al. 2013; Zorec et al. 2016; Dufton et al. 2022), and in some cases even lower (Huang et al. 2010; Zorec et al. 2016). It may be reasonably supposed that an outflowing disc will affect the structure of its host star, such that the surface flux and opacities may be different when a disc is present, thus altering the break-up velocity. There is evidence to suggest that the threshold rotation rate for the Be phenomenon, assumed to be the true break-up velocity, varies with effective temperature (Cranmer 2005; Huang et al. 2010), with hotter Be stars rotating more slowly than their cool counterparts. It is well understood that hotter stars are closer to the Eddington limit, which may suggest that indeed in the hotter Be stars, radiative acceleration does play a role in unbinding material.

2.3. Numerical method

In order to investigate the effect of our prescription on the evolution of both mass and angular momentum loss rates of rotating stars, we employ the one-dimensional detailed stellar evolution code MESA (Paxton et al. 2019), version 12115. The files required to compute models presented in this work are available online[3]. The adopted physics is largely identical, except for the stellar winds, to that of Brott et al. (2011) and implemented in MESA as by Schootemeijer et al. (2019). The models include internal angular momentum transport achieved by magnetic torques (Spruit 2002) which enforce near solid-body rotation during most of the main-sequence evolution.

We run two sets of models, one using the rotationally enhanced mass-loss scheme as it is usually implemented in MESA (named the standard scheme), where the mass-loss rates are first calculated using the recipe of Vink et al. (2001) and then following Friend & Abbott (1986)[4] increased by a factor of

$$\left(1 - \Omega \sqrt{\frac{R_e^3}{GM(1 - \Gamma)}} \right)^{-0.43}. \tag{17}$$

The second set uses mass-loss rates set by the method outlined in Sect. 2.1 and is named the local scheme. Both sets rely on the wind mass-loss recipe of Vink et al. (2001). This wind recipe includes the bi-stability jump effect (first found by Pauldrach & Puls 1990), where mass-loss rates are theorised to increase dramatically during the transition to temperatures cooler than approximately 22 kK owing to the recombination of Fe IV in the atmosphere (Vink et al. 1999). The impact of the bi-stability jump on mass-loss rates is not certain, with Björklund et al. (2023) noting that 'the drastic $\dot{M}$ increase found in earlier models in this region might simply be an artefact of not being dynamically consistent around the sonic point, and not allowing properly for the feedback between radiative and velocity acceleration'. The quantitative behaviour of models near the jump is also contested (Markova & Puls 2008; Vink 2018; Krtička et al. 2021). We stress that our method is not confined to a particular mass-loss recipe and that several others could be used, for example those of Kudritzki et al. (1989), Sundqvist et al. (2019), Björklund et al. (2023).

For the standard scheme, stellar winds are assumed to be isotropic with the angular momentum loss $\dot{\mathcal{L}}$, given by

$$\dot{\mathcal{L}} = j_{surf} \dot{\mathcal{M}}, \tag{18}$$

where j_{surf} is the specific angular momentum of the distorted surface and $\dot{\mathcal{M}}$ the global mass-loss rate (Paxton et al. 2019). The local scheme computes angular momentum loss according to Eqs. (12) and (13), taking into account both the anisotropic wind and surface deformation caused by rotation.

We compute models with a chemical mixture representing the Large Magellanic Cloud as in Brott et al. (2011). Two initial masses of $10 M_\odot$ and $20 M_\odot$ are chosen to straddle the bi-stability jump. We run models with an initial equatorial rotation velocity of $300 \, \text{km s}^{-1}$ until core hydrogen depletion, defined as a central hydrogen mass fraction of 1×10^{-4}. The chosen rotation velocity represents the typical value for early B-stars found in the Large Magellanic Cloud (Dufton et al. 2013) and corresponds to an initial critical rotation fraction of around 0.45 for both masses.

It is also useful to assess numerical models with varying rotation rates at a fixed point in their evolution. To this end

---

[3] https://zenodo.org/record/7437006
[4] See Lamers & Cassinelli (1999) for a thorough description.
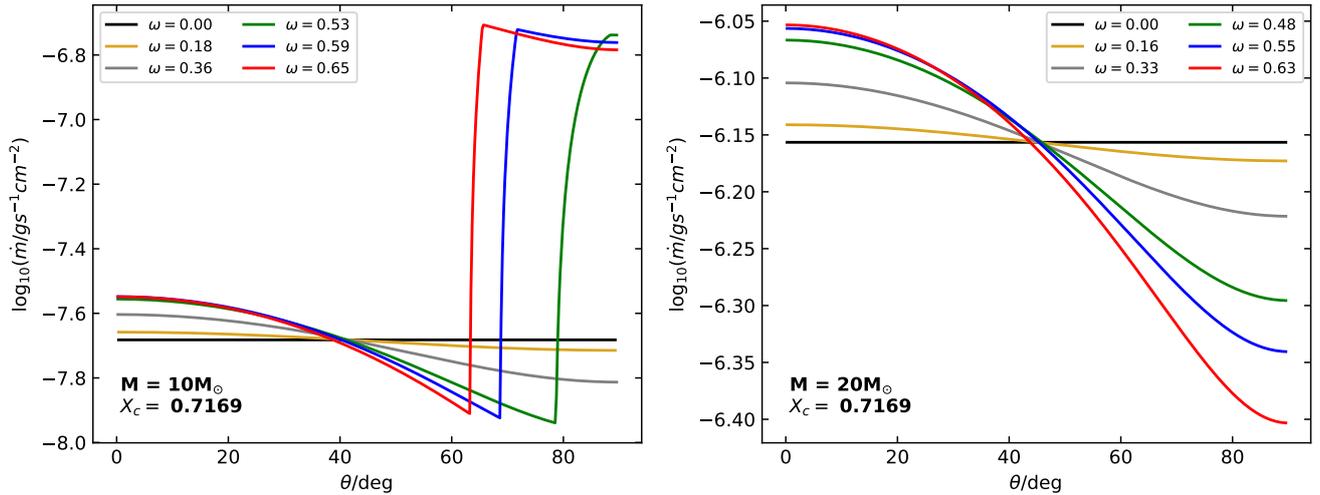
Fig. 1. Mass-loss rate per unit surface area as a function of colatitude, θ, for 10 $M_\odot$ (*left panel*) and 20 $M_\odot$ models (*right panel*) at various rotation rates. All models have burnt 3% by mass of their initial hydrogen (i.e., $X_c = 0.7169$). Critical velocity fraction, ω, is depicted in the legend.

we run models with very small timesteps until the model has burnt 3% by mass of its initial supply of hydrogen in the core ($X_c = 0.7169$). This is approximately the earliest point at which the model finds itself in thermal and nuclear equilibrium and hence is a good point in the star's evolution to investigate. We shall term the point when $X_c = 0.7169$ the zero-age-main-sequence.

Our models are numerically stable until initial critical velocity fractions, ω, of around 0.65, so to investigate stars with faster rotation, an extrapolation is performed. The local wind scheme requires as inputs the stellar mass, rotation rate, polar radius and luminosity.

The polar radius is assumed to be invariant to rotation, so this is known from a non-rotating model. For the luminosity, we extrapolate from the slower rotating models as described in Appendix B up to $\omega = 0.9$. Using the four named quantities, the effective gravity and effective temperature profiles can be calculated (as outlined in Sect. 2.1.1), and resultingly the surface mass-flux. Thus we may investigate the behaviour of our scheme for very fast rotating stars on the zero-age-main-sequence despite not having stellar models at these rotations. Stars born with moderate rotation may evolve to rotate at high critical velocity fractions owing to internal structural changes (Hastings et al. 2020b), so it is important to check the behaviour of our scheme at near critical rotations.

3. Results

3.1. Mass loss on the zero-age-main-sequence

Figure 1 shows the surface mass flux as a function of colatitude for 10 $M_\odot$ and 20 $M_\odot$ models rotating at various rates. All models displayed have a central hydrogen mass fraction of 0.7169, equating to 97% of the initial hydrogen mass fraction. It is seen that for slow rotation, mass flux is stronger at the poles and weaker at the equator. This occurs because rotation results in a hotter pole, relative to the non-rotating case, and a cooler equator, and stellar winds are very sensitive to effective temperature changes.

For faster rotating 10 $M_\odot$ models, mass-flux experiences a jump at colatitudes between 60 and 80° caused by the bi-stability jump. Moving from pole to equator across the stellar surface, effective gravity and hence effective temperature decrease. At

some point, the effective temperature subceeds the 'jump temperature' at which Fe IV recombines to Fe III causing a sudden, dramatic increase in the mass flux, as evidenced in the left panel of Fig. 1. The 20 $M_\odot$ model does not undergo the same phenomenon as here the effective temperature always exceeds the jump temperature.

The global mass-loss rate depends on both the surface mass-flux and the stellar surface area. For the wind recipe of Vink et al. (2001) used in this work, provided the ionisation equilibrium does not change significantly, faster rotation is seen to cause a decreasing surface mass-flux at the equator. Also rotation increases the surface area of the equatorial region due to the equatorial bulge. These two effects can offset one another, causing the global mass-loss rate to be roughly independent of rotation, as exemplified by models shown in Fig. 2. We note that because of the relatively small area covered by the polar region, the polar surface mass-flux does not contribute significantly to the global mass-loss rate.

For the 10 $M_\odot$ model in the local scheme, mass loss decreases slightly with faster rotation, until the bi-stability jump comes into effect at $\omega \approx 0.5$ and drives mass-loss rate up. In contrast, the 20 $M_\odot$ model displays almost no change in mass-loss rates until $\omega \approx 0.3$ and then a small increase thereafter, due to the effect of the growing surface area of the equator dominating over the diminished equatorial surface mass-flux. We note that, except for models affected by the bi-stability jump, our local scheme produces slightly weaker winds than the standard scheme. Our models show that excluding the effects of the bistability jump, mass-loss rates of a rotating star are not predicted to be significantly different to that of an equivalent non-rotating star.

At very high initial rotation rates, our estimates of the mass-loss rate from extrapolation of the luminosity show that for the 20 $M_\odot$ model, the increase in mass-loss rate is modest, 10% at most. Whereas the cooler 10 $M_\odot$ model displays mass-loss rate enhancement of a factor 9 at $\omega = 0.9$. We are thus confident that our scheme behaves reasonably at near-critical velocities.

3.2. Evolutionary models

Our evolutionary models are presented in Fig. 3 where panels a and b show the evolution of global mass-loss rates. In the standard scheme the bi-stability jump is implemented as a sharp
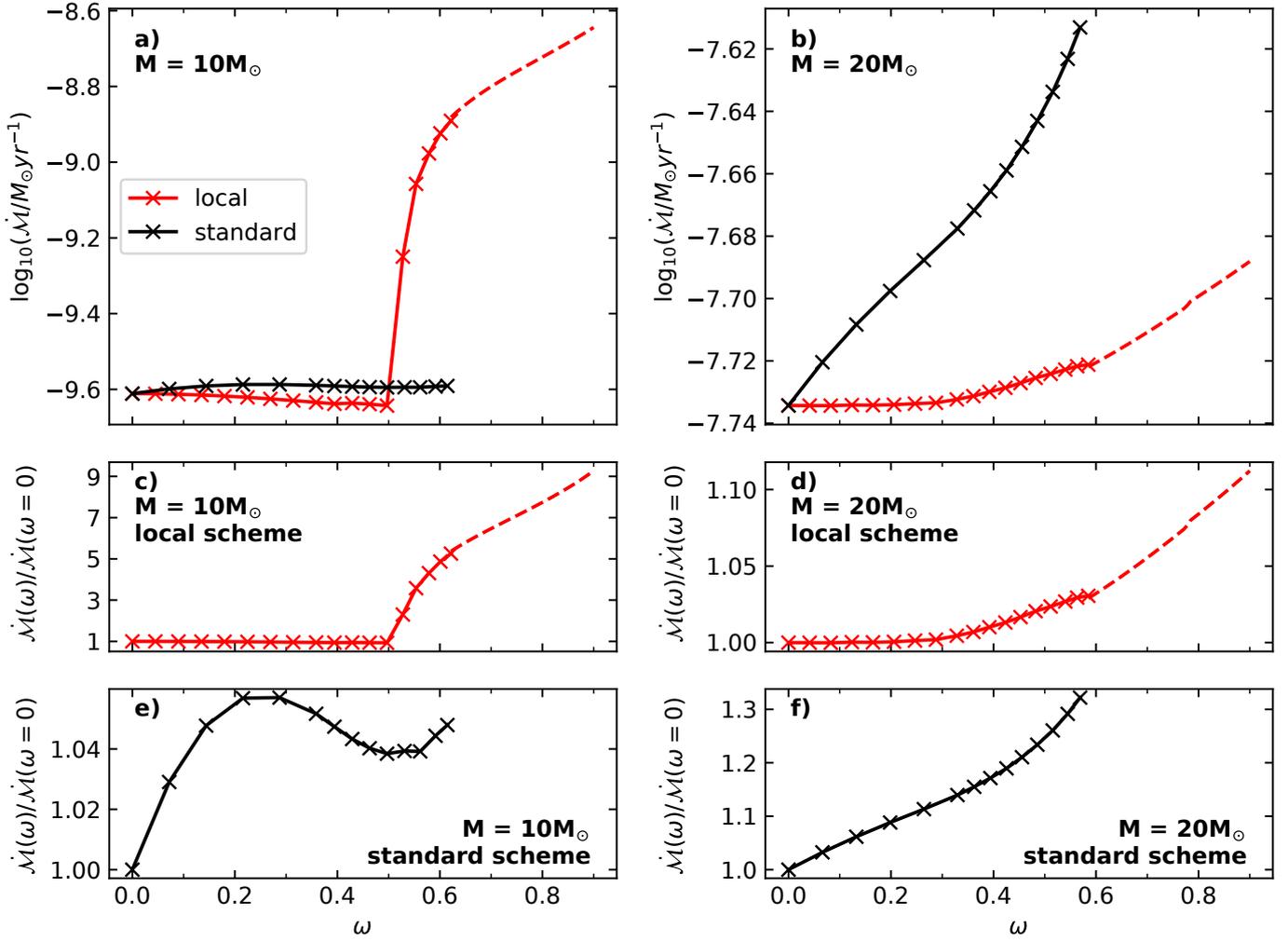
Fig. 2. *Upper panels*: global mass-loss rates as a function of critical velocity fraction, ω, for 10 $M_\odot$ (*left panel*) and 20 $M_\odot$ models (*right panel*). Predictions of the local scheme, where surface mass flux is determined by Eq. (16) and the global mass-loss rate given by Eq. (11), are given in red. The standard scheme, where the mass loss rates are increased by Eq. (17) is depicted in black. All models have burnt 3% by mass of their initial hydrogen (i.e., $X_c = 0.7169$). Dotted lines represent mass-loss rates calculated from extrapolation (see Sect. 2.3). *Lower panels*: ratios of rotating star mass-loss to non-rotating star mass loss, $\dot{\mathcal{M}}(\omega)/\dot{\mathcal{M}}(\omega = 0)$, for each combination of mass-loss model and initial mass as given in each panel.

jump, however in the local scheme the jump is more gradual, owing to the fact that as the star cools, the region of the surface affected by the jump grows, causing the mass-loss to also gradually increase.

Panels c and d of Fig. 3 show the normalised specific angular momentum loss of our evolutionary models, given as

$$\frac{\dot{\mathcal{L}}}{\frac{2}{3}\dot{\mathcal{M}}\Omega R_{eq}^2}. \tag{19}$$

This is a unitless quantity that describes the strength of angular momentum loss independently of the rotation rate and mass-loss rate. A spherical star with an isotropic wind (i.e., a slowly rotating star) has a normalised specific angular momentum loss of 1. Values larger than unity imply that the star is losing more angular momentum per unit mass than the spherically symmetric case and that spin-down will occur more rapidly. This quantity is sensitive to both the anisotropy of the wind and the deformation of the star. We see that away from the bi-stability jump temperatures, models using the local scheme suffer lower angular momentum losses than the standard scheme. This reduced normalised specific angular momentum loss means that stars may be

able to maintain faster rotation rates. The opposite is true when mass-flux across the stellar surface is increased due to the bi-stability jump, because the model loses large quantities of mass from the equatorial regions.

Panels e and f of Fig. 3 show the equatorial velocities of our models. Comparing the velocities near the end of the main-sequence, we see that the local scheme displays larger rotational velocities, due to the generally lower mass-loss and normalised specific angular momentum losses as shown in the upper two panels. The effect is greatest in the 20 $M_\odot$ model, with velocities increased by roughly 10% compared to the standard scheme.

4. Uncertainties

When attempting to describe a two-dimensional phenomenon with a one-dimensional model there are inevitably shortcomings. Most stellar evolution codes compute the structure of a rotating star by applying certain corrections to the stellar structure equations that are designed to produce the average properties along an isobar (for a detailed description see Heger et al. 2000). This approximation may break down under certain conditions,
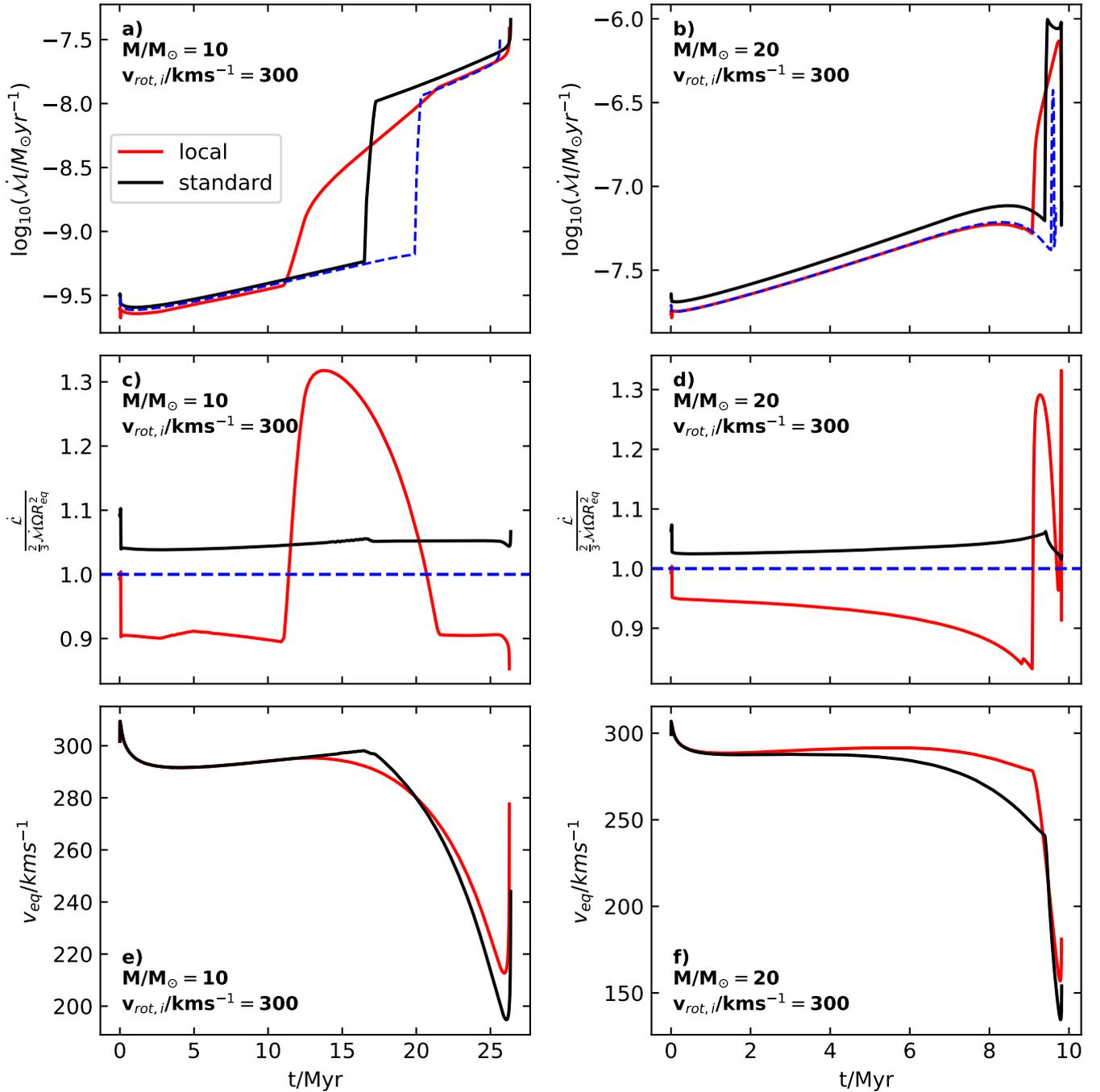
Fig. 3. *Upper panels*: evolution of global mass-loss rate as a function of time. The blue dashed line shows the mass-loss rate computed from a non-rotating model. *Central panels*: evolution of normalised specific angular momentum loss, as given by Eq. (19) (see text for details). In the limit of slow rotation this quantity is equal to unity, shown by the blue dashed line. *Lower panels*: evolution of the equatorial rotational velocity as a function of time. *The left panels* show a 10 $M_\odot$ model, the right panels a 20 $M_\odot$ model. Predictions of the local scheme, where surface mass flux is determined by Eq. (16) and the global mass-loss rate given by Eq. (11), are given in red. The standard scheme, where the mass loss rates are increased by Eq. (17) is depicted in black. All rotating models have initial equatorial rotational velocities of 300 km s^{-1}.

for example when the surface temperature at the equator is cool enough for helium-I to form yet the pole it is not, the opacity will vary greatly over the stellar surface causing different physical conditions at the equator and pole. In such a case, average quantities will not capture this diversity and may lead to different structures as computed by one and two-dimensional models.

A weakness of our wind scheme is that to determine the local mass-flux, we use a mass-loss recipe that was calculated for non-rotating stars. Such a recipe naturally ignores rotational

phenomena like non-spherical geometry and the effects of limb-darkening. What is more, the ionisation of the wind is expected to be sensitive to radiation from various latitudes on the stellar surface (Petrenz & Puls 2000), which could effect the mass-loss rates.

A fundamental assumption of our scheme is that the wind is launched from the stellar surface and moves parallel to the photon flux (which is assumed to correspond to the direction of the effective gravity). In reality, a wind is continually accel-

erated until it reaches the terminal wind velocity and during this acceleration a wind particle may be influenced by photons streaming at an oblique angle to the stellar surface. This would introduce a non-radial line force (particularly in combination with a polar-angle dependent velocity field), which may alter the wind structure and angular momentum content (Owocki et al. 1996; Gayley & Owocki 2000). What is more, in our model the effective gravity, and hence flux, have a non-radial direction, while most one-dimensional mass-loss recipes assume a purely radial flux.

When running models at large critical velocity fractions, caution must be exercised, as one may be extrapolating from the non-rotating wind recipe. For any given wind recipe, there are bounds in which the input parameters are valid and it is entirely possible that under extreme rotation the local surface conditions fall outside of the prescribed bounds. Should this occur, a second suitable wind recipe could be used to give the local mass flux for the effected regions, for example a cool star wind recipe may be appropriate for describing the equatorial wind.

5. Applicability of the local mass-loss scheme

The pre-requisites for the mass-loss scheme presented here are that the star's shape needs to be well described by the Roche potential and the gravity darkening law of Espinosa Lara & Rieutord (2011) must be valid. This is in general true for both convective and radiative stars that do not have near-Eddington luminosities and are rotating sub-critically (Espinosa Lara & Rieutord 2011), however there are further cases where these conditions are not met and other special cases which will be discussed here.

For very luminous stars, the radiative acceleration may facilitate the unbinding of material from the stellar surface at lower rotation velocities than the Keplerian velocity. As this effect is ignored in our formalism, our scheme is not appropriate for very luminous objects. In light of the findings of Maeder & Meynet (2000), we would conservatively advise the limit of applicability to be 60% of the Eddington luminosity. Improved gravity darkening laws and a more detailed account of the stellar surface opacity could possibly allow for applying our scheme also at higher Eddington factors, but this still needs to be investigated (see Sect. 2.2).

Furthermore, luminous stars may suffer the effects of inflation whereby radiation pressure "inflates" the star, producing a very tenuous, extended envelope (Ishii et al. 1999; Sanyal et al. 2015). If the radiation pressure deviates from spherical symmetry, then the strength of inflation will vary according to latitude, suggesting that the star's shape is not well described by the Roche potential. Our mass-loss scheme is therefore not applicable to inflated stellar models. Inflation is expected to occur at masses above $30\,M_\odot$ for stars with galactic metallicity, but for much higher masses at lower metallicities (Sanyal et al. 2017).

A star may suffer the effects of additional forces which can alter the surface effective gravity beyond the Roche potential. Examples include radial pulsations, accelerations from rapid expansion or contraction and a close binary companion. Such cases would need to be dealt with separately, although our scheme could be extended to them.

While our scheme may be applied to rapid rotators, once a star reaches critical velocity, evolutionary models demand that the star lose enough angular momentum to maintain sub-critical rotation. It is not entirely clear how this may happen, there are several possibilities. The star may undergo a "mechanical mass-loss episode", losing the required angular momentum through

increased mass loss at the equator only (Granada et al. 2013). The other extreme is to lose angular momentum via an isotropic wind, as is currently done in MESA models, but one may also prescribe for mass to be lost from the surface in any configuration. For at least some fast rotating stars in nature, a circumstellar decretion disc forms that can efficiently drain angular momentum from the star (Krtička et al. 2011). For lower-mass stars ($M \lesssim 10\,M_\odot$), the required angular momentum loss rates, and correspondingly required mass loss rates are low (Granada et al. 2013), hence the evolution of the star is largely insensitive to the mechanics of angular momentum loss at the critical velocity. This is not true for more massive stars, which can lose upwards of 10% of their initial mass from rotating critically (cf. Table 1 of Granada et al. 2013), so how exactly angular momentum is drained from a critical rotator becomes important. Therefore we advise caution when stellar models achieve critical rotation.

A crucial aspect of our formulation is that it demands that the wind is sensitive only to the local conditions of where on the surface it was launched from. An example where this condition is violated is the dust-driven winds of asymptotic giant branch stars. Global pulsations may lead to dust formation in the outer atmosphere, which is essential for the wind driving (Winters et al. 2000).

6. Comparison to other studies

Several authors have investigated the problem of stellar winds and rotation by directly taking into account rotation specific physics. The prescription presented here is better described as an adaptation of a wind model for non-rotating stars, so it is useful to compare our results to previous studies.

It has been reported that radiation-driven winds are most strongly affected by gravity darkening directly beneath the point from which the wind was launched (Cranmer & Owocki 1995). This suggests that the wind is only sensitive to the point form which it is launched, justifying our use of a non-rotating wind model as our basis. It is also encouraging as limb-darkening, which is not accounted for in our prescription, is deemed unimportant (Cranmer & Owocki 1995).

Petrenz & Puls (2000) calculated wind models using the concept of a mean irradiating atmosphere and found the winds to have a prolate structure, with increased mass-flux at the pole. Furthermore, for B-type stars, rotation is predicted to diminish mass-loss rates, with models rotating at around 80% of critical velocity displaying mass-loss rates a few percent lower than corresponding non-rotating models (cf. Table 4 of Petrenz & Puls 2000). Similarly, we predict a very weak rotation dependence on mass-loss rates (away from the bi-stability jump), although our models can show enhanced or reduced winds depending on the stellar parameters. Müller & Vink (2014) also find that mass-loss actually diminishes due to the effects of rotation, in contrast to the rotationally enhanced wind schemes.

Pelupessy et al. (2000) focused on B[e] stars using models including the bi-stability jump effect. They report that rotation, in general, enhances mass-flux from the poles but hardly changes that of the equator. The spatial variation in mass-flux predicted by Pelupessy et al. (2000) shows a discontinuity owing to the bi-stability jump, albeit not as steep as in our results (cf. Fig. 9 with our Fig. 1). Pelupessy et al. (2000) predict the winds of a $20\,M_\odot$ star to grow stronger with rotation, with rotation at 60% of critical velocity boosting mass-loss by 16% compared to the non-rotating case (cf. Table 3).

The works mentioned above computed only stationary models, however different stellar parameters were used in each case.

Fig. 4. Comparison of the global mass-loss rates (*left panel*) and equatorial effective temperatures (*right panel*) predicted by this work and that of Gagnier et al. (2019a). Shown are the results of 15 $M_\odot$ models with solar metallicity and initial critical velocity fraction, $\omega = 0.5$. Predictions of this work are plotted as grey lines, and those of Gagnier et al. (2019a) as cyan lines. The *x*-axis depicts the central hydrogen mass fraction normalised to the initial value. The panels in this figure are directly comparable to Figs. 13 and 14 of Gagnier et al. (2019a).

For example the 20 $M_\odot$ model of Petrenz & Puls (2000) had a radius of 20 $R_\odot$, while that of Pelupessy et al. (2000) was more than twice as large, 47 $R_\odot$. The fact that the resulting relationships between rotation and mass-loss rates disagree is therefore not surprising.

The work of Gagnier et al. (2019a) differs from this study twofold. Firstly, the two-dimensional ESTER code (Espinosa Lara & Rieutord 2013) was used to compute the stellar structure, whereas here we rely on a one-dimensional code. Secondly, the local mass-flux was calculated by calibrating the one-dimensional CAK theory (Castor et al. 1975) to the wind recipe of Vink et al. (2001). Given that models presented here and in Gagnier et al. (2019a) are based on the same wind recipe of Vink et al. (2001), a comparison between the two will highlight differences in the underlying methods.

To compare our scheme to that of Gagnier et al. (2019a), a 15 $M_\odot$ model has been computed with solar metallicity as in Brott et al. (2011) and initial critical angular velocity fraction, $\omega = 0.5$. Figure 4 compares the results of the two methods. Firstly, we see that the equatorial effective temperatures predicted by both models agree to within around 2000 K, and to within several hundred Kelvin during the early evolution. This discrepancy can largely be credited to the differences of the structures predicted by two and one-dimensional models and the implementation of rotational mixing.

A disadvantage of the method of Gagnier et al. (2019a) is that the required calibration of the surface mass-flux is sensitive to the strength of surface gravity, meaning that properly, (as stars evolve to lower surface gravities) a new calibration must be made at every timestep (see Sect. 4.2 of Gagnier et al. 2019b). However, as the calibration is onerous, it was only carried out for models on the zero-age-main-sequence, meaning that "the local mass-flux may be underestimated by a factor ∼1.7 at most". Our scheme does not suffer from this issue, which may explain partly why our model predicts slightly higher mass-loss rates in panel a of Fig. 4. Both models however show the same general trend, with a gradual increase in mass-loss rates once the equatorial effective temperature cools below 22–23 kK. The relative increase in mass-loss rates brought about by the bistability jump is approximately the same in both models. The jump temperature differs slightly in the two models because the jump

temperature is sensitive to the stellar luminosity (see Eq. (16) of Gagnier et al. 2019a). Both models naturally have different luminosities owing to their different structures, as mentioned earlier. We find it encouraging that our relatively simple scheme behaves similarly to a two-dimensional, more advanced model.

7. Conclusions

We have presented a new and simple to implement prescription for the mass and angular momentum loss rates of rotating massive stars. This represents an improvement over the widely used rotationally enhanced mass-loss schemes as we calculate the two-dimensional mass-flux over the stellar surface and are able to compute the angular momentum loss resulting from an anisotropic wind originating from a distorted star. Our method involves using a mass-loss recipe for non-rotating stars to determine the local mass-flux across the surface of a rotating star, which is then integrated to give global mass and angular momentum loss rates.

In general we notice that, away from the bi-stability jump temperature, mass-loss rates are slightly diminished compared to the rotationally enhanced mass-loss scheme. The local mass-flux scheme has the effect of smoothing out the bi-stability jump as the increase in mass-loss rate is implemented locally on the star's surface, not globally, also observed in the models of Gagnier et al. (2019a). Our models show that the presence of the bistability-jump causes a strong relationship between rotation and mass-loss. If the bistability-jump does not in fact operate in nature, as suggested by theoretical wind models of Björklund et al. (2023), moderate and even fast rotation is not predicted to strongly alter mass-loss compared to the non-rotating case. We see evidence that the detailed relationship between rotation and wind strength is complex, with mass-loss rates being either decreased or increased depending on the surface properties of the star.

Our aim to provide a scheme for one-dimensional stellar evolution codes will of course mean that simplifications must be made. In spite of our scheme's shortcomings, comparisons with similar, more physically comprehensive works deliver a broad agreement in global mass-loss rates.

Our methods are relevant to several areas of stellar astrophysics where the evolution of angular momentum plays a decisive role. For example, Be stars are known to be fast rotators, so are expected to have strongly anisotropic winds and large distortions. Models such as those presented here may therefore be used to investigate evolutionary properties of Be stars. Secondly, the evolution of models along a chemically homogeneous pathway can be interrupted by spin-down caused by stellar winds (Yoon et al. 2006). The calculations presented here suggest that angular momentum loss has been generally overestimated in stellar models, suggesting that chemically homogeneous evolution (e.g., Hastings et al. 2020a) may be more common or easier to maintain than previously thought. In the future, our wind prescription may be implemented in the next grids of stellar evolution models in order to gain further insights into the physics of rotating massive stars.

References

Aguilera-Dena, D. R., Langer, N., Antoniadis, J., & Müller, B. 2020, ApJ, 901, 114
Björklund, R., Sundqvist, J. O., Singh, S. M., Puls, J., & Najarro, F. 2023, A&A, accepted, https://doi.org/10.1051/0004-6361/202141948
Brott, I., de Mink, S. E., Cantiello, M., et al. 2011, A&A, 530, A115
Castor, J. I., Abbott, D. C., & Klein, R. I. 1975, ApJ, 195, 157
Che, X., Monnier, J. D., Zhao, M., et al. 2011, ApJ, 732, 68
Collins, G. W., I. 1965, ApJ, 142, 265
Cranmer, S. R. 2005, ApJ, 634, 585
Cranmer, S. R., & Owocki, S. P. 1995, ApJ, 440, 308
Curé, M. 2004, ApJ, 614, 929
Curé, M., & Rial, D. F. 2004, A&A, 428, 545
Curé, M., Rial, D. F., & Cidale, L. 2005, A&A, 437, 929
Curé, M., Cidale, L., & Rial, D. F. 2012, ApJ, 757, 142
de Koter, A., Heap, S. R., & Hubeny, I. 1997, ApJ, 477, 792
Domiciano de Souza, A., Kervella, P., Moser Faes, D., et al. 2014, A&A, 569, A10
Dufton, P. L., Langer, N., Dunstall, P. R., et al. 2013, A&A, 550, A109
Dufton, P. L., Lennon, D. J., Villaseñor, J. I., et al. 2022, MNRAS, 512, 3331
Ekström, S., Meynet, G., Maeder, A., & Barblan, F. 2008, A&A, 478, 467
Espinosa Lara, F., & Rieutord, M. 2011, A&A, 533, A43
Espinosa Lara, F., & Rieutord, M. 2013, A&A, 552, A35
Friend, D. B., & Abbott, D. C. 1986, ApJ, 311, 701
Gagnier, D., Rieutord, M., Charbonnel, C., Putigny, B., & Espinosa Lara, F. 2019a, A&A, 625, A88
Gagnier, D., Rieutord, M., Charbonnel, C., Putigny, B., & Espinosa Lara, F. 2019b, A&A, 625, A89
Gayley, K. G., & Owocki, S. P. 2000, ApJ, 537, 461
Glatzel, W. 1998, A&A, 339, L5
Granada, A., Ekström, S., Georgy, C., et al. 2013, A&A, 553, A25
Hastings, B., Langer, N., & Koenigsberger, G. 2020a, A&A, 641, A86
Hastings, B., Wang, C., & Langer, N. 2020b, A&A, 633, A165

Heger, A., Langer, N., & Woosley, S. E. 2000, ApJ, 528, 368
Huang, W., Gies, D. R., & McSwain, M. V. 2010, ApJ, 722, 605
Iglesias, C. A., & Rogers, F. J. 1996, ApJ, 464, 943
Ishii, M., Ueno, M., & Kato, M. 1999, PASJ, 51, 417
Krtička, J., Owocki, S. P., & Meynet, G. 2011, A&A, 527, A84
Krtička, J., Kubát, J., & Krtičková, I. 2021, A&A, 647, A28
Kudritzki, R. P., Pauldrach, A., Puls, J., & Abbott, D. C. 1989, A&A, 219, 205
Lamers, H. J. G. L. M., & Cassinelli, J. P. 1999, Introduction to Stellar Winds (Cambridge: Cambridge University Press)
Langer, N. 1997, in Luminous Blue Variables: Massive Stars in Transition, eds. A. Nota, & H. Lamers, ASP Conf. Ser., 120, 83
Langer, N. 1998, A&A, 329, 551
Lipatov, M., & Brandt, T. D. 2020, ApJ, 901, 100
Lovekin, C. C., Deupree, R. G., & Short, C. I. 2006, ApJ, 643, 460
Lucy, L. B. 1967, ZAp, 65, 89
MacLeod, M., & Loeb, A. 2020, ApJ, 902, 85
Maeder, A. 2009, Physics, Formation and Evolution of Rotating Stars (Berlin: Springer)
Maeder, A., & Meynet, G. 1987, A&A, 182, 243
Maeder, A., & Meynet, G. 2000, A&A, 361, 159
Marchant, P., Langer, N., Podsiadlowski, P., Tauris, T. M., & Moriya, T. J. 2016, A&A, 588, A50
Markova, N., & Puls, J. 2008, A&A, 478, 823
Monnier, J. D., Zhao, M., Pedretti, E., et al. 2007, Science, 317, 342
Müller, P. E., & Vink, J. S. 2014, A&A, 564, A57
Owocki, S. P., Cranmer, S. R., & Blondin, J. M. 1994, ApJ, 424, 887
Owocki, S. P., Cranmer, S. R., & Gayley, K. G. 1996, ApJ, 472, L115
Pauldrach, A. W. A., & Puls, J. 1990, A&A, 237, 409
Pauldrach, A., Puls, J., & Kudritzki, R. P. 1986, A&A, 164, 86
Paxton, B., Cantiello, M., Arras, P., et al. 2013, ApJS, 208, 4
Paxton, B., Smolec, R., Schwab, J., et al. 2019, ApJS, 243, 10
Pelupessy, I., Lamers, H. J. G. L. M., & Vink, J. S. 2000, A&A, 359, 695
Petrenz, P., & Puls, J. 2000, A&A, 358, 956
Petrovic, J., Langer, N., & van der Hucht, K. A. 2005, A&A, 435, 1013
Poe, C. H., & Friend, D. B. 1986, ApJ, 311, 317
Poe, C. H., Friend, D. B., & Cassinelli, J. P. 1989, ApJ, 337, 888
Porter, J. M. 1996, MNRAS, 280, L31
Rieutord, M. 2016, in Physical Processes Leading to Surface Inhomogeneities: The Case of Rotation, eds. J.-P. Rozelot, & C. Neiner, 914, 101
Rivinius, T., Carciofi, A. C., & Martayan, C. 2013, A&ARv, 21, 69
Sanyal, D., Grassitelli, L., Langer, N., & Bestenlehner, J. M. 2015, A&A, 580, A20
Sanyal, D., Langer, N., Szécsi, D.C., Yoon, S., & Grassitelli, L. 2017, A&A, 597, A71
Schootemeijer, A., Langer, N., Grin, N. J., & Wang, C. 2019, A&A, 625, A132
Sen, K., Langer, N., Marchant, P., et al. 2022, A&A, 659, A98
Slettebak, A. 1949, ApJ, 110, 498
Spruit, H. C. 2002, A&A, 381, 923
Sundqvist, J. O., Björklund, R., Puls, J., & Najarro, F. 2019, A&A, 632, A126
Vink, J. S. 2018, A&A, 619, A54
Vink, J. S., de Koter, A., & Lamers, H. J. G. L. M. 1999, A&A, 350, 181
Vink, J. S., de Koter, A., & Lamers, H. J. G. L. M. 2001, A&A, 369, 574
von Zeipel, H. 1924, MNRAS, 84, 665
Winters, J. M., Le Bertre, T., Jeong, K. S., Helling, C., & Sedlmayr, E. 2000, A&A, 361, 641
Yoon, S. C., Langer, N., & Norman, C. 2006, A&A, 460, 199
Zhao, M., Monnier, J. D., Pedretti, E., et al. 2009, ApJ, 701, 209
Zorec, J., Frémat, Y., Domiciano de Souza, A., et al. 2016, A&A, 595, A132
Zwillinger, D. 1996, CRC Standard Mathematical Tables and Formulae (London: Chapman and Hall/CRC)

Appendix A: Shapes of rotating stars

Here we derive the shape of the surface of a rotating star. We assume that the star is well described as a point mass enclosed by a massless envelope and that the polar radius in unaffected by rotation. The surface of the star is then an equipotential given by the Roche potential and reads

$$\frac{GM}{r(\theta)} + \frac{1}{2}\Omega^2 r(\theta)^2 \sin^2(\theta) = \text{constant}, \tag{A.1}$$

with M representing the stellar mass, Ω the angular velocity (which is assumed to be constant across both the surface and through the interior of the star), $r(\theta)$ the radial co-ordinate and θ the co-latitude. We parametrise the strength of rotation with the Keplerian angular velocity, defined using the equatorial radius R_e as

$$\Omega_{\text{Kep}}^2 = \frac{GM}{R_e^3}. \tag{A.2}$$

We let

$$\omega = \Omega/\Omega_{\text{Kep}}. \tag{A.3}$$

It is important to stress that the derivation that follows is only valid for the above parametrisation of rotation.

Combining Eqns. A.1, A.2 and A.3 gives

$$1 + \frac{1}{2}\omega^2 \frac{r^3}{R_e^3}\sin^2(\theta) = \frac{r}{R_e}\left(1 + \frac{\omega^2}{2}\right), \tag{A.4}$$

which after defining

$$\tilde{r} = r/R_e, \tag{A.5}$$

further simplifies to

$$\tilde{r}^3 - \frac{2+\omega^2}{\omega^2\sin^2(\theta)}\tilde{r} + \frac{2}{\omega^2\sin^2(\theta)} = 0. \tag{A.6}$$

Eq. A.6 is a cubic in the form $x^3 + px + q = 0$ (known as a depressed cubic) and has the general solution

$$x_k = 2\sqrt{\frac{-p}{3}}\cos\left[\frac{1}{3}\arccos\left(\frac{3q}{2p}\sqrt{\frac{-3}{p}}\right) - \frac{2\pi k}{3}\right] \tag{A.7}$$

for $k = 0, 1, 2$ corresponding to the 3 cubic roots (Zwillinger 1996).

Here we have $p = -\frac{2+\omega^2}{\omega^2\sin^2(\theta)}$ and $q = \frac{2}{\omega^2\sin^2(\theta)}$ giving

$$\tilde{r}_k = 2\sqrt{\frac{2+\omega^2}{3\omega^2\sin^2(\theta)}}\cos\left[\frac{1}{3}\arccos\left(-\frac{3}{2+\omega^2}\sqrt{\frac{3\omega^2\sin^2(\theta)}{2+\omega^2}}\right) - \frac{2\pi k}{3}\right]. \tag{A.8}$$

The periodicity of the cosine function means that if $y = \cos(x)$ then $-y = \cos(x + n\pi)$ where n is an integer so that $\arccos(-y) = x + n\pi$ and $x = \arccos(y) - n\pi$. Thus Eq. A.8 becomes

$$\tilde{r}_k = 2\sqrt{\frac{2+\omega^2}{3\omega^2\sin^2(\theta)}}\cos\left[\frac{1}{3}\arccos\left(\frac{3}{2+\omega^2}\sqrt{\frac{3\omega^2\sin^2(\theta)}{2+\omega^2}}\right) - \frac{2\pi k}{3} - n\pi\right]. \tag{A.9}$$

To be physical, the solution must be independent of n, which is only achieved when $k = 1$. Choosing $n = -1$ results in

$$\tilde{r}_{k=1} = 2\sqrt{\frac{2+\omega^2}{3\omega^2\sin^2(\theta)}}\cos\left[\frac{1}{3}\arccos\left(\frac{3}{2+\omega^2}\sqrt{\frac{3\omega^2\sin^2(\theta)}{2+\omega^2}}\right) + \frac{\pi}{3}\right]. \tag{A.10}$$

From Eqn. A.4 one can deduce the ratio of equatorial to polar radii, $\frac{R_e}{R_p}$ as

$$\frac{R_e}{R_p} = 1 + \frac{1}{2}\omega^2. \tag{A.11}$$

The final solution is arrived at by combining Eqns. A.10 and A.11 and reads

$$\frac{r(\omega,\theta)}{R_p} = (2+\omega^2)\sqrt{\frac{2+\omega^2}{3\omega^2\sin^2(\theta)}}\cos\left[\frac{1}{3}\arccos\left(\frac{3}{2+\omega^2}\sqrt{\frac{3\omega^2\sin^2(\theta)}{2+\omega^2}}\right) + \frac{\pi}{3}\right]. \tag{A.12}$$

As expected, the expression above gives the equatorial radius at critical rotation to be 1.5 times the polar radius ($\frac{r(\omega=1,\theta=\pi/2)}{R_p} = 1.5$). We note that Eq. A.12 differs from Equation 26 used by Cranmer & Owocki (1995) owing to the use of different definitions of the critical velocity (Cranmer & Owocki (1995) use $\Omega_{\text{crit}}^2 \propto M/(1.5R_p)^3$).

Appendix B: Surface properties of fast rotators close to the zero-age-main-sequence

Our numerical models are unable to compute the structure of a rotating star with initial rotation exceeding around 70% of the critical velocity. However the wind properties of very fast rotating stars on the zero-age-main-sequence may be determined via extrapolation. The wind scheme presented in this paper requires knowledge of the effective gravity and effective temperature profile of a star. To calculate these profiles, only the polar radius, luminosity, mass and rotation rate are required.

To calculate the luminosity of fast rotators on the zero-age-main-sequence, we extrapolate linearly from our models with initial critical fractions between 0.4 and 0.6. We extrapolate the luminosity normalised to the value of the non-rotating model against the initial fraction of critical velocity, where all values are defined at the point when the central hydrogen mass fraction decreases by 3% from its initial value (this we term the zero-age-main-sequence, as it is the earliest point in which the models find themselves in equilibrium). This extrapolation is shown in Fig. B.1 for 10 and 20$M_\odot$ models. We find that rotation rate and luminosity are inversely proportional. This effect is rather weak, with luminosity decreasing by approximately 6% at 60% of critical rotation. The extrapolations suggest that at up to 90% of the critical velocity, the luminosity is reduced by no more than 10% compared to the non-rotating case.

In line with the assumptions of the Roche potential, the polar radius is not affected by rotation, so this value may be assumed from a non-rotating MESA model, depicted graphically by the horizontal dashed yellow line in Fig. B.1. Indeed, as evidenced by Fig. B.1 the numerical models predict that to within a few percent, the polar radius remains unchanged by rotation.

The results of our extrapolations compare favourably to the computed stellar structures of Ekström et al. (2008). One-dimensional models of a 20$M_\odot$ star predict that the luminosity decreases by around 8% over the course of being spun up from stationary to critical rotation (Ekström et al. 2008, Fig. 5).
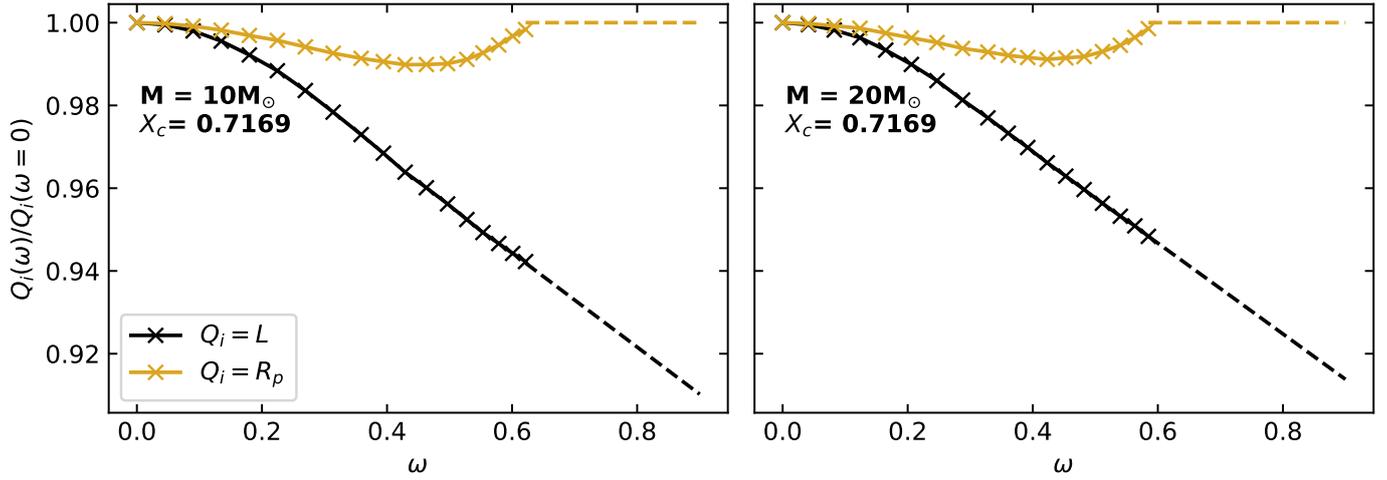
Fig. B.1. Variation of luminosity (black line), L, and polar radius (yellow line), R_p, normalised to the values of a non-rotating star as a function of critical velocity fraction, ω. The left panel shows models with masses $10M_\odot$ and the right panel $20M_\odot$. All models have burnt 3% by mass of their initial hydrogen (i.e. $X_c = 0.7169$). Each cross represents a value computed by a MESA model. Dashed lines show extrapolated values.

While the polar radius is judged to shrink very slightly with increasing rotation, but this is at most a 2% effect (Ekström et al. 2008, Fig. 2), thus justifying the assumption of the Roche potential.

List of Figures

List of Tables

Peer-reviewed publications

1. **Hastings, B.** Langer, N., and Puls, J. (2023):
   A MODEL OF ANISOTROPIC WINDS FROM ROTATING STARS FOR EVOLUTIONARY CALCULATIONS
   Astronomy & Astrophysics, Volume 672, id.A60, 12 pp.

2. Schootemeijer, A., Lennon, D. J., Garcia, M., Langer, N., **Hastings, B.** and Schuermann, C. (2022):
   A CENSUS OF OBE STARS IN NEARBY METAL-POOR DWARF GALAXIES REVEALS A HIGH FRACTION OF EXTREME ROTATORS
   Astronomy & Astrophysics, Volume 667, id.A100, 18 pp.

3. Sen, K., Langer, N., Marchant, P., Menon, A., de Mink, S., Schootemeijer, A., Schürmann, C., Mahy, L., **Hastings, B.**, Nathaniel, K., Sana, H., Wang, C., Xu, X. T. (2022):
   DETAILED MODELS OF INTERACTING SHORT-PERIOD MASSIVE BINARY STARS.
   Astronomy & Astrophysics, Volume 659, id.A98, 33 pp.

4. Wang, C., Langer, N., Schootemeijer, A., Milone, A., **Hastings, B.**, Xu, X-T., Bodensteiner, J., Sana, H., Castro, N., Lennon, D.J., Marchant, P., Koter, A., Mink, S. (2022):
   STELLAR MERGERS AS THE ORIGIN OF THE BLUE MAIN-SEQUENCE BAND IN YOUNG STAR CLUSTERS.
   Nature Astronomy, Volume 6, p. 480-487

5. **Hastings, B.**, Langer, N., Wang, C., Schootemeijer, A. and Milone, A. P. (2021):
   STRINGENT UPPER LIMIT ON BE STAR FRACTIONS PRODUCED BY BINARY INTERACTION.
   Astronomy & Astrophysics, Volume 653, id.A144, 13 pp.

6. **Hastings, B.**, Langer, N. and Koenigsberger, G. (2020):
   INTERNAL CIRCULATION IN TIDALLY LOCKED MASSIVE BINARY STARS: CONSEQUENCES FOR DOUBLE BLACK HOLE FORMATION.
   Astronomy & Astrophysics, Volume 641, id.A86, 15 pp.

7. Wang, C., Langer, N., Schootemeijer, A., Castro, N., Adscheid, S., Marchant, P., and **Hastings, B.** (2020):
   EFFECTS OF CLOSE BINARY EVOLUTION ON THE MAIN-SEQUENCE MORPHOLOGY OF YOUNG STAR CLUSTERS.
   The Astrophysical Journal Letters, Volume 888, Issue 1, article id. L12, 8 pp.

8. **Hastings, B.**, Wang, C. and Langer, N. (2020):
   THE SINGLE STAR PATH TO BE STARS.
   Astronomy & Astrophysics, Volume 633, id.A165, 14 pp.

9. Langer, N., Schürmann, C., Stoll, K., Marchant, P., Lennon, D. J., Mahy, L., de Mink, S. E., Quast, M., Riedel, W., Sana, H., Schneider, P., Schootemeijer, A., Wang, C., Almeida, L. A., Bestenlehner, J. M., Bodensteiner, J., Castro, N., Clark, S., Crowther, P. A., Dufton, P., Evans, C. J., Fossati, L., Gräfener, G., Grassitelli, L., Grin, N., **Hastings, B.**, Herrero, A., de Koter, A., Menon, A., Patrick, L., Puls, J., Renzo, M., Sander, A. A. C., Schneider, F. R. N., Sen, K., Shenar, T., Simón-Días, S., Tauris, T. M., Tramper, F., Vink, J. S. and Xu, X. -T., (2020):
   PROPERTIES OF OB STAR-BLACK HOLE SYSTEMS DERIVED FROM DETAILED BINARY EVOLUTION MODELS.
   Astronomy & Astrophysics, Volume 638, id.A39, 18 pp.